



**Faculteit Wetenschappen
Departement Fysica**

**Graphene-based Membranes and
Nanoconfined Water: Molecular Dynamics
Simulation Study**

**Grafeen-gebaseerde Membranen en
Nano-ingeperkt Water: Moleculaire Dynamica
Simulatie Studie**

Proefschrift ingediend tot het behalen van de graad van
Doctor in de Wetenschappen: Fysica
aan de Universiteit Antwerpen, te verdedigen door

Hossein Ghorbanfekr Kalashami

Promotors

Prof. dr. François Peeters

Prof. dr. Mehdi Neek-Amal

Antwerpen, June 2019

Members of the Jury:

Chair

Prof. dr. Wim Wenseleers, Universiteit Antwerpen, Belgium

Supervisors

Prof. dr. François Peeters, Universiteit Antwerpen, Belgium

Prof. dr. Mehdi Neek-Amal, Shahid Rajaei Teacher Training University, Iran

Members

Prof. dr. Sandra Van Aert, Universiteit Antwerpen, Belgium

Prof. dr. Erik Neyts, Universiteit Antwerpen, Belgium

Prof. dr. Rahul Nair, Manchester University, UK

Prof. dr. Jörg Behler, Georg-August-Universität Göttingen, Germany

Contact Information

Hossein Ghorbanfekr Kalashami

University of Antwerp

Department of Physics

Groenenborgerlaan 171 U210

2020 Antwerpen

Belgium

hgh.comphys@gmail.com

*To my father, Parviz,
who couldn't wait to see his doctor son*

ACKNOWLEDGEMENTS

I wish to express my deepest gratitude to my supervisor, Prof. François Peeters, for giving me the opportunities to pursue my dream of becoming a Ph.D. in physics. I profoundly appreciate the support and guidance he has provided throughout my doctoral study.

I have also been extremely lucky to have a co-supervisor, Prof. Mehdi Neek-Amal, who responded to my questions and queries so promptly and thank him for giving all the encouragement, motivation, and advice. I am indebted to him for sharing his knowledge and experiences during constant discussions particularly in the field of molecular dynamics simulation.

I would like to thank our collaborator from Manchester University, Prof. Rahul Nair, who has provided us the experimental data and fruitful discussions. I also thank Rebeca for her collaborations during our doctoral study.

I would like to express my appreciation to the members of condensed matter theory (CMT) group at the University of Antwerp who are friendly and helped me in every possible way.

Outside academia, I am very grateful to my friends from Antwerp Ichi Dai Kyokushin karate community who are kindly welcome and mentally supportive.

Finally, I must express my gratitude my wife, Simin, for her unconditional support and delicious food.

ABSTRACT

The primary aim of the thesis is the exploration of structural and dynamical properties of graphene-based membranes and nanoconfined water within the framework of large-scale molecular dynamics (MD) simulations. A membrane can be defined as a selective barrier that can form nanochannels able to efficiently separate specific molecules and ions. Controlled transport of water molecules through membranes and capillaries has important applications in water purification and ion sieving. MD simulation is a powerful tool that helps us to understand the underlying physics at the atomic scale of the interactions between water and graphene surfaces, that can have drastic effects. This thesis predicts, on the basis of intensive MD simulations, coupled with experimental measurements, that the shape of the graphene nanobubble can depend critically on the properties of the trapped substance such as the formation of amorphous but layered structured water bubbles caused by the extreme confinement. It provides insights into the effects of the specific material and the van der Waals pressure on the microscopic details of graphene nanobubbles. For example, nanobubbles filled with small hydrocarbons, or water, have a circular, or non-circular shape. In addition, it investigates water permeation through graphene oxide membranes, predicting a significant change in the slippage dynamics of confined water in the presence of surface functional groups. This explains the extremely strong impact of commensurability induced by nanoconfinement, on the intrinsic dynamical properties of water. We study various organic solvents intercalated in a montmorillonite clay membrane, an ionic nanochannel with interlayer metal cations. We are able to explain the solvents' observed swelling properties and anomalous permeation, using polarity and aromaticity as fundamental mechanisms at the molecular scale. The thesis also studies nitrogen-doped monolayer graphene, predicting ripples and weaker mechanical strength due to substitutional doping. Furthermore, it proposes an alternative approach for controlling the stochastic motion of a graphene flake over a graphene substrate, by engineering topological defects in the substrate.

NEDERLANDSTALIGE ABSTRACT

Het belangrijkste doel van de thesis is het onderzoeken van de structurele en dynamische eigenschappen van op grafeen gebaseerde membranen en op nanoschaal opgesloten water met behulp van grootschalige moleculaire dynamica (MD) simulaties. Een membraan kan worden gedefinieerd als een selectieve barrière die nanokanalen kan vormen welke specifieke moleculen en ionen efficiënt kunnen scheiden. Gecontroleerd transport van watermoleculen door membranen en capillairen heeft belangrijke toepassingen in waterzuivering en ionenzeving. MD simulaties zijn een goede manier om de onderliggende fysica op de atomaire schaal van de interacties tussen water en grafeenoppervlakken, welke drastische effecten kunnen hebben, te begrijpen. Deze thesis voorspelt, op basis van intensieve MD simulaties gecombineerd met experimentele metingen, dat de vorm van de grafeennanobubbel zeer sterk afhankelijk kan zijn van de eigenschappen van de opgesloten substantie, zoals de waterbubbel die een amorfe maar gelaagde structuur vormt als gevolg van de extreem nauwe opsluiting. Ze biedt inzichten in de effecten van het specifieke materiaal en de van der Waals druk op de microscopische details van grafeennanobubbels. Zo zijn bijvoorbeeld nanobubbels gevuld met kleine koolwaterstoffen (water) cirkelvormig (niet cirkelvormig). Bovendien onderzoek ik waterdoorlaatbaarheid doorheen grafeenoxidemembranen, waarvoor een significante verandering in de slippagedynamica van opgesloten water wordt voorspeld in de aanwezigheid van oppervlakte functionele groepen. Dit verklaart de extreem grote impact van commensurabiliteit geïnduceerd door opsluiting op nanoschaal, op de intrinsieke dynamische eigenschappen van water. We bestuderen verschillende organische oplosmiddelen geïntercaleerd in een montmorilloniet kleimembraan, een ionisch nanokanaal met interlaag metaalkationen. We zijn in staat om de geobserveerde zwellingeigenschappen en abnormale doorlaatbaarheid van de oplosmiddelen te verklaren. Polariteit en aromaticiteit worden als fundamentele mechanismen op de moleculaire schaal besproken. De thesis bestudeert ook monolaag grafeen gedoteerd met stikstof, waarvoor rimpelingen en verminderde mechanische sterkte worden voorspeld als gevolg van de vervangende dotering. Ze stelt ook een alternatieve aanpak voor het controleren van de stochastische beweging van een

stukje grafeen over een grafeensubstraat voor, door het construeren van topologische defecten in het substraat.

TABLE OF CONTENTS

	Page
1 Introduction	1
1 General introduction	3
1.1 Graphene	5
1.1.1 A brief history	5
1.1.2 Synthesis	7
1.1.3 Characterization	8
1.1.4 Properties	8
1.2 Graphene-based materials	9
1.2.1 Doped graphene	9
1.2.2 Polycrystalline graphene	11
1.2.3 Graphene nanobubble	13
1.2.4 Graphene-oxide	15
1.2.5 Graphene-oxide membranes	17
1.3 Water	20
1.3.1 Molecular structure	20
1.3.2 Hydrogen bond	21
1.3.3 Nanoconfinement	22
1.4 Computer simulation	24
1.5 Outline	25
2 Methodology	29
2 Theoretical framework	31

2.1	Quantum Physics	31
2.1.1	Schrödinger equation	31
2.1.2	Born-Oppenheimer approximation	32
2.1.3	Hellmann-Feynman forces	34
2.1.4	Potential energy surface	34
2.1.5	Moving atoms	36
2.2	Statistical thermodynamics	38
2.2.1	Thermodynamic limit	38
2.2.2	Microscopic states	40
2.2.3	Phase space	40
2.2.4	Time average	41
2.2.5	Thermal equilibrium	42
2.2.6	Ensemble average	42
2.2.7	Ergodic theorem	43
2.2.8	Microcanonical ensemble	43
2.2.9	Canonical ensemble	44
3	Molecular dynamics simulations	49
3.1	Introduction	49
3.2	Integration scheme	50
3.3	MD algorithm	53
3.4	Statistical ensemble	54
3.4.1	Isothermal ensemble	56
3.4.2	Isobaric ensemble	61
3.5	Molecular modeling	62
3.5.1	Bond-stretching	63
3.5.2	Bond-bending	64
3.5.3	Dihedral motions	64
3.5.4	Non-bonded interactions	66
3.6	Force fields	68
3.6.1	Parameterizing force field	69
3.6.2	Popular force fields	69
3.6.3	Machine learning potentials	75
3.6.4	Importance of force field	77

4	Methods for analysis of MD results	79
4.1	Structural properties	79
4.1.1	Radial distribution function	80
4.1.2	Coordination number	82
4.2	Hydration Properties	83
4.2.1	Hydrogen bonds	83
4.3	Dynamical properties	85
4.3.1	Diffusion coefficient	85
4.3.2	Time correlation	86
4.3.3	Green-Kubo relation	86
4.3.4	Viscosity coefficients	88
4.3.5	Friction coefficient	89
4.3.6	Slip length	90
4.4	Elastic properties	91
3	Results	95
5	N-doped graphene: polarization and structural properties	97
5.1	Introduction	98
5.2	The model and computational methods	99
5.3	Results and discussion	101
5.3.1	Charge distribution and electric dipole	101
5.3.2	Structural deformations	103
5.3.3	The formation energy	105
5.3.4	The Young's modulus and the breaking of doped graphene	107
5.4	Conclusions	110
6	Spatial design and control of graphene flake motion	111
6.1	Introduction	112
6.2	The model and method	113
6.3	Energy analysis: pristine and LAGBI system	114
6.4	Force analysis at finite temperature	117
6.5	Backscattering	118

6.6	Discussion and conclusions	120
7	Graphene nanobubbles	123
7.1	Introduction	124
7.2	Methods	126
7.2.1	MD simulations	126
7.2.2	AFM measurements	128
7.3	Results	129
7.3.1	Van der Waals pressure	129
7.3.2	Helium bubble	131
7.3.3	Water bubble	134
7.3.4	Hydrocarbon bubble: Ethanol and Hexadecane	136
7.3.5	Stress calculations	139
7.3.6	Salt (NaCl) bubble	139
7.3.7	Layered structure	142
7.3.8	Size effects	144
7.4	Discussion	145
8	Nanoconfined water in graphene oxide capillaries	149
8.1	Introduction	150
8.2	Model and methods	151
8.2.1	MD simulations	152
8.2.2	Dynamical coefficients	154
8.3	Surface charge effects	155
8.3.1	Diffusion coefficient	156
8.3.2	Viscosity	156
8.3.3	Friction coefficient	158
8.4	Effects of ions	159
8.5	Conclusions and discussion	161
9	Confined organic molecules in clay mineral membranes	167
9.1	Introduction	168
9.2	The Model and methods	169
9.3	Results	171

9.3.1	Swelling properties	171
9.3.2	Aromaticity effects	173
9.4	Future work	176
10	Summary	177
10.1	Summary	177
10.2	Outlook	180
A	Appendix A	181
A.1	Different defects in the substrate	181
A.2	Energy barriers due to LAGBI	181
A.3	Variation of the force with size of flake	182
A.4	Trajectory above perfect graphene	183
A.5	Velocity variations	183
A.6	Channel design	184
B	Appendix B	189
B.1	Bubble elasticity	189
B.2	Bubble volume and radius calculation	192
B.3	Solvents	193
B.4	Atomic force microscopy measurements	193
B.5	Deformation profile	194
B.6	The effect of bubble size on density profile	196
B.7	The effects of boundary stress	197
B.8	The effect of adhesion energy	197
C	Appendix C	201
C.1	OPLS model for Graphene Oxide	201
	Bibliography	205
	List of publications	239
	Cirriculum Vitae	241

LIST OF ABBREVIATIONS

2D	Two-dimensional
MD	Molecular dynamics
MC	Monte Carlo
AIMD	<i>Ab initio</i> Molecular dynamics
CPMD	Car-Parrinello molecular dynamics
DFT	Density functional theory
KS	Kohn-Sham
LAMMPS	Large-scale atomic/molecular massively parallel simulator
vdW	Van der Waals
MSD	Mean square displacement
RDF	Radial distribution function
ACF	Auto-correlation function
VACF	Velocity auto-correlation function
EMD	Equilibrium molecular dynamics
GK	Green-Kubo relation
LJ	Lennard-Jones
PES	Potential energy surface
ML	Machine learning
GAP	Gaussian approximated potential
NNP	Neural network potential

NEMD	Non-equilibrium molecular dynamics
HB	Hydrogen bond
CNT	Carbon nanotube
VMD	Visual molecular dynamics
FFT	Fast Fourier transform
AIREBO	Adaptive intermolecular reactive empirical bond order
OPLS	Optimized potentials for liquid simulations
GB	Grain boundary
LAGB	Large-angle grain boundary
AFM	Atomic force microscopy
FFM	Frictional force microscopy
STM	Scanning tunneling microscope
GNB	Graphene nano bubble
GO	Graphene-oxide
NG	Nitrogen-doped graphene
MB	Maxwell-Boltzmann

Part 1

Introduction

GENERAL INTRODUCTION

Graphene has emerged as the exotic material of the 21st century, and received world-wide attention due to its exceptional properties. Graphene and its derivatives are being studied in nearly every field of science and engineering [1]. In particular, permeation through nanoporous graphene and graphene-based membranes is important in the design of materials with dimensions approaching the size of small ions and molecules with applications in filtration, separation, and desalination. R. Nair *et al.* [2] for the first time observed that submicrometer-thick membranes made from graphene oxide (GO) can be completely impermeable to liquids, vapors, and gases, including helium, but these membranes allow unimpeded permeation of water. Recent progress made by K.-G. Zhou *et al.* [3] has shown precise electrical control over water transport through micrometre-thick graphene-oxide membranes from ultrafast permeation to complete blocking that is essential for developing smart membrane technologies for artificial biological systems, tissue engineering and filtration. Alongside, many researches have focused on improving ion selectivity and transport through novel nanosize membranes by mainly investigating how to control physical confinement, the interlayer spacing within an Ångstrom-scale, and achieve accurate ion sieving and selective ionic transport [4, 5]. J. Abraham and *et al.* [6] demonstrated a simple scalable method to obtain graphene-based membranes with limited swelling, which exhibit 97% rejection for NaCl aqueous solution with major applica-

tions in desalination of sea water. B. Grosjean *et al.* have recently conducted a computational study on hydroxide OH^- ions in water near graphene and hexagonal boron nitride layers. They found that the hydroxide species shows weak physisorption on the graphene surface while it exhibits also strong chemisorption on the h-BN surface. As a result, the OH^- is shown to keep very fast lateral dynamics and interfacial mobility within the physisorbed layer on graphene [7].

Despite the considerable number of experimental studies, few theoretical works have addressed such systems and investigated the anomalous behaviors of recently fabricated nanomembranes. The exceptional water permeation through graphene-oxide membrane is believed to occur along a network of pristine graphene channels that develop between functionalized areas of GO sheets [5]. However, the underlying mechanism still remains a mystery because of unusual fundamental behavior arising at the molecular scale [8]. Moreover, interactions between liquid and GO surface functionals that play a dominant role in nanofluidic transport, structural changes of materials encapsulated by nanocapillaries because of extreme confinement, and chemistry responsible for selectivity of ions remain poorly understood [9].

In this thesis, I employ large-scale molecular dynamics simulation¹ as a central tool to probe interested structural and dynamical properties of graphene-based systems and nanoconfined water from interactions and dynamics of atoms. Novel insights will be provided into some of the observed (unusual) behaviors due to low-dimensionality and extreme confinement from the atomic perspective.

This chapter firstly presents a short review of graphene which is the base material during my Ph.D. study, then it introduces several graphene-based materials that are being investigated later on. It continues by giving an overview of graphene-oxide membrane in particular and its applications, the molecular structure of water, 2D ice, and finally an overview of the relevant computer simulation methodology.

¹As implemented in LAMMPS software package [10].

1.1 Graphene

1.1.1 A brief history

Graphene is a crystalline allotrope of carbon in the form of a two-dimensional honeycomb lattice structure where each atom has in-plane sp^2 -hybridized covalent bonds that are strong and stable with a bond length of 1.42 \AA (see Fig. 1.1) [11]. Graphene as an atomic thin material² has gained great attention since it has been experimentally fabricated using the micromechanical exfoliation by Andre Geim and Konstantin Novoselov at the University of Manchester [12]. This groundbreaking achievement and the observatory of novel physical phenomena has led them to win the Nobel Prize in physics in 2010 [13]. After the realization of graphene in 2004, a considerable number of researches have been conducted to explore various properties of graphene that in some cases turned out to be extraordinary such as rich chemistry, high electrical and thermal conductivity, elasticity, and electronics with great importance in both fundamental research and practical applications.

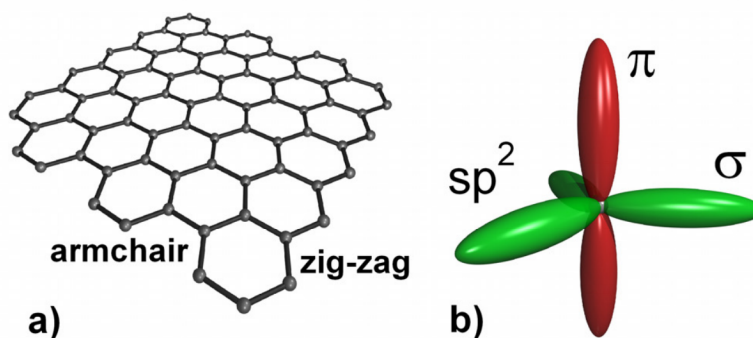


FIGURE 1.1. (a) Schematic of a graphene crystallite with characteristic armchair and zig-zag edges (b) Schematic of electron σ -orbitals (sp^2 -hybridization) and π -orbital of one carbon atom in graphene. The figures are adapted from Ref. [14].

It must be noted that abundant and naturally occurring graphite has been known as a mineral for nearly 500 years which is made of stacked layers of

²Single or few layer(s)

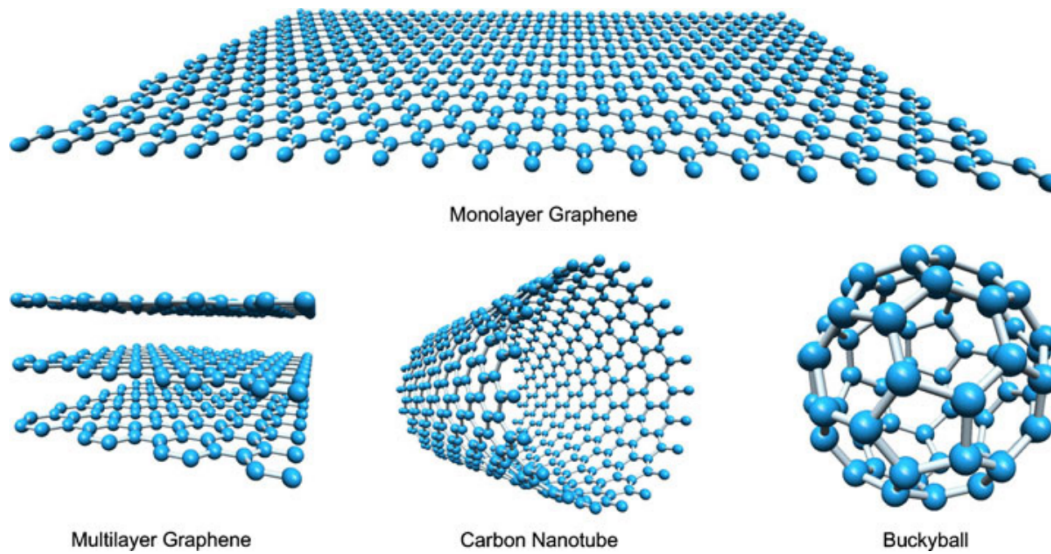


FIGURE 1.2. The structure of monolayer and multilayer graphene (graphite), carbon nanotubes, and buckyballs (fullerene). The figure is adapted from Ref. [20]

graphene that are weakly coupled through van der Waals interaction [15]. Nevertheless, the experimental challenges of graphene synthesis was due to the difficulties to extract a single layer of graphene without damaging the layer itself. Previously, graphene had been theoretically studied by P. R. Wallace in 1947 essentially as a model for graphite [16]. However, the stability of graphene at large-scale was the subject of a long standing theoretical debate due to the induced long wave-length thermal fluctuations that destroy the stability of 2D crystals. It was later found that this argument, known as Mermin-Wagner theorem [17], holds only in the second-order harmonic limit. The covalent bonds in graphene behave surprisingly beyond this approximation that grants the stability of graphene [18, 19]. In addition to graphene, there are other graphene-related materials such as fullerene and carbon nanotube³ which are quasi-sphere (0D) and cylindrical crystalline structure (1D), respectively (see Fig. 1.2). The nanotube in particular is more similar to graphene and has been shown to have superior electrical and mechanical properties along with graphene. Meanwhile, worldwide interest in the discovery of various new 2D materials has increased and efforts are made

³CNT

to uncover their interesting properties [21–23].

1.1.2 Synthesis

There are various methods and processes to controllably realize graphene that can be categorized into two main categories *top-down* and *bottom-up*. As top-down method, *mechanical exfoliation* is the simplest of the preparation methods and is the method that made stand-alone graphene a reality. It is the method first used by Geim and Novoselov [24]. In this technique, a piece of graphite undergoes repeated tape exfoliation and is then transferred to a substrate [25].

Liquid phase exfoliation is another method used widely for the production of graphene and it involves three different steps: dispersion in a solvent or surfactant, exfoliation, and purification. Eventually, it separates the exfoliated material from the non-exfoliated and, if supplied as powder, completely remove any solvent traces. Liquid phase exfoliation is known as one of the most promising techniques for the upscaling of graphene production. The simplicity, speed and high throughput that are associated with this process make the specific route attractive for mass production of graphene [26, 27].

In particular, *chemical reduction* involves the exfoliation of graphene oxides (GO) into a single-layer GO sheet, followed by the in-situ reduction of the GO for the production of graphene-like monolayers. This process is strongly affected by the choice of the solvent, the reducing agent and the surfactant, which are combined in order to maintain a stable suspension [28–30]. Moreover, *electrochemical exfoliation* is a promising bulk method for producing graphene from graphite where an applied voltage drives ionic species to intercalate into graphite where they form gaseous species that expand and exfoliate individual graphene sheets [31, 32]. In bottom-up synthesis we can separate different category of techniques to synthesize graphene. Graphene molecules are prepared starting from small and atomically-precise building blocks (bottom-up) [33, 34].

Chemical vapor deposition (CVD) is one of the most useful methods of this kind to prepare monolayer graphene of high structural quality for use in different devices [35]. Large area samples can be prepared by exposing a

metal to different hydrocarbon precursors at high temperatures. In terms of upscaling, CVD is a viable candidate for the production of high quality graphene in large area quantities.

1.1.3 Characterization

The multifunctionality of graphene is one of the reasons why it can be readily characterized by a wide variety of experimental techniques such as *scanning electron microscopy* (SEM) for surface morphology and to observe wrinkles or folds [36, 37]. *Transmission electron microscopy* (TEM) for evaluation of the different structures such as vacancy defects, bond rotations, dislocation edges, grain boundaries, layer stacking and other features [38]. *Scanning tunnelling microscopy* (STM) can provide information about the morphology and the electronic properties of graphene in three dimensions, atomic force microscopy (AFM) is one of the most widely used techniques for characterizing the number of layers, since the original work of Novoselov *et al.* established that monolayer graphene is 0.4 nm thick [12]. Finally, *Raman spectroscopy* is one of the most important methods used in the study of graphene and its derivatives [39] which *e.g.* provides information on specific properties of the material.

1.1.4 Properties

Graphene has gained great attention among scientists and engineers since it was firstly fabricated in 2007 [13] and its various properties have been intensively investigated [34]. The reason for the particular interest in graphene is mainly due to its multifunctionality which combines unique properties such as very large thermal conductivity (3000-5000 W/mK) which implies that graphene could theoretically absorb an unlimited amount of heat [40], high electron mobility at room temperature (250,000 cm²/V s) allowing for greater switching speed in transistors [41], high Young's modulus of elasticity (≈ 1 TPa) resulting in high breaking strength of graphene, up to 20% elastic strain [42], along with large surface area (2630 m²/g) suitable for vast number of applications [43]. Potential applications includes field effect transistors [44],

electromechanical systems [45], strain sensors [46], supercapacitors [47, 48], hydrogen storage [49] and solar cells [50, 51]. In recent years, interest in new families of graphene-based 2D heterostructures has emerged [52] in order to deal with some limitations that became evident, the lack of a bandgap for instance, that prevents the efficient use of graphene for several electronic and optoelectronic applications. 2D heterostructures can be made by combining graphene with one or more other materials such as hexagonal boron nitride [53], a layered insulator with a structure similar to that of graphene, as well as the family of transition metal dichalcogenides (TMDs) from the group VI [54]. Such heterostructures not only serve to overcome the inherent limitations of each of the materials but novel properties can be realized by their proper combination [52, 55]. Moreover, graphene-based materials in the form of membranes and capillaries are found to have excellent advantages in the desalination process due to their single atomic layer structure, hydrophobic property, and rich modification approaches [56]. Due to the importance and the focus of this thesis, I discuss some of graphene-based materials in a separate section.

1.2 Graphene-based materials

Recent progress has shown that graphene-based materials can have a profound impact on electronic and optoelectronic devices, chemical sensors, nanocomposites and energy storage. Consequently, the study of properties of such materials is becoming increasingly popular in both academia and industry [1, 57]. I will briefly cover some of those 2D materials that are going to be the main focus of this thesis in the next chapters.

1.2.1 Doped graphene

Doping is an efficient way to tailor properties of materials which has been widely used in semiconductor electronics. In particular, by incorporating different atoms (i.e. B, N, S, and Si) into graphene, its properties are significantly altered due to the disruption of the ideal sp^2 hybridization of the carbon atoms, thus locally inducing significant changes in their electronic properties and

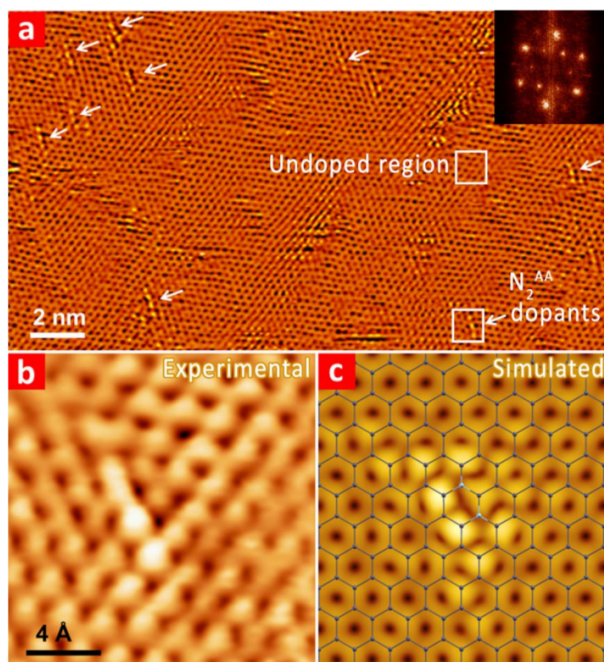


FIGURE 1.3. Experimental and simulated STM images of synthesized nitrogen doped graphene (NG) sheets. (a) Large-area STM image of the NG illustrating the presence of numerous N-dopants with similar peapod-like configuration (highlighted by white arrows). The upper and lower squares are used to indicate the undoped region and same sub-lattice dopants. (Inset) FFT of topography presents reciprocal lattice and intervalley scattering. (b) Highly resolved STM image of a N-dopant. (c) Ball-stick structural model of the simulated NG sheet. The figure is adopted from Ref. [58].

chemical reactivity [58]. Besides the doping concentration, the nature of the dopants, e.g. the bonding type, the dopant location and the induced perturbation within the graphene sub-lattices, are important to both basic research and practical applications [59–62]. Doping graphene allows us to introduce carriers which is crucial for applications in high-frequency semiconductor devices, enhanced catalysis for energy conversion and storage, photovoltaic devices. The experimental and simulated STM images of synthesized nitrogen doped graphene sheets is illustrated in Fig. 1.3. By incorporating nitrogen atoms into graphene, its physico-chemical properties could be significantly changed at doping sites depending on dopant concentrations and local arrangements. Ruitao Lv *et al.* [58] have demonstrated that N-doped graphene can be used to efficiently probe organic molecules using highly improved

graphene enhanced Raman scattering [58].

Several density functional theory studies (DFT) have been conducted to determine the structure of a single nitrogen dopant on a hosted graphene sheet [63]. Zhao et al. [58] used first principles techniques to calculate the formation energy of different N-dopant configurations. Fujimoto et al. [64] and Rani et al. [65] investigated the effect of substitutional nitrogen doping on the electronic band structure and the bond lengths. These types of studies are limited to few dopants within a relatively small unit cell. Consequently, it leads to a less realistic description of doping and their collective impact on the thermo-elasticity of a doped system. Some studies used a classical molecular dynamics (MD) approach to investigate the mechanical responds of (doped) graphene sheet(s) based on semi-empirical potentials [66, 67]. Despite all such theoretical and experimental works on N-doped graphene, the ferroelectric properties of such doped systems has not been discussed yet, and more detailed studies are needed to elucidate the structural deformation of the N-doped configurations within the graphene sheets and the corresponding charge induced polarization.

In chapter 5, I will investigate the structural deformation and mechanical properties of N-doped graphene using large-scale molecular dynamics simulations. It is shown that the uniformly random inserted nitrogen atoms in graphene changes the morphology of the system and depending on the local arrangement of the nitrogen atoms, the roughness can be very different. The nitrogen impurities decrease the elastic modulus of graphene and the fracture threshold. Furthermore, it is predicted that nitrogen-doped graphene is a ferroelectric with a permanent dipole whose strength depends on the particular distribution of the nitrogen atoms [68].

1.2.2 Polycrystalline graphene

Most materials available in macroscopic quantities are polycrystalline. Properties of the polycrystalline materials are often dominated by the size of their grains and by the atomic structure of their grain boundaries that is defined as interfaces between two domains with different crystallographic orientations. These effects should be especially pronounced in two-dimensional materials,

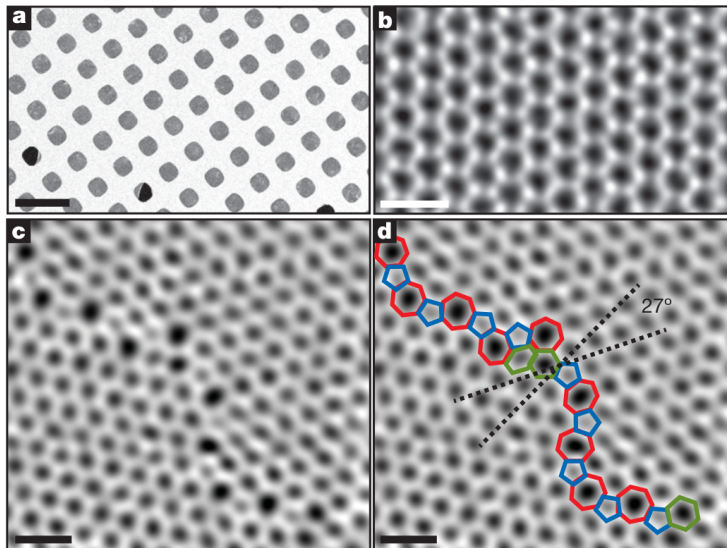


FIGURE 1.4. (a) Scanning electron microscope image of graphene transferred onto a TEM grid with over 90% coverage Scale bar, 5 μm . (b) Defect-free hexagonal lattice inside a graphene grain. (c) Two grains (bottom left, top right) intersect with a 27° relative rotation. A periodic line of defects stitches the two grains together. (d) The image from c) with the pentagons (blue), heptagons (red) and distorted hexagons (green) of the grain boundary outlined. The figure is adopted from Ref. [69].

where even a line defect (i.g. topological defects) can divide and disrupt a crystal. As a result, their distinct electronic, magnetic, and mechanical properties strongly depend on their atomic arrangement [69]. Graphite, a precursor in producing graphene by exfoliation, exists at large scale only in polycrystalline form. Dislocations and grain boundaries in graphene can heavily effect the properties of graphene that have been extensively investigated over the past few years for engineering graphene-based nanomaterials and functional devices [70–72]. In two-dimensional (2D) materials such as graphene (see Fig. 1.4), grain boundaries are the 1D interfaces between two domains of material with different crystallographic orientations. The structure of grain boundaries is defined by the mutual orientation of the angles between the corresponding crystallographic directions in the two domains and the normal of the boundary line [73].

Recent progress in controlling over the location and average complexity of defect formation in graphene, by exposure of a graphene sample to a focused

electron beam, allowed to engineer defect patterns in a desirable way [74]. Defects in graphene modify its properties and affects its functionality [73, 75]. It is interested to use such designed defects in the substrate to engineer the dynamics of a graphene flake that is put on top of it.

In chapter 6, I will show that the superlubricity of a graphene flake over a graphite substrate [76–78] is strongly influenced by the presence of defects in the substrate. The dynamics of the graphene flake is significantly altered and the well known random rotational motion and corresponding transition from incommensurate to commensurate states and related lifetime are profoundly influenced by the defected regions [79]. In particular, we computationally focus on backscattering on the motion of a flake that is moved towards a grain boundary (GB) line. Several types of grain boundaries are investigated in order to identify how they influence the trajectory of motion of a graphene flake. It is shown that several microscopic aspects of the motion of a thermally actuated flake over graphene with GB which can be helpful for developing AFM/STM driven force measurements [80, 81]. Although AFM measurement gives an estimation for the static friction force, providing any details on the complex dynamics of the sliding motion of graphene flakes is still challenging [82].

1.2.3 Graphene nanobubble

Bubbles are inevitably observed in the preparation process of graphene due to different sources of contaminations (air, water, etc.) present in the experiment such as when mechanically exfoliated graphene flakes were placed on top of a substrate [83]. For example, the silicon oxide/graphene interface when graphene is obtained by mechanical cleavage [84]. Graphene bubbles are observed with diameters ranging from tens of nanometers to tens of microns and a variety of shapes (see Fig. 1.5) i.e. circular, triangular, and diamond [85, 86]. While the origin of graphene bubbles has not been fully understood and may depend on the material system and experimental conditions, several potential applications of graphene bubbles have been suggested. *E.g.* strain induced by the bubble can generate enormous pseudo-magnetic that can tailor the electronic properties of graphene [87]. They can be used as optical

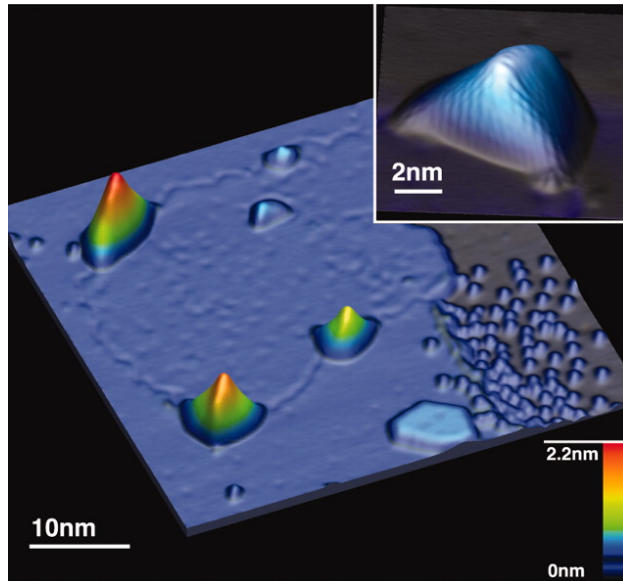


FIGURE 1.5. STM image taken at 7.5K. Graphene monolayer patch on Pt(111) with four nanobubbles at the graphene-Pt border and one in the patch interior. (Inset) High-resolution image of a graphene nanobubble showing distorted honeycomb lattice resulting from strain in the bubble. The figure is adopted from Ref. [87].

lenses with variable focal length when applying an external electric field [84]. Raman spectrum of graphene under biaxial strain [88], measure the elastic properties of top graphene layer [89, 90] or adhesion between the graphene and the substrate [91]. Figure 1.5 illustrates STM image taken at 7.5K of formed graphene nanobubbles on Pt(111) substrate [87]. Because of graphene inertness and its capability of withstanding large strains such nanobubbles offer unique opportunities to investigate nano-quantities of materials (*e.g.* liquids) under extreme conditions.

Using membrane theory, nonlinear plate theory, and the ideal gas model, Yue *et al.* [85], studied the mechanics of relatively large graphene bubbles. The pressure inside the large graphene nanobubbles ($R > 10$ nm) is predicted to be in the order of MPa, [85, 92, 93] which is essentially determined by the elastic properties of the top layer and the interfacial adhesion between top layer and the substrate. Recently, for large bubbles ($R > 50$ nm), Khestanova *et al.* [94] found experimentally a universal scaling law of h_{\max}/R where h_{\max} is the maximum height and R is the base radius of the bubble using atomic force microscopy (AFM) [85, 94]. Furthermore, possible phase transitions in

the trapped substance prevent the use of the ideal gas model and therefore the calculation of the internal pressure for small nanobubbles has been remaining a challenge. Most of the theoretical studies have addressed the deformation and structure of graphene bubbles on top of a substrate [85, 94]. Although the effects of pressure on the chemical equilibrium and kinetics is an archaic topic [95, 96] recent observations have shown that the vdW pressure can induce unusual chemical reactions where several trapped salts or compounds are found to react with water at room temperature, leading to 2D crystals of their corresponding oxides [97]. These structural transitions and corresponding chemical reaction mechanisms are not well understood yet.

In chapter 7, I will focus on how the material inside the bubble influences the microscopic shape of the bubble. By means of equilibrium molecular dynamics simulations and atomic force microscopy measurement (AFM), we are able to provide deeper insights into the microscopic details of the graphene nanobubbles and the internal pressure for small nanobubbles. We study bubbles filled by diverse substances such as helium, water, two hydrocarbons (ethanol, hexadecane) and NaCl. The vdW pressure is found to be in the order of GPa depending on the size of the bubble and the interfacial adhesion. Flat nanobubbles can be formed in case of trapped metallic substances or for large elongated hydrocarbons. AFM experiments indicate that in contrast to water bubbles, the hydrocarbon bubbles have a round shape with in-plane cylindrical symmetry which is in good agreement with the results from MD simulations. This systematic study provides a deeper understanding of the formation of graphene nanobubbles beyond simple membrane theory that extends its applicability to small nanobubbles and predicts a substance dependent nanobubble shape [98].

1.2.4 Graphene-oxide

Graphene oxide (GO) is one of the important derivatives of graphene obtained by treating graphite with oxygen-containing functional groups and results in a compound of carbon, oxygen, and hydrogen in variable ratios. Graphene oxide exhibits similar properties like graphene and it can be synthesized in large

quantities through solution routes. However, the surface functionalization of graphene oxide not only plays an important role in controlling exfoliation behavior of graphene oxide and reduced graphene oxide but also holds the key leads to various applications. Surface functionalization has taken two approaches: covalent functionalization and non-covalent functionalization. In covalent functionalization, which is the focus of this thesis, oxygen functional groups are covalently bound to the surfaces, including carboxylic acid groups at the edge and epoxy/hydroxyl groups on the basal plane. They can be utilized to change surface functionality such as hydrophilicity and reactivity [1]. Graphene oxide is one of the most popular 2D materials available which is due to the wide range of areas that it can be utilized. It has a distinct advantage over other 2D materials (such as graphene), as it is easily dispersed within solution; allowing for processing at high concentrations. This has opened up the possibility to use it in applications such as optical coatings [99], transparent conductors [100], thin-film batteries [101], chemical resistant coatings [102], filtration and many more [4, 5, 43, 97].

Determining the precise structure of GO has been the subject of considerable debate over the years, and even to this day no unambiguous model exists. It mainly traces back to the complexity of the material (i.e. sample-to-sample variability) and the lack of techniques for characterizing such materials. Despite these obstacles, many structures for GO have been proposed which are different from each other regarding the type of introduced functional groups identify (i.e. epoxy, hydrogen content, etc), the distribution of these functionalities across the basal planes of graphite, and the chemical reactivity, much of them with great success [103].

Figure 1.6 illustrates the Lerf-Klinowksi model [104] for a graphene oxide structure. It has oxidative defects which break the perfect structure of graphene. The hydroxyl (-OH) and epoxy(-O-) functionals are present at the basal plane while carbonyl (-CO₂H) are shown at the edges. These functionals significantly control the hydrophilicity of the graphene surface through the H-bonds.

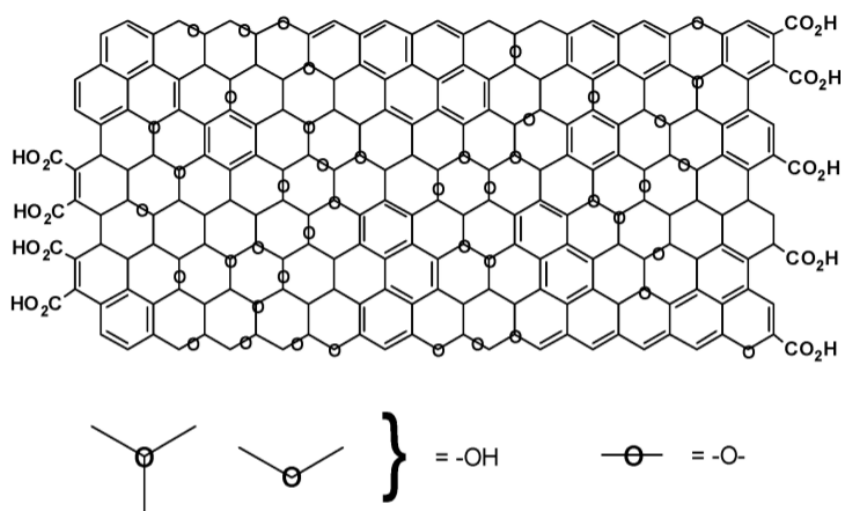


FIGURE 1.6. Schematic representation of the Lerf-Klinowksi model [104] for the graphene oxide structure. The hydroxyl (-OH) and epoxy(-O-) functionals are present at the basal plane while carbonyl (-CO₂H) are shown at the edges. The figure is adopted from Ref. [43].

1.2.5 Graphene-oxide membranes

In the past decades, ultra-thin membrane separation has become an advanced technology for solving enormous challenges resulting from the to limited resources and environmental problems. Compared with conventional methods, nanomembrane separation is found to be an energy-efficient and environmentally harmless technology with ample applications for nanofiltration such as water and gases purification [105], ion sieving [6, 106], and energy storage [31, 107]. Graphene as an atomic thick 2D structure in addition to high mechanical strength and chemical inertness makes it an excellent candidate to become nano-building blocks for separation membranes. In particular, the oxygen functional groups in graphene oxide, as one of the derivatives of graphene, can provide reactive handles to tune the microstructure and chemical properties of GO membranes leading to more effective molecular selectivity. Furthermore, hydrophilic groups enable stable dispersion of GO sheets in aqueous media, which provide a facile processing and stacking of these sheets [108]. Graphene oxide membranes is in fact partially oxidized, stacked sheets of graphene that provides ultrathin, high-flux and energy-

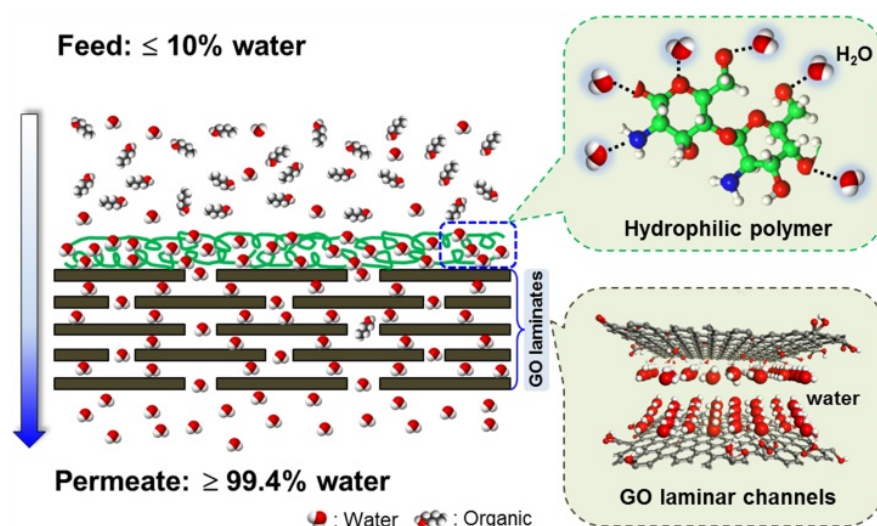


FIGURE 1.7. Schematic of the water–organic separation process using the synergistic effect of a hydrophilic polymer and graphene oxide (GO) laminates. The figure is adopted from Ref. [109].

efficient membranes for precise ionic and molecular sieving in aqueous solution. Figure 1.7 illustrate the schematic realization of fast and selective water permeation through the GO membrane in order to separate hydrophilic polymer from water [109]. Interlayer spacing is essential to GO membrane selectivity and it is experimentally difficult to reduce the interlayer spacing sufficiently to exclude small ions and to maintain this spacing against the tendency of graphene oxide membranes to swell when immersed in aqueous solution. L. Chen *et al.* have suggested a cationic control of the interlayer spacing with Ångstrom precision using K^+ , Na^+ , and Mg^{2+} ions [5].

In a recent study⁴, electrical control over water permeation was realized by graphene-oxide membrane via creating conductive filaments in the graphene oxide and controllable electrical breakdown. It allows the nearly ohmic I–V characteristics and existence of permanent electrically conductive channels. As a result, the electric field that concentrates around these current-carrying filaments ionizes water molecules inside graphene capillaries within the graphene oxide membranes, which impedes water transport (see Fig. 1.8 (a)). A precise control of water permeation, from ultrafast permeation to

⁴This work was part of my Ph.D. study in collaboration with the experimental group at Manchester University and published as: K.-G. Zhou *et al.* “Electrically controlled water permeation through graphene oxide membranes”, *Nature* **559**, 236 (2018). My contribution was the computational modeling of the ionized water permeation through the graphene-oxide membrane using MD simulations.

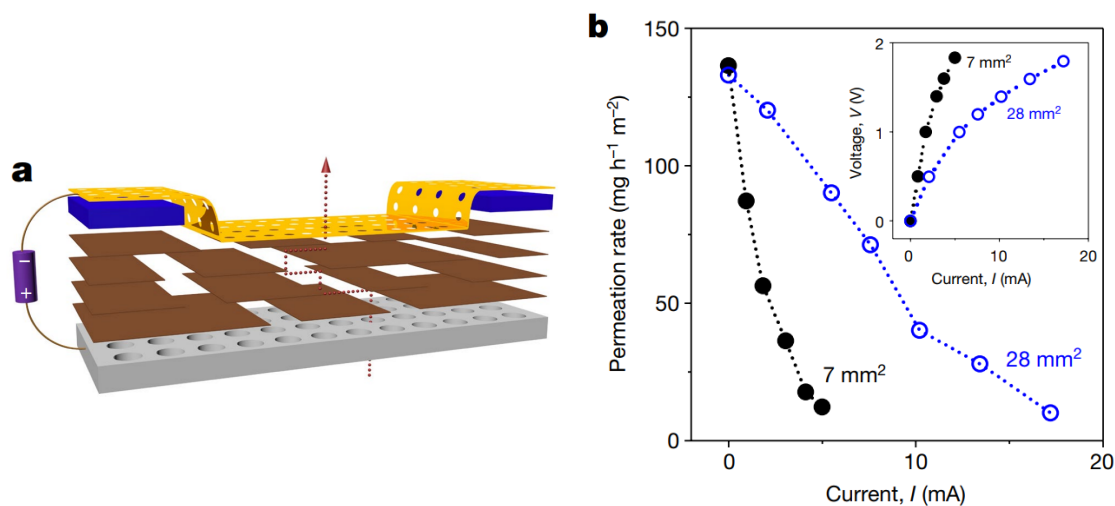


FIGURE 1.8. (a) Schematic of a graphene oxide membrane with voltage applied (b) Permeation rate as a function of the current through two graphene oxide membranes with different areas. (28 mm², open blue circles; 7 mm², filled black circles). The figures are adopted from Ref. [3].

complete blocking controlled was demonstrated by running an electrical current through the GO membrane. Figure 1.8 (b) shows measured water permeation rate as a function of the current through two graphene oxide membranes for two different areas of 28 mm² (open blue circles) and 7 mm² (filled black circles) [3]. This suggests major applications in developing smart membrane technologies for artificial biological systems, tissue engineering and filtration [3].

Numerous studies based on molecular dynamics (MD) simulations identified key factors that affect transport through nanomembranes and nanocapillaries [110–112]: the breakdown of uniform water density; the water-solid wall slip length which is found to be much larger than capillary sizes; dynamical properties different from bulk, *etc.* Despite recent progress, the molecular mechanisms underlying the diffusion of water in charged porous media (hydrophilic materials) and the interplay between the effects of a charged surface and ions are not understood so far. The behavior of Na⁺ and Cl⁻ ions in bulk water or at the interface of hydrophobic/hydrophilic media was widely investigated in recent works [4]. However, a few studies have addressed the effect of the concentration of ions on the dynamical properties of water in

charged nanocapillaries [113].

In chapter 8, I will systemically study the influence of ion concentration and surface charge on the dynamical properties of confined water and elucidate the influence of capillary size. In particular, a mixture of H_2O , Na^+ and Cl^- inside a nanocapillary made of graphene layers will be investigated. I predict a significant change in the water slip length versus surface charge while the ion concentration has much less influence on it. In particular, it is demonstrated that commensurability effects result in clear oscillations in the dynamical properties of confined water which highlight the importance of accurate size control of the nanocapillaries [114].

1.3 Water

Water is present on earth as a gas, a liquid, and a solid⁵. It provides the substrate where all biological processes occur and it is the most common of all solvents. Particularly, anomalous behavior of water under nanosize confinement has recently gained a lot of attention with potential applications in nanofluidic transport and purification [115]. As this thesis discusses the nanoconfined water⁶, I briefly review water general characteristics and properties in this section and adding more details⁷ in Chapter 4.

1.3.1 Molecular structure

At nanoscale, water is a tiny bent molecule with the molecular formula H_2O , consisting of two light hydrogen atoms attached to oxygen atom with bond length of 0.95718 \AA and bond angle of 104.474° [116]. These parameters are for the thermodynamically most stable form, but the bonds can exhibit vibrations away from these values. Each molecule is electrically neutral but polar. The latter is due to a large electronegativity difference between hydrogen and oxygen, where the electronic clouds lean a bit toward oxygen which result in an effective positive hydrogen and negative oxygen. This gives a large

⁵Hexagonal ice (Ih)

⁶Chapters 7 and 8

⁷An excellent reference for water: <http://www1.lsbu.ac.uk/water>

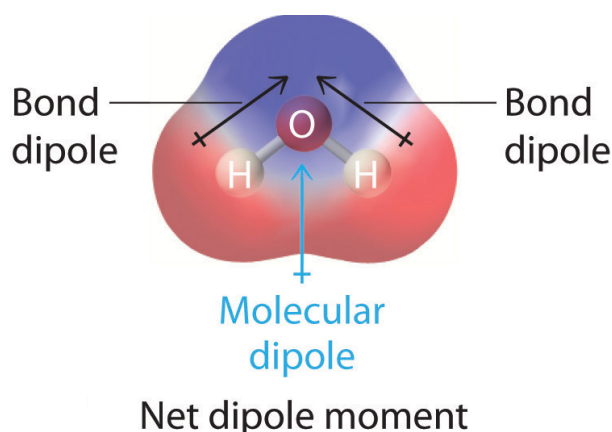


FIGURE 1.9. Schematic representation of a single water molecule. The blue (red) spot represents more (less) electronic cloud due to a large electronegativity difference between hydrogen and oxygen. The figure is adopted from <https://chem.libretexts.org>.

molecular dipole moment of 1.8546 D^8 directed from the center of negative charge to the center of positive charge (see Fig. 1.9). The presence of this dipole moment underlies water polarity and its intermolecular hydrogen bond interactions [117].

1.3.2 Hydrogen bond

Hydrogen bonds (HB) are formed when hydrogen atoms of one molecule are attracted to an electronegative atom (such as N, O, and F) through a special type of dipole-dipole attraction. These bonds are generally stronger than the ordinary dipole-dipole and dispersion forces, but weaker than true covalent and ionic bonds. Hydrogen bonds are actually intermolecular bonds and are found to have an electrostatic nature, although its quantum aspects can be important for some materials [118]. In fact, the network of HBs determines unique properties of water (structure and solvent capabilities) and its various phases. Hydrogen bonds are of great contemporary importance in nanoscience, being involved in, e.g. the functionalization and patterning of surfaces (i.e. graphene oxide) with ordered molecular overlayers [103, 119]. Figure 1.10(a) shows a schematic representation of hydrogen bonds between water molecules.

⁸Debye, one debye is equal to $3.336 \times 10^{-30} \text{ C.m}$

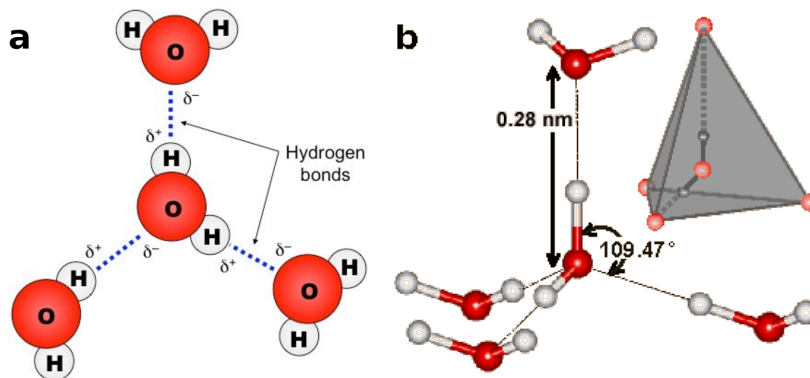


FIGURE 1.10. (a) Schematic presentation of hydrogen bonds between three water molecules. (b) Tetrahedral hydrogen-bonds network for bulk water. Figure (a) is adopted from <https://chemistryonline.guru/hydrogen-bond>. Figure (b) is adopted from <http://www1.lsbu.ac.uk/water>.

The electronegative nature of oxygen atom induced a charge transfer⁹ $\pm\delta$ that results in the attractive force between the O-H hydrogen and the O-atom of a nearby water molecule. For bulk water, it is strongest when the three atoms are in a straight line and when the O-atoms are closer than 0.3 nm *tetrahedrally*-placed¹⁰. Hydrogen bonds form a network as shown in Fig. 1.10(b) [120].

1.3.3 Nanoconfinement

Many studies have been dedicated to rapid progress in the fundamental knowledge of water at solid interfaces such as confined water in carbon nanotubes [121] and graphene-based membranes [122] where the hydrogen bond network can be significantly affected by the geometrical constraint due to confining walls. For example, it is shown that the averaged number of hydrogen bonds of liquid water inside a carbon nanotube decreases when we compare it with bulk water. Such a system is no longer isotropic and transport properties are found to be different in the axial than those in the radial direction [113]. Furthermore, the trapped water molecules between

⁹Underlies the electrostatic nature of the hydrogen bonds.

¹⁰Fourfold

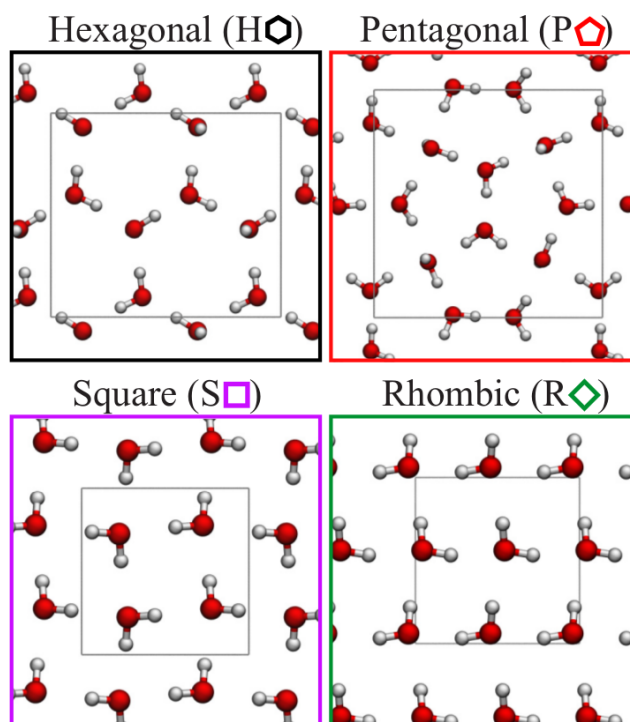


FIGURE 1.11. The four most relevant 2D ice structures: hexagonal (H), pentagonal (P), square (S), and rhombic (R) obtained from quantum Monte Carlo simulations. The gray boxes represent the primitive unit cells. The figure is adopted from Ref. [123].

two-dimensional hydrophobic crystals¹¹, have been found to experience extremely high pressures (of order 1 GPa) at room temperature [97]. As a result, it is predicted to induce non-typical phases of water, namely *2D ice* [124]. Figures 1.11 demonstrate the four most relevant 2D ice structures: hexagonal (H), pentagonal (P), square (S), and rhombic (R) obtained from quantum Monte Carlo simulations [123]. The gray boxes represent the primitive unit cells. At ambient pressure, J. Chen *et al* found that the most stable structures are hexagonal and pentagonal phases. At high pressure, 2D square ice is more stable at 0 K than the other phases considered [123]. However, the square ice structure have not been observed experimentally yet. This prediction is still controversial [125, 126] and further detailed molecular-level understanding is still required. Clearly more work is needed from experiment and theory in order to substantiate the existence of square ice. The study of such systems gets even more complicated when water chemically binds to reactive

¹¹2D heterostructures

solid surfaces (*i.e.* graphene-oxide) which underly a variety of structural and dynamical peculiarities [2].

1.4 Computer simulation

Science requires both experiment and theory. Without observation there are no facts to be explained by a theory and without a comprehensive theory science is mere documentation. The question arises as how computer modeling and simulation can help science. The answer is that on the one side, computer simulation is a test of theories and discriminate between well-founded approaches and ideas that are plausible but less successful in practice. On the other side, the result of computer simulation may also be compared with those of real experiments, in order to provide insights to the experiment that is essentially based on an underlying model (see Fig. 1.12). This dual role of computer that acts as a bridge between theoretical predications and experimental results is crucial for current status of science, in particular for material discovery and design. Because of this connecting role, and the way in which simulations are conducted and analyzed, these techniques are often termed *computer simulation* [127]. In particular, molecular simulation is beneficial to reduce reliance on costly trial and error approaches to materials research. Moreover, it increases the confidence that new materials will have the desired properties when scaled up from the laboratory level [128]. It must be noted that computer simulation relies on models that originate from theory. An understanding in the context of computer simulation is achieved once a plausible model is able to reproduce and predict experimental observation.

Molecular simulation constitutes the cornerstone of contemporary material modeling. Figure 1.13 illustrates some of the methods that have been developed to simulate phenomena at different time and length scales. These include *first principles* or *ab initio* methods which rely directly on quantum mechanics for studying electronic structure and molecular properties, *molecular dynamics* and *Monte Carlo* methods that are based on statistical mechanics and force field models appropriate for simulation microscale structures, eventually *mesoscale* and *continuum mechanics* methods are suitable

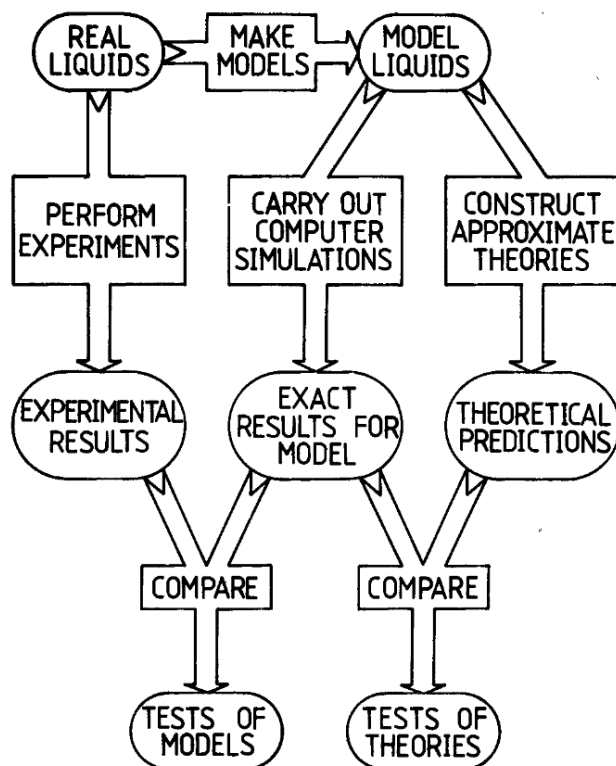


FIGURE 1.12. The connection between experiment, theory, and computer simulation (as a bridge). The flowchart is adopted from Ref. [127].

for macroscale simulations. More importantly, these methods are different in terms of accuracy and computational effort. For a certain system, first principle methods are the most accurate but computationally challenging, while the continuum methods for instance are relatively less accurate but computationally efficient. In this thesis, I discuss briefly the first principle approach and afterward explain in detail the force field based molecular dynamics methods which are mainly employed methodology.

1.5 Outline

This thesis contains three main parts organized as follows:

Part 1 - Introduction

The introductory *Chapter 1* was aimed to give an overview of the general aspects and motivations for the thesis. It presented a brief review on graphene,

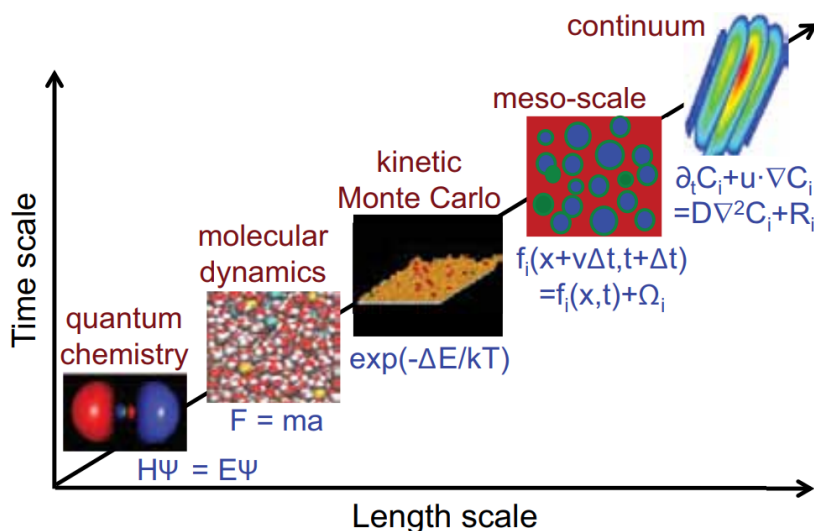


FIGURE 1.13. Various simulation methods and their suitability for multiple time and length scale. The graph is adopted from Ref. [129].

graphene-based materials, graphene-oxide membranes, water, and computer simulation as a central tool for exploring their properties.

Part 2 - Methodology

The second part of the thesis dedicated to providing required theoretical and computational backgrounds that are presented in *Chapters 2* and *3*, respectively. Moreover, *Chapter 4* introduces methods to calculate various properties through an equilibrium molecular dynamics simulation.

Part 3 - Results

In *Chapter 5*, structural and mechanical properties of nitrogen-doped graphene are studied and formation energy, ripples, mechanical properties are investigated.

In *Chapter 6*, spatial design and control of graphene flake motion are investigated. Design of particular patterns of structural defects on a graphene surface allows proposing an alternative approach for controlling the motion of graphene flake over a graphene substrate.

In *Chapter 7*, I explored the dependence of the shape of graphene nanobubbles on trapped substance nanobubble.

In *chapter 8*, permeation of water between neighboring graphene oxide flakes are investigated using a simple model for the GO membrane. I study

different transport coefficients such as diffusion, friction, shear viscosity, and slip-length at nanoconfinement.

Finally, in *chapter 9*, I briefly present the recent MD results concerning the swelling properties and the impact of aromaticity on the permeation through montmorillonite clay mineral as an ionic membrane that can keep intercalated solvents under extreme confinement.

Part 2

Methodology

THEORETICAL FRAMEWORK

Theory is an essential part of our true understanding of physical phenomena even through numerical approaches. In this chapter, I start by introducing the Schrödinger equation and then discussing theories that underly atomic dynamics, Born-Oppenheimer approximation, potential energy surface. Furthermore, I cover the important aspects of statistical thermodynamics, ergodicity, statistical ensembles, and free energy with emphasis on topics relevant to molecular simulations.

2.1 Quantum Physics

2.1.1 Schrödinger equation

At microscopic scale, every material is a system composed by mutually interacting electrons and nuclei. The evolution of these particles is governed by laws of quantum mechanics, namely *Schrödinger equation* [130] which is basically an eigenvalue problem. For a non-spin polarized system of electrons and nuclei, time-independent Schrödinger equation is written as

$$H \Psi(\mathbf{R}_I, \mathbf{r}_i) = E_{\text{tot}} \Psi(\mathbf{R}_I, \mathbf{r}_i), \quad (2.1)$$

where \mathbf{R}_I and \mathbf{r}_i represent respectively all nuclear and electronic coordinates, $\Psi(\mathbf{R}_I, \mathbf{r}_i)$ is the many-body wave function which principally contains all physi-

cal information about the system, it is in general a complicated function of all nuclear and electronic coordinates, and E_{tot} is the corresponding total energy levels of the system [131]. The non-relativistic Hamiltonian including mutual electron (charge e) and nuclei (charge Z_I) interaction through Coulomb forces can be expressed by adding up their contributions to the total energy

$$\begin{aligned}
 H &= T_e + V_{e-e} + T_n + V_{n-n} + V_{e-n} & (2.2) \\
 &= \sum_i -\frac{\hbar^2}{2m_e} \nabla_i^2 + \sum_{i<j} \frac{1}{4\pi\epsilon_0} \frac{e^2}{|\mathbf{r}_i - \mathbf{r}_j|} \\
 &\quad + \sum_I -\frac{\hbar^2}{2M_I} \nabla_I^2 + \sum_{I<J} \frac{1}{4\pi\epsilon_0} \frac{z_I z_J e^2}{|\mathbf{R}_I - \mathbf{R}_J|} \\
 &\quad + \sum_i \left\{ \sum_I -\frac{1}{4\pi\epsilon_0} \frac{z_I e^2}{|\mathbf{r}_i - \mathbf{R}_I|} \right\}. & (2.3)
 \end{aligned}$$

The different terms in Eq. (2.3) denote the kinetic energy of the electrons (T_e), the electron-electron repulsion potential energies (V_{e-e}), the kinetic energy of the nuclei (T_n), the nuclei-nuclei repulsion potential energies (V_{n-n}), and the last expression containing the electron-nucleus attractive potential energies (V_{e-n}), where sums run over electrons i and nuclei I with exclusion of self and double counting interactions, respectively [132, 133].

Solving Eq. (2.1) for a large number of particles is an impressive endeavor and in practice is not feasible except for extremely simple systems for instance hydrogen-like atoms or molecules. Several major approximations such as Born-Oppenheimer [134], one-electron¹, variational methods, etc are inevitably needed to achieve at least a workable computational framework [131].

2.1.2 Born-Oppenheimer approximation

The first major and obvious step to deal with a many-body Hamiltonian is to exploit the mass difference between electron and nuclei in order to separate the problem into an electronic problem with fixed nuclei and a nuclear problem under the effective potential generated by the electrons. This separation is known as *Born-Oppenheimer* approximation² [133]. An electron

¹Independent electron picture

²Also known as *adiabatic* approximation

has a mass almost 2000 times smaller than a nucleon and its motion is consequently much faster than nuclear motion. This fact allows us to assume that at any given time the electrons follow the nuclear motion while nucleon at any given time experience an effective potential that is produced by the electrons. Accordingly, we assume that the wavefunction has the form of a product between a nuclear and electronic part:

$$\Psi(\mathbf{R}_I, \mathbf{r}_i) = \Phi(\mathbf{R}_I) \psi_{\mathbf{R}}(\mathbf{r}_i) \quad (2.4)$$

where $\psi_{\mathbf{R}}(\mathbf{r}_i)$ is the electronic wavefunction that solves the electronic Schrödinger equation that concerns the electronic Hamiltonian plus external potential created by fixed nuclei. It is written as

$$(T_e + V_{e-e} + V_{e-n}) \psi_{\mathbf{R}}(\mathbf{r}_i) = E_{\mathbf{R}} \psi_{\mathbf{R}}(\mathbf{r}_i), \quad (2.5)$$

where the index \mathbf{R} refers to the fact that both wavefunction and the electronic contribution to the energy depend on the nuclear coordinates because of the V_{e-n} term. Next, by inserting Eq. (2.4) into Eq. (2.1) and noticing that the electronic kinetic energy operator has no effect on the nuclear part due to the fast motion of electrons and the fixed nuclei assumption, we obtain the following equation:

$$(T_n + V_{n-n} + E_{\mathbf{R}}) \Phi(\mathbf{R}_I) \psi_{\mathbf{R}}(\mathbf{r}_i) = E_{\text{tot}} \Phi(\mathbf{R}_I) \psi_{\mathbf{R}}(\mathbf{r}_i). \quad (2.6)$$

We eventually reach the Schrödinger equation for nuclear coordinates alone that is given by

$$(T_n + V_{n-n} + E_{\mathbf{R}}) \Phi(\mathbf{R}_I) = E_{\text{tot}} \Phi(\mathbf{R}_I). \quad (2.7)$$

We assume here that nuclei kinetic operator has no the influence on the electronic wavefunction because they only experience an average and effective potential induced by following electrons which are hidden into $E_{\mathbf{R}}$.

The Born-Oppenheimer approximation allows us to separate the Schrödinger equation into two principal equations. The one that involves the electronic wavefunction as a function of atomic positions (Eq. (2.5)), and the other equation that treats the nuclei (Eq. (2.7)). The former is a serious topic of electronic structure calculations in particular density functional theory (DFT)

that attempts to find a precise solution for Eq. (2.5) [135, 136]. The latter is basically approximated to a classical equation of motion due to the relatively slow dynamics of nuclei. We are interested in the term $V_{n-n} + E_{\mathbf{R}}$ in Eq. (2.7) because it determines the interaction potential among nuclei, it is crucial for the dynamics of atoms (electrons and nuclei as an individual entity), which is the main focus of this thesis [133].

2.1.3 Hellmann-Feynman forces

Hellmann-Feynman force between atoms (more precisely nuclei) is a direct derivative of the total energy with respect to atomic position \mathbf{R}_i [137–139]. For many-body Hamiltonian and wavefunctions, it is written as

$$\mathbf{F}_i = -\frac{d}{d\mathbf{R}_i} \langle \Psi | H | \Psi \rangle = -\langle \Psi | \frac{\partial H}{\partial \mathbf{R}_i} | \Psi \rangle - \tilde{\mathbf{F}}_i, \quad (2.8)$$

where the first term contains explicit derivative in the Hamiltonian, it is shown as a partial derivative, and an additional term $\tilde{\mathbf{F}}_i$ that refers to implicit derivative through wavefunctions that vanishes due to the derivative of a constant quantity as follows

$$\tilde{\mathbf{F}}_i = \langle \frac{d\Psi}{d\mathbf{R}_i} | H | \Psi \rangle + \langle \Psi | H | \frac{d\Psi}{d\mathbf{R}_i} \rangle = E \frac{d}{d\mathbf{R}_i} \langle \Psi | \Psi \rangle = 0. \quad (2.9)$$

Hellmann–Feynman force is essential for calculation of interatomic forces through first principle approaches. This allows optimizing geometries of the atomic positions or performing *ab initio* MD simulation where the forces acting upon the nuclei has to be directly obtained from electronic structure.

2.1.4 Potential energy surface

If we consider nuclei as classical objects (atoms), they interact via an effective interatomic potential which is only a function of atomic coordinates $\mathbf{R}^N = \{\mathbf{R}_1, \mathbf{R}_2, \dots, \mathbf{R}_N\}$ where N is the number of atoms. This effective potential is the sum of the electronic energy E and the nuclei-nuclei electrostatic interaction V_{n-n} that is expressed by

$$U(\mathbf{R}^N) = E(\mathbf{R}^N) + V_{n-n}(\mathbf{R}^N). \quad (2.10)$$

The impact of electronic cloud interactions is implicitly taken into account through the term E . The nuclear motion is completely determined by $U(\mathbf{R}^N)$ which is known as *potential energy surface* (PES) [140, 141]. This allows us to approximately treat nuclei (atoms) as classical particles with a classical Hamiltonian

$$H(\dot{\mathbf{R}}^N, \mathbf{R}^N) = \sum_{I=1}^N \frac{1}{2} M_I \dot{\mathbf{R}}_I^2 + U(\mathbf{R}^N), \quad (2.11)$$

where $\dot{\mathbf{R}}$ refers to the time derivative. Accordingly, the equations of motion is governed by

$$M_I \ddot{\mathbf{R}}_I = - \frac{\partial U(\mathbf{R}^N)}{\partial \mathbf{R}_I}, \quad (2.12)$$

which is Newtonian equation instead of Schrödinger equation, Eq. (2.7). The forces acting on nuclei are subsequently evaluated from the gradient of the potential. However, there are exceptions for the lightest atoms (H) and vibrational modes around equilibrium at low temperature can exhibit quantum effects and the assumption of atom, as a single classical particle, is no longer applicable [133].

In general, PES is a complicated mathematical function of atomic positions, electronic states, and its precise determination is extremely critical for performing a correct molecular simulation in terms of structural relaxation or molecular dynamics. The most interesting points on PES are stationary points, where the gradients with respect to all internal coordinates (forces) are zero. During many years, extensive effort has been devoted to accurately and efficiently obtain this function which we can basically divide them into two main categories:

- A) Methods based on direct quantum mechanical principles, namely *ab initio* methods, provide the energy function which can be exact in principle and works for any system such as molecules or crystals. Approximate quantum methods are used in practice due to computational expense [142].
- B) Methods based on molecular mechanical models, namely force field models, provide a functional form of the energy in terms of stretches,

bends, torsions, etc. These are approximate methods that break down in some situations (e.g. breaking bonds), and only works when appropriate parameters are available. I will extensively discuss the force field based methods in molecular mechanics section in Chapter 3.

2.1.5 Moving atoms

In this section, I briefly explain the two most popular frameworks for *ab initio* MD, namely Born-Oppenheimer and Car-Parrinello molecular dynamics [142]. It is assumed that the reader is familiar with electronic structure theories in term of density functional theory (i.e. Kohn-Sham method). A detailed description of these methods can be found in previous works [135, 136, 143].

2.1.5.1 Born-Oppenheimer molecular dynamics

The effective potential energy $U(\mathbf{R}^N)$ in molecular dynamics has the same physical meaning as the Kohn-Sham (KS) [143] energy within the Born-Oppenheimer [134] approximation. This means that Kohn-Sham energy depends only on the nuclear positions and determines the hypersurface for the movement of nuclei that we discussed as PES. The Hamiltonian for the Born-Oppenheimer molecular dynamics (BOMD) therefore is expressed as

$$H(\dot{\mathbf{R}}^N, \mathbf{R}^N) = \sum_{I=1}^N \frac{1}{2} M_I \dot{\mathbf{R}}_I^2 + \min_{\{\phi_i\}} E^{\text{KS}}[\{\phi_i\}, \mathbf{R}^N], \quad (2.13)$$

where $\{\phi_i\}$ and E^{KS} refer to the Kohn-Sham orbitals and energy, respectively. The second term in Eq. (2.13) is obtained by minimizing E^{KS} with respect to $\{\phi_i\}$ which gives the ground-state energy of the interacting electrons in the presence of the nuclei at fixed positions \mathbf{R}^N . Similarly, the equations of motion are given by the gradient of the KS energy

$$M_I \ddot{\mathbf{R}}_I = \frac{\partial}{\partial \mathbf{R}_I} \left(\min_{\{\phi_i\}} E^{\text{KS}}[\{\phi_i\}, \mathbf{R}^N] \right), \quad (2.14)$$

$$= -\frac{\partial E^{\text{KS}}}{\partial \mathbf{R}_I} + \sum_{i,j}^{\text{occ}} \Lambda_{ij} \frac{\partial}{\partial \mathbf{R}_I} \langle \phi_i | \phi_j \rangle. \quad (2.15)$$

It must be noted that the minimization is constrained to orthogonal sets of $\{\phi_i\}$ over occupied orbitals ($\sum_{i,j}^{\text{occ}}$) via Lagrange multipliers Λ_{ij} , and we need

to repeatedly calculate E^{KS} at each time step as the nuclei positions are updated [142].

2.1.5.2 Car-Parrinello molecular dynamics

The basic idea of Car–Parrinello molecular dynamics (CPMD) is to exploit the time scale difference between fast electronic and slow nuclear motion by transforming them into two components of a purely classical system with two sorts of energy scales. It means that even the dynamics for electrons is treated classically which is fictitious and has nothing to do with real electron dynamics. Consequently, the energy is evaluated from both electronic and ionic degrees of freedom. As long as there is no energy transfer from ionic to the electronic part which is likely the case when analyzing the minimum typical frequency associated to fictitious electron and the maximum typical frequency of phonons for ions, the fast electron dynamics keeps the electron close to the BO surface³, as a result, the much slower ionic dynamics follows closely the BO dynamics [144].

This is achieved by considering the Kohn–Sham energy functional E^{KS} that depends on $\{\phi_i\}$ and \mathbf{R}^N . In classical mechanics, the force on the nuclei is obtained from the derivative of a Hamiltonian with respect to the nuclear positions. This suggests that a functional derivative of a given suitable Hamiltonian with respect to the orbitals, which are interpreted as classical fields, might yield the force on the orbitals. Accordingly, Car and Parrinello proposed [142] the following Hamiltonian

$$H[\dot{\mathbf{R}}^N, \mathbf{R}^N, \{\dot{\phi}_i\}, \{\phi_i\}] = \sum_{I=1}^N \frac{1}{2} M_I \dot{\mathbf{R}}_I^2 + \sum_i^{\text{occ}} \frac{1}{2} \mu \langle \dot{\phi}_i | \dot{\phi}_i \rangle \quad (2.16)$$

$$+ E^{\text{KS}}[\{\phi_i\}, \mathbf{R}^N] + \sum_{i,j}^{\text{occ}} \Lambda_{ij} (\langle \phi_i | \phi_j \rangle - \delta_{ij}), \quad (2.17)$$

where μ is the fictitious mass or inertia parameter assigned to the orbital degrees of freedom. The units of the mass parameter μ are energy times a squared time for reasons of dimensionality. The last term Eq. (2.17) creates a constraint to ensure orthogonality of the KS orbitals with Lagrange multipliers Λ_{ij} . Therefore, Car–Parrinello equations of motion are found to be of the

³where the electronic and ionic degrees of freedom remain adiabatically separated

form

$$M_I \ddot{\mathbf{R}}_I = -\frac{\partial E^{\text{KS}}}{\partial \mathbf{R}_I} + \sum_{i,j}^{\text{occ}} \Lambda_{ij} \frac{\partial}{\partial \mathbf{R}_I} \langle \phi_i | \phi_j \rangle, \quad (2.18)$$

$$\mu \ddot{\phi}_i = -\frac{\delta E^{\text{KS}}}{\delta \langle \phi_i |} + \sum_i^{\text{occ}} \Lambda_{ij} | \phi_j \rangle. \quad (2.19)$$

where $\sum_{I=1}^N \frac{1}{2} M_I \dot{\mathbf{R}}_I^2$ stands for the physical temperature of the nuclei at given time, whereas a fictitious temperature $\sum_i^{\text{occ}} \frac{1}{2} \mu \langle \dot{\phi}_i | \dot{\phi}_i \rangle$ is associated to the electronic degrees of freedom. At low electronic temperature, the electronic subsystem stays close to its instantaneous minimum energy $\min_{\{\phi_i\}} E^{\text{KS}}$. Thus, a ground–state wavefunction optimized for the initial configuration of the nuclei will stay close to its ground state also during the time evolution [133, 142]. The first term in Eq. (2.19) indicates a functional derivative of KS energy with respect to KS orbitals.

One advantage of CPMD over BOMD method is that there is no need to recalculate the Schrödinger equation for electrons at each time step which is computationally expensive. Instead, the ground–state wavefunction is evaluated for a given initial configuration, and since then the KS orbitals are propagated through Eq. (2.19). For liquid water at ambient condition, partial radial distribution function (RDF)⁴ of oxygen atoms reveals an excellent agreement between these methods and X-ray scattering experiments as shown in Fig. 2.1 [145]. There are many more details how the *ab initio* MD methods are different from each other and can be implemented in a periodic computational unit cell that can be found in original works [144].

2.2 Statistical thermodynamics

2.2.1 Thermodynamic limit

A physical system typically composed of a large number of particles (N), of order 10^{23} , confined to a space of volume V (L^3). Consequently, it is normal to analyze such a system in the so-called *thermodynamic limit* where $N, V \rightarrow \infty$, while the particle density N/V remains fixed [148]. In this limit, the intensive

⁴See Chapter 4.

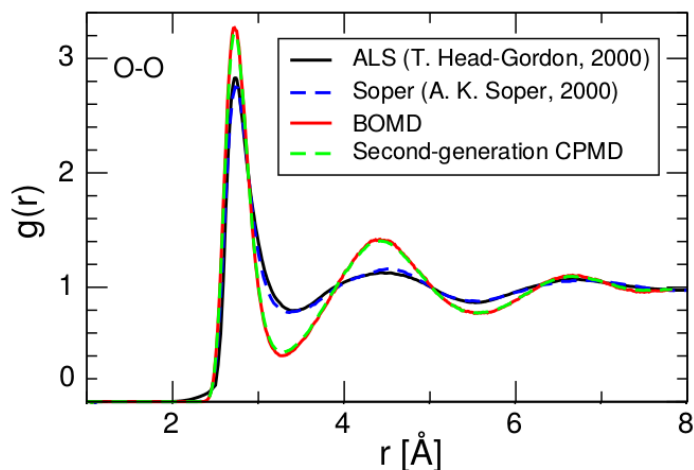


FIGURE 2.1. Radial distribution function (RDF) between oxygen atoms of liquid water at ambient conditions obtained from X-ray scattering experiments (ALS [146] and Soper [147]) and two *ab initio* MD methods (BOMD and CPMD [145]). The position of the peaks obtained from theoretical modeling are in excellent agreement with experiments. For the definition of RDF please refer to Chapter 4. The figure is adapted from Ref. [145].

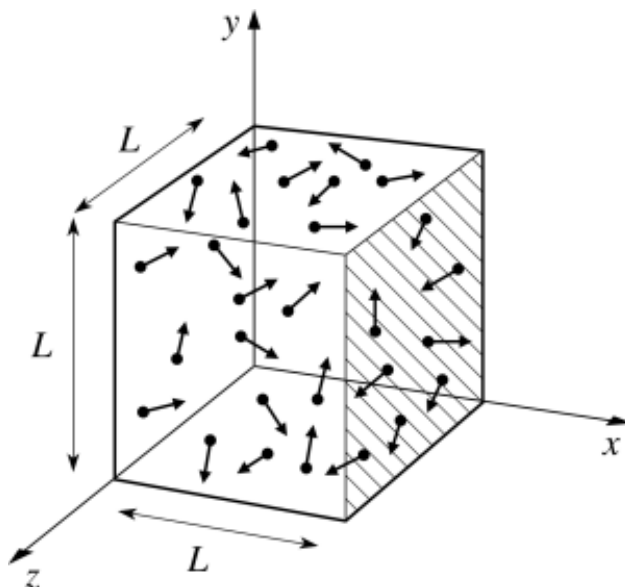


FIGURE 2.2. A schematic representation of N molecules of a gas, as a statistical system, in a volume L^3 . The direction of molecular motion is shown by the arrows. The figure is adapted from <https://cosmolearning.org/courses/statistical-mechanics-particles>.

properties of matter (i.e. density, pressure) in contrast to extensive properties (i.e. volume, mass) remain independent. Furthermore, the possible discrete values of some physical properties, the total energy in a quantum system as an example, might be regarded as continuous variables due to the large number of particles.

2.2.2 Microscopic states

A large number of atoms or molecules forming materials introduces an enormously large number of degrees of freedom (i.e. particle's positions and velocities) that certainly has to be considered when describing precisely the state of the system. But in practice, only a few physical quantities such as temperature, pressure, and density are (or can be) measured. An observable state that represents the collective physical properties of the system is called *macroscopic state* or *thermodynamical state*. Each state that includes all internal degrees of freedom is referred as *microscopic state*. Figure 2.2 illustrates a schematic representation of N molecules of a gas, as a statistical system, in a volume L^3 . The direction of molecular motion is shown by the arrows. The degree of freedom, that certainly has to be considered when describing precisely the state of the system, includes positions and velocities of the particles is an extremely large number. While in practice, only a few physical quantities such as temperature, pressure, are (or can be) measured. It is important to note that a set of possible microscopic states can be realized by the system under a certain macroscopic state.

2.2.3 Phase space

Let $\mathbf{R}^N = \{\mathbf{R}_1, \mathbf{R}_2, \dots, \mathbf{R}_N\}$ be the coordinates of a system and $\mathbf{P}^N = \{\mathbf{P}_1, \mathbf{P}_2, \dots, \mathbf{P}_N\}$ their corresponding momenta. A microscopic state of the system is defined by specifying the Hamiltonian of the system $H(\mathbf{R}^N, \mathbf{P}^N)$ with $6N - N_c \simeq 6N$ degrees of freedom in the thermodynamic limit, where N_c indicate the few number of constraints present in the system (i.e. fixed center of mass). The $6N$ -dimensional space constructed from these variables as the generalized coordinates is known as *phase space* of the system, and each point in the

phase space corresponds to a microscopic state of the system at a given time. In context of quantum mechanics, the position and the momentum can not be determined simultaneously due to the uncertainty principle of Heisenberg, the phase point is still defined with less rigorous meaning and is treated by a coefficient \hbar along each direction of particle, where \hbar refers to Planck's constant. Moreover, if the system contains identical particles, in the quantum mechanical sense that they are impossible to distinguish even in principle, then the number of microstates be divided by a $N!$ (N factorial). For a quantum system, the microscopic state is defined as a quantum state that is typically discrete and denoted by a set of quantum numbers.

The dynamics of the system, given by equations of motion, leads to a set of continuous points (trajectory) in the phase space known as phase orbit. For an isolated system the energy is constant

$$H(\mathbf{R}^N, \mathbf{P}^N) = E, \quad (2.20)$$

and the phase orbit must lie on a hyper surface of constant energy.

2.2.4 Time average

When a dynamical system is kept in equilibrium at a certain thermodynamical state (i.e. constant temperature), it never stays in a particular microscopic but moves in phase space. We can not precisely determine at which specific microscopic state the system is at given time. These dynamical states are demonstrated by the motion of a phase point in phase space. A physical quantity A is shown by a time-dependent quantity $A(t)$ which represents a point in phase space. The observed value A_{obs} of A can be intuitively defined as a time average of A_t over trajectories that is given by

$$A_{\text{obs}} = \langle A \rangle_{\text{time}} = \lim_{t \rightarrow \infty} \frac{1}{t} \int_0^t A(t') dt'. \quad (2.21)$$

With molecular simulations time is in discrete steps, Eq. (2.21) becomes

$$\langle A \rangle_{\text{time}} = \frac{1}{L} \sum_{k=1}^L A(t_k),$$

where L is the number of time steps [149].

2.2.5 Thermal equilibrium

The laws of thermodynamics are primarily based on equilibrium. Thus the thermodynamical variables describing the macroscopic states of a system remain stationary. Thus a transition from one such state to another is reversible. It is important to note that the existence of thermal equilibrium in contrast to mechanical equilibrium does not demand the strict absence of any variation in time, and there will be fluctuations over a range that can be relatively significant. Thermodynamic equilibrium is characterized by the requirement that the average value of thermodynamical variable, as a macroscopic quantity, should be constant in time [150]

$$\frac{d}{dt}\langle A \rangle_{\text{time}} = 0. \quad (2.22)$$

2.2.6 Ensemble average

In such thermal equilibrium, we can approach the problem by defining a probability distribution for the set of microscopic states instead of considering the time evolution of the system. An observable physical quantity A_{obs} is related to the average of the possible microscopic states in phase space, namely ensemble average, as follows

$$A_{\text{obs}} = \langle A \rangle_{\text{ensemble}} = \int_{\Xi} A(P) f(P) d\Gamma, \quad (2.23)$$

where $A(P)$ represents the microscopic value of a physical quantity A at phase point P , $f(P)$ is the corresponding probability density for the system to be at that phase point, $d\Gamma$ is the volume element of phase space, and Ξ indicates a subspace of phase space that specifies a certain macroscopic condition [150]. Equation (2.22) implies that the probability density must contain no explicit dependence on the time. In fact, what we do is to make a very large number of copies of the system having the same macroscopic state but consisting of different microscopic states. We then calculate the average values over this large number of replicas, namely ensemble [151, 152].

2.2.7 Ergodic theorem

There is an equivalence between ensemble average and time average

$$\langle A \rangle_{\text{time}} = \langle A \rangle_{\text{ensemble}}, \quad (2.24)$$

for a system in thermal equilibrium which is known as the *Ergodic theorem* [153]. It has been initially studied as a mathematical problem but has various physical significances. As a consequence of equilibrium, any microscopic state that belongs to the same energy surface has equal probability to be occupied. Or, the system passes all the points on its energy surface with the same chance. The system that conform to such probability is called *ergodic*, and most physical systems are ergodic [150, 153]. However, there are physical systems that clearly do not exhibit ergodic behavior such as a box of non-interacting particles when the particles bounce back and forth due to elastic collisions to the walls where the phase orbit can not pass through all points on the energy surface in phase space.

2.2.8 Microcanonical ensemble

As long as a system is kept isolated in the sense that there is no energy exchange with the surrounding environment, then the total energy E remains stationary. This is known as the microcanonical ensemble. The system has the same chance to be found in each microscopic state according to the principle of equal weight. The probability density in Eq. (2.23) is therefore a constant value that can be obtained from

$$f(P) = \frac{1}{\int d\Gamma} = \frac{1}{\int \prod_{i=1}^{3N} d\mathbf{P}_i d\mathbf{R}_i}, \quad (2.25)$$

where the integration is done over all phase points P belonging to the surface energy $H(\mathbf{R}^N, \mathbf{P}^N) = E$, and $\prod_{i=1}^{3N} d\mathbf{P}_i d\mathbf{R}_i$ refers to the volume element in $6N$ -dimensional phase space. A related point to consider is that if we apply quantum mechanics, including identical particles and the uncertainty principle, then integration over phase space becomes

$$\int \prod_{i=1}^{3N} d\mathbf{P}_i d\mathbf{R}_i \Rightarrow \frac{1}{N! \hbar^{3N}} \int \prod_{i=1}^{3N} d\mathbf{P}_i d\mathbf{R}_i. \quad (2.26)$$

In practice, the microcanonical ensemble does not correspond to an experimentally realistic situation. Most experimental observations are performed in canonical (or isothermal) ensemble NVT ⁵, isothermal–isobaric ensemble NPT ⁶, and grand canonical ensemble μVT ⁷. In what follows, I only discuss the canonical ensemble.

2.2.9 Canonical ensemble

If a system is kept in thermal equilibrium in contact with a heat bath at temperature T , the system can exchange energy, so that the states of the system differ in total energy. This is called *canonical* ensemble or *isothermal* ensemble. The probability density of the system is then given by

$$f(P) = \frac{e^{-\beta H(P)}}{\int e^{-\beta H(P)} d\Gamma} = \frac{e^{-\beta H(\mathbf{R}^N, \mathbf{P}^N)}}{\int e^{-\beta H(\mathbf{R}^N, \mathbf{P}^N)} \prod_{i=1}^{3N} d\mathbf{P}_i d\mathbf{R}_i}, \quad (2.27)$$

where the integration is done over all points in phase space, $\beta = 1/k_b T$ with the Boltzmann constant k_b . Above equation implies that at a given temperature, the system is more probable to be found in microscopic states with a lower energy. Moreover, it is proven that regardless of different probability distributions of the ensembles, a statistical system shows the same observable behavior in the thermodynamic limit. This property is an universal one, namely statistical ensemble equivalence, which can be observed even in the simplest case of the grand canonical and canonical ensembles of classical statistical physics [154].

2.2.9.1 Partition function

For a large system in canonical ensemble, the energy from the point of view of statistical ensemble can be expected to be found close to the average value

⁵Constant number of particles (N), volume (V), and temperature (P) of the system.

⁶Constant number of particles, pressure (P), and temperature.

⁷Constant chemical potential (μ), volume, and temperature.

given by Eq. (2.23)

$$\begin{aligned}
 E = \langle H \rangle &= \int H(P) f(P) d\Gamma, \\
 &= \frac{\int H(P) e^{-\beta H(P)} d\Gamma}{\int e^{-\beta H(P)} d\Gamma} = \frac{-\frac{\partial}{\partial \beta} \int e^{-\beta H(P)} d\Gamma}{\int e^{-\beta H(P)} d\Gamma}, \\
 &= -\frac{\partial}{\partial \beta} \left(\ln \int e^{-\beta H(P)} d\Gamma \right). \tag{2.28}
 \end{aligned}$$

The energy can be written more compactly in terms of the *partition function* defined as

$$\begin{aligned}
 Z &= \ln \int e^{-\beta H(P)} d\Gamma \\
 &= \int e^{-\beta H(\mathbf{R}^N, \mathbf{P}^N)} \prod_{i=1}^{3N} d\mathbf{P}_i d\mathbf{R}_i, \tag{2.29}
 \end{aligned}$$

where we equivalently obtain

$$E = \frac{-\frac{\partial Z}{\partial \beta}}{\beta} = -\frac{\partial \ln Z}{\partial \beta}. \tag{2.30}$$

The partition function Z is a function of the thermodynamic state (i.e. temperature and volume) of the system, and most of the aggregate thermodynamic variables of the system, such as the total energy, free energy, and pressure, can be expressed in terms of the partition function or its derivatives. This function principally provides all the thermodynamic functions of a macroscopic system and their relation with the properties of the microscopic system. It is in fact an important mathematical tool that makes a connection between statistical mechanics and thermodynamics [127, 150]. However, determining the partition function for a system of interacting particles, even numerically, is a challenge [127].

2.2.9.2 Free energy

Free energy⁸ is perhaps the most important thermodynamical quantity that determines the final state of a statistical system rather than the conventional total energy. Consider an isolated box of volume $2V$ divided into two equal

⁸The general term is *thermodynamical energy*

compartments. An ideal gas occupies half of the container and the other half is empty. When the partition separating the two halves of the box is removed, the system reaches equilibrium by filling the whole box also known as *free expansion*. Such behavior of the thermodynamical system can not be explained by finding the minimum of the conventional total energy. Instead, we have to consider the free energy to obtain the thermodynamical equilibrium of the system⁹. The free energy of a system in the canonical ensemble, namely *Helmholtz* free energy, has the form

$$F = E - TS \quad (2.31)$$

that includes additionally a contribution from *entropy* S at finite temperature T . Entropy has statistical nature in contrast to the energy term E that has a mechanical significant. It is must be noted that MD simulation also seeks the minimum of the free energy¹⁰ rather than the total energy and this explains why it predicts correctly the free expansion of a gas. The entropy and the free energy are related to the partition function as follows

$$S = k_b \left[\ln Z - \beta \frac{\partial Z}{\partial \beta} \right], \quad (2.32)$$

$$F = -\frac{1}{\beta} \ln Z. \quad (2.33)$$

Except for an ideal gas and few simple examples, the explicit calculation of the free energy is a complicated task even in a computational framework. However, its evaluation or more precisely its relative change sometimes is necessary when studying phase transitions, critical phenomena, or other transformations. Computer simulations can be extended to facilitate the calculation of the free energy using important sampling [155–157]. Furthermore, the free energy is basically a function of the phase space coordinates, however, typically calculated as function of a few variables, namely *order parameters*. The behavior of the system is thus studied in terms of the introduced order parameters [158]. A detailed description of the entropy and different definitions for the free energy¹¹ that depend on thermodynamical variables that

⁹It is originated from the second law of thermodynamics.

¹⁰Although it is not an easy task to calculate it explicitly.

¹¹Such as Enthalpy, Gibbs, and Landau.

are held constant in the process, can be found in many standard statistical mechanics textbooks [148, 150]. Throughout the thesis, I do not explicitly calculate the free energy function for the MD simulated systems but it is the relevant thermodynamical energy that its (local) minimum results in the equilibrium state.

MOLECULAR DYNAMICS SIMULATIONS

Molecular dynamics (MD) simulation and more precisely classical molecular dynamics simulation is today a powerful tool to explore the equilibrium and transport properties of many-body systems. The term classical stands for the motion of atoms that obeys the laws of classical mechanics. The key idea behind molecular dynamics simulations is an attempt to generate interatomic interactions that basically consist of nuclei and electrons in a functional form that only depends on the nuclei positions. This is an approximation but further boosts the computational efficiency that lets us reach time and length scales far greater than first principle approaches.

In this chapter, I introduce a general framework of performing molecular dynamics simulation¹ by discussing integration scheme, MD algorithm, statistical ensemble implementation, molecular modeling, and force fields.

3.1 Introduction

Molecular dynamics (MD) is a dynamics-based approach when the time development of a system of particles, trajectories, are deterministic and given

¹Thereafter the term *molecular dynamics* is used instead of the *force field based molecular dynamics* for sake of simplicity and I explicitly mention the complete term in any other case such as *ab initio* molecular dynamics.

by the equations of motion. It is in contrast to the alternative Monte Carlo method² when positions of the particles are updated randomly based on the Metropolis algorithm [159, 160]. In the simplest physical terms, molecular dynamics is characterized as a method of particle tracing and it essentially consists of three major parts [148]:

- 1) The first is a model which describes the interatomic potential, suitable initial and boundary conditions. We assume for now that the potential term, the most computationally expensive part, is a known function and I will further elaborate it within the molecular modeling and the force field potentials sections.
- 2) The second is a direct solving of the equations of motion via a time integrator which has to be carried out numerically.
- 3) The third is employing statistical ensembles in order to extract measurable thermodynamical properties from a system of numerous particles with an extreme large number of degrees of freedom.

It is important to note that MD is an atomistic approach that treats the ions and electrons as a single, classical entity. The underlying assumption is that this classical entity forms the material and when this is no longer a reasonable approximation, we need to drop the idea of atoms and treating separately the nuclear and the electronic degrees of freedom through more advanced methods known as *ab initio* MD [142].

3.2 Integration scheme

Assume a system of N interacting particles (see Fig. 3.1). The Hamiltonian of such a system expressed as a function of all positions $\mathbf{r}^N = \{\mathbf{r}_1, \mathbf{r}_2, \dots, \mathbf{r}_N\}$ ³ and momenta $\mathbf{p}^N = \{\mathbf{p}_1, \mathbf{p}_2, \dots, \mathbf{p}_N\}$ is given by

$$H(\mathbf{p}^N, \mathbf{r}^N) = \sum_{i=1}^N \frac{\mathbf{p}_i^2}{2m_i} + U(\mathbf{r}^N), \quad (3.1)$$

²It must be noted that Monte Carlo is another simulation method than molecular dynamics. The latter is the method I have employed throughout the thesis.

³From now on we use \mathbf{r} instead of \mathbf{R} when referring to the coordinate of an atom.

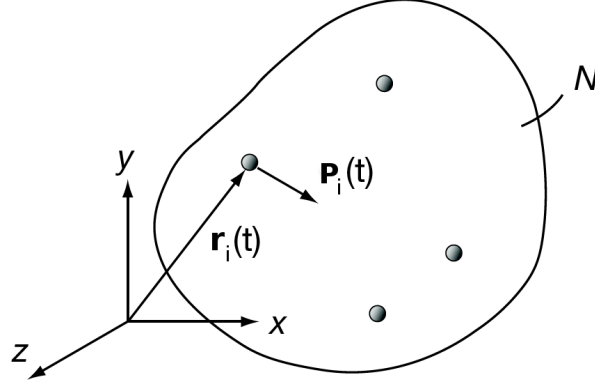


FIGURE 3.1. A system of N interacting particles with specified initial and boundary conditions. It consists of a set of coordinates $\mathbf{r}^N = \{\mathbf{r}_1, \mathbf{r}_2, \dots, \mathbf{r}_N\}$ and momenta $\mathbf{p}^N = \{\mathbf{p}_1, \mathbf{p}_2, \dots, \mathbf{p}_N\}$ that describe the Hamiltonian $H(\mathbf{p}^N, \mathbf{r}^N)$. The figure is adapted from Ref. [149].

where H is the sum of the kinetic and the potential energy terms. The equations of motion of the system are given by Hamilton's equations:

$$\frac{d\mathbf{r}_i}{dt} = \frac{\partial H}{\partial \mathbf{p}_i}, \quad \frac{d\mathbf{p}_i}{dt} = -\frac{\partial H}{\partial \mathbf{r}_i}, \quad (3.2)$$

that means we need to solve Newton's equation of motion for each particle $i = \{1, 2, \dots, N\}$ in order to have position \mathbf{r}_i and velocity \mathbf{v}_i at any given time t . For a particle i with mass m_i , it can be rewritten equivalently as two equations

$$\frac{d\mathbf{r}_i}{dt} = \mathbf{v}_i, \quad \frac{d\mathbf{v}_i}{dt} = \mathbf{F}_i(\mathbf{r}^N)/m_i, \quad (3.3)$$

where $\mathbf{F}_i(\mathbf{r}^N)$ is the total force acting on particle i and in principal it is a function of all particles

$$\mathbf{F}_i(\mathbf{r}^N) = -\frac{\partial U(\mathbf{r}^N)}{\partial \mathbf{r}_i}. \quad (3.4)$$

For a system with $3N$ sets of coupled equations, Eq. (3.4) may look deceptively simple. Actually, as complicated as the famous N-body problem, we are not able to generally find an analytical solution when $N > 2$. Consequently, we have to carry out numerical calculations with a finite difference integrator. At infinitesimal time steps δt , it can be found by considering Taylor expansions

for $\mathbf{r}(t)$ as follows

$$\begin{aligned}\mathbf{r}(t + \delta t) &= \mathbf{r}(t) + \frac{d\mathbf{r}(t)}{dt}\delta t + \frac{1}{2}\frac{d^2\mathbf{r}(t)}{dt^2}\delta t^2 + \mathcal{O}(\delta t^3), \\ \mathbf{r}(t - \delta t) &= \mathbf{r}(t) - \frac{d\mathbf{r}(t)}{dt}\delta t + \frac{1}{2}\frac{d^2\mathbf{r}(t)}{dt^2}\delta t^2 - \mathcal{O}(\delta t^3).\end{aligned}\quad (3.5)$$

After summing the equations and rearranging, we will have

$$\mathbf{r}(t + \delta t) = \mathbf{r}(t) + \mathbf{v}(t)\delta t + \frac{1}{2}\mathbf{a}(t)\delta t^2 + \mathcal{O}(\delta t^4), \quad (3.6)$$

where $\mathbf{a}(t)$ refers to acceleration and the expression for the velocity can be simply obtained from the finite difference formula

$$\mathbf{v}(t) = \frac{\mathbf{r}(t + \delta t) - \mathbf{r}(t - \delta t)}{2\delta t} + \mathcal{O}(\delta t^2). \quad (3.7)$$

This is the so-called *Verlet algorithm* [161] which is one of the most accurate and stable algorithms for MD with minimum attainable energy drift. A suitable time increment δt is a femtosecond (10^{-15} s). This algorithm uses positions and accelerations at time t and the position at time $t - \delta t$ to calculate a new position at time $t + \delta t$. All these have to be stored at every iteration which is inefficient in term of memory-usage.

There is a variant *velocity Verlet* [162] algorithm that can be obtained by replacing $t \rightarrow t + \delta t$ in Eq. (3.6) and considering $t + 2\delta t$ as $(t + \delta t) + \delta t$ in Eq. (3.5). Finally it takes the form

$$\mathbf{r}(t + \delta t) = \mathbf{r}(t) + \mathbf{v}(t)\delta t + \frac{1}{2}\mathbf{a}(t)\delta t^2 + \mathcal{O}(\delta t^4), \quad (3.8)$$

$$\mathbf{v}(t + \delta t) = \mathbf{v}(t) + \frac{1}{2}(\mathbf{a}(t) + \mathbf{a}(t + \delta t))\delta t + \mathcal{O}(\delta t^2). \quad (3.9)$$

This integrator requires only the storage of positions, velocities and accelerations that all correspond to the same time step. As a result, the trajectories of N particles are evaluated by repeatedly calculating the interactions between the particles and integrating their equations of motion one step at a time.

There are many other numerical integrators in the literature such as *Leapfrog*, *Beeman*, etc that can be used to update atoms however each with their own strengths and weaknesses [141, 163]. In the absence of floating-point round-off errors, the discrete mapping rigorously preserves a proper MD

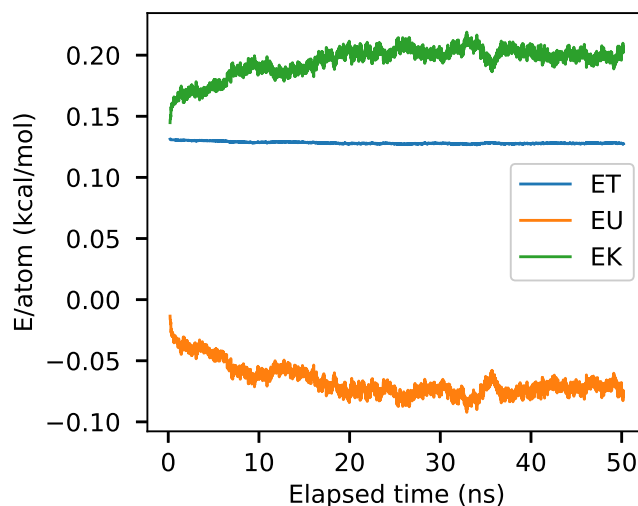


FIGURE 3.2. The variation of the total energy (ET), potential energy (EU), and kinetic energy (EK) of MD simulated Argon with LJ (12-6) interatomic potential, 650 atoms, and at constant-NVE ensemble. As can be seen, the *velocity Verlet* integrator works decently even for a long simulation time (50 ns). For test reasons, setting time step to 10 fs, we still see a relatively small energy drift. The employed LAMMPS script for the figure is available at <https://github.com/hghcomphys>.

(see Fig. 3.2). However, there are several criteria to determine the accuracy of a MD algorithm by inspecting the energy drift, phase spaces, and trajectory deviation after a long simulation time [149].

3.3 MD algorithm

A typical MD simulation has certain sequences of steps that is illustrated in Fig. 3.3 and briefly as follows [149]:

- 1) Setting the initial conditions that includes the initial particles position as input structure, it can be experimentally determined from NMR spectroscopy or X-ray crystallography measurements, and randomly assigning the initial velocities to the particles according to the initial temperature.
- 2) Calculating the force on each atom which is a function of the position of

particles is the most computationally challenging part. The efficiency of MD simulation therefore depends on how the force can be calculated as simple as possible without compromising the physical description.

- 3) Updating particles positions and velocities using a time integrator (i.e. Eq. (3.9)). Important to know that any desired statistical ensemble (such as constant pressure or constant temperature) has to be treated in this step.
- 4) Repeating steps 2 and 3 until reach a preset number of steps.
- 5) Further statistical analysis can be done on the particles trajectory, which in fact are the system configurations, micro states, as a function of time in order to calculate properties of the system.

The boundary of the simulation cell or the shape of the simulation box are crucial and must be properly treated due to the limited number of simulated particles in comparison to a realistic and practically infinite system that typically contains of the order of 10^{23} particles. Boundary has a dramatic impact on the small size system while it is not the case for a large system where almost all particles are interacting with each and less effected by the presence of the confining walls. A common approach in order to reduce the impact of the boundary is to employ periodic boundary conditions (PBC) which are often chosen to approximate a large system by using a small part called a unit cell. Accordingly, a particle close to a boundary interact with image particles which is in fact a copy of the original unit cell (see Fig 3.4).

3.4 Statistical ensemble

In a standard molecular dynamics simulation, the total energy (E) and total momentum are constants of motion. This means that any (time) averages over macroscopic parameters of an ensemble are equivalent to microcanonical [165], namely constant-NVE ensemble. In contrast, a conventional Monte Carlo simulation simulates a canonical ensemble (constant-NVT) [160]. It is

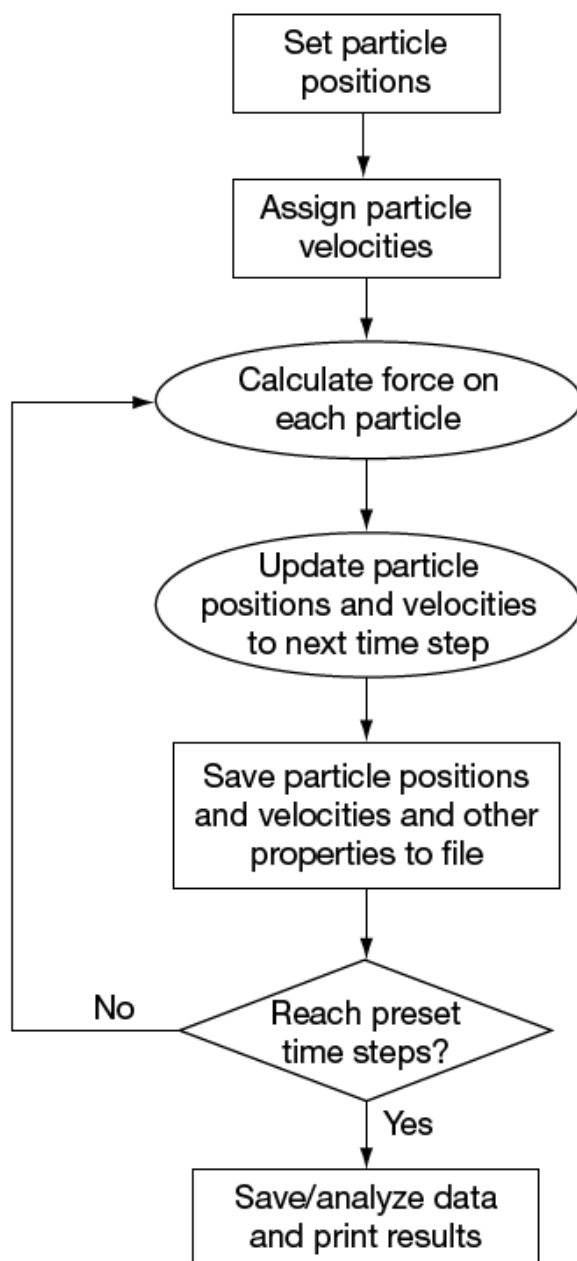


FIGURE 3.3. Flow chart of a standard MD simulation. The figure is adapted from Ref. [149].

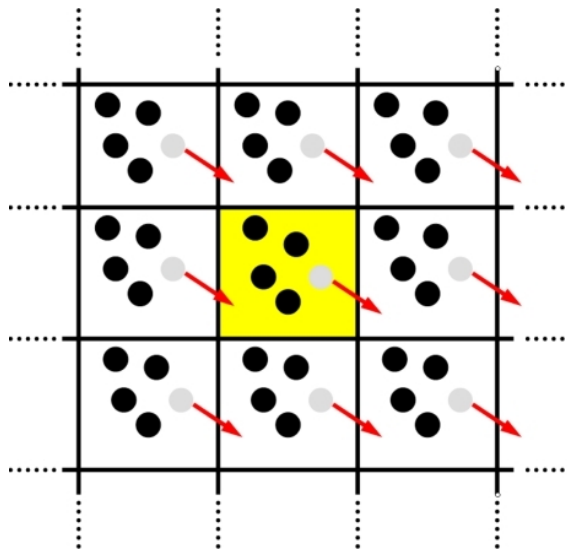


FIGURE 3.4. Two-dimensional schematic of periodic boundary conditions. Particle trajectories in the central simulation box (unit cell) are copied in every direction (image particles). Subsequently, particles at the boundary interact with those particles located in image unit cell but at closer distance. The figure is adapted from Ref. [164].

important to note that the difference between the statistical averages disappear in the thermodynamic limit even for a system of a few hundred particles. However, it is often more convenient to perform a simulation in a specific ensemble. In addition, we sometimes limited ourselves to a specific ensemble that is similar to what applies in experiment (such as constant temperature, pressure, stress, etc).

In this sections, I explain how to implement molecular dynamics simulation at constant-temperature and constant-pressure. Subsequently, more advanced ensemble such as *i.e. constant-NPT* [166] can be implemented by employing the two approaches together.

3.4.1 Isothermal ensemble

In term of statistical mechanics, the instantaneous value of the temperature is related to the kinetic energy via the particles velocities as follows:

$$\sum_{i=1}^N \frac{1}{2} m_i \mathbf{v}_i^2 = \frac{1}{2} k_b T N_{\text{dof}}, \quad (3.10)$$

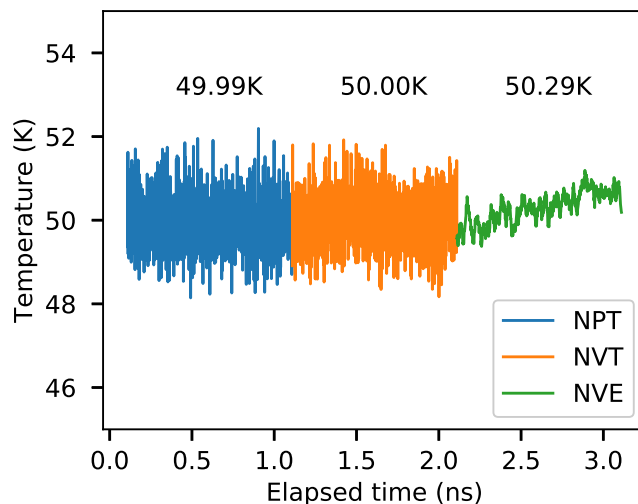


FIGURE 3.5. Equivalence between different statistical ensembles NPT, NVT, and NVE in thermodynamics limit obtained from MD simulation of Argon at 50K. The figures represent instantaneous temperature as function of time and the numbers represent average temperature $\langle T \rangle$ separately at each ensemble. The employed LAMMPS script for the figure is available at <https://github.com/hghcomphys>.

where k_b is Boltzmann constant and N_{dof} is the number of degrees of freedom which is the total number of freedom for kinetic terms subtracted by the number of constraint $N_{\text{dof}} = 3N - N_c$. For conventional MD all particles are free to move, N_c is 3 because of fixed center of mass along x , y , and z -directions. However, if there would be extra constrains such as fixing a group of atoms in certain directions or using a rigid model for the molecules, these constrains also have to be taken into account. Macroscopic measurable temperature is then an ensemble average or equivalently time average of the instantaneous temperature $\langle T \rangle$.

The temperature can be controlled by connecting a thermostat to the atoms through manually changing the velocities or introducing extra terms in the Hamiltonian and allowing energy exchange between the particles and an imaginary thermal bath. There are different thermostats such as velocity scaling, Berendsen [167], and Nosé-Hoover [168] which I will discuss now.

3.4.1.1 Velocity scaling

An obvious way to alter the temperature of the system is through a *velocity scaling* method. If the temperature at time t is T and the velocities are multiplied by a factor λ , then the associated temperature change can be calculated as

$$\Delta T = \sum_{i=1}^N m_i (\lambda \mathbf{v}_i)^2 - \sum_{i=1}^N m_i \mathbf{v}_i^2,$$

$$\Delta T = (\lambda^2 - 1)T, \quad (3.11)$$

$$\lambda = \sqrt{T_0/T}. \quad (3.12)$$

The simplest way to control the temperature is thus to multiply the velocities at each time step by the factor λ , and T_0 is the desired temperature (thermal bath). One problem with this approach is that it does not allow fluctuations in temperature and undesirably destroys the Maxwell-Boltzmann (MB) distribution of velocities which is crucial for a system at thermodynamics limit.

3.4.1.2 Berendsen thermostat

A softer formulation of this approach is the *Berendsen* thermostat [167]. To maintain the temperature the system is coupled to an external heat bath with fixed Temperature T_0 . The velocities are scaled at each step, such that the rate of change of temperature is proportional to the difference between the current and the desired temperature:

$$\frac{dT}{dt} = \frac{1}{\tau}(T_0 - T), \quad (3.13)$$

where τ is the coupling parameter which determines how tightly the bath and the system are coupled. This method gives an exponential decay of the system towards the desired temperature. The change in temperature between successive time steps δt is

$$\Delta T = \frac{\delta t}{\tau}(T_0 - T),$$

$$\Delta T = (\lambda^2 - 1)T,$$

$$\lambda = \sqrt{1 + \frac{\delta t}{\tau} \left(\frac{T_0}{T} - 1 \right)} \quad (3.14)$$

In practice, τ is used as a parameter to adjust the strength of the coupling with the thermal bath. Its value has to be chosen carefully and not out of range. For too large value of τ the Berendsen thermostat is inactive and the run is sampling a microcanonical ensemble (constant-NVE). On the other hand, too small value of τ will cause unrealistically low temperature fluctuations. If τ is chosen the same as the timestep δt , the Berendsen thermostat is nothing else than the simple velocity scaling. Recommended values is $\tau \approx 100\delta t$ which is typically used in MD simulations of condensed-phase systems. The Berendsen thermostat is extremely efficient for relaxing a system to the target temperature, but once the system has reached equilibrium, it might be more important to use the canonical ensemble because of distorted Boltzmann distribution of velocities.

3.4.1.3 Nosé-Hoover thermostat (canonical ensemble)

The extended system method was originally introduced by Nosé [169]. It is based on defining a new Hamiltonian for an extended system of N particles plus additional coordinate s in order to couple the real system with an artificial heat bath. The Hamiltonian of the extended system is defined as

$$H_{\text{ext}}(\{\mathbf{p}^N, p_s\}, \{\mathbf{r}^N, s\}) = \sum_{i=1}^N \frac{\mathbf{p}_i^2}{2m_i s^2} + U(\mathbf{r}^N) + \frac{p_s^2}{2Q} + gk_B T_0 \ln s \quad (3.15)$$

that probes microcanonical ensemble of $6N + 2$ degree of freedom. Where, s is the artificial coordinate, associated with a mass $Q > 0$ as well as the momentum p_s . The magnitude of Q determines the coupling between the heat bath and the real system and so influences the temperature fluctuations. It is proved that a microcanonical ensemble of the extended system is mathematically equivalent to the canonical ensemble of the original system when $g = 3N + 1$. In fact, the extra terms have no physical interpretations, and they are introduced to ensure that the algorithm produces a canonical ensemble for the original system. Accordingly, the equations of motion of the extended

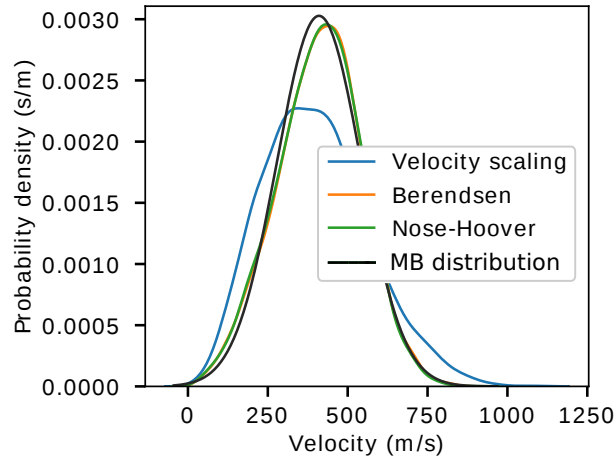


FIGURE 3.6. Velocity distribution function of MD simulated Argon for three different velocity scaling, Berendsen, and Nosé-Hoover thermostats at 300K. Notice that velocity scaling does not give a proper velocity distribution. However, Berendsen thermostat and Nosé-Hoover thermostat work very well. The MB stands for Maxwell-Boltzmann. The employed LAMMPS script for the figure is available at <https://github.com/hghcomphys>.

system become

$$\frac{d\mathbf{p}_i}{dt} = \mathbf{F}_i(\mathbf{r}^N), \quad \frac{dp_s}{dt} = \left(\sum_{i=1}^N \mathbf{p}_i^2 / (m_i s^2) - g k_B T_0 \right) / s, \quad (3.16)$$

$$\frac{d\mathbf{r}_i}{dt} = \mathbf{p}_i / (m_i s^2), \quad \frac{ds}{dt} = p_s / Q. \quad (3.17)$$

In practice, due to problems encountered in the numerical implementation, the *Nosé* extended system Hamilton was developed by *Hoover* and is suitable for generating more accurate canonical ensemble [168]. The simplified equations of motion can be obtained by introducing a friction coefficient ξ and $g = 3N$ that has the form of

$$\frac{d\mathbf{p}_i}{dt} = \mathbf{F}_i(\mathbf{r}^N) - \xi \mathbf{p}_i, \quad \frac{d\xi}{dt} = \left(\sum_{i=1}^N \mathbf{p}_i^2 / m_i - g k_B T_0 \right) / Q, \quad (3.18)$$

$$\frac{d\mathbf{r}_i}{dt} = \mathbf{p}_i / m_i, \quad \frac{d \ln s}{dt} = \xi. \quad (3.19)$$

The comparison between the three introduced thermostats: velocity scaling, Berendsen, and Nosé-Hoover are illustrated in Fig. 3.6 for liquid Argon at

300K. It can be seen that velocity scaling does not give a proper velocity distribution. However, Berendsen thermostat works just well as the Nosé-Hoover thermostat.

3.4.2 Isobaric ensemble

Conventional MD simulation is at constant volume. However, most experiments are performed at constant pressure and the volume is thus a dynamical variable to adjust the system to the desired pressure. The usual approach to the evaluation of the pressure P in a molecular simulation involves (time) averaging of the instantaneous or microscopic pressure using *Clausius virial* theorem [170]. As a result, the pressure of a classical N -body system is defined as

$$P = \left\langle \frac{1}{3V} \sum_{i=1}^N (m_i \mathbf{v}_i^2 - \mathbf{F}_i \cdot \mathbf{r}_i) \right\rangle, \quad (3.20)$$

$$= \rho k_B T - \left\langle \frac{1}{3V} \sum_{i=1}^N \mathbf{F}_i \cdot \mathbf{r}_i \right\rangle \quad (3.21)$$

where $\rho = N/V$ is the number density and V is the volume of the simulation box. The first term includes the kinetic energy contribution, and the second term is the inner *virial* for interactions [171]. We have considered coupling of a system with a heat bath. The same principle is applied to couple a system to a pressure bath with fixed reference pressure of P_0 . For instance, *Berendsen* barostat varies the volume instead of the particles velocity by resetting the pressure of the system through rescaling the system volume and the atoms coordinates within the simulation box at every time step [167], Analogously, we have a similar expression for gentle pressure resetting as follows:

$$\frac{dP}{dt} = \frac{1}{\tau_P} (P_0 - P) \quad (3.22)$$

where τ_P controls the coupling between the simulated system to the pressure bath, see Eq (3.13). A simple proportional coordinate scaling, associated with volume scaling, is applied by adding an extra term to the equation of $\frac{d\mathbf{r}}{dt} = \mathbf{v}$ and consequently the volume that are given by

$$\frac{d\mathbf{r}}{dt} = \mathbf{v} + \alpha \mathbf{r}, \quad \frac{dV}{dt} = 3\alpha V. \quad (3.23)$$

The pressure change related to the isothermal compressibility is

$$\frac{dP}{dt} = -\frac{1}{\gamma V} \frac{dV}{dt} = -\frac{3\alpha}{\gamma}, \quad (3.24)$$

and using Eq. (3.22) we finally obtain

$$\alpha = -\frac{\gamma(P_0 - P)}{3\tau_P}. \quad (3.25)$$

Assume an isotropic system in a cubic box (L^3), a proportional scaling of coordinates $\mathbf{r} \rightarrow \mu\mathbf{r}$ and box length $L \rightarrow \mu L$ per time step at first order in δt accordingly is

$$\mu = \left[1 - \frac{\delta t}{\tau_P} (P_0 - P) \right]^{1/3}. \quad (3.26)$$

In practice, the compressibility γ may not be accurately known. Since an inaccuracy in γ only influences the accuracy of the noncritical time constant τ_P , the imprecision of γ has no consequence for the dynamics. A recommended value for τ_P in MD simulation is $1000\delta t$. More advanced methods such as the extended system method is also applicable to the barostat, namely, *Nosé-Hoover* barostat [172].

3.5 Molecular modeling

In previous sections, we have discussed algorithms developed to solve the equations of motion and employing statistical ensembles in order to perform the standard MD simulations. Since, we have assumed that particle interactions are described by a known interatomic potential function $U(\mathbf{r}^N)$. It is clear from Eqs. (3.3 and 3.4) that the interaction potential is the most critical quantity in MD modeling and simulation. It basically controls the simplicity of the MD algorithm and physical fidelity of the simulation results. In this section, I will further explain this interaction potential and explore particles interplay forces in terms of intra and inter molecular interactions.

In the field of molecular mechanics or force field development, a molecule is classically modeled as a series of charged points (atoms) linked through bonds where the topology of the molecule is described by additional many body terms

that concerns angles, dihedrals, etc. Furthermore, non-bond interactions between the atoms are also given by pair-wise expressions. A force field is a mathematical expression describing the dependence of the energy of a system on the coordinates of all particles. It consists of an analytical form of the interatomic potential energy, $U(\mathbf{r}^N)$ and a set of parameters entering into this framework. For a typical system, it is expressed as [141]

$$\begin{aligned}
 U(\mathbf{r}^N) = & \sum_{\{i,j\}} U^{\text{bond}}(\mathbf{r}_i, \mathbf{r}_j) + \sum_{\{i,j,k\}} U^{\text{angle}}(\mathbf{r}_i, \mathbf{r}_j, \mathbf{r}_k) \\
 & + \sum_{\{i,j,k,l\}} U^{\text{dihedral}}(\mathbf{r}_i, \mathbf{r}_j, \mathbf{r}_k, \mathbf{r}_l) + \sum_{\{i,j\}} U^{\text{nb}}(\mathbf{r}_i, \mathbf{r}_j), \quad (3.27)
 \end{aligned}$$

which involves distinct U functions for the bonds, angles, dihedrals, and non-bond interactions. The summations run over all bonded pair ($\sum_{\{i,j\}}$), triple ($\sum_{\{i,j,k\}}$), and quadruple ($\sum_{\{i,j,k,l\}}$) set of atoms belonging to each molecule. Advanced force fields can also include additional terms resulting in a more realistic description of a simulated system.

It is important to note that molecular modeling introduces a set of parameters that are fixed by fitting to selected experimental and/or first principles data based on the assumption that these parameters are transferable to other molecules. To validate it, it is best to calculate a known property not used in the fitting and compare with the results. This would provide a test of transferability of the potential and measure of robustness of the model [149]. Eventually, the interaction potential $U(\mathbf{r}^N)$ allows us to obtain the energy of a group of molecules as a function of their conformations and to study the equilibrium geometries and transition states. I will next elaborate on each terms in Eq. (3.27).

3.5.1 Bond-stretching

In case that there is no chemical bond breaking or forming, we assume that Hooke's Law is adequate, then each bond stretching between atom types makes a simple harmonic potential contribution to the total molecular potential energy of

$$U^{\text{bond}}(\mathbf{r}_i, \mathbf{r}_j) = \frac{1}{2} k_r (r_{ij} - r_{\text{eq}})^2. \quad (3.28)$$

Here k_r is the force constant, $r_{ij} = |\mathbf{r}_i - \mathbf{r}_j|$ the instantaneous bond length, and r_{eq} the equilibrium bond length. There are also more complicated potentials that can be used such as the Morse potential [173]

$$U^{\text{bond}}(\mathbf{r}_i, \mathbf{r}_j) = D(1 - e^{-\alpha(r_{ij} - r_{\text{eq}})})^2, \quad (3.29)$$

or the one with an extra term to the simple harmonic expression

$$U^{\text{bond}}(\mathbf{r}_i, \mathbf{r}_j) = k_1(r_{ij} - r_{\text{eq}})^2 + k_2(r_{ij} - r_{\text{eq}})^4. \quad (3.30)$$

The introduced parameters (k_r , r_{eq} , *etc.*) can be obtained from experiment or by a full quantum mechanical calculation [174].

3.5.2 Bond-bending

The bond-stretching is crucial for molecular modeling. However, we also need to consider additional many-body terms in the molecular potential energy, namely, bond-bending (three-body) and dihedral (four-body), in order to be able to properly describe the topology of molecules [148, 149]. It is usual to write bond-bending in the form of a harmonic function and for each three-connected atoms i - j - k (see Fig. 3.7) it is expressed as

$$U^{\text{angle}}(\mathbf{r}_i, \mathbf{r}_j, \mathbf{r}_k) = \frac{1}{2}k_\theta(\theta_{ijk} - \theta_{\text{eq}})^2, \quad (3.31)$$

where k_θ is the force constant due to the bending, and the subscript θ_{eq} refers to the equilibrium angle where the molecule is at rest. A variation on the bond-bending approximated function, squared-cosine, is given by

$$U^{\text{angle}}(\mathbf{r}_i, \mathbf{r}_j, \mathbf{r}_k) = \frac{k_\theta}{2\sin^2(\theta_{\text{eq}})}(\cos(\theta_{ijk}) - \cos(\theta_{\text{eq}}))^2. \quad (3.32)$$

3.5.3 Dihedral motions

Next, we consider the dihedral (torsion) between the four bonded atoms i , j , k and l (see Figs. 3.8 and 3.9). Some authors divide these into proper dihedrals, where we might expect full rotation about the connecting bond j - k ,

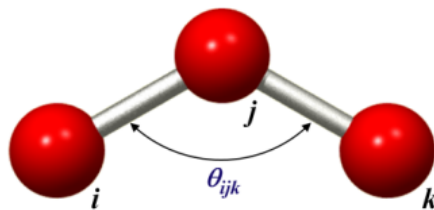


FIGURE 3.7. The angle θ_{ijk} between three consecutive atoms i , j , and k where two bonds sharing a common atom is used to define the bond-bending potential. The figure is adapted from <http://cbio.bmt.tue.nl/pumma/index.php/Theory/Potentials>.

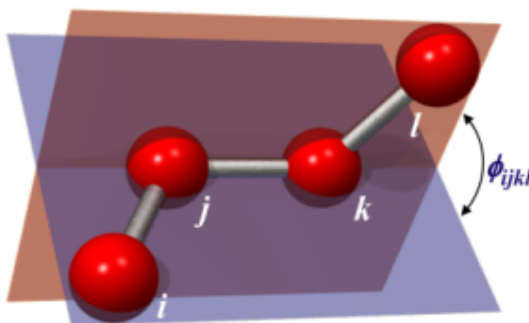


FIGURE 3.8. The proper dihedral angle definition. The torsional angle ϕ_{ijkl} is the angle between the plane going through the atoms i , j and k and the plane going through the atoms j , k and l . The figure is adapted from <http://cbio.bmt.tue.nl/pumma/index.php/Theory/Potentials>.

and improper dihedral where the rotation is limited [148, 149]. If we use ϕ_{ijkl} to denote the torsional angle, then a popular dihedral potential is given by

$$U^{\text{dihedral}}(\mathbf{r}_i, \mathbf{r}_j, \mathbf{r}_k, \mathbf{r}_l) = \frac{1}{2} U_0 (1 - \cos(n(\phi_{ijkl} - \phi_{\text{eq}}))), \quad (3.33)$$

here n is the periodicity parameter and generally depends on the symmetry of the molecule. The term ϕ_{eq} is the equilibrium torsional angle (see Fig. 3.8). A more complicated variant is given by

$$U^{\text{dihedral}}(\mathbf{r}_i, \mathbf{r}_j, \mathbf{r}_k, \mathbf{r}_l) = V_1 (1 + \cos(n_1 \phi_{ijkl} - g_1)) + V_2 (1 + \cos(n_2 \phi_{ijkl} - g_2)) + V_3 (1 + \cos(n_3 \phi_{ijkl} - g_3)), \quad (3.34)$$

where V coefficients are energy terms, the n_i are periodicity parameters, and g_i are phase parameters. The improper dihedral is obtained in the same way

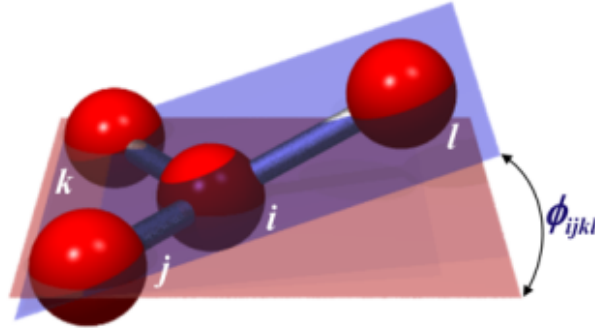


FIGURE 3.9. The definition of the improper torsional angle. The angle ϕ_{ijkl} still depends on the same two planes ijk and jkl , since the atoms have been chosen in a clever way as can be seen in the figure with the atom i in the center on one of the ends of the dihedral chain. The figure is adapted from <http://cbio.bmt.tue.nl/pumma/index.php/Theory/Potentials>.

as the bond-bending, and contributes to the molecular potential energy as

$$U^{\text{dihedral}}(\mathbf{r}_i, \mathbf{r}_j, \mathbf{r}_k) = \frac{1}{2} k_{\phi} (\phi_{ijkl} - \phi_{\text{eq}})^2, \quad (3.35)$$

where ϕ_{ijkl} is the improper torsional angle as defined in Fig. 3.9.

3.5.4 Non-bonded interactions

In addition to intra molecular considerations, when molecules are near enough to influence one another, we need to concern ourselves with the balance between the forces of attraction and repulsion. We know that such forces exist, for otherwise there would be nothing to bring molecules together into the solid and liquid states, and all matter would be gaseous. Molecules attract at long range but repel strongly at short range. Nevertheless, even for the simplest pair of molecules, the inter molecular mutual potential energy will depend on their relative orientations in addition to their separation. Basically, the non-bond interaction is given by

$$U^{\text{nb}}(\mathbf{r}_i, \mathbf{r}_j) = U^{\text{vdW}}(\mathbf{r}_i, \mathbf{r}_j) + U^{\text{Coul}}(\mathbf{r}_i, \mathbf{r}_j), \quad (3.36)$$

which is basically the sum of the van der Waals and Coulomb interactions.

3.5.4.1 Van der Waals interactions

Van der Waals potential U^{vdW} is usually taken in the form of Lennard-Jones (12-6)⁴, which is considered to be a reasonable description of the interaction for closed-shell atoms (noble gas elements) [175], and they are considered between all non-bonded pairs of atoms

$$U^{\text{LJ}}(\mathbf{r}_i, \mathbf{r}_j) = 4\epsilon_{ij} \left(\left(\frac{\sigma_{ij}}{r_{ij}} \right)^{12} - \left(\frac{\sigma_{ij}}{r_{ij}} \right)^6 \right) \quad r > r_c, \quad (3.37)$$

where ϵ_{ij} is an energy constant, σ_{ij} is the zero-crossing distance for the potential that is proportional to the effective atom radius, and r_{ij} is distance between two atoms i and j . The Lennard Jones potential is a combination of attractive van der Waals forces due to dipole-dipole interactions and empirical repulsive forces due to Pauli repulsion.

The Born–Mayer–Huggins potential [176]

$$U^{\text{BMH}}(\mathbf{r}_i, \mathbf{r}_j) = A \exp(-Br_{ij}) - \frac{C_6}{r_{ij}^6} - \frac{C_8}{r_{ij}^8}, \quad (3.38)$$

is sometimes used when dealing with polar species. B is a parameter determined by the size and softness of an ion, C_6 has to do with dipole–dipole interactions while C_8 is determined by the dipole–quadrupole interactions.

Van der Waals energies are usually computed for atoms which are connected by no less than two atoms (e.g., 1-4 interactions between i and j in i - j - k - l and higher). Interactions between atoms closer than this are already accounted for by stretching and/or bending terms. At intermediate to long ranges, the attraction is proportional to $(\frac{\sigma}{r})^6$, and at short ranges, $(\frac{\sigma}{r})^{12}$ is responsible for hard core repulsion. Commonly the parameters (such as σ_{ij} and ϵ_{ij}) are not given for a specific pair, but as a parameter of the atom itself. To be able to calculate the van der Waals interactions the Lorentz—Berthelot mixing rules [177] are applied to determine the values for the parameters, which are then given by

$$\sigma_{ij} = \frac{1}{2}(\sigma_{ii} + \sigma_{jj}), \quad \epsilon_{ij} = \sqrt{\epsilon_{ii}\epsilon_{jj}}. \quad (3.39)$$

⁴LJ (12-6)

Due to the dominant costs of force-field calculation and short-range nature of LJ (12-6) potential that decays rapidly at relatively small atomic separation, the potential is truncated and it is evaluated only for atoms with separation distance less than a certain cut-off radius r_c which is take to be 10 Å. The rest interactions is normally ignored or taken into account by adding a constant value to the total potential which is known as the tail correction

$$U^{\text{tail}} = \frac{N\rho}{2} \int_{r_c}^{\infty} U(r) 4\pi r^2 dr, \quad (3.40)$$

where ρ is the average number density and $U(r)$ refers to the used van der Waals potential. We implicitly assumed that for $g(r > r_c) \approx 1$, where $g(r)$ stands for radial distribution function (see Chapter 4), otherwise we need also to include it in Eq. (3.40) as follows:

$$U^{\text{tail}} = \frac{N\rho}{2} \int_{r_c}^{\infty} U(r) g(r) 4\pi r^2 dr.$$

3.5.4.2 Coulomb interactions

Many force fields take account of electronegativity differences between atoms and add electrostatic terms describing the Coulomb interaction between atoms with partial charges according to

$$U^{\text{Coul}}(\mathbf{r}_i, \mathbf{r}_j) = \frac{1}{4\pi\epsilon_0} \frac{q_i q_j}{r_{ij}}, \quad (3.41)$$

where ϵ_0 is an effective dielectric constant and q is the partial charge that is assigned to each atom type. Like van der Waals terms, electrostatic terms are typically computed for nonbonded atoms. Electrostatic interaction is a long-range interaction and it can dominate the computation time. The reason is that it decays slower and it is much harder to treat with cutoffs. It requires more advanced approaches such as *Ewald* sums or *particle-particle particle-mesh*⁵ methods in a system with perodic boundary conditions [178–180].

3.6 Force fields

Force field treats molecules as mechanically connected systems of atoms. In contrast to quantum mechanical methods, electrons are not treated explicitly

⁵pppm

but together with the nuclei as effective atoms. Reactions or transformations with bond formation and breaking can be described with appropriate changes in atomic hybridization which is not possible with most conventional approaches. The ultimate goal of a force field is to describe in classical terms all the quantum mechanical effects. It should be clear that the development of a force field is not a trivial task [181].

3.6.1 Parameterizing force field

Once a particular form for a force field has been chosen, different parameters have to be determined. Even for a simple force field that models a small number of systems this can involve a large number of parameters, and for a more complicated force field with more atom types, the number of different parameters that is needed grows rapidly. Traditionally, one makes use of experimental data through X-ray and electron diffraction, neutron scattering, etc. However, even when experimental data is available, some force field parameters can be hard to be determined such as torsional potentials and atomic charges. Recently, some force fields have been parameterized using data from first principle methods employing density functional theory, and quantum mechanical calculations [174]. This allows the determination of force field parameters for molecules where little or no experimental data exists.

Furthermore, various properties of a material can be inspected in order to determine force field parameters. Depending on the class of a selected force field and investigated properties, the emphasis can be on molecular structures, structural stability (phonon spectrum), enthalpies, mechanical modulus, and so on.

3.6.2 Popular force fields

The first force fields appeared in the 1960's, with the development of molecular mechanics for isolated molecules. Since then the scope of force field development moved to deal with much more complex systems, leading to different classes of more widely applicable force fields. Good examples are

the DREIDING [182] and Universal force fields (UFF) [183], that contain parameters for all the atoms in the periodic table. Other well-known force fields are CHARMM [184], AMBER [185], GROMOS [186], OPLS [187], and COMPASS [188]. All of them are quite general, but the first three are often employed in simulations of biomolecules, while OPLS and COMPASS were originally developed to simulate condensed matter such as liquid hydrocarbons. In addition to those general force fields, there is a vast number of specific potentials developed to describe just a particular system or a class of compounds. Water merits a particular mention in this respect, as due to its importance and currently a large number of water models (TIP3P [189], TIP4P [189], TIP5P [190], SPC [191] and SPC/E [192]) has been proposed since the first MC simulation of Barker and Watts [193]. Moreover, embedded atom method (EAM) is a semi-empirical class of force fields developed to adequately reproduce the properties of metals and metal alloys [194, 195].

Another category of force fields belongs to bond-order and reactive force fields capable of modeling chemical bonds in terms of classical molecular dynamics. The early formulation and parametrization of such force fields is REBO for carbon systems [196], and it is subsequently developed and expanded in different forms by Tersoff [197] and Brenner potentials [198]. ReaxFF potentials is another example that targets a wide range of materials [181, 199]. In this section, I will discuss in detail some of these force fields that I used in this work.

3.6.2.1 Water models

A Recent review listed numerous distinct models for water that showed the limitation of several of them in quantitatively reproducing various properties of water and found some of them even anomalous. Nevertheless, several of the current models give reasonable structural and thermodynamic descriptions of liquid water and they are useful in simulations of aqueous solutions. The simplicity of such models is also attractive from a computational standpoint. Over the years, a number of authors have tackled the problem of finding a suitable potential for liquid water [141, 189, 190]. One can simply write a potential for N water molecules as the sum of two inter and intra molecular

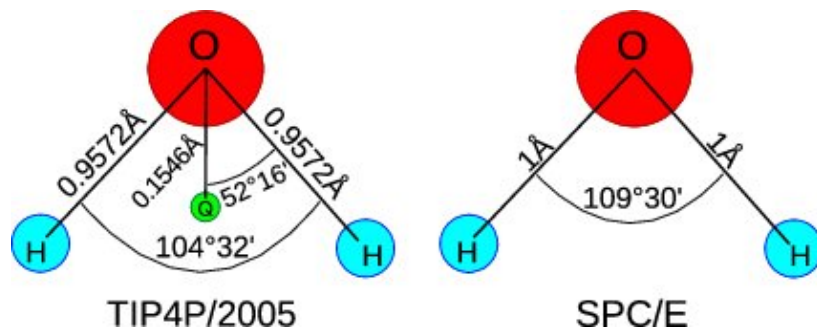


FIGURE 3.10. Schematic representation of the SPC/E and TIP4P/2005 molecular models for water. Both are rigid models where bond length and angle are constrained. It is to be noted that the latter model has an extra interaction site (dummy charged site) at point charge Q leading to a more accurate model. The figure is adapted from Ref. [200].

terms (see molecular mechanics section) that takes the form of

$$\begin{aligned}
 U(\mathbf{r}^N) &= U^{\text{intra}}(\mathbf{r}^N) + U^{\text{inter}}(\mathbf{r}^N) \\
 &= \sum_{\{i,j\}}^{\text{bonds}} \frac{1}{2} k_r (r_{ij} - r_{\text{OH}})^2 + \sum_{\{i,j,k\}}^{\text{angles}} \frac{1}{2} k_\theta (\theta_{ijk} - \theta_{\text{HOH}})^2 \\
 &\quad + \sum_{i < j}^N \left\{ \frac{1}{4\pi\epsilon_0} \frac{q_i q_j}{r_{ij}} + 4\epsilon \left(\left(\frac{\sigma}{r_{ij}} \right)^{12} - \left(\frac{\sigma}{r_{ij}} \right)^6 \right) \right\},
 \end{aligned} \tag{3.42}$$

with the parameters q_i , ϵ , σ , k_r , r_{OH} , k_θ , and θ_{HOH} . This potential is very flexible which means that the bond lengths and bond angles are allowed to freely vibrate and change. In some models, known as rigid models, bonds and angles are constrained that will save computational efforts and one can use a larger timestep. As a result, the intra molecular potential is ignored and water is only described by non-bond pair potential. Actually, these models involve a rigid water monomer with a number of interaction sites.

Some water models have either rigid [192] or flexible [201] versions with their own appropriate set of parameters. All have basically positive charges on the hydrogens and a negative charge ($q_{\text{O}} = -2q_{\text{H}}$) on the oxygen, and the interaction potential is taken as the sum of all intermolecular Coulomb terms together with a single Lennard-Jones (12-6) potential between the oxygens. Furthermore, in attempts to reoptimize water models, some authors introduce extra interaction sites beyond the typical three atomic sites. In the case of

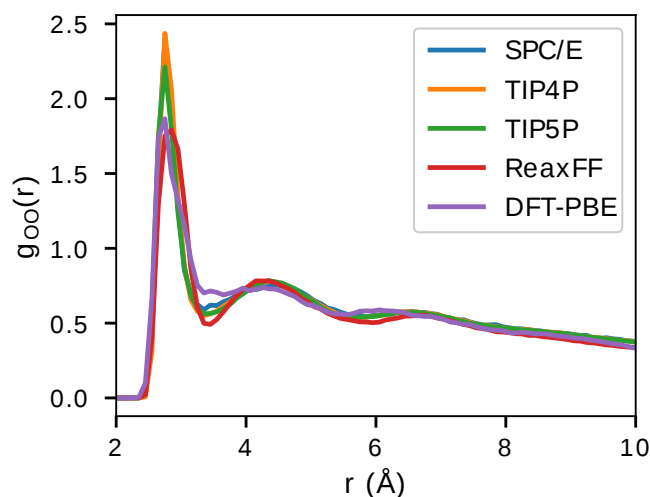


FIGURE 3.11. Radial distribution function between oxygen atoms of liquid water at 300K for different water models SPC/E, TIP4P, and TIP5P. As it can be seen the result is in good agreement with the reactive force field (ReaxFF) and first principle (DFT) method [202].

4-sites model, the negative charge is moved off the oxygen and towards the hydrogens at a point along the bisector of the HOH angle. The pair potential is still calculated according to the equation above, but more distances have to be evaluated, and they are relatively computationally expensive (see Fig. 3.10). For instance, successful TIP4P (4-sites) and TIP5P (5-sites) models were initially proposed by W. L. Jorgensen *et al* [189].

In Fig. 3.11, for comparative reasons, the radial distribution function between oxygen atoms for liquid bulk water at 300K is demonstrated using different water models and shows good agreement with the complicated reactive potential (ReaxFF [203]) and the first principle method. In this thesis, the SPC/E and TIP4P/2005 models for water have been used.

3.6.2.2 OPLS potential

Optimized potential for liquid simulations (OPLS) force field is one of the most commonly used force fields developed by William L. Jorgensen at Purdue University and later at Yale University [187]. In this thesis, we used it particularly for hydrocarbon liquids (ethanol, methanol, hexane, etc) Jorgensen *et*

al. created the OPLS force field using the following functional form [204]

$$\begin{aligned}
 U(\mathbf{r}^N) = & \sum_{\{i,j\}}^{\text{bonds}} \frac{1}{2} k_r (r_{ij} - r_{\text{eq}})^2 + \sum_{\{i,j,k\}}^{\text{angles}} \frac{1}{2} k_\theta (\theta_{ijk} - \theta_{\text{eq}})^2 \\
 & + \sum_{\{i,j,k,l\}}^{\text{dihedrals}} \left\{ \frac{V_1}{2} (1 + \cos(\phi_{ijkl})) + \frac{V_2}{2} (1 - \cos(2\phi_{ijkl})) \right. \\
 & \left. + \frac{V_3}{2} (1 + \cos(3\phi_{ijkl})) + \frac{V_4}{2} (1 - \cos(4\phi_{ijkl})) \right\} \quad (3.44)
 \end{aligned}$$

$$+ \sum_{i < j}^N \left\{ \frac{1}{4\pi\epsilon_0} \frac{q_i q_j}{r_{ij}} + 4\epsilon \left(\left(\frac{\sigma}{r_{ij}} \right)^{12} - \left(\frac{\sigma}{r_{ij}} \right)^6 \right) \right\}. \quad (3.45)$$

Bonds and angles are described by harmonic potentials, similar to water models (i.e SPC/E), since they are very strong and fluctuate only slightly around their equilibrium values at room temperature. In many simulations, rigid models are employed due to the computational efficiency, where the whole molecule is considered as a rigid body with only (non-bonded) intermolecular interactions. The extra term here refers to a dihedral potential that is described by a cosine expansion and may take any value within 360° depending on the height of the barrier between the low energy conformations. Dihedral potentials have always a symmetry i.e. around 180° . The long range interactions are only counted for atoms with three or more bonds apart.

3.6.2.3 Bond-order reactive potentials

In the present thesis, I widely used two bond-order reactive force fields, namely AIREBO [196] and ReaxFF [199], for simulating graphene-based systems. The bond-order term reflects that the potential is a simple pair potential depending on the distance between two atoms, but the strength of this bond is modified by the (local) environment of the atom, namely many-body potential, and the term reactive means that it allows the formation and dissociation of chemical bonds during the simulation. The bond-stretching is expressed by a simple harmonic potential which does not allow in bond breaking and formation. With this approach, atoms are not constraint to remain attached to specific neighbors, or maintain a particular coordination number.

One successful method for treating covalent bonding in computer simulation of hydrocarbon materials is the adaptive intermolecular reactive bond-order (AIREBO) potential. It includes covalent bond contributions of a slightly modified REBO [198] potential plus Lennard-Jones (intermolecular) and torsional interaction potentials that is written as

$$U(\mathbf{r}^N) = U^{\text{REBO}}(\mathbf{r}^N) + U^{\text{LJ}}(\mathbf{r}^N) + U^{\text{tor}}(\mathbf{r}^N). \quad (3.46)$$

The U^{LJ} and U^{tor} terms are similar to what we have explained in previous sections. The REBO potential is a bit more complicated and exclusively devoted to short-range covalent bonds. For each pair of bonded atoms i and j , it has the form

$$U_{ij}^{\text{REBO}}(\mathbf{r}^N) = U^{\text{R}}(r_{ij}) + b_{ij} U^{\text{A}}(r_{ij}), \quad (3.47)$$

where $U^{\text{R}}(r_{ij})$ and $U^{\text{A}}(r_{ij})$ are repulsive and attractive pairwise potentials determined by the atom types and depend only on the distance r_{ij} between the two atoms. However, the bond-order term b_{ij} underlies the many-body dependence of U_{ij}^{REBO} , its value is a function of position and chemical identity of the atoms close to $i - j$ bond. A detailed description of REBO and methods to evaluate b_{ij} can be found in the original works [196–198].

ReaxFF is another general bond-order reactive potential that utilizes a bond angles in addition to bond distances to describe bond formation and dissociation. The non-bonded interactions are calculated between every pair of atoms, while close range interactions are excluded. In contrast to AIREBO, ReaxFF uses additional electrostatic interaction between atoms, and partial charge on the atoms are calculated every time step from the geometry via the electronegativity equilibrium scheme of Mortier *et al.* [205]. Essentially, ReaxFF is applicable to any system such as graphene, water, etc. However, for a certain system, it has a set of parameters which is not necessarily transferable to other systems and it should be used cautiously because it can predict unrealistic results. A detailed description of ReaxFF terms and their functional forms can be found in A. Duin *et al.* [199].

3.6.3 Machine learning potentials

Data-intensive computing is beginning to emerge as a separate discipline and is being viewed by some as a “fourth paradigm” for scientific discovery, complementing discoveries made by theory, experiment, and simulation. Furthermore, data-driven models help us to develop an alternative approach to construct force fields that relies on available datasets and allowing large-scale atomistic simulations with the accuracy of first principle methods [206]. B. Cheng *et al.* has recently investigated the thermodynamics of liquid and solid water using machine learning potential as intermediate steps. That work provides a large-scale but *ab initio* simulation of hexagonal and cubic ice based on density functional theory at the hybrid functional level that rigorously takes into account quantum nuclear motion, anharmonic fluctuation, and proton disorder. As a results, they observed nuclear-quantum effects, a classical treatment of nuclear degrees of freedom particularly is no longer valid for light nuclei, contribute a crucial 0.2 meV/H₂O to the stability of hexagonal structure and making it more stable than cubic one [207].

The power of atomistic simulations would be enormously enhanced if the interatomic potentials used to simulate materials were not limited by the simple empirical functional forms but would accurately approach the Born-Oppenheimer potential energy surface, similarly to the case of small molecules for which quantum chemists have been fitting accurate potential energy surfaces for decades [208]. In recent years, machine learning (ML) methodologies have emerged as an exciting new tool within chemical and materials science. The application of ML algorithms to the development of interatomic potentials also represents an innovative approach which has attracted much attention [209, 210]. It is important to note that conventional interatomic potentials, that we previously discussed, are based on presumed functional forms. For example, in bond stretching section, we treat a bond between two atoms as a simple spring that originates from a simple harmonic potential form of the bond length close to the equilibrium distance, and this physical interpretation underlies the approximations we employed to obtain the potential in the form of analytical functions. However, suggested models are not always sufficient to provide a reactive molecular simulation of a

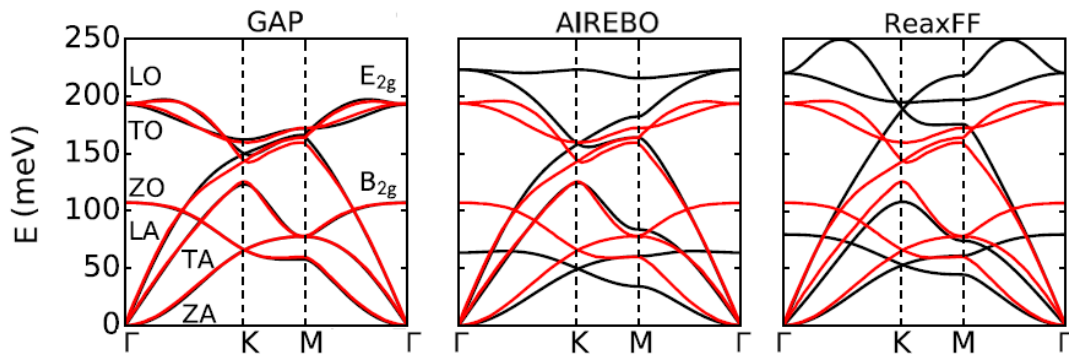


FIGURE 3.12. Comparison of model predictions to phonon dispersion of graphene monolayer. Black lines represent the calculated phonon spectrum using GAP, AIREBO, and ReaxFF. The red is the reference XRD [211, 212]. Labels for branches are shown on the graphene GAP plot (left) along with symmetry labels (right). The figure is adapted from Ref. [213].

system.

As a general approach, there is alternatively an accurate interatomic potential for materials that are mathematically constructed by Gaussian approximated potential (GAP) using machine learning methodology [213]. This framework is a data-driven approach which relies purely on data obtained from first principles calculations, and attempts to approximate a faithful representation of the potential energy surface (PES). This is achieved at a computational cost which is orders of magnitude lower than that of comparable calculations which directly invoke electronic structure methods while preserving quantum mechanical accuracy. Gaussian approximation potential can be considered as a new road towards an accurate, computationally efficient, and universal force field development. As an example, a comparison of model predictions to phonon dispersion of the graphene monolayer using conventional MD potentials (ReaxFF and AIREBO) and machine-learning based potential (GAP) are shown in Fig. 3.12. The black lines represent the calculated phonon spectrum using either computational model. The red curves are the reference XRD results [211, 212]. The GAP model accurately reproduces the experimentally determined phonon spectrum over all the high-symmetry directions. Labels for branches are shown on the graphene GAP plot (left)

along with symmetry labels at the point (right).

Neural network is another machine learning approach that has been successfully used to accurately represent (reactive) potential energy surfaces that are constructed from computationally demanding electronic structure calculations [214]. For example, V. Quaranta *et al.* studied recently interfaces between water and metal oxides using a high-dimensional neural network potential. Variety of structures and dynamical liquid water surface interaction properties including hydration and water dissociation and recombination time have been investigated [215].

Nevertheless, more studies are required to inspect all aspects of this new class of force field, particularly its transferability. Unlike additive potentials, a developed ML based potential is specific to the studied system. It is better to adopt this approach when there is no conventional potentials available for a system or there is a need for an accurate and large-scale reactive molecular dynamics simulation [216].

3.6.4 Importance of force field

From computational perspective, an ideal molecular simulation should be carried out directly using first principles in the framework of density functional theory. It might be thought that regenerating quantum potential energy surface by employing a collection of functional forms in terms of force fields potentials is only an additional approximation. This is true to some extent. For systems when applying direct first principle methods are feasible, doing force field based molecular simulation might not be the best solution. However, for many systems that needs large simulation time and/or size are required to properly investigate certain properties that are way beyond the first principle methods due to computational challenges. Regarding such limitations, large-scale molecular simulation based on force field model is considered as powerful computational tools that comes with the price of quantum accuracy. It opens subsequently a way to always question the accuracy of an employed force field particularly for systems with strong chemistry and its transferability. Besides, the complexity of force field can be constantly enhanced in order to provide a more realistic description of the studied system.

In this thesis, it is attempted to use the simplest possible forced fields but accurate enough to capture the essential physics of the system. This is done by considering the dominant interactions that exist between atoms and ignore insignificant aspects and then setting up the models and simulations accordingly. Nevertheless, there are many ways to extend employed potentials or using complex force fields such as machine-learning based potentials to improved the accuracy of predictions.

METHODS FOR ANALYSIS OF MD RESULTS

MD simulation has the ultimate goal of obtaining positions, velocities, and forces for each atom within a simulated system in successive time steps. Assuming that we have all the required data regardless of its technical and computational details, an important question is which physical insights can we gain from these data? and how? This chapter attempts to answer these questions by introducing various frameworks and related methods in order to explore relevant structural and dynamical properties of the simulated systems.

I will discuss methods such as correlation functions and the Green-Kubo formalism for calculating physical quantities that help us to inspect the structural, hydration, dynamical, and elastic properties of materials from atomistic simulations.

4.1 Structural properties

The structure of materials on the atomic scale underlies many physical properties in the macroscopic world. There are different properties that can be quantified in order to characterize the atomic structure and comparing them directly with experiments. I explain some of them, mainly used in this thesis, in more detail in this section.

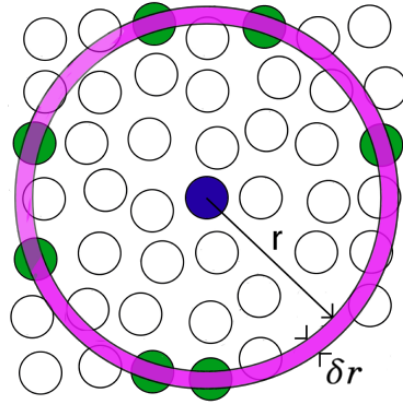


FIGURE 4.1. Space discretization for calculating the radial distribution function (RDF) where the number of specific type of particles (green points) is counted within a spherical shell between r and $r + \delta r$. Adapted from <http://isaacs.sourceforge.net/phys/rdfs.html>

4.1.1 Radial distribution function

The radial distribution function (RDF) is undoubtedly an useful tool that measures the relative atomic distances, and helps to distinguish between gas, liquid, or solid phases of materials based on atomic coordinates. This is relevant for studying structural transitions, and calculating lattice constants for a crystal. RDF is defined as the ratio of the atomic density at radial distance r to the total density $\rho = N/V$, and is interpreted as the probability of finding a specified type of atom at a certain radial distance. Radial distribution function is evaluated by counting the number of atoms found at a given radial distance from a particular atom which is given by

$$g(r) = \frac{1}{\rho} \frac{\langle \langle n(r) \rangle_t \rangle_i}{4\pi r^2 \delta r}, \quad (4.1)$$

where $g(r)$ refers to the radial distribution function, $n(r)$ is the number of atoms in a spherical shell volume of $4\pi r^2$ between r and $r + \delta r$, see Fig. 4.1, and the brackets $\langle \rangle_t$ and $\langle \rangle_i$, respectively, denote the averages over time (or equivalently micro states) and atoms [217]. The term $g(r)$ converges to 1 at large radial distance except when there is long-range ordering in the system (i.e. crystals). For a confined system that is restricted along a certain direction, and which is no longer isotropic, it is better to use a lateral variant $g_{\parallel}(r)$

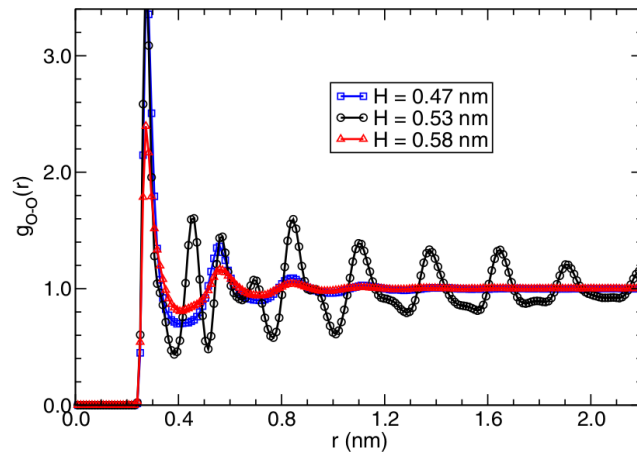


FIGURE 4.2. The radial distribution function of oxygen atoms for a system of water confined between two slabs with interlayer distances H . The presence of many peaks at $H = 0.53\text{nm}$ shows there is a phase transition (long-range ordering) between ice and amorphous water. The figure is adapted from Ref. [219].

instead given by

$$g_{\parallel}(r) = \frac{1}{\rho} \frac{\langle \langle n(r) \rangle_t \rangle_i}{2\pi r \delta r \delta z}, \quad (4.2)$$

where similarly $n(r)$ is the number of atoms in a cylindrical shell volume of $2\pi r \delta z$ between r and $r + \delta r$ [218]. As an example in Fig. 4.2, the peaks obtained from RDF of oxygen atoms for a system of water confined between two confining walls allows to distinguish between a crystalline and an amorphous structure when the interlayer distance (H) is slightly change. The presence of many peaks for $H=0.53\text{nm}$ shows that there is a phase transition (long-range ordering) between ice and amorphous water.

We can principally count the particles at any given vector position \mathbf{r} rather than at a radial distance r . This is known as spatial pair correlation (SDF) function and it is defined as

$$g(\mathbf{r}) = \frac{1}{\rho} \langle \langle \sum_{i=1}^{N-1} \delta(\mathbf{r} - \mathbf{r}_i) \rangle_t \rangle_i, \quad (4.3)$$

where $\delta(\mathbf{r})$ is the Kronecker delta function, and the summation runs over all particles excluding one particle [220]. Figure 4.3 shows top and side views of water molecules (blue) spatial distribution functions around a single ion

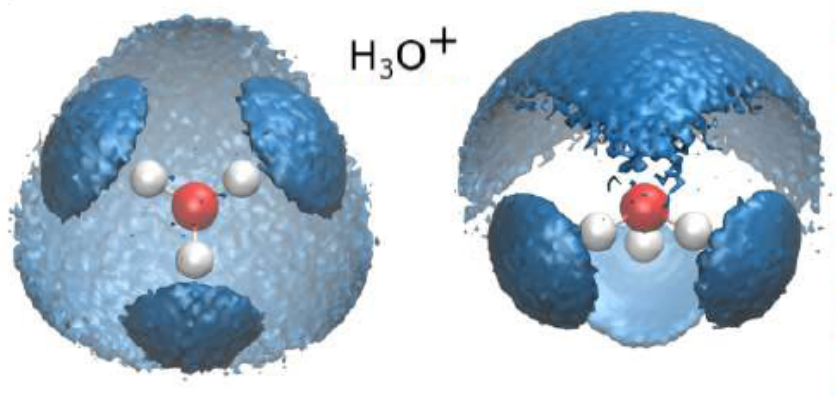


FIGURE 4.3. Top (left) and side (right) representations of spatial distribution functions (SDF) of water molecules (blue) surrounding a single ion of H_3O^+ (red and white balls) [202].

H_3O^+ (red and white) generated due to water ionization [202]. It can be seen that SDF provides more detailed information about the spatial distribution of (water) molecules rather than the conventional RDF. In fact, the radial distribution function is a specific case of spatial correlation function that its angular terms (4π) are integrated out and it depends only on the radial distance.

4.1.2 Coordination number

The coordination number determines how many molecules are found at radial distance r [217]. Integrating $g(r)$ in spherical coordinates to the first minimum of the RDF will give the coordination number of a molecule.

$$n(r) = \rho \int_0^r g(r') 4\pi r'^2 dr'. \quad (4.4)$$

In this thesis, the coordination number of the first and second shells have been used to study the hydration of ions by water or other molecules, and how it is influenced by confinement due to a nanochannel. As an example, in Fig. 4.4, the time evolution of coordination number ($n(r)$) of Li^+ cation inside a clay membrane at different elapsed simulation times of 1, 5, 10, 16, 20 ns is shown. The membrane is initially filled with water and gradually exposed to ethanol and forms a mixed water-ethanol solution. As can be seen from

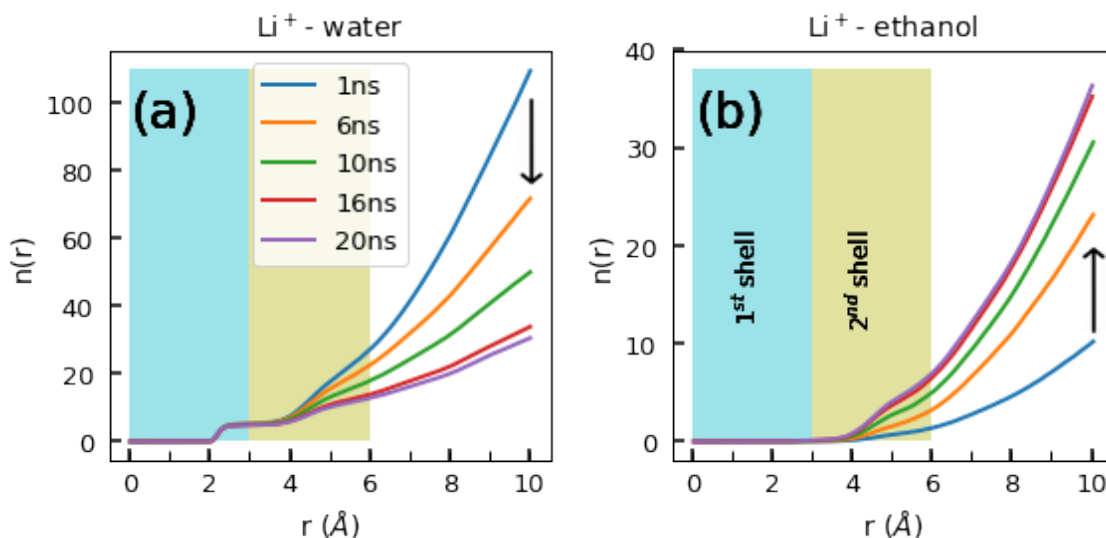


FIGURE 4.4. Time evolution of coordination number ($n(r)$) of Li^+ cation inside a clay membrane at different elapsed simulation time of 1, 5, 10, 16, 20 ns. The membrane is initially filled with water and gradually exposed to ethanol and forms a mixed water-ethanol solution. As can be seen from $n(r)$ the water molecules are gradually replaced by ethanol at the second hydration shell of the cation while the first shell remains unchanged.

$n(r)$, the water molecules are gradually replaced by ethanol at the second hydration shell ¹ of the cation while the first shell remains unchanged.

4.2 Hydration Properties

Hydrogen bond is electrostatic in nature with some covalent character. This allows us to easily implement it in the framework of MD simulations using proper assigned atomic charges [121, 221, 222].

4.2.1 Hydrogen bonds

Two kinds of hydrogen bond definitions are commonly used in molecular simulations and are based on energetic or geometrical criteria used mainly in the case of water [223, 224]. Here, I only discuss the latter. We cannot determine with absolute precision whether two molecules are H-bonded or

¹It describes how water molecules as solvent arrange around an ion.

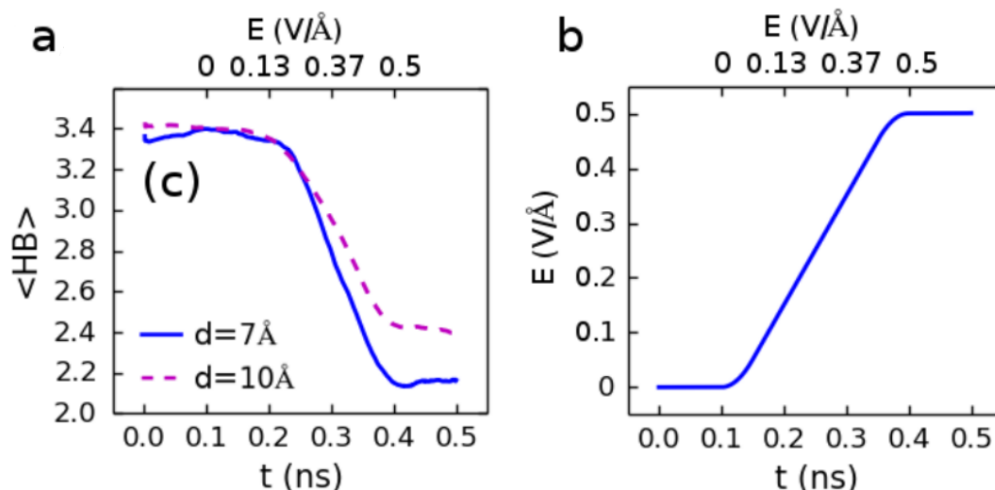


FIGURE 4.5. (a) Average number of hydrogen bonds $\langle HB \rangle$ per water molecule as function of (b) applied external electric field that gradually increases over time for a system of confined water between two graphene monolayers at interlayer distances of 7 and 10 Å [225].

not, and one can estimate it according to the radial distribution functions and the bond angle distributions corresponding to the system. For geometrical definition of a hydrogen bond, three conditions need to be fulfilled [221]:

- A) The distance r_{OO} between the oxygens of both molecules is smaller than a cutoff value r_{OO}^c
- B) The distance r_{OH} between the oxygen of the acceptor molecule and the hydrogen of the donor is less than r_{OH}^c .
- C) The bond angle ϕ between the O–O direction and the molecular O–H direction of the donor, where H is the hydrogen which forms the bond, has to be less than ϕ^c .

As the cutoff value r_{OO} , we selected the position of the first minimum of the radial distribution function $g_{OO}(r)$, *i.e.*, $r_{OO} = 3.6\text{\AA}$ for normal water at ambient conditions. Similarly, the cutoff r_{OH}^c can be unambiguously determined from the first minimum of $g_{OH}(r)$ with the value 2.4\AA . It is important to note that the value of the cutoffs can slightly change as function of temperature or density but they can always be determined from appropriate

radial distribution function at a given condition. The value of ϕ^c is considered in all simulations as 30° [221]. Finally, the average number of H-bonds per individual water molecule can be obtained from the geometrical analysis that results in the value of ≈ 3.4 for bulk water at ambient condition and 4.0 for ice crystal.

Figure 4.5(a) demonstrates the number of hydrogen bonds $\langle HB \rangle$ per water molecule for a system of confined water encapsulated between two graphene sheets at two different interlayer distances of 7 and 10 Å. It starts with a value of 3.4 and found to gradually decrease when an external E-field increases, as shown in Fig 4.5(b), due to the water molecules alignment which destroys the bond network.

4.3 Dynamical properties

4.3.1 Diffusion coefficient

The translational diffusion coefficients D can be determined directly from the mean square displacement (MSD) method

$$D = \lim_{t \rightarrow \infty} \frac{1}{3} \frac{\langle [\mathbf{r}(t) - \mathbf{r}(0)]^2 \rangle_i}{2t}, \quad (4.5)$$

where $\mathbf{r}(0)$ refers to the initial position of atoms and $\langle \rangle_i$ is an average over all atoms [141]. In practice, this means that we have to verify that we used uncorrelated samples, sampling interval has to be chosen each ~ 100 timesteps, and running the simulation time of a few nanoseconds in order to ensure MSD is really proportional to t . The diffusion coefficient can be determined equivalently from the velocity autocorrelation functions (VACF), which describes the correlation between velocities at different times along an equilibrium trajectory [127, 226] and it is given by

$$D = \lim_{t \rightarrow \infty} \frac{1}{3} \int_0^t \langle \langle \mathbf{v}(t_0 + t') \cdot \mathbf{v}(t_0) \rangle_{t_0} \rangle_i dt', \quad (4.6)$$

$$= \lim_{t \rightarrow \infty} \frac{k_b T}{m} \int_0^t X(t') dt', \quad (4.7)$$

here $\langle \rangle_{t_0}$ indicates the average of the velocity correlation with respect to the time origin, and $X(t)$ is given by

$$X(t) = \frac{\langle \langle \mathbf{v}(t_0 + t) \cdot \mathbf{v}(t_0) \rangle_{t_0} \rangle_i}{\langle \langle \mathbf{v}(t_0) \cdot \mathbf{v}(t_0) \rangle_{t_0} \rangle_i} = \frac{m}{3k_b T} \langle \langle \mathbf{v}(t_0 + t) \cdot \mathbf{v}(t_0) \rangle_{t_0} \rangle_i, \quad (4.8)$$

where we used the relation $\frac{3}{2}k_b T = \frac{1}{2}m \langle \mathbf{v} \cdot \mathbf{v} \rangle_i$, and assumed that the particles have the same mass m . Due to the thermal fluctuations that induce randomness into the system, the correlation between velocities always begins at 1 and expectedly decays relatively fast. Consequently, the truncation of the integration to a few picoseconds² is sufficient in practice.

4.3.2 Time correlation

The *time correlation* function is a time-dependent quantity which represents dynamical information of the system. In general, for two dynamical variables A and B , it is give by

$$\langle A(t_0) B(t_0 + t) \rangle_{t_0} = \frac{1}{L'} \sum_{k=1}^{L'} A(t_k) B(t_k + 1),$$

where L' is the number of time origins [149]. In particular, auto-correlation function (ACF) refers to the correlation of a dynamical variable with the delayed copy of itself. For example, the velocity auto correlation, in Eq. (4.8), gives the diffusion coefficient D . Many dynamical coefficients can be derived from this function on the basis of the Green-Kubo formalism [227]. Force components auto-correlation functions (ACF) as function of time for a system of water confined between two graphene sheets with interlayer distance of 10 Å [114], is shown in Fig. 4.6. It decays quickly and becomes uncorrelated after a few picoseconds. The force auto-correlation, as discuss later in section 4.3.5, can be used in the calculation of friction coefficient between the liquid/solid interface.

4.3.3 Green-Kubo relation

In general, there are two principal methods to explore the dynamical coefficients in the framework of equilibrium molecular dynamics simulations:

²Lag time

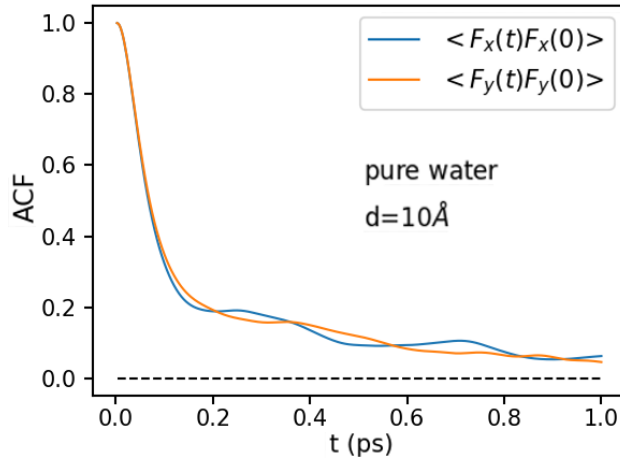


FIGURE 4.6. Force components auto-correlation functions as function of time for a system of water confined between two graphene sheets with interlayer distance of 10\AA [114].

direct method based on the Einstein relation (mean square approaches) and integrating the autocorrelation function [228]. In the thermodynamic limit, using the equilibrium canonical ensemble under the assumption that ergodicity holds, these two methods are equivalent

$$\lim_{t \rightarrow \infty} \frac{[G(t) - G(0)]^2}{2t} = \int_0^\infty \langle \dot{G}(t_0) \dot{G}(t_0 + t) \rangle_{t_0} dt, \quad (4.9)$$

where $G(t)$ is any dynamical variable related to some particular transport coefficient, $\dot{G}(t)$ is the corresponding time derivative. In fact, different transport properties can be evaluated using one of these two equivalent expressions. Such a relation between a transport coefficient and an integral over a time correlation function is called *Green-Kubo* (GK) relation [229–231]. Similar relations have been derived for many other transport coefficients (*i.e.* viscosity, friction, thermal conductivity, etc) that I will explain in the next sections. Besides, the nonequilibrium molecular dynamics method (NEMD) which relies on the fluid flow is another alternative to calculate transport coefficients. This approach has its own advantages and disadvantages, a detailed description can be found in previous works [232].

4.3.4 Viscosity coefficients

Viscosity is a measure of the resistance of fluid flow due to shear or tensile stress. It describes the difference in internal friction of a moving fluid, for instance water or honey. The viscosity components $\eta_{\alpha\beta}$ can be similarly determined from the GK formula that is based on the macroscopic stress tensor autocorrelation. Accordingly, it is directly obtained from Eq. (4.9) by using

$$\begin{aligned} G(t) &= \sum_i m_i r_i^\alpha(t) v_i^\beta(t), \\ \dot{G}(t) &= VP_{\alpha\beta}(t) = \sum_i m_i v_i^\alpha v_i^\beta + \frac{1}{2} \sum_{i \neq j} F_{ij}^\alpha r_{ij}^\beta, \end{aligned} \quad (4.10)$$

where F_{ij}^α and r_{ij}^α represent, respectively, the specified component of the force and distance between i and j atoms. For simplicity, we assumed here that particles interact through pairwise interaction, however the same relation can be obtained in the presence of a many-body potential [10]. As a result, $\eta_{\alpha\beta}$ is given by

$$\begin{aligned} \eta_{\alpha\beta} &= \lim_{t \rightarrow \infty} \frac{1}{V k_b T} \frac{1}{2t} [\sum_i m_i (r_i^\alpha(t) v_i^\beta(t) - r_i^\alpha(0) v_i^\beta(0))]^2, \\ &= \frac{V}{K_B T} \int_0^\infty \langle P_{\alpha\beta}(t_0) P_{\alpha\beta}(t_0 + t) \rangle_{t_0} dt, \end{aligned} \quad (4.11)$$

the expression $P_{\alpha\beta}$ indicates the instantaneous stress tensor in the form of the virial equation [233]. The shear viscosity is defined when a system is placed between two plates and then pulling the plates apart in opposite directions. The shear viscosity is obtained from averaging over the time correlation of the off diagonal components of the symmetric tensor $\eta_{\alpha\beta}$ as follows

$$\eta_S = \frac{1}{3} \sum_{\alpha \neq \beta} \eta_{\alpha\beta}, \quad (4.12)$$

that includes three possible $\alpha\beta$ permutations ($\alpha \neq \beta = x, y, z$) aiming to reduce the statistical error [233]. Similarly, the bulk viscosity, i.e. the resistance of a fluid to be compressed, is defined as

$$\eta_B = \frac{V}{K_B T} \int_0^\infty \langle \delta P(t_0) \delta P(t_0 + t) \rangle_{t_0} dt, \quad (4.13)$$

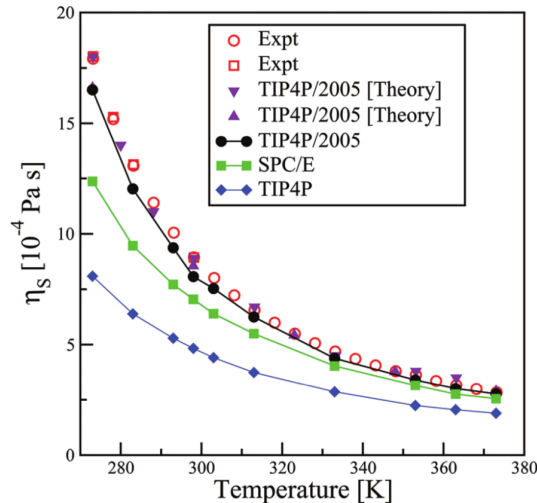


FIGURE 4.7. Temperature dependence of the experimental and theoretical computed water shear viscosities. The legend refers to the different versions of water models TIP4P and SPC/E. The figure is adapted from Ref. [229].

where $\delta P(t) = P(t) - P$ refers to the difference between the instant pressure with respect to the external pressure. Figure 4.7 demonstrates the temperature dependence of the experimental and theoretical computed (TIP4P and SPC/E models) liquid water shear viscosities [229].

4.3.5 Friction coefficient

Friction is one of the main sources of dissipation at liquid/solid interfaces and it is an essential quantity when studying membrane filtration. Accordingly, the friction coefficient between the two interfaces is obtained from the linear response theory and the Mori-Zwanzig formalism [234, 235] based on the force autocorrelation function

$$\xi_\alpha = \frac{1}{SK_B T} \int_0^\infty \langle F^\alpha(t_0) F^\alpha(t_0 + t) \rangle_{t_0} dt, \quad (4.14)$$

here S stands for interfacial area and F^α refers to the total shear force for each of the lateral components acting on the solid due to the fluid. Molecular dynamics simulation can be used to calculate the friction coefficient, and unraveling its dependence on the structure of the liquid at the atomic scale. Figure 4.8 shows ab-initio MD simulations of liquid water in contact with

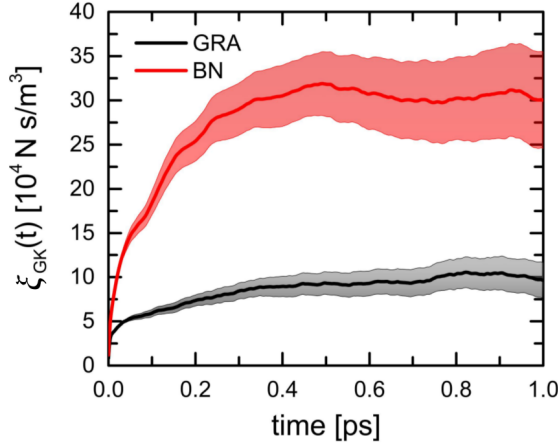


FIGURE 4.8. Comparison between the Green-Kubo estimation of the friction coefficient (Eq. (4.14)) of liquid water on graphene (GRA) and on hexagonal boron nitride (BN). The shaded areas represent the uncertainties obtained by performing a block average. The figure is adapted from Ref. [236].

graphene and with hexagonal boron nitride. The shaded areas represent the uncertainties obtained by performing a block average and the friction coefficient ζ_{GK} is given by the plateau value at long times. There is an evident increase in the friction coefficient on BN. As a result, it predicts a larger friction coefficient for boron nitride which is in agreement with experiment [236]. However, due to computational challenges of the first principle methods, the simulation time is limited up to few picoseconds.

4.3.6 Slip length

While liquid/solid friction is the relevant microscopic property that quantifies the dynamics of a fluid at the nanoscale, a length scale that is characteristic of flow is often measured experimentally. The slip length is defined as the distance into the surface at which the tangent to the fluid velocity becomes zero in a field driven flow (see Fig. 4.9). Slip length L_s relates to the slip velocity v_0 over the surface using

$$v_0 = L_s \frac{\partial v}{\partial z}. \quad (4.15)$$

Zero slip length corresponds to no-slip boundary condition. This is the cornerstone assumption of classical fluid dynamics that is usually verified in

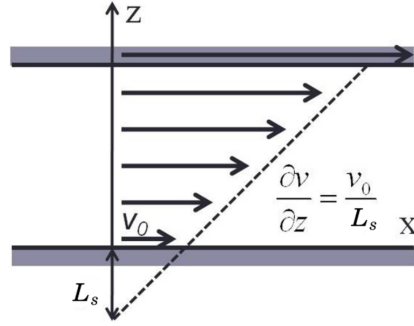


FIGURE 4.9. Schematic representation of slip-boundary conditions. L_s is the slip length and v_0 is the velocity of the liquid layer adjacent to the solid surface. The figure is adapted from Ref. [239].

macroscale flows. However, it does not hold in nanoconfined flows, namely slip boundary conditions, which have been experimentally [237] and numerically [238] observed. Eventually, a rough estimate of the Navier slip length in terms of the viscosity and the friction coefficients is given by

$$L_s = \frac{\eta s}{\xi}. \quad (4.16)$$

Slip length L_s characterizes the degree of interfacial friction which depends on the molecular structure of the surface and the fluid.

4.4 Elastic properties

The definition of Young's modulus traces back to the study of applying stress (negative pressure) on a solid material. In the elastic regime the stress-strain relation obeys Hook's law. For an isotropic solid and uniaxial deformation along the x -axis, it can be written as

$$\begin{aligned} \sigma_x &= \frac{F}{A} = \frac{kx}{A} \\ &= \frac{kx}{A} \times \left(\frac{L_0}{L_0}\right) = \left(\frac{kL_0}{A}\right) \left(\frac{x}{L_0}\right) \\ &= Y \varepsilon_x \end{aligned} \quad (4.17)$$

where Y as an elastic constant refers to Young's modulus and ε indicates the ratio between the initial and strained lengths, namely axial strain. The

terms σ_x , F , A , k , x respectively refer to stress applied along x -direction, applied force, area of the surface, Hooke's constant, and small displacement. Equivalent definition of Y is given based on the elastic energy as

$$Y = \frac{1}{V_0} \frac{\partial^2 U}{\partial \varepsilon_x^2} \Big|_{\varepsilon_x=0}, \quad (4.18)$$

where V_0 refers to the initial volume of structure. For 2D materials, in particular graphene, the volume is redefined as $3.4 \text{ \AA} \times \text{Area}$ and there exist only tensile stress. Alternatively, Y can be describe in units of Nm^{-1} instead of Nm^{-2} . The elastic properties of graphene is determined by atomic force microscope nanoindentation measuring how the deformation of a free-standing monolayer [42]. The reported experimental value for Young's modulus of the graphene monolayer is $340 \pm 40 \text{ Nm}^{-1}$ [240]. Poisson's ratio ν is another important elastic constant that measures the material tends to compress in directions perpendicular to the direction of stretching. It is defined as

$$\nu = -\frac{\varepsilon_y}{\varepsilon_x} = -\frac{\varepsilon_z}{\varepsilon_x}, \quad (4.19)$$

where ε_y and ε_z are transversal strains. The theoretical predicted values, on the basis of MD simulations, for Y and ν are 348 ± 36 and 0.22 ± 0.1 , respectively, which are remarkably in good agreement with experiment [240].

There are two methods, based on MD simulations, to calculate elastic constants: i) deformation-control methods e.g. deforming unit cell, ii) force-based methods e.g. aniso³ NPT ensemble. In the deformation-control method, an increasing strain is applied on the structure with an extremely small rate of order 0.001/ps. While, in force-control method, the force is applied on the edge atoms, or analogously applying stress on the simulation box, with a small rate load increment of 0.1 eV/Å. Accordingly, elastic constants Y and ν are obtained from linear relation between the stress and strain given by Eqs. (4.17) and (4.19). Other nonlinear elastic behavior is describe by the ultimate stress and strain which is the maximum load that a structure can withstand before breaking (see Fig. 4.10). A detailed description of the simulation of elastic and ultimate properties of carbon 2D structures can be found in previous works [240, 242]. An example of MD predicted stress-strain

³Applying pressure independently along each direction

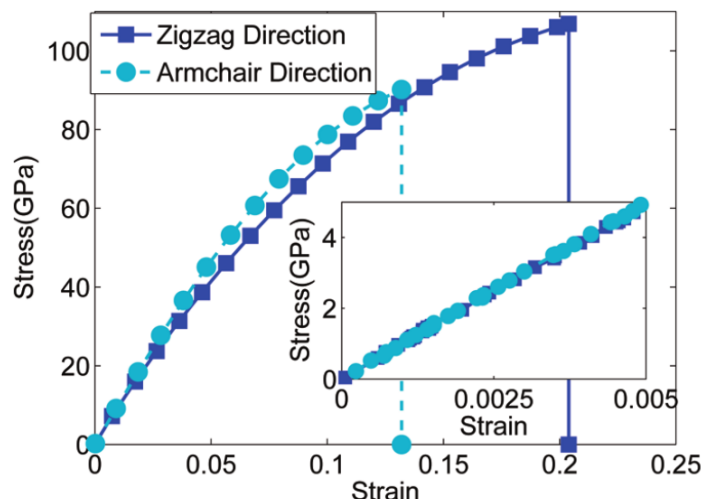


FIGURE 4.10. Stress-strain relation of monolayer graphene under uniaxial tensile in the armchair direction (dashed line with circles) and the zigzag direction (solid line with squares) at 300K. The inset shows the isotropic elasticity of a monolayer graphene sheet in the linear regime (small strain). The figure is adapted from Ref. [241].

curve for a monolayer graphene along the zigzag and armchair directions [241] are shown in Fig. 4.10. The inset shows the linear elastic behavior for a small strain range without chirality effects which can be directly used to calculate Young's modulus. The inset demonstrates the isotropic elasticity monolayer graphene sheet in the linear regime (small strain).

Part 3

Results

N-DOPED GRAPHENE: POLARIZATION AND STRUCTURAL PROPERTIES

Structural and mechanical properties of nitrogen-doped graphene (NG) are investigated using the ReaxFF potential in large-scale molecular dynamics simulations. We found that ripples, which are induced by the dopants, change the roughness of NG that depends on the number of dopants and their local arrangements. For any doping ratio N/C the NG becomes ferroelectric with a net dipole moment. The formation energy increases non-linearly with N/C ratio, while Young's modulus, tensile strength, and intrinsic strain decrease with the number of dopants. The results for the structural deformation and the thermo-electricity of the NG sheet are in agreement with recent experiments and ab-initio calculations.

This work is published as: H. Ghorbanfekr-Kalashami, M. Neek-Amal, and F. M. Peeters, "N-doped graphene: Polarization effects and structural properties", *Physical Review B* **93**, 174112 (2016). As the first author, I performed all MD simulations and contributed to the scientific interpretation of the results and in the writing of the manuscript.

5.1 Introduction

Graphene is a crystalline allotrope of carbon with a two dimensional honeycomb lattice structure, which has sp^2 in-plane covalent bonds [12, 13]. This atomic thin material has gained considerable attention in recent decade due to its exceptional physical properties [243–246]. Substitutional (N-) doping is an effective way to intrinsically modify the electric, chemical, and mechanical properties of carbon-based materials. Chemical vapor deposition (CVD) and ammonia heat-treatment processes are two of the practical techniques for fabricating nitrogen doped graphene sheets. The produced samples have been investigated by several characterization techniques including tunneling microscopy and spectroscopy [58, 63, 247, 248]. Because of the higher electronegativity of the nitrogen atoms it leads to significant charge redistribution. The N-dopants also influences the spin density, which causes that region to be more chemical active. Such regions participate directly in catalytic reactions, such as oxygen reduction reaction as well as anchoring sites for metal nanoparticles used in the catalytic reaction [249–251]. By doping with nitrogen a band gap is opened and the Fermi level is shifted above the Dirac point [58, 249] (more details about different nitrogen doping methods, characterization methods and applications can be found in Refs. [247, 249]).

Density functional theory studies (DFT) have been conducted to determine the structure of a single nitrogen dopant on a hosted graphene sheet [63]. Zhao et al. [58] used first principles techniques to calculate the formation energy of different N-dopant configurations. Fujimoto et al. [64] and Rani et al. [65] investigated the effect of substitutional nitrogen doping on the electronic band structure and the bond lengths. These types of studies are limited to few dopants within a relatively small unit cell. Consequently, it leads to a less realistic description of doping and their collective impact on the thermo-elasticity of a doped system. Some studies used a classical molecular dynamics (MD) approach to the investigate mechanical respond of (doped) graphene sheet(s) based on semi-empirical potentials [66, 67]. Despite all such theoretical and experimental works on N-doped graphene, the ferroelectric properties of such doped systems has not been discussed yet, and more detailed studies are needed to elucidate the structural deformation of

the N-doped configurations within the graphene sheets and the corresponding charge induced polarization.

In this chapter, we investigate the structural deformation and mechanical properties of N-doped graphene using large scale molecular dynamics simulations. We show that the uniformly random inserted nitrogen atoms in graphene changes the morphology of the system and depending on the local arrangement of the nitrogen atoms, the roughness can be very different. The nitrogen impurities decreases the elastic modulus of graphene and the fracture threshold. We predict that nitrogen doped graphene is a ferroelectric with a permanent dipole whose strength depends on the particular distribution of the nitrogen atoms.

5.2 The model and computational methods

The simulation box (that is periodically repeated) for pristine graphene contains 11,200 carbon atoms. We randomly distributed N atoms over graphene by substituting carbon atoms by nitrogen. Each site of the graphene sheet has an equal chance to be replaced by an N atom, see Figs. 5.1. When we randomly generate N atoms in the graphene sheet, there is a chance for the appearance of some nitrogen atoms that are bonded to each other which result in nitrogen clusters. In Fig. 5.1(d) we show a typical nitrogen cluster. For each concentration of N atoms we generated a set of systems and made an average in order to obtain the different physical quantities. Typically we generated 5 systems per concentration and we used a computation unit cell of dimension $18 \times 18 \text{ nm}^2$.

In this way, we produce various dopant configurations similar as observed in the experiment [58]. We apply periodic boundary conditions (PBC) in both x and y directions and choosing the reactive force field (ReaxFF) potential [199, 252] because it is suitable for describing covalent bonds between C and N atoms, given partial charge over atoms for exploring the ferroelectric properties, and bond breaking capability needed for calculating the ultimate strain. The NPT ensemble (Nose Hoover thermostat [169] and barostat [168]) are used to keep the temperature and pressure constant. The simulation

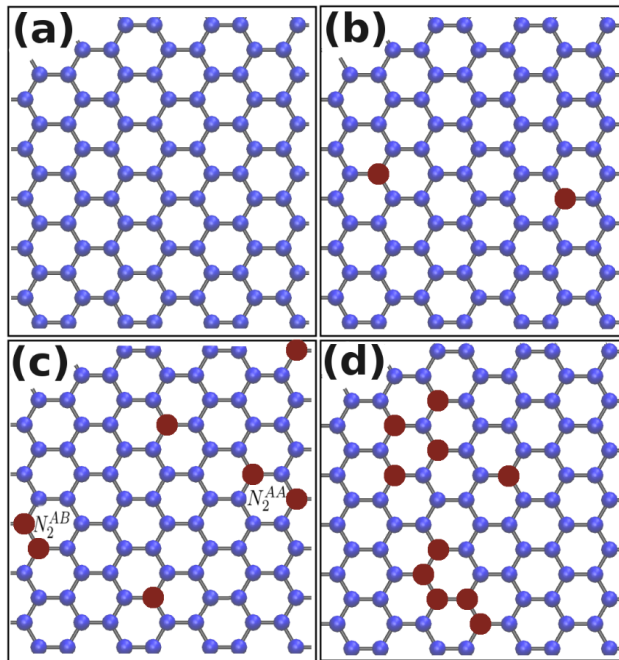


FIGURE 5.1. (a) Pristine graphene, (b) graphene with 1% nitrogen, (c) graphene with 3% nitrogen where double substitution of dopants N_2^{AA} (N_2^{AB}) are present within the same (different) nearest sublattice. (d) Graphene with 5% nitrogen where a single carbon (nitrogen) atom is connected to more than one nitrogen in the system (nitrogen clusters). The carbon and nitrogen atoms are shown as blue and brown (bigger) balls, respectively.

time step is 0.1 fs. All calculations have been performed by using the MD, large-scale atomic/molecular massively parallel simulator¹ [253, 254].

Figures 5.1 show a top view of some of the studied systems, i.e. (a) pristine graphene, (b-d) doped graphene where some carbon atoms (blue balls) are randomly replaced by nitrogen atoms (brown balls) with respectively 1%, 3% and 5% N-doping. Different local N-configurations are possible. In Fig. 5.1(b), we depict single dopants which are surrounded by three carbon atoms. Figure 5.1(c) is an example of double substitution of dopants N_2^{AA} (N_2^{AB}) on the same (different) nearest sublattice, In Fig. 5.1(d), we demonstrate a nitrogen cluster when a single carbon atom is connected to more than one nitrogen. The studied systems resemble the experimental sample where several nitrogen species such as pyridine-like, pyrrole-like, and quaternary nitrogen have been formed [247]. In this study, we dope the system up to 5% that is close to the

¹LAMMPS software package

experimental concentrations of 2.8% (5.6%) which have been realized by the heat-treatment of graphene under ammonia² [247, 248].

To investigate the mechanical properties we relaxed the system for about 10 ps, and subsequently subjected it to an in-plane tensile stress for 200 ps which was realized by changing the length (width) of the system in x (y)-direction using the displacement-control method [67, 255]. The strain increment is applied each 5000 time steps with the rate value of 0.001ps^{-1} . We set x (y)-direction to be in armchair (zig-zag) direction. By calculating the stress tensor elements, we are able to estimate the Young's modulus and the breaking stress (strain) of N-doped graphene.

5.3 Results and discussion

5.3.1 Charge distribution and electric dipole

First we study the electric charge distribution over NG at zero temperature. The density plot of the electric charge distribution on a system with 1% and 5% nitrogen is depicted in Figs. 5.2(a,b). It shows how nitrogen doping changes the local charge distribution and it leads to a (local) dipole in the graphene layer. To improve the quality of the pictures the space between the atoms was interpolated using the nearest neighbor algorithm. When the nitrogen atoms are surrounded by three carbon atoms the local dipole is zero while for the other N-configurations a local net electrical dipole appears (e.g. when two nitrogen atoms are linked). The total net dipole in each panel is shown by the thick arrow in the center of the picture. Note that the ensemble average of the net dipole should be zero after ensemble average, however any individual sample has a net dipole with a random orientation that depends on the local arrangement of the dopants (i.e. the presence of N-clusters). In Fig. 5.2(c), we show the variation of the absolute value of the total dipole of the N-doped system with p . In fact, Fig. 5.2(c) represents the total absolute dipole of the system $|\vec{P}|$, where $\vec{P} = \sum_{i=1}^{atoms} q_i \vec{r}_i$ is averaged over five samples. The error bars shown in Fig. 5.2(d) correspond to the averaging over those five

²Atmospheric pressure CVD

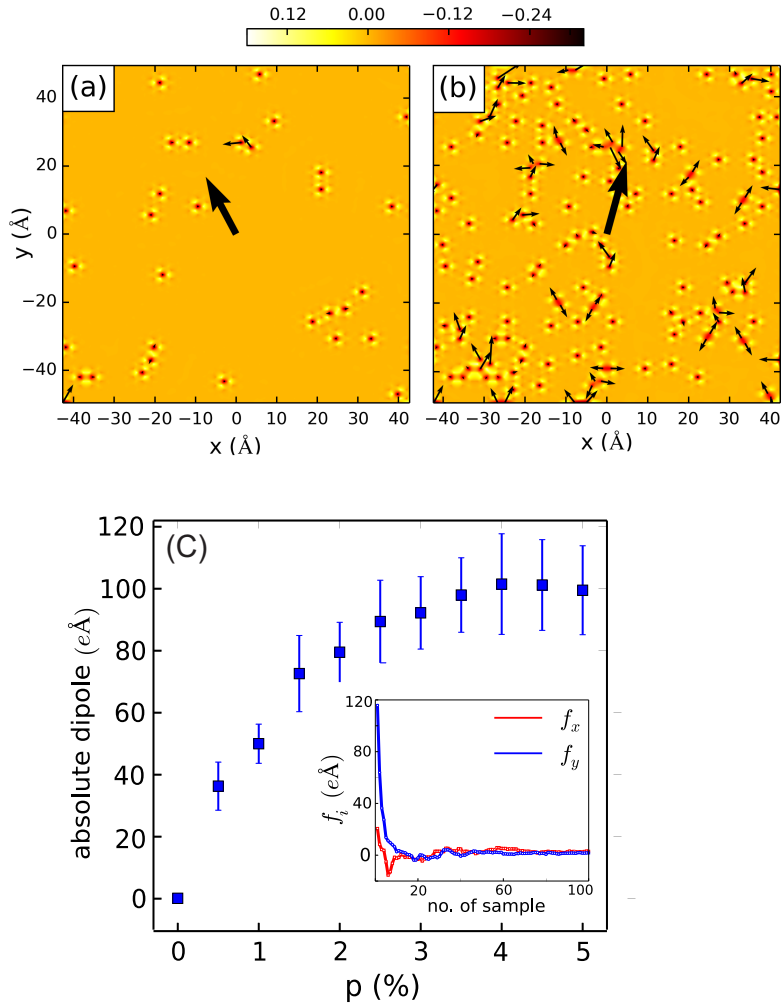


FIGURE 5.2. Density plot of the charge distribution of doped graphene with (a) 1% and (b) 5% nitrogen doping. Small arrows indicate the local dipoles and the thick arrow, corresponds to the net dipole. The color scale is in units of the elementary charge. (c) Absolute value of the net dipole as function of the N-dopant concentration. The inset indicate vanishing of total dipole when we average over many samples where f_x and f_y are x and y-components of the total dipole of n_s samples.

samples. In order to confirm that the net dipole is zero, we performed extra simulations and averaged over 100 samples. By defining $f_i(n_s) = \sum_{j=1}^{n_s} P_{j,i} / n_s$ where i refers to x or y and n_s is the number of samples. As expected, it can be seen in Fig. 5.2(c) inset that the sum of each component of the net dipole approaches zero when the number of samples increases.

The net dipole increases fast up to 4%, then it decreases slowly. The latter is due to the presence of many nearest N-C bonds which can cancel each other and causes a reduction in the net dipole. Due to the increase in the number of neighboring nitrogens that cancels out their contributions to the total dipole of a formed cluster, we conclude that the maximum dipole in the system occurs around 4% random doping. This is very promising for using the ferroelectric effect of N-doped graphene. The induced polarization in the system strongly affects the electronic transport in the system [256]. The strength and direction of the net dipole can be controlled by positioning the nitrogen atoms on predefined locations. This will allow one to engineer the piezoelectric response of an NG sheet which under applied stress leads to possible technological applications such as the conversion of mechanical stimuli into an electrical signal and vice versa [257].

5.3.2 Structural deformations

Height variation at the position of the dopants is in good agreement with recent experimental studies. They measured the height variation of single, double, and more complex dopant configurations using experimental and simulated STM imaging [58, 63]. In Fig. 5.3(a) we show typical height distribution of doped graphene with 5% nitrogen concentration as obtained from the MD simulation. Fig. 5.3(b) shows the height profile across two typical N-clusters. Carbon (nitrogen) atoms are shown as the blue (brown) balls. Note that local ripples appear when N atoms form a cluster (adjacent brown balls). Here, the NG sheet was simulated at room temperature as in the recent experiment. These results for the average peak height for a dopant ($\approx 1.0\text{\AA}$) is in good agreement with the STM images in Ref. [67]. It was found experimentally that the apparent out-of-plane height of N-dopant varies between 0.4\AA and 0.8\AA , and this is consistent with an N-substitution for C atom in the plane of

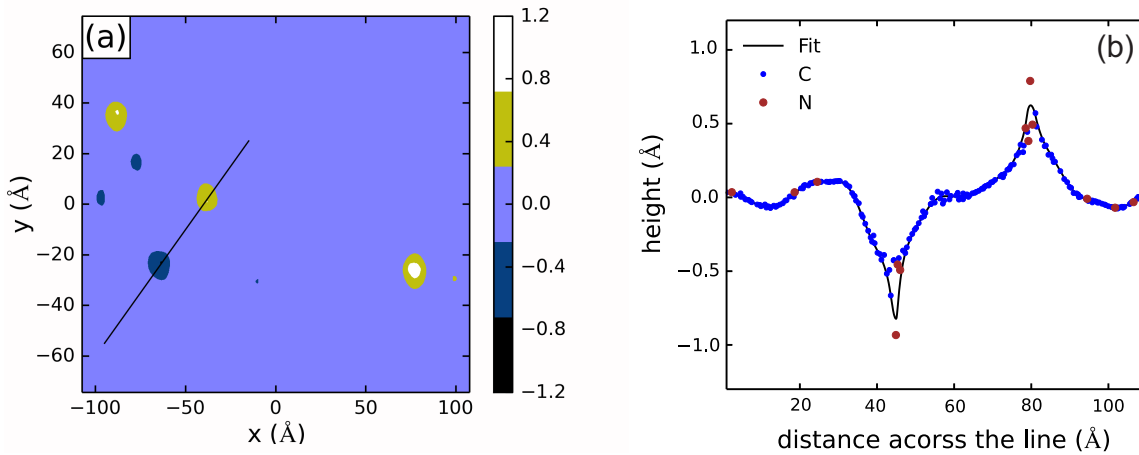


FIGURE 5.3. (a) Height distribution of the NG atoms at room temperature for 5% N-doping. Color scale is in units of Å. (b) Height variation across the line in (a).

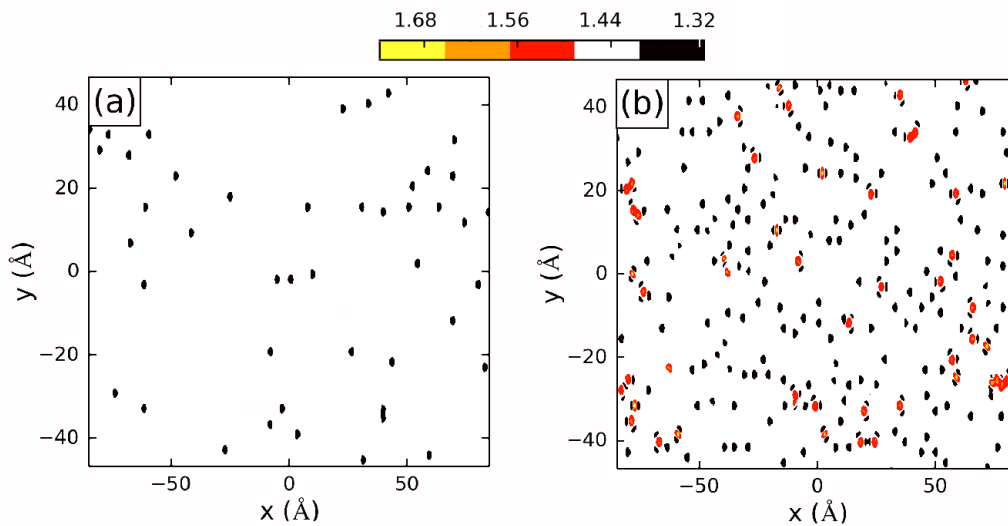


FIGURE 5.4. Bond length distribution for the N-doping concentrations (a) 1% and (b) 5%. Dark spots show single nitrogen atom where C-N bond length becomes shorter. Bright spots indicate the N-N bond length which is longer than C-C (1.42Å). The scale is in Å.

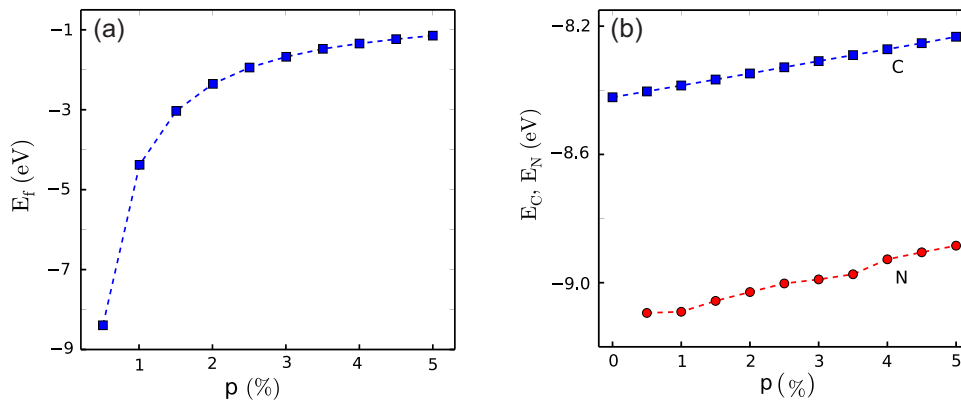


FIGURE 5.5. (a) The formation energy E_f and (b) energy per atom for carbon E_C and nitrogen E_N as function of doping concentration at zero temperature.

graphene.

We also studied the effect of N dopants on the length of the C-C, C-N, and N-N bonds. This helps us to figure out the strength corresponding to each bond. In Fig. 5.4(b), we show the density plot of the bond length distribution at 0K. For pristine graphene the C-C bond length is 1.43\AA while in the presence of 5% N-concentration the C-N bond length is found to be 1.37\AA (dark spots). The N-N bond has an average length of 1.57\AA (bright spots). The results are in good agreement with recent ab-initio calculations [64, 65] where they reported C-N and N-N bonds length of 1.30\AA and 1.60\AA , respectively. Note that the bond length slightly depends on the dopant configuration which is the reason why we give the average C-N and N-N bonds length for different possible N-configurations.

5.3.3 The formation energy

The formation energy E_f is an interesting quantity to measure the stability of a system. For doped graphene, it is given by

$$E_f = [E_{NG} - n_C \varepsilon_C - n_N \varepsilon_N] / n_N, \quad (5.1)$$

where E_{NG} is the total energy of the studied system, n_C (n_N) is the number of carbon (nitrogen) atoms, ε_C (-8.39 eV) and ε_N (-4.77 eV) are respectively

ReaxFF calculated atomic binding energy for pristine graphene and free N_2 molecule as reference systems [64, 258].

Energy per atom E_C (E_N) is the average total energy of all carbon (nitrogen) atoms for a specific N-doping concentration:

$$E_C(p) = [\sum_{i=1}^{n_C} E_i^{tot}(p)]/n_C \quad (5.2)$$

$$E_N(p) = [\sum_{i=1}^{n_N} E_i^{tot}(p)]/n_N \quad (5.3)$$

$n_N = pN$, $n_C + n_N = N$, and E_i^{tot} is the energy of the atom i . In ReaxFF, E_i^{tot} contains many terms such as bond order, coulomb, van der Waals, etc. The major contributions for carbon atoms are due to the bond order term (for more details see Ref. [199]). The larger the absolute value of E_c and E_N the closer carbon atoms and nitrogen atoms to their ground state energy as compared to one carbon atom in pristine graphene and N_2 molecules, respectively.

We present in Fig. 5.5(a) the formation energy of NG systems as a function of dopant concentration. Notice that the formation energy increases non-linearly with dopant concentration. This confirms that N-doped graphene is less stable than pristine graphene. At low doping concentrations ($p < 1\%$), E_f rapidly increases due to the single-substitution of dopants. While for higher concentration ($p > 3.0\%$), the doped system becomes predominantly saturated by N-clusters and then E_f increases more. This result is qualitatively in agreement with the ab-initio calculations for small size systems [58]. In a recent study, the formation energy of different N-doping configurations was computed and it was found that each configuration reduces the system stability for single (0.2 eV), double (0.5-1.7 eV), and more complex (1.9-11.6 eV) substitution of nitrogen dopants. We also calculated the energy per atom for carbon (E_C) and nitrogen (E_N) for different NG systems. The results are shown in Fig. 5.5(b). It is seen that the binding energy of nitrogen atoms increases linearly with the number of dopants which is due to the sharing of electrons of nitrogen atoms with several carbon atoms. However, the binding energy of the carbon atoms loses less energy as compared to those of the nitrogen atoms.

5.3.4 The Young's modulus and the breaking of doped graphene

TABLE 5.1. Young's modulus (Y), breaking stress (σ_{int}) and braking strain (ϵ_{int}) in doped graphene for different concentration of nitrogen atoms. NG sheet is subjected to stress in the armchair (xx) and zig-zag (yy) direction . Y_0 is Young's modulus of pristine graphene.

p(%)	$Y^{xx}(\frac{N}{m})$	Y^{xx}/Y_0	$\sigma_{int}^{xx}(\frac{N}{m})$	$\epsilon_{int}^{xx}(\%)$
Ref.[42]	340±50	-	42±4	25.0
pristine	372	1.00	54	19.4
1	362	0.97	46	15.5
2	353	0.94	42	14.4
3	347	0.93	39	14.0
4	341	0.91	35	12.7
5	335	0.90	34	12.7

p(%)	$Y^{yy}(\frac{N}{m})$	Y^{yy}/Y_0	$\sigma_{int}^{yy}(\frac{N}{m})$	$\epsilon_{int}^{yy}(\%)$
Ref.[42]	340±50	-	42±4	25.0
pristine	376	1.00	67	18.4
1	364	0.97	48	14.4
2	354	0.94	45	14.4
3	350	0.93	41	12.9
4	338	0.90	38	12.9
5	331	0.88	36	11.9

The mechanical properties of graphene have been intensively investigated using simulations at the atomic level. These studies obtained various elastic properties including Young's modulus Y , Poisson's ratio ν , breaking (intrinsic) strength σ_{int} and strain ϵ_{int} . Both DFT and tight binding approaches were used [67, 258–261]. Moreover, experiments used nanoindentation technique to measure linear and nonlinear elasticity of free-standing pristine graphene [42]. Here, we study the effects of substitutional nitrogen doping on the Young's modulus, intrinsic stress, and strain of a graphene monolayer. We found that N-doping decreases Young's modulus (see Fig. 5.6(a)). The result for pristine graphene Y_0 (369 Nm^{-1}) is in good agreement with the reported experimental [42] value $340 \pm 50 \text{ Nm}^{-1}$. The reason for the weakening of NG is the non-uniformity of the bond length distribution. The longer the bond length and the non-uniform distribution of the bond lengths causes a more

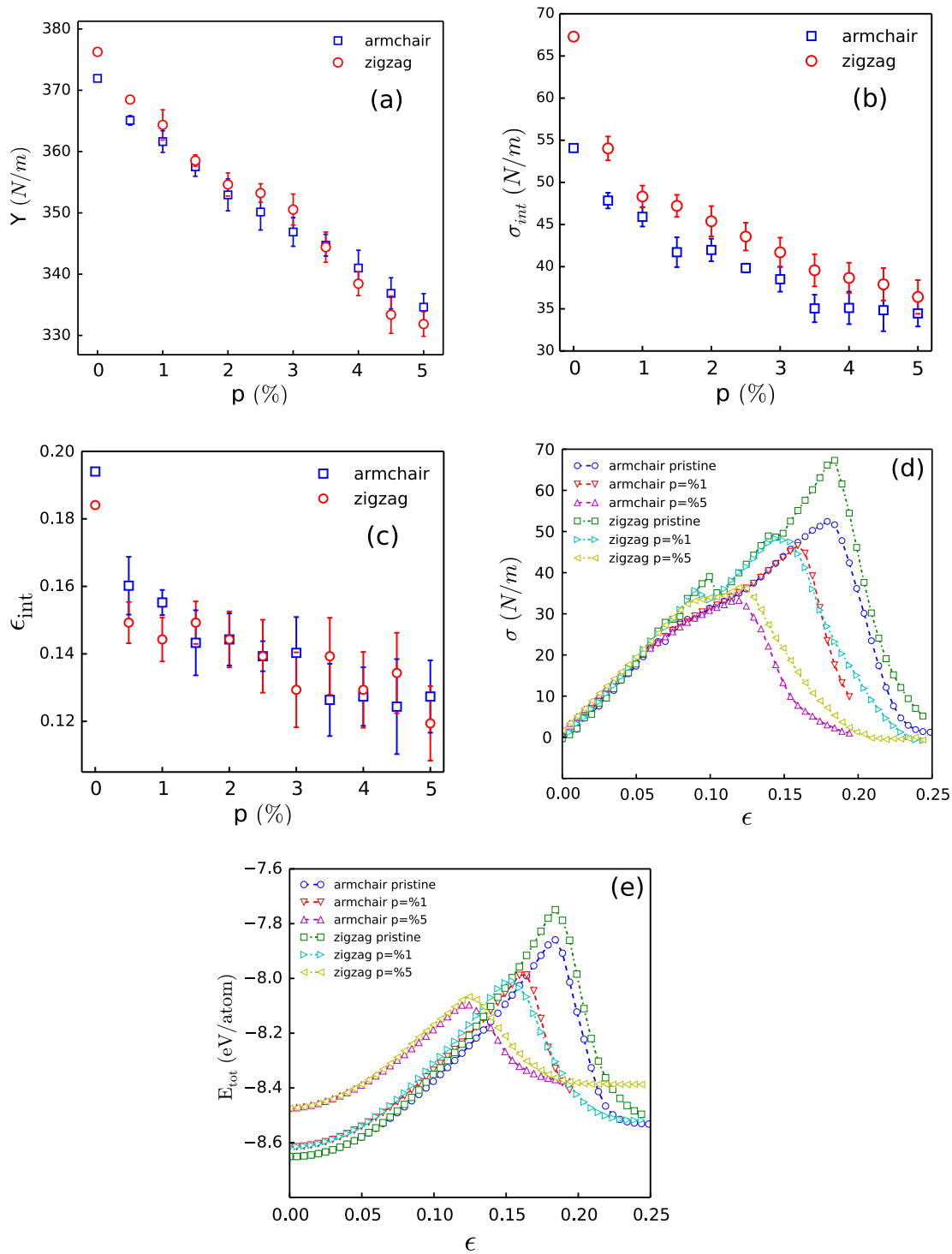


FIGURE 5.6. (a) The Young's modulus Y , (b) breaking stress σ_{int} , and (c) breaking strain ϵ_{int} as function of the concentration of the N-dopants p in both armchair (x) and zig-zag (y) directions. The stress-strain curve, the total energy for different systems pristine, 1%, and 5% NG sheet versus applied strain along x (y) are shown respectively in (e) and (d). σ , ϵ are the applied stress and strain.

local rippling of the position where the dopants are inserted. The decrease in the Young's modulus was also reported by Mortazavi et al. [66] where they used an optimized Tersoff potential [197], however our results show a very smooth linear decrease which is different what was found in previous study [66]. It is also important to note that the optimized Tersoff potential yields barely a noticeable reduction in the Young's modulus of graphene with 5% nitrogen doping in contrast to the obtained results that indicate a 10% reduction in Y . In Table 5.1, we list a set of elastic constants for different N-dopant concentrations (p) and we compare the results with the experiment for pristine graphene. In Figs. 5.6(b,c) σ_{int} and ϵ_{int} are found to decrease with the number of dopants. We report a significant drop at low concentration (i.e. $p < 1\%$), while at high concentrations (i.e. $p > 3\%$) these parameters slowly decrease due to weak N-N bonds inside the N-clusters. The exponential decreasing behavior is more favorable than a linear one because by increasing the N concentration the number of C-N bonds (and N-N bonds) increases and there is an increased chance to have two C-N bonds adjacent to each other. The latter results in a nonlinear increasing disturbance in the C-N, C-C and N-N bond lengths. Note that the breaking stress (strain) is defined as its maximum stress reached before breaking occurs. We found the intrinsic stresses (strains) for pristine graphene $54 Nm^{-1}$ (19.4%) along the armchair and $67 Nm^{-1}$ (18.4%) along the zig-zag direction which are larger (smaller) than the measured value $42 \pm 4 Nm^{-1}$ (25) in Refs. [42, 240]. The reason for this discrepancy might be due to the presence of defects and impurities in the experimental samples. A typical stress-strain curve is shown in Fig. 5.6(d). It is seen that pristine graphene has larger breaking stress and strain as compared to the case of 1, 5% nitrogen doped counterpart. It is also interesting to note that the potential energy has the same quadratic increase versus the strain in both armchair and zig-zag directions before the breaking point which indicates that the NG samples obey linear elasticity, see Fig. 5.6(e). Notice that Young's modulus of the graphene sheet was found to be almost independent of the loading direction (see Fig. 5.6(a)), while the intrinsic stress and strain, as shown in Figs. 5.6(b,c), depending on the direction of the applied force. This is in agreement with previous reports by Mortazavi et. al.

and Zhao et. al. [66, 67]. In fact, graphene is isotropic from the point of view of the linear elasticity and anisotropic from the point of view of the nonlinear elasticity. This is obtained from the group theory applied to the graphene crystal structure [262]. For example, the total energy shown in Fig. 5.6(e) for pristine graphene is the same for applied stress along zig-zag and arm-chair direction for strains smaller than 10% while they start to be different beyond this number where the non-linear effects become important.

In a recent study, Mortazavi et al. [66] used an optimized version of the Tersoff potential to study the mechanical properties of defected and doped graphene nanoribbons. They found that Y was independent of N concentration. In contrast, we found a linear decreasing of Y with N concentration. On the other hand, the calculated breaking stress (strain) in this study is in agreement with their results that is 52.7 N/m (0.23) [66].

5.4 Conclusions

In summary, using molecular dynamics simulation the structural and mechanical properties of nitrogen-doped graphene were explored. We found that the roughness of the NG systems is sensitive to the dopant concentration. The major contribution to the ripples are from the nitrogen cluster formation in the graphene layer. The graphene layer is mechanically weaker when doped with nitrogen resulting in a decrease of Young's modulus and the breaking stress. The formation energy increases as a function of the number of dopants which results in a decrease in the stability of the nitrogen-doped graphene.

SPATIAL DESIGN AND CONTROL OF GRAPHENE FLAKE MOTION

Force between a sharp scanning probe tip and a surface can drive a graphene flake over crystalline substrates. The recent design of particular patterns of structural defects on a graphene surface allows proposing an alternative approach for controlling the motion of graphene flake over a graphene substrate. The thermally induced motion of a graphene flake is controlled by engineering topological defects in the substrate. Such defected regions lead to an inhomogeneous energy landscape and are energetically unfavorable for the motion of the flake, and will invert and scatter graphene flakes when they are moving toward the defected line. Engineering the distribution of these energy barriers results in a controllable trajectory for the thermal motion of the flake without using any external force. We predict superlubricity of the graphene flake for motion along and between particular defect lines. This work provides new insights into frictional forces of interfaces and opens a novel route to the engineering of the stochastic motion of a graphene flake over any crystalline substrate.

This work is published as: H. Ghorbanfekr-Kalashami, F. M. Peeters, K. S. Novoselov, and M. Neek-Amal, “Spatial design and control of graphene flake motion”, *Physical Review B(R)* **96**, 060101 (2017). As the first author, I performed all MD simulations and contributed to the scientific interpretation of the results and in the writing of the manuscript.

6.1 Introduction

Atomic scale precision and control of the motion of graphene flakes over crystalline substrates are used for atomic scale design of novel systems targeted for operations at the atomic scale [80, 81, 263, 264]. The lateral frictional force between a sharp tip and a surface, for driving a nanometer-sized graphene flakes over the surface of graphite, can be measured by atomic force microscopy (AFM) and scanning tunneling microscopy (STM) [80, 81]. This is related to the self-reorientation of interacting two-dimensional crystals recently studied for other layered crystals beyond graphene over graphite [263, 264]. The diffusion after rotation of a graphene flake into superlubric states is controlled by the size of the flake, temperature, and the presence of contamination bubbles or defects in the underlying substrate. For instance, superlubric to commensurate ground states gives longer sliding distance (95 nm) at low temperature 5 K as compared to (33 nm) 77 K [80]. It has also been reported that a misaligned graphene flake (3° rotated) can be returned to the commensurate state by annealing the sample up to 200°C [263]. On the other hand, recent control over the location and average complexity of defect formation in graphene (by exposure of a graphene sample to a focused electron beam) allowed to engineer defect patterns in a desirable way [74]. Defects in graphene modify its properties and affects its functionality [73, 75]. We are interested to use such designed defects in the substrate to engineer the dynamics of a graphene flake that is put on top of it.

In this chapter, we reveal that the superlubricity of a graphene flake over a graphite substrate [76–78] is strongly influenced by the presence of defects in the substrate. The dynamics of the graphene flake is significantly altered and the well-known random rotational motion and corresponding transition from incommensurate to commensurate states and related life time are profoundly influenced by the defected regions. In particular, we observe backscattering in the motion of a flake that is moved towards a grain boundary (GB) line. Notice that the commensurate to incommensurate transition is the main reason for locking of the flakes on the substrate. This transition is determined by the competition between the GB line size, initial velocity and size of the flake. Several types of grain boundaries - different arrays of 5-7 defects - are

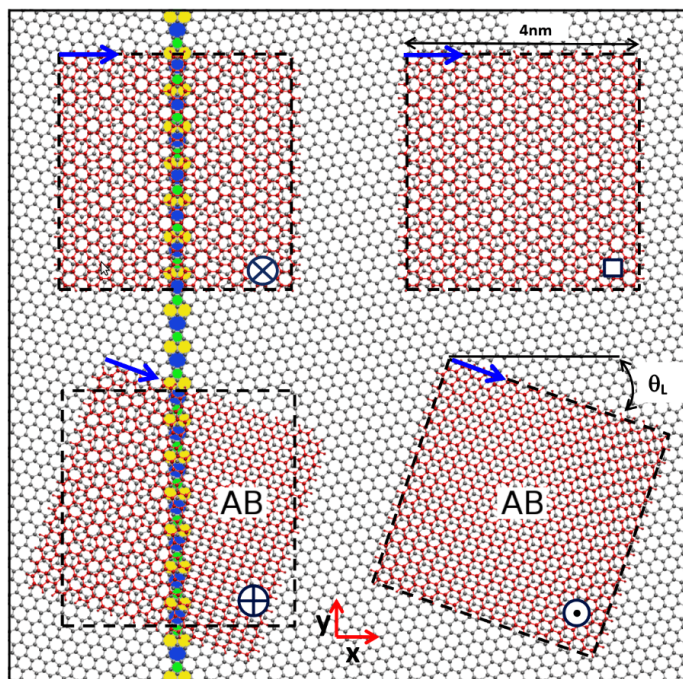


FIGURE 6.1. A hydrogen edge-passivated flake is put over graphene which initially is in one of the positions labeled by square, \odot , \oplus , and \otimes . The black dashed lines indicate the region that is scanned for finding the energy landscape, see Fig. 6.2. The blue vector (\hat{u}_{ac}) is a unit vector along the armchair direction of the flake which helps us to determine the mutual orientation between the flake and the x -axis of the substrate.

investigated in order to identify how they influence the trajectory of motion of a graphene flake. This work reveals several microscopic aspects of the motion of a thermally actuated flake over graphene with GB which can be helpful for developing AFM/STM driven force measurements [80, 81]. Although AFM measurements give an estimation for the static friction force, but providing any details on the complex dynamics of the sliding motion of graphene flakes is still challenging [82].

6.2 The model and method

Molecular dynamics simulations are used to simulate a graphene flake with 750 carbon atoms and 72 hydrogen atoms at its edges. The substrate is a graphene layer which contains a GB line at the middle. We study several

types of GB where the mutual orientations of the two crystalline domains is described by the misorientation angle which e.g. for Large-Angle Grain Boundary (LAGBI) [73] is $\theta_L = 21.8^\circ$ with respect to x -axis (for more types of grain boundary see Fig. A.1 in Appendix A). A square-shaped flake (dimension $l^2 = 4 \text{ nm} \times 4 \text{ nm}$ terminated by hydrogen atoms) positioned over the substrate. Such a small size graphene nanoribbon can be fabricated using e.g. bottom-up approach [265]. We associate a unit vector that is always along its armchair direction (independent of its orientation with the substrate \hat{u}_{ac}). Therefore the orientation of the flake with respect to the substrate is determined by the angle θ which is defined by $\hat{x} \cdot \hat{u}_{ac} = \cos(\theta)$. To model the covalent bonds formed between the different carbon atoms within the same flake, we used the AIREBO potential [196] and a registry-dependent potential developed by Kolmogorov and Crespi (KC [266]) for the interlayer interaction which are implemented in LAMMPS [10]. The AIREBO potential is a reliable force field for hydrocarbons which incorporates different atomic hybridizations particularly suitable for the graphite. However, its treatment of non-bond interaction for the graphene interlayer coupling relies on the Lennard-Jones (LJ) potential that still gives an essential part of total interlayer binding energy but it weakly depends on the interlayer alignment. Therefore, we employed KC potential on the top of AIREBO that even for different alignments gives almost the same energy barriers as DFT-D between the flake and the substrate [77]. In contrast to simple LJ potential that underestimates the experimental and DFT-D energy barrier by an order of magnitude [78, 267].

6.3 Energy analysis: pristine and LAGBI system

We depict a graphene substrate containing a LAGBI line which is located at $x=0$ and elongated along the y -axis with a flake put on top of it (see Fig. 6.1). A typical incommensurate state for the flake (that is, $\theta = 0^\circ$) is shown by the square symbol. The other possible configurations can be as those shown by symbols \odot , \oplus , and \otimes which have $\theta = \theta_L$, θ_L , and 0° , respectively. Notice that

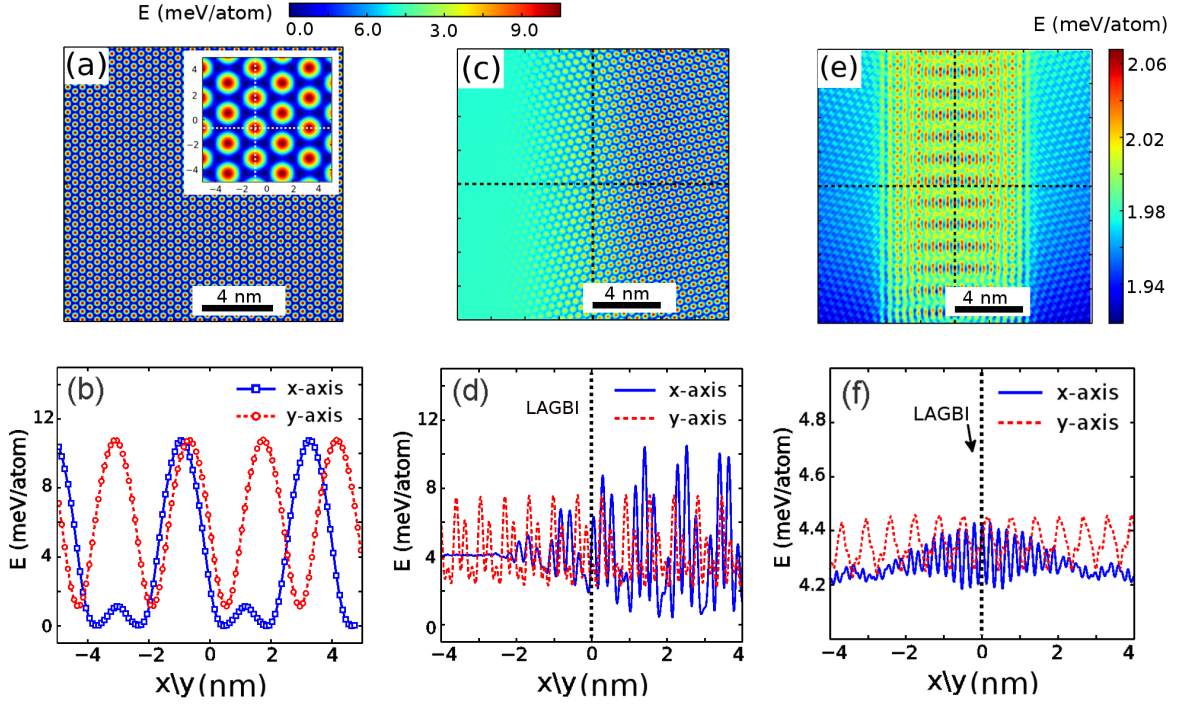


FIGURE 6.2. (a) The vdW-energy landscape resulting from the vdW-energy stored between the graphene flake above a perfect graphene substrate at $z=0.34$ nm and (b) two corresponding cross sections along the armchair and zig-zag directions indicated by dashed lines in the inset of (a). In (c) ((e)), we show the energy landscape of the flake rotated with $\theta = \theta_L(0^\circ)$ scanned inside the box \oplus (\otimes) as shown in Fig. 6.1 and the corresponding cross sections along the dashed lines are shown in (d) ((f)). Energy reference is chosen to be $E_{AB}=0$.

in the RHS (LHS) of the LAGBI line, the system shown by \ominus (\oplus) is completely (partially) in the AB-stacking configuration. First, we relaxed the substrate in the xy -plane, then we made it rigid and studied the dynamics of the top flake. In Figs. 6.2, we depict three vdW-energy landscapes (2D-density plots) wherein all cases the flake (which is located at average height $z=0.34$ nm above the substrate) is moved to scan a 4×4 nm² area (the dashed squares in Fig. 6.1). The corresponding energy landscape (for scan area indicated by the black dashed square \ominus in Fig. 6.1) is shown in Fig. 6.2(a). The substrate below the square \ominus consists of pristine graphene (the flake is initially in the AB-stacking configuration). We show the corresponding profiles along the

indicated vertical and horizontal dashed lines in Fig. 6.2(b). These results are in good agreement with previously reported vdW-energy landscape for graphene over graphite [77]. The energy barriers are found to be about 10 meV/atom which is the energy difference between two well-known stacking states in graphite $\Delta_0 = E_{AA} - E_{AB}$. We set E_{AB} as the energy reference.

In Figs. 6.2(c,d), we show the energy landscape and corresponding profiles, respectively, for an energy scan inside the dashed square \oplus , i.e. a rotated square with respect to the underlying flake. The blue (dashed red) line in Fig. 6.2(d) refers to the energy profile along x -axis at $y=0$ (y -axis at $x=0$, i.e. along the GB line). The periodic function for the profile along y -axis (GB line) is as expected - the maximum barrier is found to be about $\Delta = 5$ meV/atom - however the energy profile along x -axis is unexpected. It is seen that until almost $x \simeq -l/2$ the fluctuations in the solid blue line are negligible (as compared to the dashed red line) and after $x \simeq -l/2$ it oscillates (Δ grows) with a nonuniform larger amplitude. The latter is due to the fact that crossing the GB brings us to the AB-stacking region as seen from the right-hand side part of the flake \oplus in Fig. 6.1. The maximum energy barrier is found to be around 10 meV/atom where x varies in the range 1-2 nm. Notice that the flake \oplus is rotated by an angle θ_L with respect to the x -axis. In fact, the flake is affected by very small energy barriers for $x \leq -l/2$, i.e. the superlubricity states. The honeycomb pattern in the right-hand side of Fig. 6.2(c) clearly indicates this effect.

In Fig. 6.2(e) we plot the energy landscape for a scan of the flake \otimes inside the corresponding black-dashed square shown in Fig. 6.1. Here the flake in both sides of the GB is located at incommensurate states. The corresponding energy profiles along x - and y -axis are shown in Fig. 6.2(f). One naturally expects to find periodic oscillations for the energy barriers along the GB line where the maximum barrier is about 0.2 meV/atom. However, along the x -axis, only when the flake is close to the GB line (its neighborhood), it is influenced by larger energy barriers of ~ 0.13 meV/atom ($|x| \leq l/2$). Therefore, although in Fig. 6.2(f) the energy barriers along x -axis where $|x| \leq l/2$, are larger than both the energy in $|x| \geq l/2$, but they are still much smaller than the energy barrier Δ_0 see also Figs. A.2 for the energy barriers against

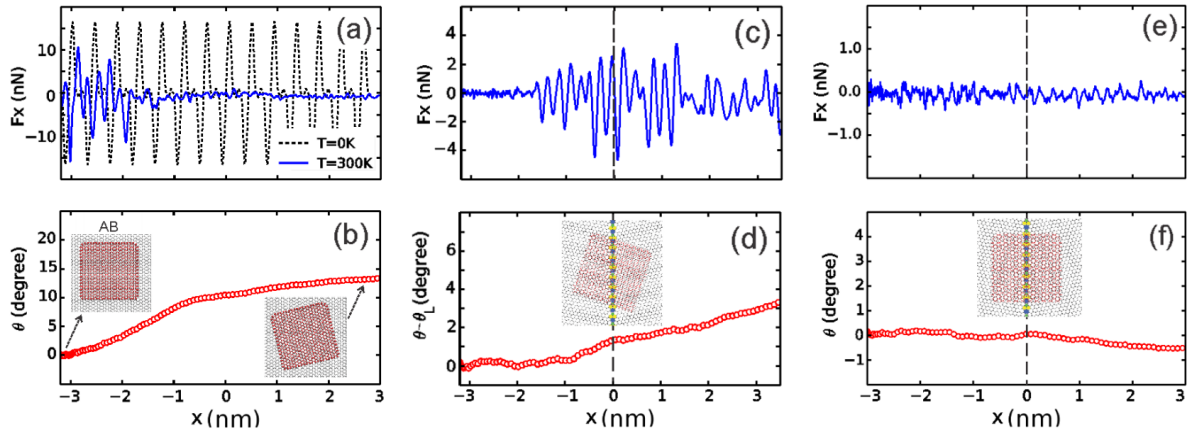


FIGURE 6.3. The variation of x-component of the total force of a flake moving on (a) pristine graphene, (c,e) a graphene substrate containing a GB line. The variation of corresponding direction θ of the flake are shown in (b,f) and $\theta - \theta_L$ in (d). The orientation of the flake are shown as insets which have 0° , θ_L , and 0° in (b), (d), and (f), respectively.

rotation above pristine graphene/LAGBI). Notice that the total barrier energy is $750 \times E$ which is the relevant energy for practical applications. E indicates the calculated energy of the flake per atom. Crudely thinking about the latter energy barriers represented in Fig. 6.2(d,f), in comparison to the energy barriers in Figs. 6.2(a,b), leads us to conclude that the flake should be able to pass the GB easily at any finite temperature. However, surprisingly, this turns out not to be the case (see backscattering).

6.4 Force analysis at finite temperature

By identifying the force between a sharp tip and a surface, while keeping the temperature fixed at $T = 300$ K [80, 81], frictional effects can be understood. We found that the lowest force which enables us to move the flake continuously over the GB depends strongly on the initial θ (stacking) of the flake. We applied a constant force¹ of $f_0 = 6.5$ pN/atom along the armchair direction which drives the flake (initially started its motion from AB-stacking) to the

¹This force can be approximated by $f_0 \approx \Delta_0/a_{CC}$ where $a_{CC} = \sqrt{3} \times 1.42\text{\AA}$ and it might be scaled depending on particle orientation and crystallinity [268].

right. Interestingly, after a shift of about 1 nm (see Fig. 6.3(a)) the flake rotates (see the variation of θ in Fig. 3(b)). We demonstrate the net friction force F_x in Fig. 6.3(a). The flake rotates and reorients itself after $x \approx -1.5$ nm in order to minimize its energy. The dashed line in Fig. 6.3(a) is the result of sliding the flake over graphene without relaxing it at each step, i.e. a rigid flake is moved with fixed θ along the armchair direction of pristine graphene. Comparing the dashed black line and the blue line leads us to conclude that the results of Ref [269] are questionable because of the non-relaxed sample.

We also applied f_0 on the flake along the x -axis to move it over the GB line. The results for two different initial θ , i.e. flake \oplus with initial $\theta = \theta_L$ and \otimes with $\theta = 0^\circ$, are shown in Figs. 6.3(c) and 6.3(e). The corresponding variation of θ is shown in Figs. 6.3(d) and 6.3(f), respectively. The flake \oplus passes the GB line by experiencing large forces around/on the GB line (Fig. 6.3(c)) but in parallel, it is rotated to minimize its energy. The $\theta - \theta_L$ (see Fig. 6.3(d)) changes to larger values. The inhomogeneous energy landscape around the GB line creates a lateral force (F_y) on the front of the flake (located in $x < -l/2$) which induces a net torque ($\tau_z \sim lF_y/2$) and eventually changes the path (note in the beginning $F_y = 0$). The angular velocity can be approximated by $\omega \simeq \sqrt{6(v^2 - v_0^2)/l^2}$ if the initial and current states are incommensurate with small potential energy. Surprisingly, when the flake \otimes is subjected to f_0 , it passes the GB line i.e. $\theta \sim 0^\circ$ without changing its orientation and it experiences a larger force. In fact if the flake approaches the GB line and is located in the state \otimes it can pass the GB line easily, however, this rarely happens because reaching the state \otimes is difficult (it is an incommensurate state) except when moving with high kinetic energy. The latter effect is directly related to the well-known superlubricity effect, see Fig. A.3 in Appendix A for more details on the effect of the flake size.

6.5 Backscattering

The interface between two domains of graphene with different crystallographic orientation (GB) changes the energy landscape on both sides. If the flake is diffusing on one side of the GB it prefers to stay away from the GB

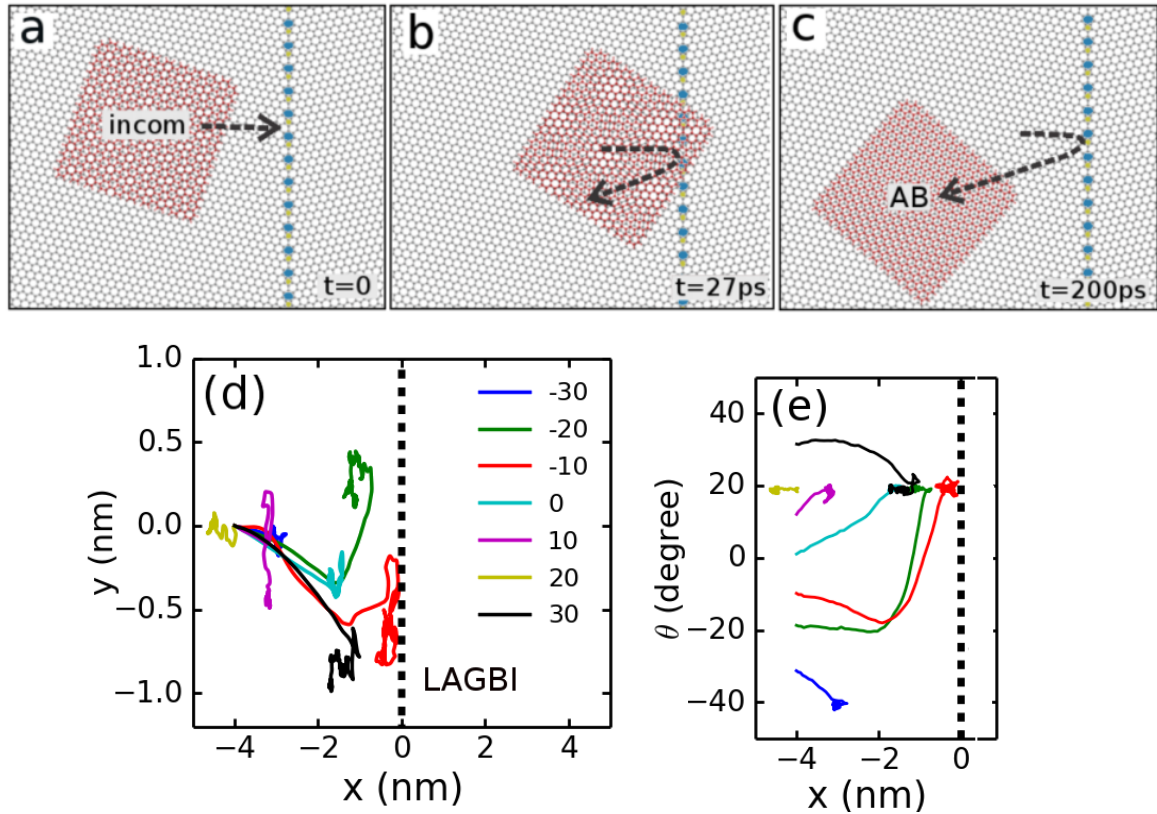


FIGURE 6.4. Backscattering of a flake moving towards a LAGBI GB when initially it was in an incommensurate state (a,b,c). The path of motion are shown in (d,e) for $v_0 = 100$ m/s where different colors refer to different initial θ (given in the inset of (d)).

line. In order to quantify this effect, we shoot the graphene flake to the right with initial velocity $\vec{v}_0 = v_0 \hat{x}$ over perfect graphene and given graphene with a GB line where v_0 is the velocity of the center of mass of the flake. The velocity $\vec{v} = (v_x, v_y)$ varies with time after shooting. In Figs. 6.4(a-c) we show three different snapshots of a flake moving towards a LAGBI line where initially it started from an incommensurate state. It is clearly seen that the flake is backscattered in (c) when it approaches the GB line. In Fig. 6.4(d) we show backscattering of the flake moving toward the GB line with different initial θ s, see Fig. A.4 for a case of moving flake on perfect graphene. The corresponding variation of θ with x are shown in Fig. 6.4(e) (velocities are shown in Fig. A.5). Different colors refer to different initial θ which are shown in the legend. The dotted line in Figs. 6.4(d,e) refers to the LAGBI line. They

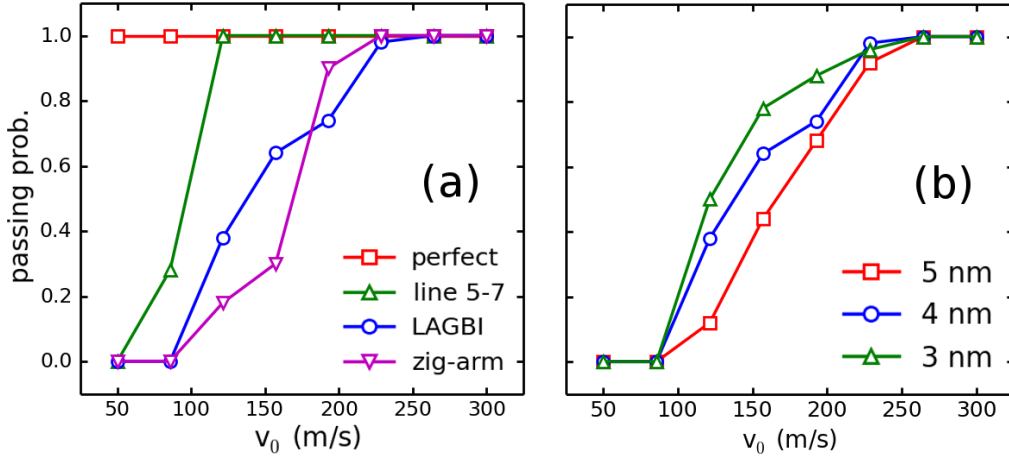


FIGURE 6.5. (a) The passing probability of a flake with size $4 \text{ nm} \times 4 \text{ nm}$ moving over a perfect graphene substrate and three different defected substrates as function of the initial shooting velocity (v_0). In (b), the passing probability for different sizes 3, 4, and 5 nm over LAGBI is shown.

arrive eventually into the AB-stacking configuration² (“AB” symbol in (c)). Examples of the motion of one such flake are shown in Figs. 6.4(a,b,c). The above described mechanism can be used to design ultra-low dissipation nano mechanical devices. The flake avoids the region over the LAGBI line except for the situation when there are two LAGBI lines on both sides of the flake (panel (b) of Fig. A.6 in Appendix A).

6.6 Discussion and conclusions

In order to see the influence of the shooting velocity (v_0) of the flake, we show the passing probability as a function of v_0 for perfect and defected substrates (see Fig. 6.5(a)). The passing probability in each case was calculated employing an ensemble of different initial incommensurate states. The passing probability for small/large flake can be given by $P_l(v) = 1 - (\frac{v-v_{max}}{\bar{v}})^2$ and $\frac{1}{4}(\frac{v}{v_i} - 1)^2$, respectively shown by triangular and square symbols in Fig. 6.5(b), where $v_{max} = 3v_i = 3/2\bar{v}$ with $v_i=100\text{m/s}$. By increasing v_0 the passing probability increases. In fact, the lattice orientation on both sides of the GB

²Notice that there is a critical length beyond which the super low frictional regime for motion of the flake disappears [270].

line determines the passing probability. The smallest passing probability is found for LAGBI (and larger flake with 5 nm size, see Fig. 6.5(b)) and trivially the largest probability should be for motion over perfect graphene. It is interesting to note that after $x = x_m \simeq -l/2$ most of the flakes start to change their direction of motion (see Fig. 6.4(d)). Therefore, the flake's portion that enters in the x_m region is affected by LAGBI. We performed additional simulations for two flakes with different sizes of 3 and 5 nm. We found that the effect of the GB is enhanced when the flake is made larger. Size effects for backscattering demand a new scaling which is different from the one for structural lubricity [268]. We emphasize that the obtained results are general and independent of the shape of the flake, i.e. the minimum energy configuration corresponds to maximizing the commensurate coverage of the flake and substrate independent of its shape.

The design of defect patterns is an active area of research [74, 271], *e.g.* A. W. Robertson *et al.* conducted an experimental study to induce topological atomic defects in graphene using the technique of ion irradiation [74]. Achieving high velocities of the order of 100 m/s for the motion of a flake over a substrate is experimentally challenging. In the past decade, several studies attempted to produce high velocities [272, 273], *e.g.* Nikhil *et al.* use modified an existing commercial AFM setup and achieved velocities between 1 $\mu\text{m/s}$ and 10 mm/s [272]. When the flakes move with high supported velocities above the defected regions, we found that the motion can be controlled/scattered by designing particular defect patterns. This study would be an endeavor worth taking and is promising for future studies.

The obtained scattering/backscattering (mirror reflection) phenomena can be realized experimentally. Many experimental samples contain GBs and by moving a graphene flake through/over the GB region the motion of the flake should be strongly affected by the presence of the defected region especially when both sides of that region correspond to different crystallographic orientations. For instance, we found that for LAGBI and "zig-arm" substrates see Fig. A.1 in Appendix A, passing a graphene flake over this GB line has a very small probability, i.e. it only happens for very large v_0 of the flake (see Fig. 6.5). Moreover, by designing a particular pattern of topological defects

on the graphene substrate (see Figs. A.6 in Appendix A), the thermally induced motion of graphene flakes follows the designed path if the flake can not find an AB-stacking configuration in nearby regions. This is similar to what happens when a flake approaches the edge of the graphene substrate. Such controllable paths can be realized by designing a particular defect pattern on various substrates enabling control of stochastic motion of the flake.

GRAPHENE NANOBUBBLES

Van der Waals (vdW) interaction between two-dimensional crystals (2D) can trap substances in high pressurized (of order 1 GPa) on nanobubbles. Increasing the adhesion between the 2D crystals further enhances the pressure and can lead to a phase transition of the trapped material. We found that the shape of the nanobubble can depend critically on the properties of the trapped substance. In the absence of any residual strain in the top 2D crystal, flat nanobubbles can be formed by trapped long hydrocarbons (that is, hexadecane). For large nanobubbles with the radius of 130 nm, atomic force microscopy measurements show nanobubbles filled with hydrocarbons (water) have a circular (non-circular) shape which is in agreement with our molecular dynamics simulations. This chapter provides insights into the effects of the specific material and the vdW pressure on the microscopic details of graphene bubbles.

This work is published as: H. Ghorbanfekr-Kalashami, K. S. Vasu, R. R. Nair, F. M. Peeters & M. Neek-Amal, “Dependence of the shape of graphene nanobubbles on trapped substance”, *Nature Communications* **8**, 15844 (2017). As the first author, I performed all MD simulations and contributed to the scientific interpretation of the results and in the writing of the manuscript. The AFM measurements and Raman spectroscopy have been conducted by our collaborator experimental group lead by Prof. Rahul Nair at Manchester University.

7.1 Introduction

Graphene is known to be a robust elastic crystal capable of holding mesoscopic volumes of liquids, gases, organic fluids, hydrocarbons, and nanocrystals [83, 86, 274]. Such graphene nanobubbles can have sizes from 0.37 nm (which is the minimum observed height of a monolayer of atomically flat water adlayer on mica substrate) to a few micron in height and diameter depending on the initial amount of trapped substance [84, 275, 276]. Xu *et al.* used single layer graphene as an atomically flat coating to visualize the water adlayer islands grown on mica substrates. [275]. Using infrared spectroscopy, the pressure within the formed nanobubble was measured to be around 1 GPa at 600 K [96]. This resulted in novel and unpredicted chemical reactions inside the trapped bubbles due to the presence of extremely high pressure [97]: for instance, it was found that a strong confinement effect is observed on the chemistry of CO molecules captured between graphene and a Pt surface [277]. The size, shape, and their statistics can be monitored by various techniques such as atomic force microscopy [86]. Because of graphene inertness and its capability of withstanding large strains such nanobubbles offer unique opportunities to investigate nano-quantities of materials under extreme conditions.

Using membrane theory, nonlinear plate theory, and the ideal gas model, Yue *et al.* [85], studied the mechanics of relatively large graphene bubbles. The pressure inside the large graphene nanobubbles ($R > 10$ nm) is predicted to be in the order of MPa, [85, 92, 93] which is essentially determined by the elastic properties of the top layer and the interfacial adhesion between top layer and the substrate, $P \propto \frac{\Gamma}{R}$ [85], where Γ is the adhesion energy per unit area and R is the radius of the nanobubble. Recently, for large bubbles ($R > 50$ nm), Khestanova *et al.* [94] found experimentally a universal scaling law of h_{\max}/R where h_{\max} is the maximum height and R is the base radius of the bubble filatonic force microscopy (AFM) [85, 94]. Moreover, for a nanobubble filled by ethylene with $R = 4$ nm and height 0.5 nm, it was shown that this results in a pseudo magnetic field of 100 Tesla [87] which changes fundamentally the electronic spectrum of graphene. The latter is a consequence of the large induced strain in graphene. Furthermore, possible phase transitions in the trapped substance prevent the use of the ideal gas

model, i.e. $PV=NK_{\text{B}}T$, and therefore the calculation of the internal pressure for small nanobubbles has been remaining a challenge. Most of the theoretical studies have addressed the deformation and structure of graphene bubbles on top of a substrate [85, 94]. Although the effects of pressure on the chemical equilibrium and kinetics is an archaic topic [95, 96] recent observations have shown that the vdW pressure can induce unusual chemical reactions where several trapped salts or compounds are found to react with water at room temperature, leading to 2D crystals of their corresponding oxides [97]. These structural transitions and corresponding chemical reaction mechanisms are not well understood yet. In this chapter, I focus on how the material inside the bubble influences the microscopic shape of the bubble. For illustrative purposes, we considered four materials with very different properties. Hydrocarbons are often present as contaminants [85, 94]. Several studies exist on confined water [125, 218, 278, 279] while ethanol, helium and NaCl have not been considered. By means of equilibrium molecular dynamics simulations and atomic force microscopy measurement (AFM), we are able to provide deeper insights into the microscopic details of the graphene nanobubbles and the internal pressure for small nanobubbles. We study bubbles filled by diverse substances such as helium, water, two hydrocarbons (ethanol, hexadecane) and NaCl. The vdW pressure is found to be in the order of GPa depending on the size of the bubble and the interfacial adhesion. Flat nanobubbles can be formed in case of trapped metallic substances or for large elongated hydrocarbons. The AFM experiments indicate that in contrast to water bubbles, the hydrocarbon bubbles have round shape with in-plane circular symmetry which is in good agreement with the MD simulations results. This systematic study provides a deeper understanding of the formation of graphene nanobubbles beyond simple membrane theory that extends its applicability to small nanobubbles and predicts a substance dependent nanobubble shape.

7.2 Methods

7.2.1 MD simulations

We performed molecular dynamics (MD) simulations using reactive force field ReaxFF [199] to simulate the interaction between carbon, oxygen, and hydrogen in form of a water bubble. However, it must be noted that any combination of two potentials¹ that are separately fitted for the graphene and the water at of order GPa pressure, and treating the repulsive interaction through LJ potential would be sufficient as well due to the dominant vdW interaction between graphene and a trapped substance within the nanobubble. Accordingly, a Lennard-Jones potential is used to describe the helium atoms² ($\epsilon_{\text{He}} = 0.02166 \text{ kcal mol}^{-1}$, $\sigma_{\text{He}} = 2.64 \text{ \AA}$) as well as the helium-carbon ($\epsilon_{\text{He-C}} = 0.0334 \text{ kcal mol}^{-1}$, $\sigma_{\text{He-C}} = 2.98 \text{ \AA}$) interactions [280].

In order to simulate trapped ethanol, we used the hybrid OPLS potential [281] for ethanol and the ReaxFF potential for the graphene layers. Liquid and solid phases of ethanol have been tested by the molecular model proposed by Jorgensen [281]. In the recent study, the introduced OPLS potential that includes different bond, angle, and dihedral terms regarding the covalent bonds and non-bonded LJ, and Coulomb interactions that have been accurately determined for various types of hydrocarbons³. As a result, thermodynamical and structural results predicted from OPLA potential were shown to be in good agreement with available experimental and theoretical studies [282, 283]. Furthermore, the reactive empirical bond order potential⁴ [196] was employed for the graphene sheets and the trapped hexadecane due to the availability of the potential parameters for hydrocarbon systems.

For trapped NaCl nanocrystal simulations, we used a hybrid potential that consists of the AIREBO [196] for graphene layers, the EIM [284] potential for NaCl crystal suitable for structures with ionic bonds, and the LJ (12-6) repulsive interaction between ions and carbon atoms. For carbon or

¹Hybrid potential

²Rare gases are simply modeled by non-bond interaction such as LJ (12-6) potential due to their closed shell electronic structure.

³See force field section in Chapter 3

⁴AIREBO

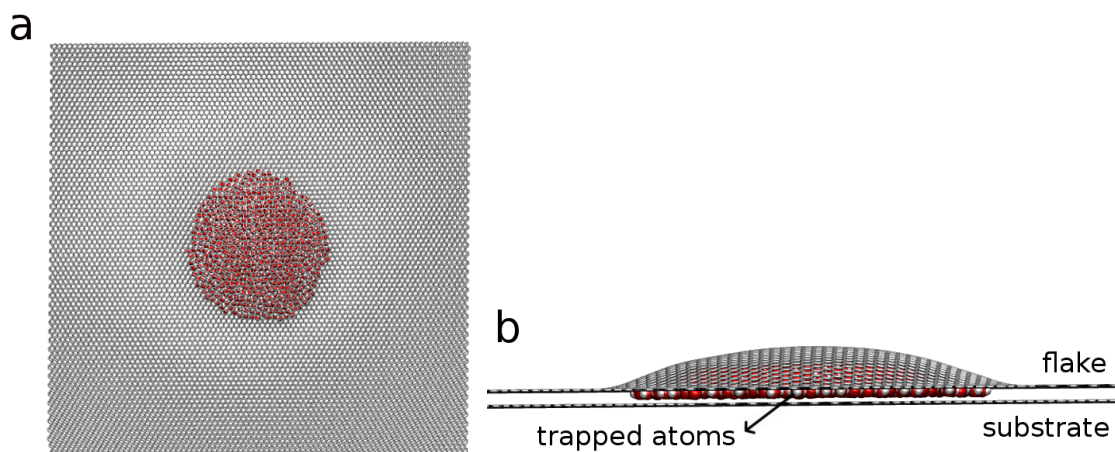


FIGURE 7.1. (a) Top and (b) side view of nanobubble setup model for the MD simulation. The atoms/molecules trapped between the substrate and the top flake.

hydrocarbon systems in which chemical reactions are of interest, and which may also require non-bonded interactions, the AIREBO many-body potential provides an effective and accurate method for the molecular simulations [196]. This force field provides both carbon-carbon stretching and bending energy terms as well as bond dissociation/formation. On the other hand, the EIM potential captures also charge-transfer effects and environment dependence of the ionic bonding [284]. Regarding the multi-body nature of EIM, it provides a more realistic description of the ionic compounds than the more common models which simply use Coulomb and van der Waals interactions between ions with fixed point charges. The cross LJ potential parameters were obtained by the Lorentz-Berthelot combining rules ($\epsilon_{\text{Na-C}} = 0.006505 \text{ kcal mol}^{-1}$, $\sigma_{\text{Na-C}} = 2.78 \text{ \AA}$, $\epsilon_{\text{Cl-C}} = 0.001153 \text{ kcal mol}^{-1}$, $\sigma_{\text{Cl-C}} = 4.115 \text{ \AA}$) [285]. The cut-off potential for the LJ potential was chosen at 10 \AA . The simulation setup comprises three different parts: i) the substrate which is a rigid graphene sheet with 120,000 carbon atoms, ii) a top flake of graphene with 72,000 atoms with a typical size of 17 nm, and iii) the trapped molecules, see Figs 7.1. In order to study the deformation of the top graphene layer, we first deformed it manually so that it covers the molecules underneath, then we performed an annealing molecular dynamics simulation by cooling down the system to 0 K. The latter optimizes the bump and the trapped molecules and allows us to achieve the minimum energy configuration. In the second step, we heat

the system until room temperature. The Nosé-Hoover thermostat [169] is used with time step 0.5 fs. The boundary around the flake is terminated by hydrogen in order to keep them chemically inactive. Note that the size of the flake is taken large enough as compared to the bump radius ($4x$) in order to avoid edge effects. We set the number of atoms for each bubble type such that we obtain approximately the same bubble size. This allows us to compare the different bubble types with each other. In this work, all the simulations were carried out using the large scale atomic/molecular massively parallel simulator LAMMPS [253]. Visual molecular dynamics⁵ package has been used to visualize the atoms/molecules [286, 287].

7.2.2 AFM measurements

Graphene nanobubbles filled with water/ethanol molecules were fabricated by wet transfer technique using single and few layer graphene flakes ($50\mu\text{m} \times 50\mu\text{m}$ or above) prepared on the oxidized silicon substrate via mechanical exfoliation, as described previously [97]. In brief, single layer graphene supported on poly (methyl methacrylate) (PMMA) layer prepared by wet etching method, was used as a top layer to enclose the solvent (water/ethanol) placed on another few layer graphene or graphite flake prepared on SiO_2/Si substrate. A well-controlled micro-manipulation setup was used to transfer the top layer for successful encapsulation of the solvent. After placing the single layer graphene on top of $2\mu\text{l}$ solvent, most of it was spontaneously squeezed out by leaving only a very small amount in between the top and bottom graphene layers. Overnight drying of the prepared samples at room-temperature led to the gradual evaporation of the solvent which allows the top graphene layer to completely collapse onto the bottom graphene flake with a tiny amount of solvent captured in between. These samples were placed in vacuum (~ 1 mbar) for few hours before removing the PMMA layer using acetone wash. As prepared sandwich samples, containing the water/ethanol filled graphene nanobubbles, were used for atomic force microscope imaging using Bruker Dimension Fastscan AFM operating in peak force tapping mode. In-plane radius of the bubble in this study refers to the base radius measured

⁵VMD

using AFM profile. Height profile is taken across the bubbles by allowing the measuring line to pass through the center of the bubble.

7.3 Results

7.3.1 Van der Waals pressure

The size of a bubble depends on the number of trapped atoms/molecules and the induced hydrostatic pressure inside the bubble is determined by the adhesion forces between the layers forming the bubble [126]. Using membrane theory for round shape bubbles, the hydrostatic pressure and adhesion energy of the graphene bubbles are respectively given by [85]:

$$P_{\text{hyd}} \cong 2.85 \frac{Y h_{\text{max}}^3}{R^4}, \quad \Gamma \cong 1.79 \frac{Y h_{\text{max}}^4}{R^4}, \quad (7.1)$$

where Y , h_{max} and R are respectively the Young's modulus of graphene (340 N m^{-1}), the height, and radius of the bubble (see Section B.1 in Appendix B). For $h_{\text{max}} \sim 1 \text{ nm}$ this results into $P_{\text{hyd}} \approx 1.6 \text{ GPa}$ ($\Gamma \sim 1 \text{ N m}^{-1}$) and 100 MPa ($\Gamma = 0.1 \text{ N m}^{-1}$) for bubbles with radii of $R=5 \text{ nm}$ and $R=10 \text{ nm}$, respectively. The obtained adhesion energy for larger bubbles are in agreement with the previous first-principles calculations [288] and semi-empirical calculations [289]. In fact, the notable elastic properties of monolayer graphene and the strong interfacial adhesion between graphene and the substrate causes the intercalated atoms to be squeezed into extremely small volumes ($R \sim 1\text{-}10 \text{ nm}$) where they can experience a pressure of the order of GPa. Furthermore, nonlinear plate theory modifies Eq. (7.1) as follows: [85]

$$P_{\text{hyd}} \cong 2.56 \frac{Y h_{\text{max}}^3}{R^4} + 64 \frac{\kappa h_{\text{max}}}{R^4}, \quad \Gamma \cong \frac{Y h_{\text{max}}^4}{R^4} + 32 \frac{\kappa h_{\text{max}}^2}{R^4}. \quad (7.2)$$

The second terms in Eq. (7.2) are the contributions of bending energy where $\kappa \cong 0.24 \text{ nN-nm}$ is the bending stiffness of graphene [290]. For $h_{\text{max}} \sim 1 \text{ nm}$ this gives $P \sim 1.42 \text{ GPa}$ ($\Gamma = 0.56 \text{ N m}^{-1}$) and 89 MPa ($\Gamma = 0.035 \text{ N m}^{-1}$) for $R=5 \text{ nm}$ and $R=10 \text{ nm}$, respectively. It is seen that by including the second terms, pressure decreases with about 10% and the adhesion energy with 50-80%. Notice that in Eqs. (7.1) and (7.2) both Y and κ varies slightly with

temperature [291]. It is important to note that for larger h_{\max}/R the contribution of the second terms in Eq. (7.2) become more important [85] (see section B.1).

In common molecular dynamics simulations [122, 126], the pressure is calculated using the virial method which requires a homogeneous system [85, 92]:

$$P_{\text{hyd}} = \frac{1}{V_b} N K_B T + \frac{1}{3V_b} \sum_i \langle \mathbf{r}_i \cdot \mathbf{f}_i \rangle, \quad (7.3)$$

where the first term is the ideal gas pressure and the second term is due to the interatomic potential force (\mathbf{f}_i). In Eq. (7.3), the volume of the trapped substance is taken as independent of temperature. Also, note that the rigid boundaries in common simulations cause inhomogeneous and non-equilibrium conditions which may invalidate Eq. (7.3).

The above drawbacks are overcome using the stress tensor based method [292]: for fluid in equilibrium, the trace of the stress tensor per volume⁶ is balanced by the hydrostatic pressure, i.e. $P_{\text{hyd}} = P_{\text{vdW}}$. Therefore, one can use the following equations to evaluate the density (ρ) and the vdW pressure (P_{vdW}) induced inside a bubble

$$P_{\text{vdW}} = - \left\langle \frac{\text{Tr}(\boldsymbol{\sigma})}{3V_b} \right\rangle, \quad (7.4)$$

$$\rho = \left\langle \frac{Nm_u}{N_A V_b} \right\rangle, \quad (7.5)$$

where $\langle \rangle$ represents a time average over several realizations and $\boldsymbol{\sigma}$, V_b , N , m_u , and N_A are, respectively, the trapped atoms stress tensor in unit of pressure \times volume [292], bump volume, number of trapped atoms, atomic mass, and Avogadro's number. This method will enable us to find the vdW pressure inside nanobubbles that are filled by inhomogeneous substances with different density (see section B.2). We emphasized that the method based on the virial stress tensor is more general than Eqs. (7.1,7.2). The latter originates from elasticity theory with the assumption of a round-shape and using the large bubble limit. Accordingly, it fails in general to describe various bubble shapes such as semi-circular or non-circular in the simulated system.

⁶It is given by

$$\sigma_{\alpha\beta} = \sum_i m_i v_i^\alpha v_i^\beta + \frac{1}{2} \sum_{i \neq j} \mathbf{F}_{ij}^\alpha \mathbf{r}_{ij}^\beta.$$

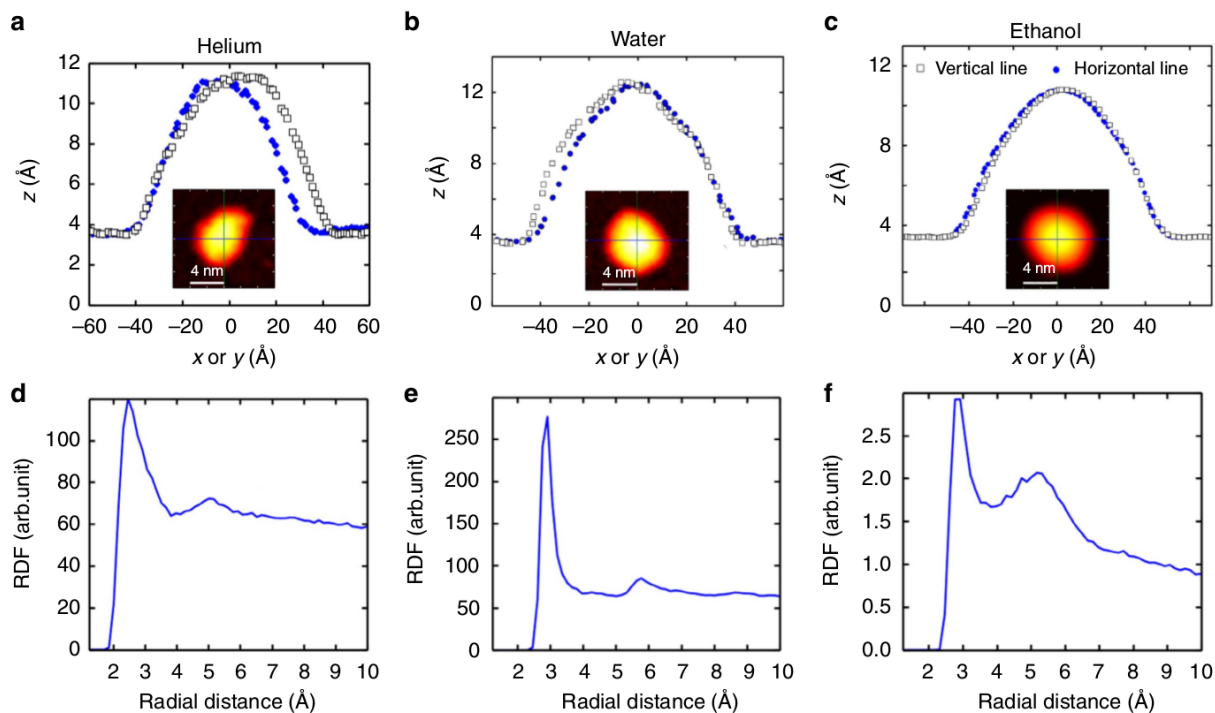


FIGURE 7.2. The cross sections of the graphene nanobubbles filled with (a) helium (b) water (c) ethanol at room temperature. The insets represent the height deformation (which is time dependent). (d) The corresponding radial distribution function of He-He distance of trapped helium and O-O distance of trapped (e) water and (f) ethanol.

7.3.2 Helium bubble

First, we simulate 792 helium atoms below the bumped graphene and found the optimized structure at $T=0$ K. This is equivalent to the previous approach based on elasticity theory [94] where the bump energy was minimized with respect to h_{\max} and R . Subsequently, we increased T up to room temperature, and investigated the spatial structure of the trapped helium atoms. We found that the non-zero temperature results are different from the ground state results (*i.e.* $T=0$). At room temperature, thermal fluctuations occur in the trapped substance while the bottom graphene layer is supported by the substrate and therefore remained fixed. The bubble is found to fluctuate randomly and has in general a non-round shape. The inset of Fig. 7.2(a) shows a typical 2D plot of the bubble filled by helium and the height profiles

are shown along the two cross-sections are shown in Fig. 7.2(a). This figure is a single snapshot of the bubble at a particular time. Based on the MD simulations, we concluded that He forms a non-circular bubble.

Using lateral radial distribution function along the direction perpendicular to the substrate (z -axis) [218] we found a second peak, see Fig. 7.2(d), indicating that the trapped helium has a relatively long range ordering at room temperature and it exhibits denser phase respect to its gas phase. These results are comparable with the experimentally obtained scanning tunneling microscopy image for graphene nanobubble filled by argon [293]. We do not expect differences between He and Ar. We found that trapped helium behaves highly fluidic. The structure of the bump continuously changes due to thermal fluctuations and the helium bubble diffuses randomly over the graphene substrate.

In order to obtain further insight in the arrangement of the He atoms, we evaluated the density profile of trapped helium along the z -axis (see Fig. 7.3(a)). At 0 K, three peaks are observed at 2.75, 4.85, and 7.25 Å indicating a well defined layered structure (i.e. the solid phase of helium). The inset shows the RDF of each layer at 0 K indicating the same crystal structure in each layer. At room temperature, there is only a single peak (2.70 Å) representative for a single He wetting layer close to the bottom graphene layer and a disordered arrangement of He atoms above it. It is worthwhile to mention that for a He bubble at 0 K, we found a layered structure and the corresponding microscopic structure confirms the well known hexagonal close-packed (hcp) lattice structure of helium at 0 K which is consistent with the results reported by Hodgdon *et al.* [293, 294].

Using Eqs. (7.4,7.5) the density of trapped helium at room temperature and corresponding induced pressure are estimated to be 0.225 gr cm^{-3} and 0.65 GPa, respectively. Notice Eq. (7.2) overestimates the pressure, i.e. using h_{max} and R are given in Table 7.1, $P_{\text{hyd}} = 1.25 \text{ GPa}$. The latter difference is due to the non-round shape of the helium bubble. The obtained fluid helium density is comparable with experimental results (0.28 gr cm^{-3}) where a non-linear increase of the fluid helium density was measured up to a pressure of 2 GPa at room temperature [280]. We found that the pressure within the

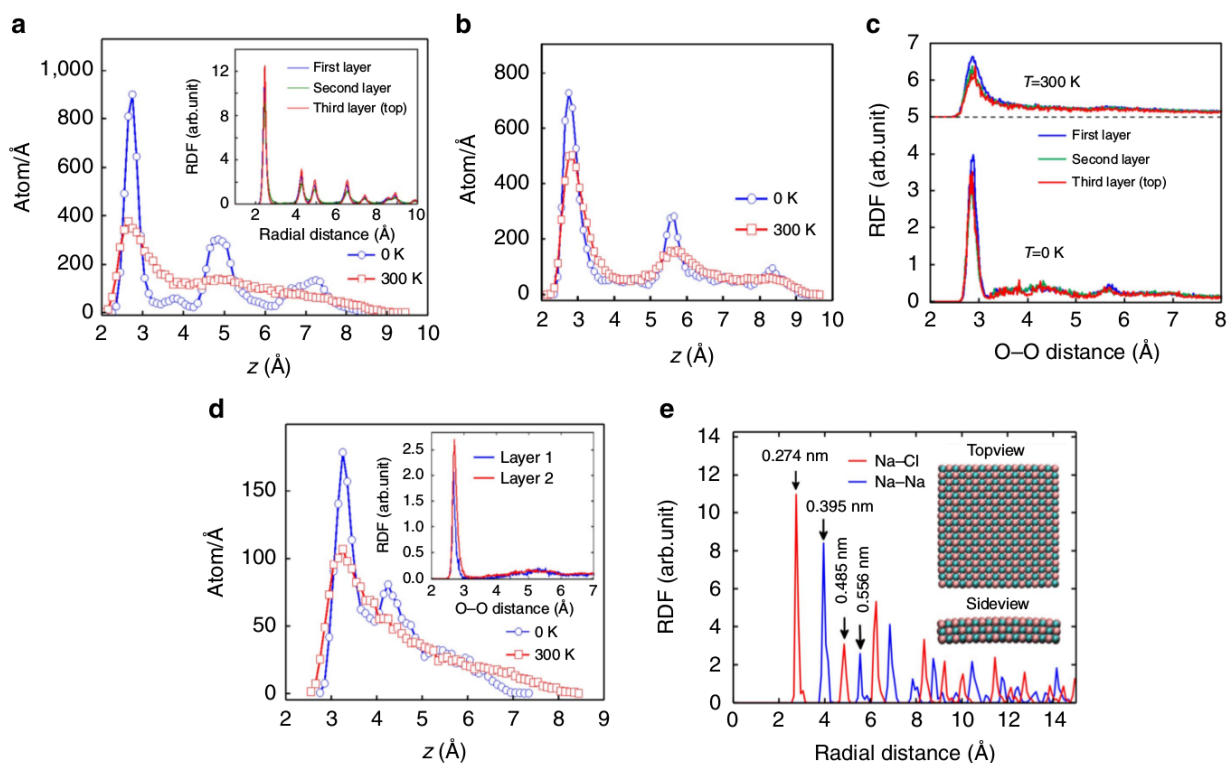


FIGURE 7.3. (a) The density of the trapped helium along z -direction for 0K and 300K. The inset represents RDF of each individual layer of trapped helium at $T=0$ from bottom to top. (b) Density profile of the oxygen atoms of trapped water along the z -axis at zero and room temperature. (c) Corresponding radial distribution function of O-O distance for the three layers of water at 0 K and 300 K. The RDF at room temperature is shifted by 5\AA . (d) Density profile of the oxygen atoms from trapped ethanol for zero and room temperature. The inset shows the oxygen radial distribution for the first two layers at $T=0$. (f) MD predicted partial Na-Na and Na-Cl radial distribution function of encapsulated square NaCl at 0 K. The inset shows corresponding side and top views of the bubble. The simulated graphene top and bottom flake are not shown.

nanobubble increases with temperature due to the increasing kinetic energy contribution to the stress [292]. The latter is consistent with recently reported results using a hydrothermal anvil cell made of graphene nanobubbles on diamond [276] and with the high-pressure chemistry in the graphene bubble by monitoring the conformational change of pressure-sensitive molecules [96].

7.3.3 Water bubble

Water is a polar liquid with a hydrogen bond network. We theoretically predicted previously the square-rhombic lattice structure for monolayer ice confined between graphene layers [278]. Here, we trapped 792 water molecules below the bump and report room temperature results. We found that the water bubble is immobile even when temperature fluctuations are present. The fluidity of water under the graphene flake is less than that of helium. A typical 2D-plot of the deformation of graphene is shown in the inset of Fig. 7.2(b). The corresponding profiles along the x- and y-directions and the RDF are given in Figs. 7.2(b,e), respectively. The first peak in Fig. 7.2(e) corresponds to an O-O distance of 2.8 Å which is consistent with results from neutron diffraction spectroscopy [279]. Notice that there is a second peak in the RDF, and therefore water has weak long-range ordering and exhibits a rather amorphous structure. Next, we considered larger bubbles and compare them with typical bubbles measured in the experiment. In Figs. 7.4(a,b), we depict an AFM image of a water bubble and corresponding profiles along two perpendicular lines. We performed extensive simulations for larger water bubbles having an average in-plane radius of 18 nm. The result is presented in Fig. 7.4(c) and corresponding profiles along the two perpendicular lines are shown in Fig. 7.4(d). Although the size of the experimental bubble is larger than the simulated sample, both the AFM image and MD results confirm the non-round shape of the water bubble (more AFM images for water bubbles are presented in section B.4).

Figure 7.3(b) shows the density profile of the oxygen atoms along the z -direction at two different temperatures 0 K and 300 K. At the zero temperature, the trapped water molecules have a layered structure, *i.e.* it shows three layers which are located at $z=2.76$, 5.66, and 8.36 Å. Surprisingly, confined water preserves its layered structure even at room temperature representing the amorphous-solid for trapped water. The corresponding peaks are located at 2.82, 5.76, and 8.65 Å. At higher temperature, the inter-larger distance becomes larger. The density and the induced vdW pressure are estimated to be $\rho=1.03 \text{ gr cm}^{-3}$ and $P_{\text{vdW}}=0.93 \text{ GPa}$. Again, due to the non-round shaped water bubble Eq. (7.2) overestimates the pressure, *i.e.* $P_{\text{hyd}} = 1.4 \text{ GPa}$. The present

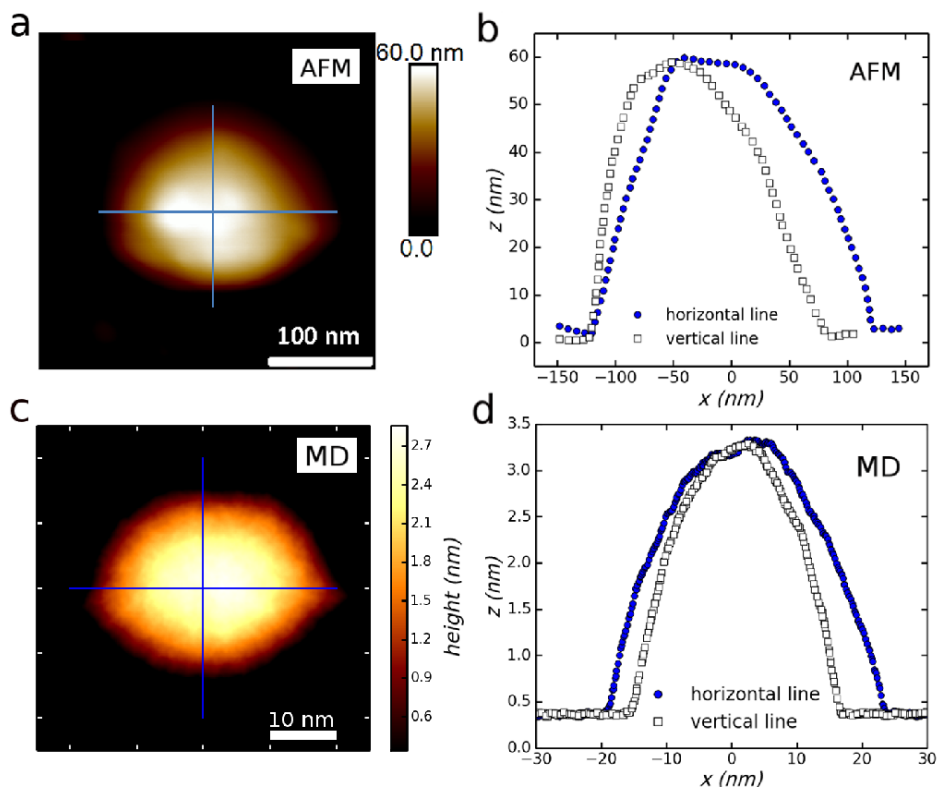


FIGURE 7.4. (a) Atomic force microscopy (AFM) image of water bubble and (b) the corresponding profiles along two lines. (c) The MD results for water bubble having $R = 18$ nm and (d) two corresponding profiles along two perpendicular directions.

study on the size effect shows the limitation of Eq. (7.2), see Section 7.3.8.

A wide range of stable amorphous ice structures are possible due to the adaptability of perturbations in hydrogen bond networks between the water molecules. All water layers exhibit a similar microscopic structure at room temperature which can be seen from Fig. 7.3(c) where we show the RDF's of the O-O distance for each individual layer for both 0 K and 300 K. In Fig. 7.3(c), notice that the water bubble at room temperature is less ordered as compared to the 0 K. A square-rhombic structure is found only at the bottom layer of confined water where $T=0$ K. However, the top layers do not show any signs of the square ice structure and are less ordered than the bottom layer. In contrast to Ref. [122], we argue that the density and size of water bubbles are important factors that control the microscopic structure of trapped water which was not considered in other theoretical works [125].

7.3.4 Hydrocarbon bubble: Ethanol and Hexadecane

It is noteworthy to look at the microscopic structure of trapped hydrocarbons. We found very good agreement between the MD results for bubbles filled with small hydrocarbons, the predictions from the elasticity theory (Eqs. (7.1,7.2)), and AFM measurements. As an example, we simulated 200 trapped ethanol molecules. At room temperature, the average shape was found to be circular. In Fig. 7.5(c), we show a 2D-plot of the bump (inset) and its profile across indicated lines. The RDF of O-O shown in Fig. 7.2(f) indicates that trapped ethanol is in the liquid phase. The estimated density and pressure are $\rho=0.987 \text{ gr cm}^{-3}$ and $P_{\text{vdW}}=0.49 \text{ GPa}$, respectively. This is consistent with the fact that ethanol crystallizes for pressures around 1.5 GPa [295]. Using the numbers given in Table I, Eq. (7.2) gives $P_{\text{hyd}} = 0.5 \text{ GPa}$ which is in very good agreement with the MD results that is due to the round shape of the bubble. Therefore, the experimental nanobubbles reported in Ref.[94] are more likely to be filled by hydrocarbon (ethanol, methanol and other small hydrocarbons) contaminants rather than water or rare gases. The results are qualitatively in agreement with the experimentally reported liquid phase of bulk ethanol under 1 GPa pressure using dielectric spectroscopy [295].

In Figs. 7.5(a,b) we depict an AFM image of a hydrocarbon filled bubble (likely filled by small hydrocarbons) and corresponding profiles along two perpendicular lines. Raman spectroscopy as characterization technique confirms the presence of trapped ethanol (see section B.3). In Figs. 7.5(c,d) the MD results for a larger ethanol bubble is shown ($R \sim 15 \text{ nm}$). Again, the size of the bubble is larger than the simulated sample, however, the AFM images show a round shape with in-plane circular symmetry in agreement with the MD. More AFM images for hydrocarbon bubbles are presented in section B.4.

In Fig. 7.3(d), we show the density profile of the oxygen atoms of trapped ethanol for both zero and room temperature. Peaks at 3.4, 4.2 and 5.6 Å indicate that at 0 K trapped ethanol has a layered structure. The inset shows similar pronounced peaks of the RDF of the two first layers indicating that they have similar ordering. As temperature increases, only a single wetting layer next to the substrate is formed [295].

Next, we performed additional simulations using large hydrocarbons, *i.e.*

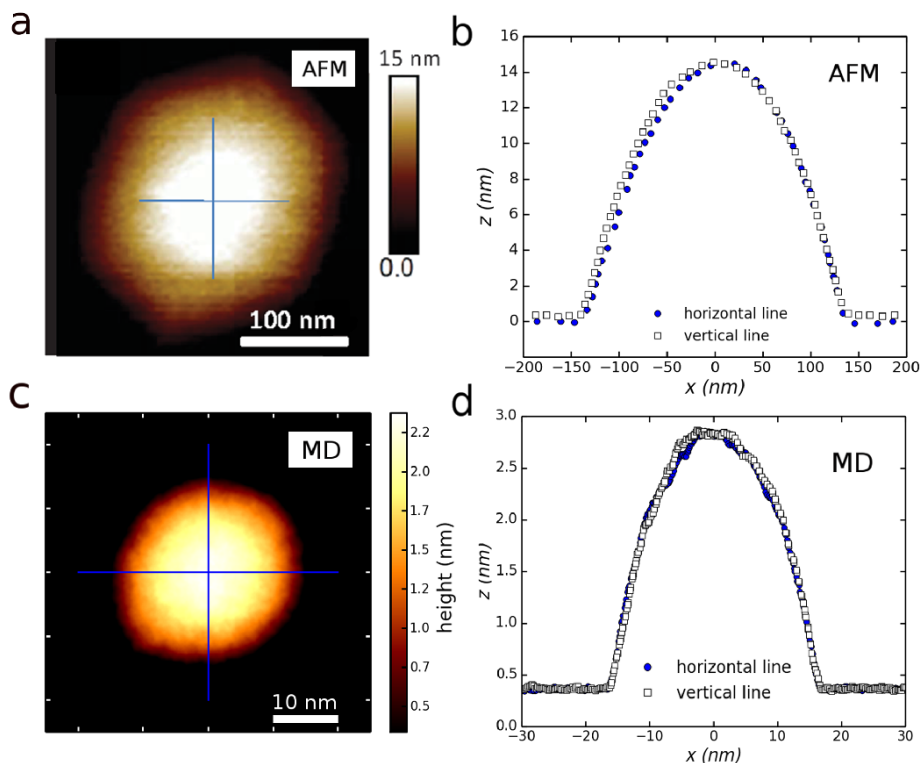


FIGURE 7.5. (a) Atomic force microscopy (AFM) image of a hydrocarbon bubble and (b) the corresponding profiles along two lines. (c) The MD results for larger ethanol bubble having size of 15 nm and (d) two corresponding profiles along two perpendicular lines.

$C_{16}H_{34}$ known as hexadecane. We captured 160 molecules and optimized the structure. We found that they tend to be aligned with each other and form a bubble with a larger flat area. In Fig. 7.6, we compared the MD predicted height profile of helium, ethanol, water, and hexadecane (long hydrocarbon) at room temperature. In the molecular dynamics simulations without residual strain in graphene, small hydrocarbon molecules (ethanol) always form round shape bubbles with in-plane circular symmetry and water forms non-round shape bubbles while large linear molecules are arranged in a crystalline-like structure (i.e. being aligned) and form a bubble. There is a flat region on top of the hexadecane bubble.

In Table 7.1, we report geometrical properties such as the bump radius (R), maximum height (h_{\max}), and aspect ratio (h_{\max}/R) for the studied small nanosize bubbles ($R < 10$ nm). We obtained h_{\max}/R values between 0.17 and 0.20 which is larger than the experimentally reported value of 0.11 for large

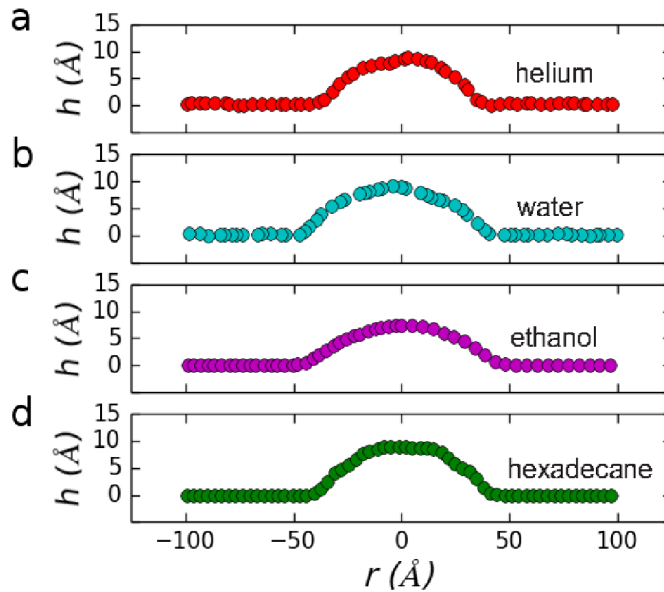


FIGURE 7.6. MD predicted height profile for helium (a), (b) ethanol, (c) water, and (d) hexadecane (long hydrocarbon) at room temperature. The latter forms a bubble with larger flat area at the top of the bubble in contrast to the other substances.

TABLE 7.1. The radius, maximum height (h_{\max}), h_{\max}/R ratios, pressure and corresponding densities for trapped and bulk helium, water, and ethanol at room temperature (MD).

Trapped substance	$R(\text{nm})$	$h_{\max}(\text{nm})$	h_{\max}/R	P_{vdW} (GPa) bubble	ρ (gr cm^{-3}) bubble	ρ (gr cm^{-3}) bulk	ρ (gr cm^{-3}) bulk, P=1 atm
Helium	4.5	0.83	0.18	0.65	0.225	0.283 (P=0.65GPa)	0.004
Water	4.6	0.90	0.20	0.93	1.103	1.191 (P=0.93GPa)	1.044
Ethanol	5.4	0.78	0.14	0.49	0.987	1.051 (P=0.49GPa)	0.862

bubbles ($R > 10\text{nm}$) and it is in agreement with the experimental results on small size bubbles. [94] Therefore, in agreement with the experimental results of Ref. [94] the universal scaling (i.e. $h_{\max}/R \cong 0.1$) is not applicable for small size bubbles ($R < 5\text{ nm}$).

We compared the density of trapped materials with those for bulk helium, water, and ethanol at room temperature at two different pressures and listed the results in Table 7.1. The density of encapsulated ethanol is larger than that for bulk at normal conditions. This is additional support for the high vdW pressures present inside the nanosize graphene bubble. We studied the deformation profiles of the graphene sheet. For small bubbles, it is found that

it can be fitted by a polynomial function (see Figs. B.4(a-c)) which does not necessarily follows the universal scaling law [94].

7.3.5 Stress calculations

Here, we study the radial and circumferential components of the stress tensor ($\sigma_{rr}, \sigma_{\theta\theta}$) of the top graphene sheet for ethanol bubbles and found very good agreement with those predicted by membrane theory. [85]. In Fig. 7.7, we present the average σ_{rr} and $\sigma_{\theta\theta}$ as a function of radius obtained from the MD simulation for an ethanol bubble (radius ~ 4 nm) at 0 K. Stress components and radii are scaled to the maximum stress and bubble radius (R), respectively:

$$\tilde{\sigma}_{rr} = \sigma_{rr}/\sigma_{rr}^{\max}, \quad \tilde{\sigma}_{\theta\theta} = \sigma_{\theta\theta}/\sigma_{\theta\theta}^{\max}, \quad x = r/R \quad (7.6)$$

The solid back curves in Fig. 7.7 are prediction from elasticity theory (see section B.1). We found that only for ethanol elasticity theory provides good fits of the MD data. Using the non-linear plate model [85], the σ_{rr} and $\sigma_{\theta\theta}$ stress components can be determined from $f_{\sigma}(x)$ which is a polynomial function of the radius ($x < 1$) given by

$$f_{\sigma}(x) = 1 + Ax + Bx^2 + Cx^4 \quad (7.7)$$

The quality factor⁷ for two sets of fitting parameters of $f_{\sigma_{rr}}(x)$ and $f_{\sigma_{\theta\theta}}(x)$ results in the values of 0.994 and 0.987, respectively (see Table B.1). The inset of Fig. 7.7 shows the stress distribution of the carbon atoms of the top graphene sheet for the ethanol bubble at 0 K. The coloring is based on the value of J_2 [296] which is determined by

$$J_2 = \frac{1}{6}[(\sigma_{xx} - \sigma_{yy})^2 + (\sigma_{xx} - \sigma_{zz})^2 + (\sigma_{yy} - \sigma_{zz})^2 + 6(\sigma_{xy}^2 + \sigma_{xz}^2 + \sigma_{yz}^2)]. \quad (7.8)$$

7.3.6 Salt (NaCl) bubble

As an example of a very different material, we simulated 1000 NaCl molecules with four different initial nanocrystal shapes *i.e.* round, triangular, ellipsoid,

⁷It is defined as $Q = 1 - \sqrt{\frac{1}{N} \sum_{i=1}^N (\sigma_i - f_{\sigma}(x_i))^2}$.

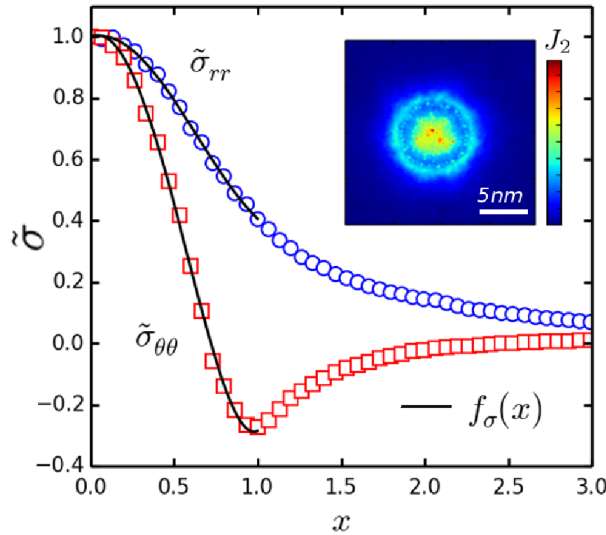


FIGURE 7.7. MD predicted radial ($\tilde{\sigma}_{rr}$) and circumferential ($\tilde{\sigma}_{\theta\theta}$) stress components of an optimized ethanol bubble ($R \sim 4$ nm) as a function of normalized radial distance (x) at 0K. The results can be fitted by a polynomial function $f_{\sigma}(x)$ within the region of bubble ($x < 1$). Inset shows the corresponding stress distribution based on the value of J_2 (Eq. (7.8)).

and square. We found that the encapsulated NaCl nanocrystals keep their cubic structure. This may be relevant to Ref. [126] that proposed that the reported experimental data on square ice [125] can be better explained by NaCl contaminants that are precipitated as nanocrystals in the dried-out graphene liquid cells. The deformation of the top graphene flake with four different initial shapes (round, triangular, ellipsoidal and square) are shown in Fig. 7.8(a). The crystal will adapt the shape of graphene by forming rough surfaces. In all cases optimized shapes remain unchanged even under high vdW pressure between the graphene cover and the substrate. This is in contrast to the minimized configuration for trapped helium, water, and hydrocarbons, regardless of their initial configurations of the molecules result always in semi-circular bump shapes. The corresponding height-profile along horizontal and vertical lines, as indicated in Fig. 7.8(a), are respectively shown in Figs. 7.8(b,c). We found that by increasing the size of the initial NaCl crystal (which contains a larger flat side) in the x-y plane, the flat region in the formed bubble increases. Such flat bubbles were found in Ref. [125] further supporting the proposal

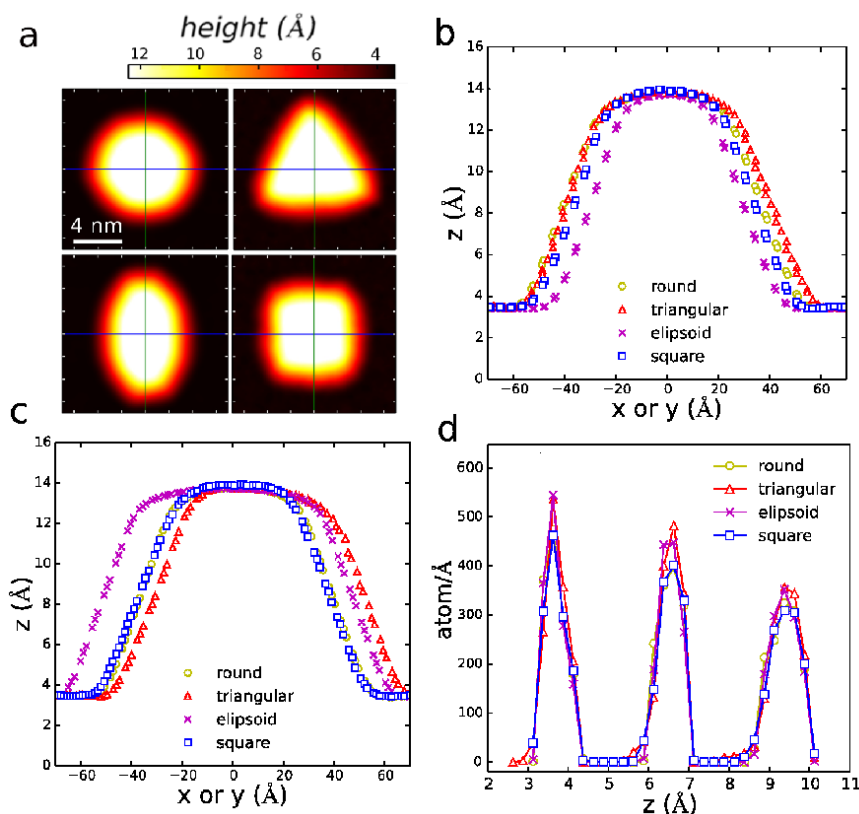


FIGURE 7.8. (a) 2D-plot of height profiles of graphene nanobubbles filled with NaCl for four different initial configurations: round, triangular, ellipsoid, and square shape at $T=0\text{K}$. The height profile of corresponding cross sections along indicated horizontal (b) and vertical (c) lines in (a). (d) The density profile of Na/Cl atoms along z -axis for the four NaCl bumps.

made in Ref. [126]. Although the resistance of the NaCl crystal against the lateral pressure induced by the graphene flake might be as expected, our calculations, reveal the atomistic details for this phenomena. In Fig. 7.8(d), we depict the density profile of the simulated square shaped NaCl bump along the z -direction. The height of the peaks and their distance ($\sim 2.9\text{Å}$) correspond to the cubic crystalline structure of NaCl which is not influenced by the vdW pressure in the nanocapillary. The inset of Fig. 7.3(e) depicts side and top views of the minimized encapsulated sample of square NaCl at 0 K. We calculated the partial radial distribution function (RDF) of the Na-Na and Na-Cl distance and show it in Fig. 7.3(e). The first peak appears at 2.74Å which is very close to the reported structure in Ref. [126], *i.e.* 2.8Å . The presence of many peaks is an indication of the crystalline structure of

encapsulated NaCl which can be accurately approximated by its original cubic-structure. By increasing temperature up to room temperature, we found almost the same RDF indicating that the solid phase of NaCl is preserved at room temperature (results are not shown here). We attribute this to the large bulk modulus (24.42 GPa), Young's modulus (~ 40 GPa) and shear modulus (~ 12.6 GPa) of the NaCl crystal [285, 297] which is larger than the pressure inside the nanocapillary (1-2 GPa). The higher elastic modulus of the NaCl crystal results in the final cubic structure. The latter originates in the strong ionic bond between Na and Cl which is ~ 1000 kJ mol $^{-1}$, two orders of magnitude larger than the hydrogen bond, *i.e.* 10 kJ mol $^{-1}$ in ice.

7.3.7 Layered structure

The aim of this section is to provide a closer look into the structure of the trapped materials inside the bubble and elaborate on their layered structure. It is important to note that different bubbles (helium, water, and ethanol), regardless of their size and/or type, have perfectly optimized round shapes at zero temperature. Even at higher temperature as the bubble gets smaller, it attains a more round-like shape. This is the reason why we obtained a non-circular shape for the large water bubble in agreement with AFM experiment (Fig. 7.4), while it is semi-circular for small bubble size (see Fig. 7.6). As an extreme example, we do not expect the non-round shape of a water bubble filled with too few numbers of water molecules due to the lack of sufficient H-bonds. Figure 7.9(a) presents the radial distribution function of He-He atoms for bulk and trapped helium at room temperature. The two RDFs are very close together which supports the presence of pressures of order GPa inside the nanosize helium bubble. Different views of the layered structure of trapped helium at zero temperature are presented in the inset of Fig. 7.9(a). For larger helium bubbles, the MD results in the hcp structure of encapsulated helium. However, at the higher temperature, such a hcp lattice and the layered structure no longer exist (see Fig. 7.3(a) where different colors indicate different trapped material layers).

Figure 7.9(b) shows RDF of bulk and trapped water subjected to the same pressure 0.9 GPa at 300K (see Table 7.1). The presence of the second peak and

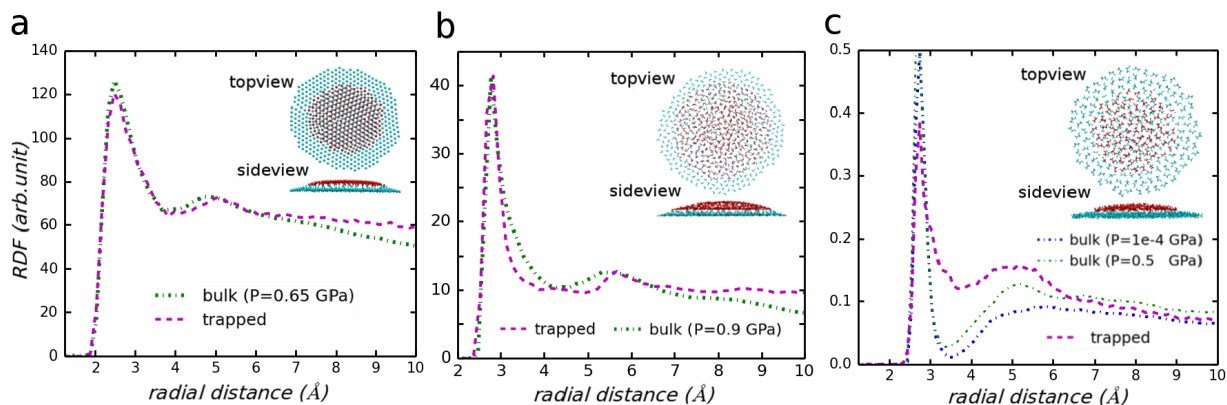


FIGURE 7.9. The RDF of trapped and bulk (a) helium (b) water (c) ethanol subjected to the same amount of pressure at room temperature (see Table 7.1). Each inset shows top and side views of corresponding trapped substances. The cyan and red balls represent the two different layers (graphene top layer and the graphene substrate are not shown here).

the resemblance of the two RDFs indicates that the entire structure of water inside the bubble does not resemble a solid phase. The top and side views of the formed layers at 0 K, shown in the inset of Fig. 7.9(b), clearly demonstrate the layered structure of water. Similarly, the first and the second layer are indicated by different colors. It can be seen from the figure that the bottom layer of water has likely an ordered structure due to the high confinement, however upper layers have an amorphous structure. At low temperature, our simulation predicts that water bubble has a more round shape.

Finally, Fig. 7.9(c) shows the radial distribution function of O-O atoms for bulk and trapped ethanol for two values of pressure (1 atm and 0.5 GPa) at room temperature. For bulk, the second peak becomes pronounced when we increase pressure (see Table 7.1). This indicates that encapsulation induces high pressure inside the ethanol bubble. The top and side views of the layered structure of trapped ethanol at 0 K are shown in the inset of Fig. 7.9(c). The first and second layer are plotted in different colors. The ethanol bubble has a perfect round shape with distinguishable layers. The latter is due to the interaction with the substrate.

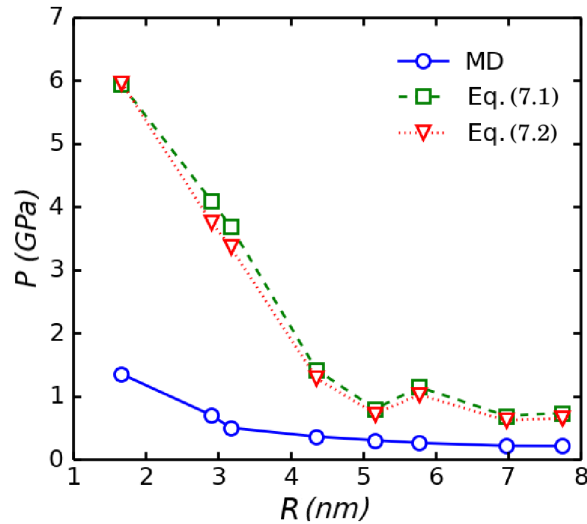


FIGURE 7.10. Calculated pressure by MD (Eq. (7.4)) and elasticity theory for ethanol bubble as a function of radius. Eqs. (7.1) and (7.2) are from the membrane and the nonlinear plate models, respectively.

7.3.8 Size effects

The size of the bubble which is determined by the amount of trapped material has an impact on the physical properties of the bubble such as the density, the induced pressure, and the layered structure. To investigate this effect, we carried out different simulations in order to compare P_{vdW} and ρ obtained from MD and elasticity theory. Figure 7.10 shows the calculated pressure versus the radius of the ethanol bubble. The predicted pressure is calculated through the stress tensor (Eq. (7.4)) and elasticity theory (Eqs. (7.1) and (7.2)). As can be seen, for the small radius ($R < 4$ nm) the latter overestimates the pressure inside the bubble while for a larger bubble radius the two approaches result in the same pressure. We believe that the simulated bubble would converge to the predicted pressure as obtained from elasticity theory in the limit of a large bubble. However, for a small bubble both membrane and nonlinear plate models predict unrealistic extremely high pressures. Note that barely noticeable difference between the two models is due to the small contribution of the bending rigidity (κ) to the elastic energy of graphene beyond the length scale of 4 \AA (see Figs. B.5(a,b)).

7.4 Discussion

We presented an extensive atomistic molecular dynamics simulation study to probe the van der Waals (vdW) pressure at atomically smooth graphene interfaces by intentional trapping different types of materials (water, gas, hydrocarbons, and salt). The correlation between the shape of the graphene bubble and the physical properties of the trapped substances were pointed out. Temperature and concentration of trapped material have a strong influence on the bubble formation. The detailed simulations coupled with the experimental observations provide insightful information about the formation of bubbles (including flat nanobubbles) and the effect of vdW pressure on the structural and conformational changes of the trapped substance.

We found that the bump shape and height depend on the thickness and elastic properties as well as on the specific trapped molecules. Experimental investigations on the geometrical and physical properties of graphene bubbles filled with different substances have motivated us to perform extensive atomistic simulations to determine the microscopic structure of the trapped substances and the corresponding deformation of the graphene flake. We tested five different substances namely, helium, water, ethanol, hexadecane and NaCl inside the graphene nanobubble with an effective radius smaller than 10 nm using appropriate interatomic potentials. Significant differences in the microscopic details of the bubbles were found for different encapsulated substances. Trapped helium behaves like a liquid with the highest degree of fluidity subjected to a pressure of 0.65 GPa, while NaCl is very rigid and resists against pressures of order GPa and forms a flat-like bubble in contrast to the bubbles found for helium, water, and ethanol. On the other hand, helium exhibits a layered structure only at low temperature while water and ethanol preserve their layered structure even at room temperature. The deformed graphene over NaCl follows the shape of the NaCl crystal, except if it is in solution. An amorphous and layered structure of water was found even when subjected to 0.93 GPa pressure at room temperature. The water nanobubbles do not have a perfect round shape. Ethanol behaves like a liquid at room temperature, while it forms an amorphous solid at 0 K. The deformation profile for bubbles filled by hydrocarbons (ethanol) are more relevant to

the AFM images and the recently reported graphene nanobubbles [94] and the corresponding pressures can be obtained using elasticity theory. Long hydrocarbons, *i.e.* hexadecane, form a flat-like bubble at 0 K and 300 K. The pressure inside the bubble can be tuned by changing the adhesion energy which results in an ordered phase of the trapped substance (*i.e.* amorphous-ice in case of water).

We found that boundary stress on the graphene flake results in the formation of wrinkles and removes the round shape of the water nanobubbles (see Figs. B.6(a,b)). By observing the shape of the bubble it should be possible to obtain information about the physical and chemical changes that may occur in nano-enclosures under the influence of high pressure and different temperatures [298, 299]. As mentioned in a previous report [97], Raman spectroscopic measurements on nanobubbles have clearly shown that a small amount of strain develops in the graphene flake depending on the height of the bubbles. For example, the strain developed in graphene for a bubble of height 60 nm is ~ 0.7 . Moreover, we have shown that even by increasing the adhesion energy between two graphene sheets, which is equivalent to increasing the vdW pressure, a more ordered structure for water is obtained while the square ice structure and its stacking structure cannot be seen (see section B.8 in Appendix B). We found that the bubbles filled with small hydrocarbons can be reasonably well described by elasticity theory in contrast to the other investigated material materials and are therefore suitable test materials for studies of elasticity theory.

Furthermore, there are also various accurate force fields available for hydrocarbons which allow to simulate them accurately using MD simulations. The microscopic structure of trapped water and ethanol are very different, *e.g.* the RDF of bulk ethanol and trapped ethanol are very different than that of water. The latter is due to the different distribution of H-bonds in ethanol. Finally, we concluded that previously proposed universal scaling law of height and radius of bubbles is limited to round shape bubbles such as found for graphene bubbles filled with hydrocarbons. But, such a scaling law is not generally applicable for any bubble type. As an extreme case, a bubble filled with NaCl does not follow the universal scaling law found in

Ref. [94]. This study provides fundamental insights into the formation of graphene nanobubbles and the effect of the microscopic details of the trapped substances in it.

NANOCONFINED WATER IN GRAPHENE OXIDE CAPILLARIES

Permeation of water between neighboring graphene oxide (GO) flakes, *i.e.* 2D-nanochannels, are investigated using a simple model for the GO membrane. We simulate the hydrophilic behavior of nanocapillaries and study the effect of surface charge on the dynamical properties of water flow and the influence of Na^+ and Cl^- ions on water permeation. Our approach is based on extensive equilibrium molecular dynamics simulations to obtain a better understanding of water permeation through charged nanochannels in the presence of ions. For example, we showed a significant change in the slippage dynamics of confined water such as a profound increase in viscosity/slip length with increasing charges over the surface. The slip length decreases one order of magnitude (*i.e.* 1/30) with increasing density of surface charge, while it increases by a factor of 2 with ion concentration. We found that commensurability induced by nanoconfinement plays an important role in the intrinsic dynamical properties of water such as diffusion and friction coefficients.

This work is published as: H. Ghorbanfekr-Kalashami, M. Neek-Amal, and F. M. Peeters, “Slippage dynamics of confined water in graphene oxide capillaries”, *Physical Review Materials* **2**, 074004 (2018). As the first author, I performed all MD simulations and contributed to the scientific interpretation of the results and in the writing of the manuscript.

8.1 Introduction

Nanocapillaries play an important role in the design of materials for filtration and separation because of their unusual fundamental behaviour arising at the molecular scale [110, 111]. Stacked graphene oxide (GO) sheets are the oxidized form of hydrophilic graphene nanosheets with a high density of oxygen containing functional groups (*e.g.* hydroxyl, carboxyl, carbonyl, and epoxy groups). Individual GO flakes are exfoliated by dissolving GO in water with the help of ultrasonication and bulk residues. The space between the neighboring GO flakes creates 2D-nanochannels that may allow water to pass through while rejecting the flow of contaminants. The ultrafast permeation of water through GO membranes has led to a large interest in the development of nanofiltration membranes. Nair, *et al.* observed that sub-micrometer-thick GO membrane can be completely impermeable to liquids, vapors, and gases, including helium, whereas it allows unimpeded permeation of water [2]. This is very promising for water desalination and gas selection applications, and for experimental and theoretical studies of nanofluidics [300]. The nanoscale GO membranes can be used to achieve accurate and tunable ion sieving [6]. Numerous studies based on molecular dynamics (MD) simulations identified key factors that affect transport through nanocapillaries [110–112]: the breakdown of uniform water density; the water-solid wall slip length which is found to be much larger than capillary sizes; dynamical properties different from bulk, *etc.* Despite recent progress, the molecular mechanisms underlying the diffusion of water in charged porous media (hydrophilic materials) and the interplay between the effects of a charged surface and ions are not understood so far.

The behavior of Na^+ and Cl^- ions in bulk water or at the interface of hydrophobic/hydrophilic media was widely investigated in recent works [4]. However, a few studies have addressed the effect of the concentration of ions on the dynamical properties of water in charged nanocapillaries [113]. Determining the slip length of water permeating through GO membranes is urgently needed because it will be helpful to understand the flow through nanocapillaries as mentioned in recent experimental studies [2, 106, 300–303]. In fact, the slip length ($L = \eta/\xi$) is a crucial parameter that determines

water flow within nanochannels. Despite many reports on the slip length for hydrophobic surfaces [304], there are very few reports on the slip length over hydrophilic surfaces or charged surfaces. For instance Wei *et al.* reported two orders of magnitude reduction of the slip length of water in the presence of chemical functionalization and nanoconfinement in graphene oxides [305].

Here, we study systemically the influence of ion concentration and surface charge on the dynamical properties of confined water and elucidate the influence of capillary size. In particular, a mixture of H_2O , Na^+ and Cl^- inside a nanocapillary made of graphene layers will be investigated. We found a significant change in the water slip length versus surface charge while the ion concentration has much less influence on it. The charge distribution over graphene sheets mimics the microscopic nature of a GO membrane (see Fig. C(a)). The distributed charge plays the role of functional groups in graphene oxide. In the Appendix C, we showed the consistency of this simple model. In fact, such model can be promising because it ignores unnecessary details and reduces the complexity while allowing to reproduce the essential physical features. In particular, commensurability effects result in clear oscillations in the dynamical properties of confined water which highlight the importance of accurate size control of the nanocapillaries.

8.2 Model and methods

The continuum hypothesis relying on the Navier-Stokes equation breaks down when the length scale of the nanofluidic system approaches the molecular scale. Since fluids are composed of molecules, one approach will be to calculate dynamical properties through directly considering the motion of the molecules. Molecular dynamics simulations is a standard tool to investigate nanofluidics at molecular scales because it enables us to study molecular details of fluid flow (*e.g.* nanofluidics). The employed methodology and models are suitable to allow MD simulations of nanoconfined water in the range of nanoseconds which are reliable enough to reproduce the relevant effects related to water permeation through nanocapillaries.

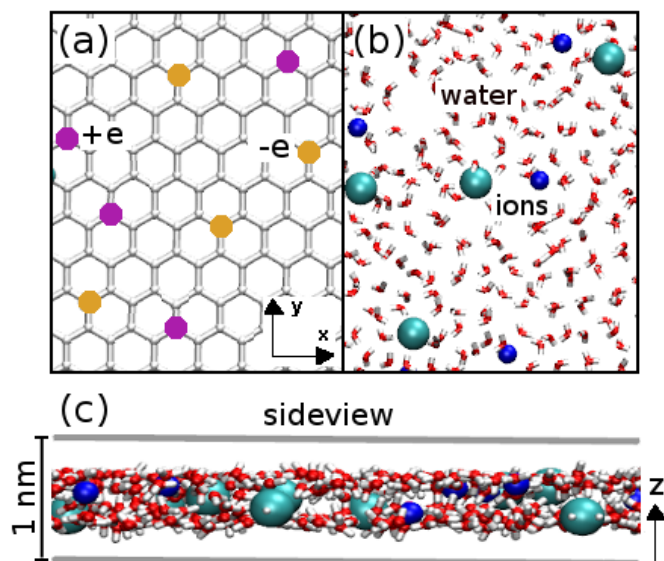


FIGURE 8.1. The surface charge distribution over a graphene layer (a). Top (b) and side (c) view snapshots of ions (cyan and blue balls) mixture in water (red and white molecules) confined between a graphene capillary (gray lines). Periodic boundary conditions are employed in x and y directions and confinement was along the z -axis.

8.2.1 MD simulations

Using the LAMMPS software package [253], we investigated the impact of surface charges in the confining walls and ion hydration on the dynamical properties (*i.e.* diffusion, viscosity, and friction coefficient) of water confined inside graphene capillaries. The simulated system contains two layers of graphene each with 680 carbons, *i.e.* the configuration unit cell has dimensions 42 \AA (l_x) \times 43 \AA (l_y). The number of water molecules varies between 180 to 4640 depending on the interlayer separation h , *i.e.* capillary size. In order to add ions to the system, every two randomly selected H_2O molecules are replaced by an Na^+ and Cl^- ion, keeping the total net charge of the system zero. The graphene layers were fixed at their positions. The SPC/E model was employed to describe the water molecules [192].

The particles interact via Lennard-Jones (LJ) pair potentials using $\epsilon_{\text{C}}=0.071224 \text{ kcal mol}^{-1}$, $\sigma_{\text{C}}=3.41 \text{ \AA}$, $\epsilon_{\text{Na}^+}=0.130019 \text{ kcal mol}^{-1}$, $\sigma_{\text{Na}^+}=2.35 \text{ \AA}$, $\epsilon_{\text{Cl}^-}=0.100143 \text{ kcal mol}^{-1}$, and $\sigma_{\text{Cl}^-}=4.40 \text{ \AA}$, and cross LJ potential parameters were obtained

by the Lorentz-Berthelot combining rules [234, 306].

The cut-off radius for the LJ potential was chosen at 10 \AA . The NVT ensemble (Nose-Hoover thermostat) is used to keep the temperature at 300 K. Periodic boundary conditions are employed along x , y directions and the confinement was along the z -axis. The particle-particle particle-mesh method was used to compute the long-range Coulomb interaction with a relative accuracy of 10^{-4} . Water bonds and angle was fixed by the SHAKE algorithm [307]. In all cases, the total density of water and ions was kept fixed at 1 g cm^{-3} and a timestep of 1 fs was chosen. After relaxing the system for 1 ns, the thermodynamical sampling was done for 5 ns to ensure the smoothness of the correlation function and to realize convergence to zero for large t . The volume of the capillary is defined by $l_x l_y \times (h - \sigma_{\text{C-O}})$. Here $\sigma_{\text{C-O}}$ is subtracted to exclude the effective graphene inter-layer distance of carbon-oxygen, *i.e.* the excluded volume effect.

In order to explore the impact of surface charges, we modeled the graphene oxide membrane by introducing excessive charge on some carbon atoms. Accordingly, we randomly assigned positive and negative charges ($\pm e$) to the atoms with an average surface charge density of σ , the total net charge on each graphene layer was set to zero. We ensured that the minimum distance between charges is 3 \AA . Figure 8.1(a) gives an schematic view of the surface charge distribution over a graphene sheet, and Figs. 8.1(b), (c) show corresponding top and side views where red and white colors refer to the water molecules and Na^+ , and Cl^- are shown by blue and cyan balls which are trapped between the two graphene layers (gray lines). The concentration of ions is given by $n_i/(n_i + n_w)$, where n_i and n_w refer to the number of ions and water molecules, respectively.

The average number of neighboring water molecules at radial distance r of an individual ion is evaluated by (see Eq. (4.4))

$$n(r) = \frac{N}{V} \int_0^r g(r) 4\pi r^2 dr, \quad (8.1)$$

where N/V is the total water density and $g(r)$ is the appropriate radial distribution function (RDF) between the ion and oxygen atoms. We used n_1 and n_2 as the number of water molecules within the first and second hydration shells, respectively.

8.2.2 Dynamical coefficients

Components of the diffusion coefficient D_α , where $\alpha = x, y, z$, can be determined by inserting the position $G(t) = r^\alpha(t)$ and velocity $\dot{G}(t) = v^\alpha(t)$ into Eq. (4.9). As a result, D_α can be calculated using

$$\begin{aligned} D_\alpha &= \lim_{t \rightarrow \infty} \frac{1}{2t} \langle [r^\alpha(t) - r^\alpha(0)]^2 \rangle_i \\ &= \int_0^\infty \langle \langle v^\alpha(t_0)v^\alpha(t_0+t) \rangle_{t_0} \rangle_i dt, \end{aligned} \quad (8.2)$$

where $\langle \rangle_i$ denotes averaging over all atoms [113, 308]. Bulk diffusion coefficient (D) is computed as the average over all the components of D_α in Eq. (8.2). In the present study, we calculated the diffusion constants using the mean square displacement method taking one sample per 10 fs for the linear regression.

Similarly, the (shear) viscosity η can be determined from the Green-Kubo (GK) formula [229–231] that is based on the stress tensor auto-correlation function (ACF). It can be directly obtained from Eq. (4.9) by using

$$\begin{aligned} G(t) &= \sum_i m_i r_i^\alpha(t) v_i^\beta(t), \\ \dot{G}(t) &= VP_{\alpha\beta}(t) = \sum_i m_i v_i^\alpha v_i^\beta + \frac{1}{2} \sum_{i \neq j} F_{ij}^\alpha r_{ij}^\beta, \end{aligned} \quad (8.3)$$

which gives

$$\begin{aligned} \eta_{\alpha\beta} &= \lim_{t \rightarrow \infty} \frac{1}{VK_B T} \frac{1}{2t} \left[\sum_i m_i (r_i^\alpha(t) v_i^\beta(t) - r_i^\alpha(0) v_i^\beta(0)) \right]^2, \\ &= \frac{V}{K_B T} \int_0^\infty \langle P_{\alpha\beta}(t_0) P_{\alpha\beta}(t_0+t) \rangle_{t_0} dt, \end{aligned} \quad (8.4)$$

where $\eta_{\alpha\beta}$, V , T , K_B , m_i are viscosity tensor component, volume, temperature, Boltzmann constant, and atomic mass of particle i , respectively [228]. The summations are taken over all atoms, and F_{ij}^α and r_{ij}^α represents the specified component of the force and distance between i^{th} and j^{th} atoms, respectively. The expression $P_{\alpha\beta}$ is defined as the microscopic stress tensor in the form of the virial equation [171]. The viscosity of bulk water is subsequently evaluated from averaging over the time ACF of the off diagonal components of this symmetric tensor that include three possible $\alpha\beta$ permutations ($\alpha \neq \beta = x, y, z$) aiming to reduce the statistical error [233].

We use the GK method to calculate the viscosity (Eq. (8.4)). There are also other alternatives using either equilibrium or non-equilibrium MD simulations which have some technical limitations. For instance, using the non-equilibrium approach, the obtained viscosity was found to be highly sensitive to the velocity profile of the flowing water molecules [112, 309]. The stress tensor components in this work were calculated using the LAMMPS routines [253].

Transport properties in the presence of confinement, due to inhomogeneities of density, induced by the graphene capillary are not equal along the lateral (x, y) and the perpendicular (z) directions. When the confinement is removed, all corresponding components converge to their bulk values. In the presence of confinement, the diffusion coefficient, D_α along perpendicular direction is insignificant *i.e.* $D_z \ll D_x, D_y$. Here we report the lateral diffusion coefficient, *i.e.* the diffusion coefficient for confined system is given by $D = (D_x + D_y)/2$. In order to calculate the viscosity, we define two different components as follows

$$\eta_{xy}, \quad \eta_z = \frac{1}{2}(\eta_{xz} + \eta_{yz}), \quad (8.5)$$

where η_{xy} and η_z are the in-plane (along the channel) and lateral shear (perpendicular to the channel) viscosities, respectively [310]. We will show that both η_{xy} and η_z are affected by the confinement and $\eta_z < \eta_{xy}$. Since the viscosity is a collective property rather than a property of a single molecule, we would expect that the corresponding numerical results using Eq. (8.4) are less accurate as compared to the diffusion coefficient [113] due to the lack of extra atomic averaging $\langle \rangle_i$ present in Eq. (8.2). In MD simulations, an accurate calculation of the ACF tail is very demanding when evaluating the viscosity, hence we used the upper limit of 1 ps in Eq. (8.4) taking one sample per 2fs [234]. The friction coefficient and the slip-length between water and graphene surface are obtained from Eqs. (4.14) and (4.16), respectively.

8.3 Surface charge effects

Nanoconfinement changes the intrinsic properties of water and the interfacial coefficients. Here, we report results for the variation of the diffusion coefficient,

viscosity, friction coefficient and slip length with the height of the channel (h) for pure water confined between charged graphene surfaces.

8.3.1 Diffusion coefficient

In general, confinement suppresses the diffusion coefficient [311]. We found that the diffusion coefficient oscillates as a function of the thickness of the water layer due to commensurability effects [112]. In Fig. 8.2, we show the variation of D versus h in a semi-log scale for graphene sheets with three different surface charge densities, $\sigma = 0, 0.1, \text{ and } 1 \text{ e nm}^{-2}$. These densities correspond to typical charge densities observed over carbon and hexagonal boron nitride nanotubes [312, 313]. When there is no surface charge, the calculated diffusion coefficient oscillates for small h . A sudden drop in D (about two orders of magnitudes) was found for $h = 7.0 \text{ \AA}$ which is attributed to a 2D solidification of water at commensuration of the water molecule sizes and the channel gap distance [112, 278]. The exact value of the solid size depends slightly on the particular used force field. In contrast to Ref. [113], here we found that the diffusion coefficient oscillates and is very sensitive to the height of the channel which is consistent with the previous work [112]. The horizontal dash-dotted line in Fig. 8.2 corresponds to the calculated diffusion coefficient for bulk water, *i.e.* $2.83 \text{ cm}^2 \text{ s}^{-1}$, which is in good agreement with previous reports $2.79 - 3.02 \text{ cm}^2 \text{ s}^{-1}$ [314]. In the presence of surface charges, *e.g.* $\sigma = 1 \text{ e nm}^{-2}$, the water molecules near the surface of the confining walls are bonded to the charged sites causing D to decrease and it reduces the amplitude of the oscillations. A comparison between the diffusion coefficient of neutral and charged surfaces, reveals that the surface charge increases the water diffusion for $h \sim 8 \text{ \AA}$ while it decreases beyond this threshold. As one naturally expects, by increasing h , the diffusion coefficient very quickly approaches the bulk value.

8.3.2 Viscosity

In Figs. 8.3, we depict the variation of η_{xy} and η_z (Eq. (8.5)) with the height of the channel. The dash-dotted line represents the computed η for bulk water

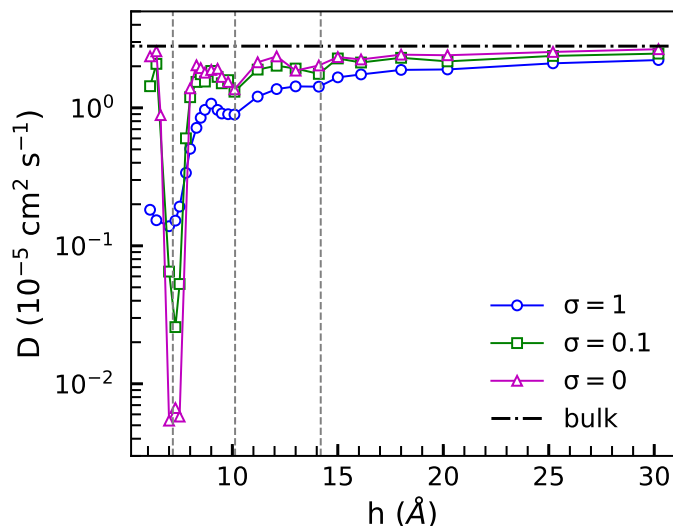


FIGURE 8.2. The variation of the diffusion coefficient with respect to the graphene capillaries gap in semi-log scale for different surface charge densities of $\sigma = 0, 0.1,$ and 1 e nm^{-2} . The commensurability of confined water (dashed vertical lines) leads to oscillatory variations in diffusion coefficient for $h < 20 \text{ \AA}$.

$6.6 \times 10^{-4} \text{ Pa s}$ which agrees with the reported value of $6.72 \times 10^{-4} \text{ Pa s}$ obtained using the same SPC/E model [229]. In the absence of surface charges, we found that in-plane viscosity η_{xy} shows similar oscillations at small separation distances which is consistent with the previous work [112], see Fig. 8.3(a). Interestingly, we found a maximum of η_{xy} at 7.0 \AA which corresponds to the minimum in D (Fig. 8.2). The lateral component of viscosity η_z is insignificant for small gap distances and it drastically increases when confinement is gradually removed, see Fig. 8.3(b), except for $\sigma = 1 \text{ e nm}^{-2}$. The latter is due to the stronger adhesion between water and the charged surface and it is larger than the bulk value. For instance, at $h = 15 \text{ \AA}$ we found $\eta_{xy}^{[\sigma=1]} \approx \eta_z^{[\sigma=1]}$, and the ratios $\eta_z^{[\sigma=1]}/\eta_z^{[\sigma=0]} = 55$ and $\eta_z^{[\sigma=0.1]}/\eta_z^{[\sigma=0]} = 11$ which shows that surface charges strongly enhance η_z . Moreover, the two viscosity components decrease in the presence of surface charges which indicates that the interaction with the surface has a larger effect than confinement. These results indicate that adding surface charges increase the viscosity components at small separation distance while they approach the bulk value for large h .

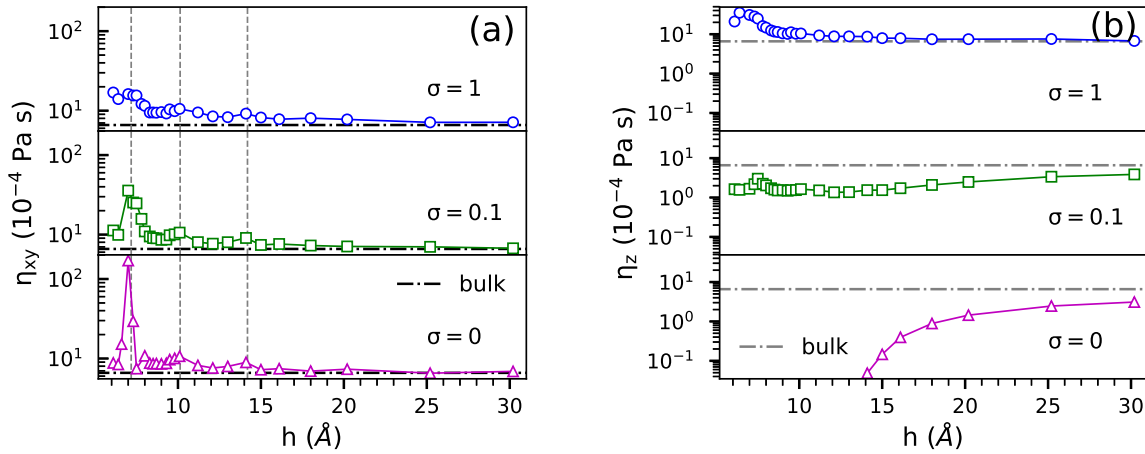


FIGURE 8.3. The variation of the components of viscosity (a) η_{xy} , and (b) η_z as function of the graphene capillary gap distance in semi-log scale for different surface charge densities, *i.e.* $\sigma = 0$, 0.1, and 1 e nm $^{-2}$. The dash-dotted line refers to the viscosity of bulk water (6.72×10^{-4} Pa s). The vertical dashed lines indicate the commensurate distances.

8.3.3 Friction coefficient

We further calculated the friction coefficient for confined water using Eq. (4.14). The results are shown in Fig. 8.4 for three typical charge surface densities. The calculated ξ for pure water (2.3×10^4 N s m $^{-3}$) over neutral surfaces is close to the recently reported value of 2.0×10^4 N s m $^{-3}$ for $h = 50$ Å [234]. The surface charge enhances the water/graphene interfacial attraction, and as a result, the friction coefficient ξ increases with up to two orders of magnitude. A noticeable oscillatory behavior can also be seen for $\sigma=0$ and even $\sigma=0.1$ e nm $^{-2}$. For small h , the friction σ increases very strongly which is due to the stronger adhesion between water and the charged surfaces. For a given $h=15$ Å, we can compare the frictional coefficient for different surface charges *i.e.* $\xi^{[\sigma=1]}/\xi^{[\sigma=0]} = 24$ and $\xi^{[\sigma=0.1]}/\xi^{[\sigma=0]} = 6.5$ indicating the hydrophilicity of GO surfaces. It is also interesting to note that the larger the surface charge density, the less pronounced are the commensurability effects. The larger difference $\xi^{[\sigma=0.1]} - \xi^{[\sigma=0]}$ as compared to $\xi^{[\sigma=1]} - \xi^{[\sigma=0.1]}$ shows the strong impact of functional groups (over GO) on the interfacial friction coefficient.

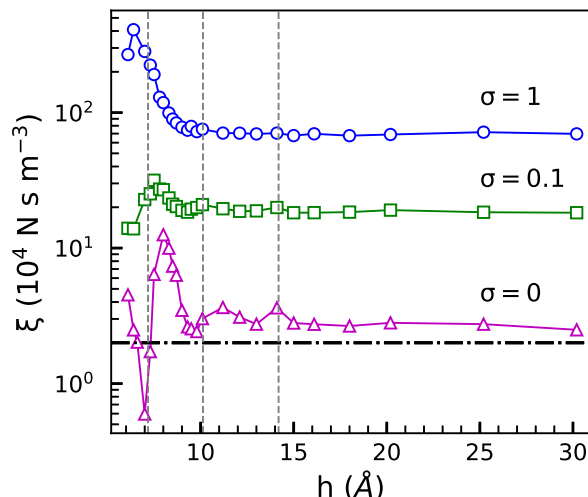


FIGURE 8.4. The variation of the frictional coefficient ξ as function of the graphene capillary gap distance in semi-log scale for different surface charge densities of $\sigma=0, 0.1,$ and 1 e nm^{-2} . The dash-dotted line represents the reported ξ ($2.0 \times 10^4 \text{ N s m}^{-3}$) for $h = 50 \text{ \AA}$ [234].

8.4 Effects of ions

To investigate the effect of solvation we consider as an example Na^+ and Cl^- ions and study its effect on the dynamical properties of confined water. In agreement with previous works [315], we found that adding ions linearly decreases the diffusion coefficient while it increases the viscosity regardless of confinement. This can be attributed to the hydration effect of ions which decreases the mobility and suppresses the dynamics of the water molecules. Hydration is a crucial phenomenon in the water filtration process which is altered by nanosize confinement [4]. In Figs. 8.5(a) and (b), we demonstrate the average number of water molecules $n(r)$ (Eq. (8.1)) near Na^+/Cl^- ions at radial distance r for few confinement distances: bulk, $h=8, 10, 20 \text{ \AA}$. The number of H_2O at the first (n_1) and second (n_2) hydration shells are listed in Table 8.1. It is seen that n_1 is not affected by h except for Cl^- at the very small slid size of 8 \AA which is due to its relatively large effective atomic radius. Notice that confinement reduces drastically the number of water molecules in the second hydration shell (with about a factor of 2) which is an important parameter for water/ion permeation through GO capillaries [6].

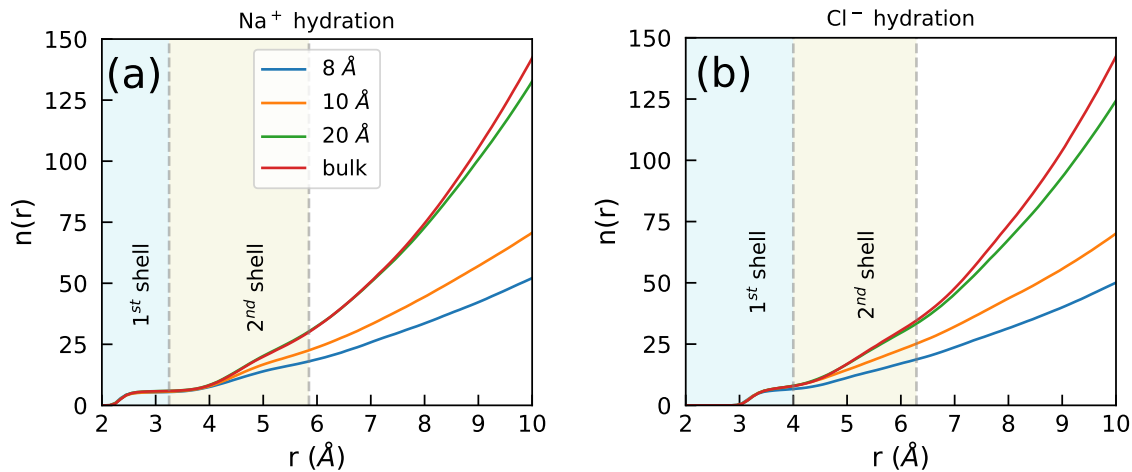


FIGURE 8.5. The variation of the average number of water molecules $n(r)$ from Na^+ (a) and Cl^- (b) ions calculated by using Eq. (8.1) as function of radial distance r for difference graphene interlayer distances. The two vertical dashed lines indicate the first and second hydration shells which are obtained from appropriate RDFs between ions and oxygen atoms of the water molecules.

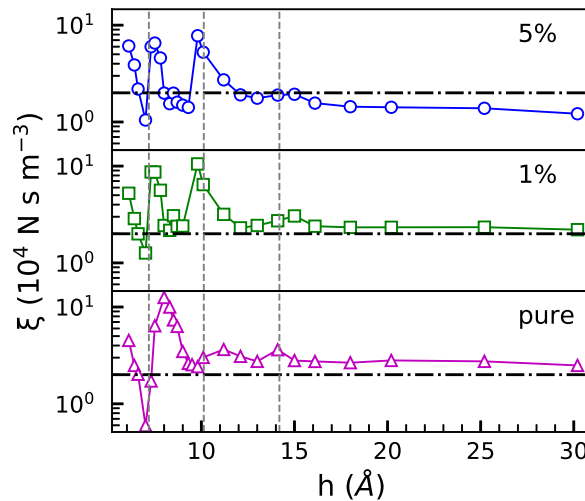


FIGURE 8.6. The friction coefficient ξ as a function of nanocapillary distance for pure water, 1%, and 5% ion concentrations. The dash-dotted line represents the reported ξ ($2.0 \times 10^4 \text{ N s m}^{-3}$) for $h = 50 \text{ Å}$ [234].

Table 8.1: The number of water molecules in the first and second hydration shell which are accumulated around Na^+ and Cl^- ions, see Figs. 8.5(a,b), for different confinement.

Ion	8Å		10Å		20Å		bulk	
	n_1	n_2	n_1	n_2	n_1	n_2	n_1	n_2
Cl^-	6.5	12.3	8.2	16.9	8.2	24.3	8.2	26.7
Na^+	5.7	12.3	5.7	16.9	5.7	24.2	5.7	24.5

We found that the presence of ions reduces the frictional coefficient. Figure 8.6 shows the variation of ξ with separation distance h for three different ion concentrations, *i.e.* 0, 1 and 5%. The dash-dotted line represents the reported ξ ($2.0 \times 10^4 \text{ N s m}^{-3}$) for $h = 50 \text{ \AA}$ [234]. At large h the suppression of the friction due to the presence of ions is clear. For example, for 15 \AA the decrease of ξ with ion concentration is $\xi^{[5\%]}/\xi^{[\text{pure}]} = 0.69$ and $\xi^{[1\%]}/\xi^{[\text{pure}]} = 0.91$. The reason is that when ions are present, they are surrounded by water molecules because of the hydration effect. As a result, water molecules will contribute less to water-surface interactions. Moreover, we obtained similar fluctuations in the friction coefficient at small h due to the previously discussed commensurability effects.

8.5 Conclusions and discussion

The MD simulations revealed that the intrinsic dynamical properties of water strongly depends on the commensurability of water molecules encapsulated in graphene oxide capillaries. More importantly, the transport parameters exhibit oscillatory variations particularly when the confinement is less than 20 \AA . At such commensurate states, confined water forms distinct layers which occur at specific gap distances [112]. We found that almost all dynamical properties are affected by this commensurability effect. Table 8.2 quantifies the diffusion, viscosities, frictional coefficient, and slip lengths for several selected confinement distances. It is important to note that all extrema occur at the same interlayer distances that support the fact that commensurability underlies oscillatory behaviors. The underlined (double underlined) colored numbers represent the local maximum (minimum) in their corresponding

figures. Here we considered only pure water without surface charges. By increasing the slid size commensurability disappears gradually and the results coincide with the bulk values.

Table 8.2: Dynamical properties *i.e.* diffusion, viscosities, frictional coefficient, and slip lengths for several selected confinement distances exhibiting oscillatory behaviors induced by the commensurability effect. The underlined (double underlined) colored numbers represent the local maximum (minimum) values. For simplicity, we only consider pure water without surface charges.

h (Å)	6.1	7.0	8.3	10.1	12.1	14.1	20.2
D ($10^{-5}\text{cm}^2\text{s}^{-1}$)	<u>2.3</u>	<u>0.005</u>	<u>2.0</u>	<u>0.03</u>	<u>2.3</u>	<u>0.14</u>	2.4
η_{xy} (10^{-4}Pa s)	<u>8.6</u>	<u>155</u>	<u>8.3</u>	<u>10</u>	<u>7.4</u>	<u>8.8</u>	7.4
η_z (10^{-4}Pa s)	-	-	-	-	-	0.04	1.3
ξ (10^4N s m^{-3})	<u>4.5</u>	<u>0.5</u>	<u>1.4</u>	<u>3.0</u>	<u>3.1</u>	<u>3.6</u>	2.7
L_{xy} (Å)	<u>195</u>	<u>24457</u>	<u>59</u>	<u>377</u>	<u>150</u>	<u>250</u>	263
L_z (Å)	-	-	-	<u>0.27</u>	<u>2.95</u>	<u>1.40</u>	48

The density profile along the confinement direction (z -axis) is shown in Fig 8.7 to demonstrate the commensurability. The graphs are shifted for different interlayer distances and the colored zones refer to the specific number of water layer. The red colors (6.1, 8.3, and 12.1 Å) represent the commensurate states with a distinct number of water layers, and the blue colors (7.0, 10.1, and 14.1 Å) refer to the state just before a new layer of water forms. Interestingly, the colored density profiles correspond to the extrema in the values of dynamical properties, see Table 8.2. Moreover, the number of intra (inter) hydrogen bonds of the layers is an additional quantity that gives us similar information on the commensurability effect.

We calculate the slip lengths for all the cases using Eq. (4.16). The slip length is the distance at which the linearly extrapolated velocity reaches a no-slip condition. Figure 8.8(a) shows the two components of the slip length, L_{xy} , and L_z , for different surface charge densities σ as a function of the slid size. When $\sigma = 0$ and for large h , the slip lengths for L_{xy} (250 Å) and L_z (200 Å) are comparable with the reported values of 290 Å [234] (dash-dotted line) for

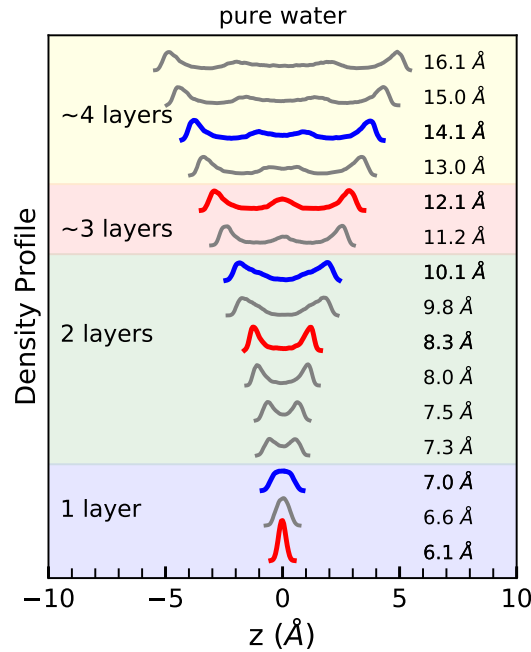


FIGURE 8.7. Density profile of oxygen atoms along the confinement direction (z -axis) for pure water without surface charges. The graphs are shifted for the different interlayer distances and the colored zones refer to the numbers of water layer. The red color (6.1, 8.3, and 12.1 Å) represent the commensurate states with distinct water layers, and the blue colors (7.0, 10.1, and 14.1 Å) refer to the state just before a new water layer forms.

bulk water over graphene. Note that in recent studies [234, 305], a constant bulk viscosity was assumed in the calculation of the slip length even for small gap distance *i.e.* $h < 30$ Å. If we use the bulk viscosity (6.72×10^{-4} Pa s) in the numerator of the slip length equation namely η/ξ without taking into account the impact of confinement, we found $L=285$ Å which is in agreement with their reported slip length. In order to find a h -dependent slip length, we include the effects of confinement on both viscosity and friction coefficient. We found that L_{xy} fluctuates particularly at small h , however, L_z is much smaller at small distances *i.e.* $h < 15$ Å while it rapidly increases to the bulk value, see Fig. 8.8. In the presence of surface charges, slip-lengths drastically reduces due to the fact that water molecules bind to the graphene surfaces. This is qualitatively in agreement with the experimental results for GO with oxygen-groups [316]. It was also reported that a GO with 20% oxygen-groups has a slip length

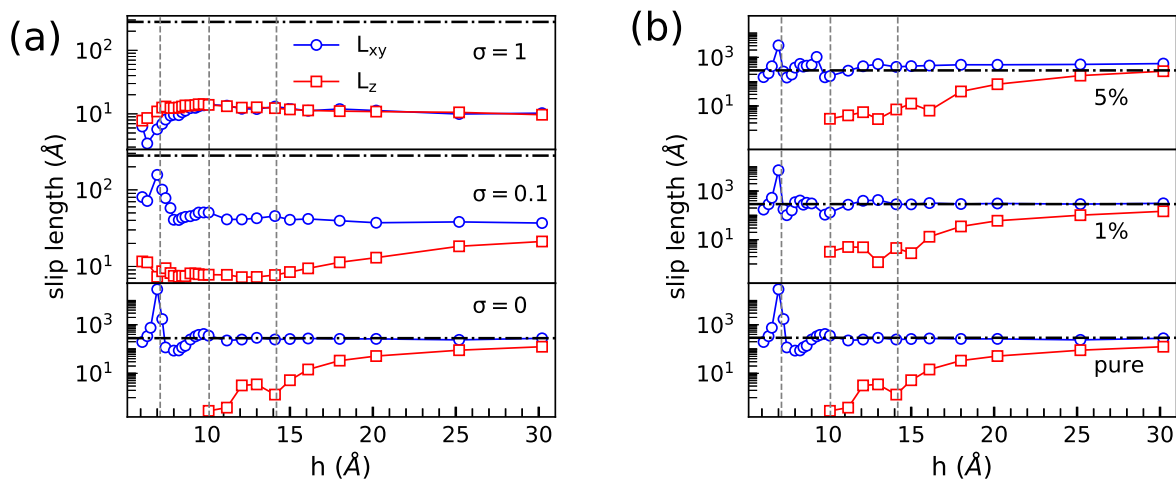


Figure 8.8: Components of the slip length L_{xy} and L_z for different surface charge densities of $\sigma=0, 0.1,$ and 1 e nm^{-2} (a) and for pure water, 1%, and 5% ion concentrations (b). The dash-dotted line indicates the reported hydrodynamic slip length (280\AA) for gap distance of 30\AA [234].

of two orders of magnitude smaller than that over a graphene sheet which is comparable with the results shown in Fig. 7(a) [305, 316]. In fact water permeability through a GO membrane is very complicated, for instance, the water permeating through nanochannels made of GO is controlled by the size, structure and distribution of pores as well as the length of the channels [316]. We argue that when water is confined in a nanocapillary with Ångstrom scale size, the major influence on the slip length is due to L_{xy} while L_z is much more sensitive to channel height.

The slip length components for different ion concentrations of Na^+/Cl^- 0, 1, 5% are shown in Fig. 8.8(b) which reveals only a small influence of the presence of ions. The effect is considerable for large concentration if we compare the two top panels of Fig. 8.8(b) with the bottom one. Recently, Abraham *et al.* [6] studied the importance of the size of ions and its corresponding hydration. They found that water molecules stabilize ions by forming concentric hydration shells such that when an ion enters a channel some water molecules must be removed from the hydration shell leading to the effect that if ions are weakly bound by water molecules, they can easier enter into nanochannels. Here, we did not study the entrance barrier of the channels, instead we focused on the dynamical properties and resistance against diffusion

of the ions inside the channel. Therefore, the results represented in Fig. 8.8(b) are not directly comparable with experimental results [6]. However, it is seen that by increasing the concentration of ions the slip length slightly increases and the sensitivity of the hydration shell to the channel size is shown in Figs. 8.5(a,b), which are consistent with recent experiments [5, 6]. It would be also interesting to note that GO membrane spacings can be controlled by certain type of cations (*e.g.* K^+) which can efficiently and selectively exclude permeation of other cations that have larger hydrated volumes [5].

Finally, we conclude that the concentration of ions does not dramatically change the slip length (this is relevant for recent experiments where the effects of ions with different hydrated diameters were found to be minimal [4]) while surface charges on the graphene surface and commensurability induced by confinement have a profound influence on the dynamical properties. The significant variation of the slip length with respect to the microscopic details of nanocapillaries and the complexity of the problem shows that more studies are needed.

CONFINED ORGANIC MOLECULES IN CLAY MINERAL MEMBRANES

Clay minerals are very soft layered materials of magnesium or aluminum silicates that can form a nanosize ionic channel. Swelling properties of the clay are quite relevant to several engineering applications including environmental remediation and repository design for waste disposal. We employ molecular dynamics simulation in order to investigate the impact of the interlayer cations of montmorillonite clay and the specifics of the intercalated hydrocarbon solutions on membrane interlayer spacing, swelling, and permeation. It is found that swelling is energetically favorable for polar (water and ethanol) or aromatic molecules (benzene) due to cationic hydration through dipole-dipole and π -cation interactions, respectively. Therefore, no swelling is predicted for molecules without cationic hydration such as hexane. In agreement with the recent experiment, we show that benzene, as an aromatic molecule, permeates through the clay membrane much faster when cations are hydrated under humidity. These results emphasize the importance of π -cation interactions and provide insights into the underlying mechanism of intercalated hydrocarbons inside the clay membrane.

This work is ongoing research in collaboration with the experimental group led by Prof. R. Nair at Manchester University. My contribution is the modeling of the Clay mineral and the diffusion of water through it using MD simulations.

9.1 Introduction

Clay mineral consists of layers of negatively charged mica-like sheets where each layer has two to four sheets of tetrahedral silicon oxide and octahedral aluminum or magnesium oxide, held together by charge-balancing metal cations such as Na^+ and K^+ . Density of the cations is determined by number of magnesium that replaced aluminum in the octahedral site, or aluminum has replaced a silicon in a tetrahedral site (see Fig. 9.1). In the presence of water, these cations are hydrated, and force the clay layers apart in series of discrete steps [317–319]. The equilibrium distance is determined by the balance between the mechanical pressure exerted on the layers and swelling pressure induced by the hydration on interlayer cations. Several of studies claim that the absorption of water into the interlayer spacing is mainly determined by the size and charge of the internal counterions. Even though the net silicate layer charge and charge location are also addressed in other studies to play a major role [320]. Clay mineral has low crystal symmetry that is characterized by a variety of multicomponent substitutions in the tetrahedral and octahedral sheets. Depending on the type of structural substitutions and net charge, the clay may become expandable and provide a suitable hosts for hazardous chemical and waste materials [321].

Molecular dynamics simulations can provide an atomistic perspective on the structural and behaviors of clay minerals. Monte Carlo and molecular dynamics are typically employed to predict the interlayer structure and the swelling with emphasis on aqueous solutions in the framework of classical [319, 322, 323] or *ab initio* simulations [324, 325]. In particular, intercalated water inside clay mineral and its swelling curve and interlayer spacing has been widely studied in previous works [320]. S. Teich-McGoldrick *et al.* have conducted a computational study to investigate temperature, interlayer cation, and charge location effects on swelling properties of montmorillonite and beidellite clay minerals [321]. A. Delville *et al* studied the structural properties of confined water using a molecular model of the clay-water interface [326]. It is important to note that clay membrane forms ionic nanochannel that keeps the intercalated solution under extreme confinement. We are interest to study swelling properties and permeability of such sys-

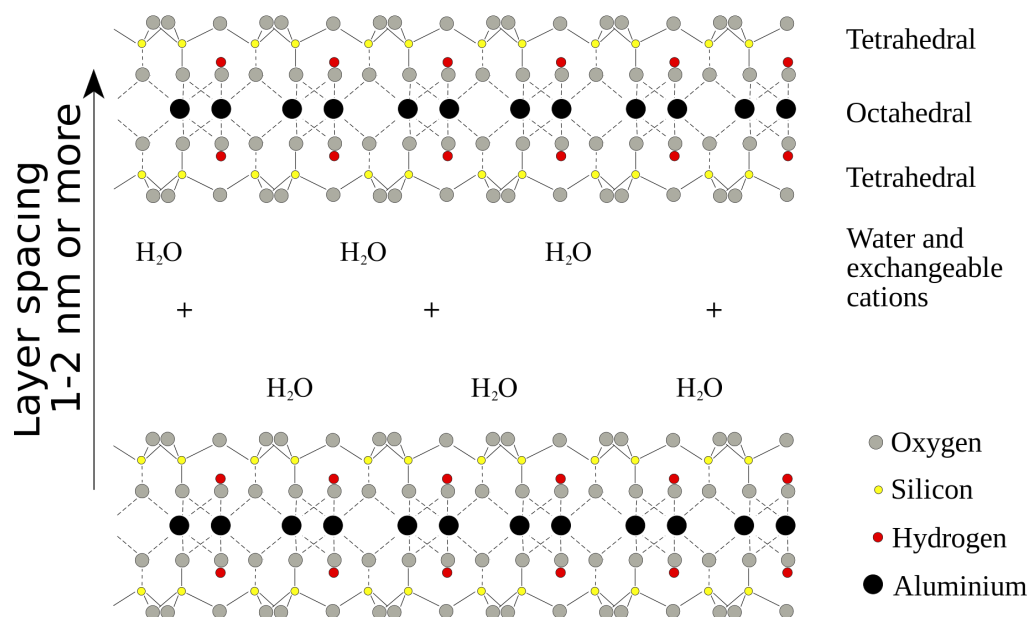


FIGURE 9.1. Schematic representation of montmorillonite clay membrane with the presence of water molecules between the layers. Its octahedral layer is sandwiched between two tetrahedral layers that known as 2:1 clay mineral or a T-O-T clay mineral. The figure is adapted from <https://commons.wikimedia.org>.

tems in particular for organic molecules that is quite relevant to the recent experiments done in the group of Prof. R. Nair at Manchester University.

In this chapter, I briefly present the recent MD results concerning the swelling properties and the impact of aromaticity on the permeation of montmorillonite clay mineral with K^+ and Na^+ interlayer cations. I focus first on polarity effects and explore how it influences swelling energy and interlayer spacing. For illustrative reasons, ethanol (hexane) as a typical polar (nonpolar) liquid is investigated and the results are compared with those for water. After that the aromaticity impact on permeation of benzene as typical aromatic hydrocarbon is considered.

9.2 The Model and methods

The tilted simulated box in Fig. 9.2 contains three layers of the clay which has lateral dimensions of $4\text{nm} \times 3\text{nm}$. $Y_{0.75} Si_8 [Mg_{0.75} Al_{3.25}] O_{20} (OH)_4 X_n$ model was used to express the clay mineral [321], where Y stands for interlayer

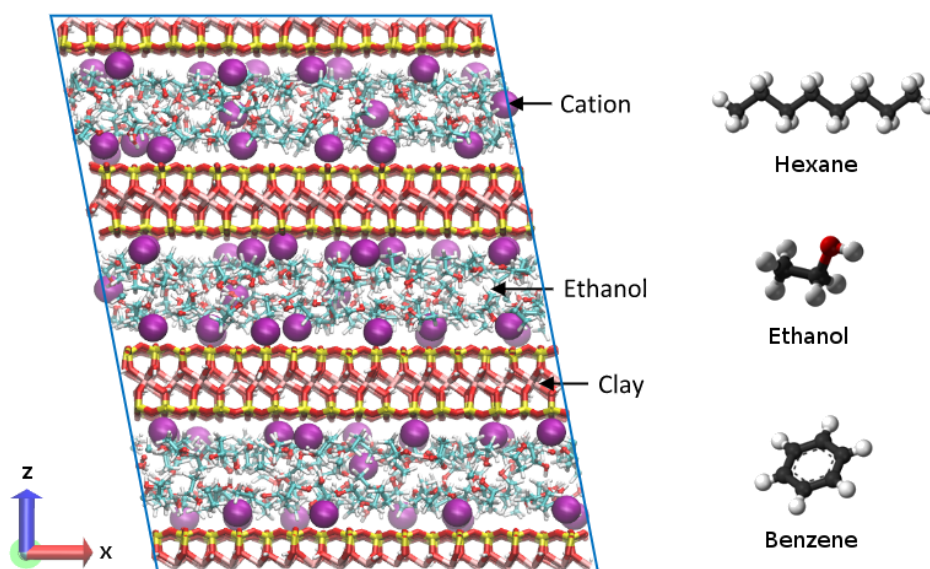


FIGURE 9.2. Snapshot of the equilibrated MD simulation for the montmorillonite clay mineral with K^+ interlayer cations (purple colored balls) and ethanol at 300K and 1 atm. The tilted super cell (blue box) contains three clay layers and periodic boundary conditions are apply along x , y , and z directions. Schematic representation of the C_6H_{14} (hexane), C_2H_6O (ethanol), and C_6H_6 (benzene) molecules. The figures for the molecular structures are adapted from <https://commons.wikimedia.org>.

cations and X can be either H_2O (water), C_6H_{14} (hexane), C_2H_6O (ethanol), or C_6H_6 (benzene). Figure 9.2 (left side) shows a snapshot of the MD simulation for the clay mineral with K^+ interlayer cations (purple colored balls) and the ethanol solution. Moreover, schematic molecular representation of studied solvents (X) are shown (right side). In order to describe the interatomic potentials, we used the SPC/E model [192] for water, OPLS potential for the hydrocarbons (hexane, ethanol, and benzene) [281], and a flexible model CLAYFF for the montmorillonite clay membrane [321]. The latter consists of non-bonded electrostatic and van der Waals terms which has been shown to accurately reproduce bulk properties of dry and hydrated clays as well as interlayer and interface properties in fair agreement with experiments [327, 328]. All cross atomic interactions are evaluated from the Lorentz-Berthelot

combining rules¹. The cut-off radius for the short and long-range interactions was chosen at 15Å. The NPT ensemble (Nosé-Hoover thermostat and barostat) was used to keep the temperature at 300K and pressure applied independently along all three directions (aniso) at 1 atm. The particle-particle particle-mesh method was used to compute the Coulomb interaction with a relative accuracy of 10^{-5} . Water molecules bond and angle were fixed by the SHAKE algorithm. Periodic boundary conditions are employed along the x , y , and z directions. Time step set to 1 fs and the simulated system was relaxed for 500 ps. Molecular dynamics simulations have performed as implemented in LAMMPS package [253]. Diffusion coefficient (lateral) was calculated by evaluating the mean square displacement of liquid molecules along the membrane for one sample per 10 fs and eventually averaging the diffusion coefficient in the lateral directions.

9.3 Results

9.3.1 Swelling properties

To study the swelling properties, we manually increased the amount of each liquid and separately evaluated the associated energy and interlayer spacing for each sample. The content of the intercalated liquid is given by the ratio of the masses (M_X/M_{clay}) that varies from 0.0 (dry clay) to 0.6 which is independent of the specifics of the solvent. Furthermore, associated swelling energy is defined as

$$E_{\text{sw}} = (E_{\text{tot}} - E_{\text{dry}} - E_{\text{bulk}})/n_X \quad (9.1)$$

where E_{sw} is the difference between the total energy of the whole system (E_{tot}), dry clay (E_{dry}), and the bulk that is normalized to the number of molecules of the liquid (n_X). Figures 9.3 (a) and (b) show the swelling energy and corresponding swelling curves for water, hexane, and ethanol. The highest tendency to swell occurs at the minimum of the swelling energy which is the case for water and ethanol as polar liquids, while no minimum was

¹See Eq. (3.39)

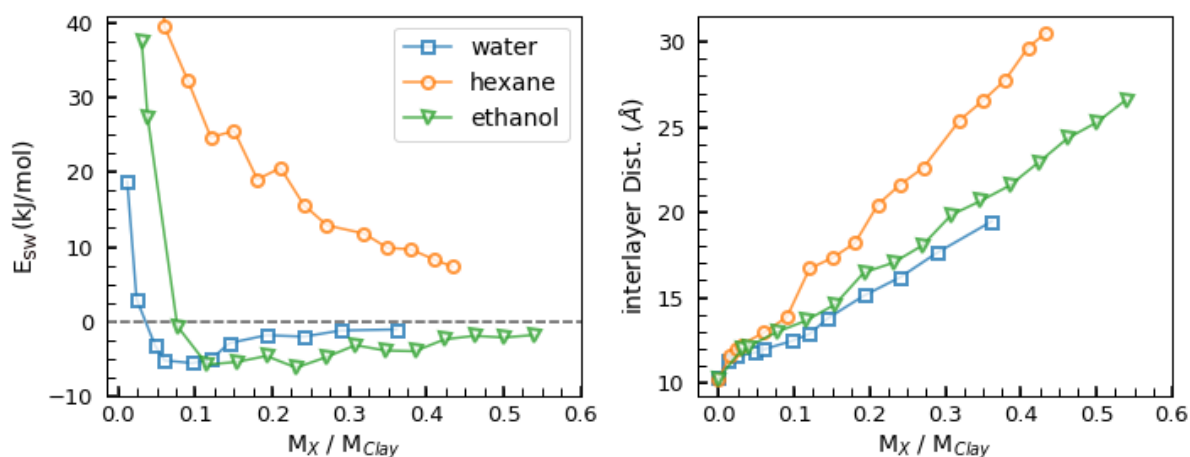


FIGURE 9.3. Swelling energies (a) and interlayer distance (b) for K^+ -montmorillonite mineral clay as function of the intercalated content of water, hexane, and ethanol.

found for hexane. The interaction between water (ethanol) and the surface is through hydrogen bond, and the structure of the intercalated solvent is different from bulk [325]. Moreover, we predict larger interlayer spacing for ethanol than water in the presence of the K^+ cation, and in general terms, we concluded that swelling in the presence of hexane as a non-polar liquid is not energetically favorable due to the lack of cationic hydration. The impact of the interlayer cations on hydration energy for two polar liquids, water, and ethanol, are shown in Figs. 9.4 (a) and (b). The different behaviors account are due to the effective hydration shell size and the associated hydration energy of the interlayer cations. In Table 9.1 we listed the optimal interlayer distance of the montmorillonite mineral clay for dry, water, ethanol, and hexane in the presence of K^+ and Na^+ cations and compare the MD simulations with experiments. Furthermore, we reported the corresponding diffusion coefficient for water and ethanol at the optimal distances. Due to the dominant hydrogen bond interactions of the liquids with the charged surface, we obtained a smaller diffusion coefficient than for bulk systems. Accordingly, we also found that pure intercalated ethanol diffuses one order of magnitude smaller than water through the clay membrane.

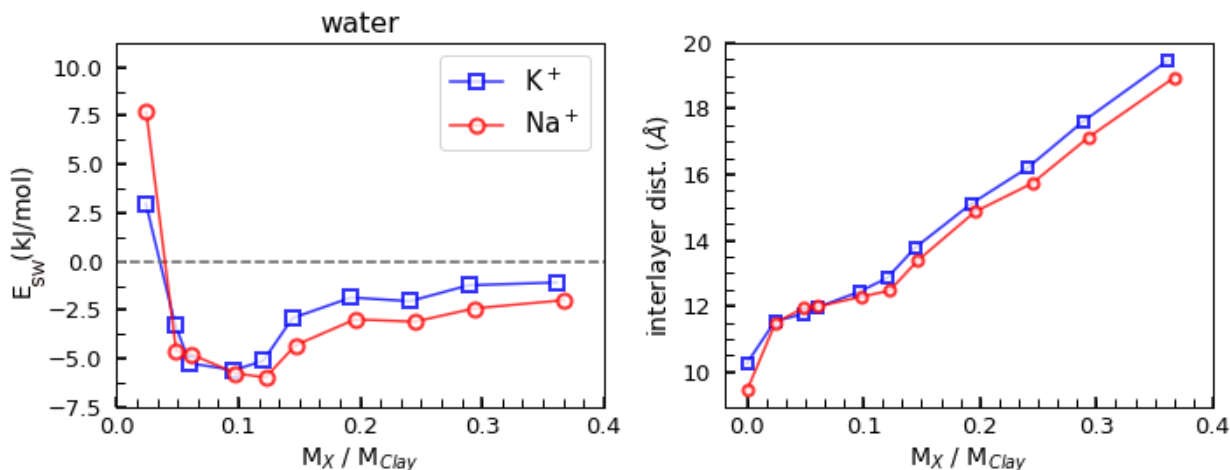


FIGURE 9.4. Swelling energies (a) and interlayer spacing (b) for K^+ -montmorillonite mineral clay as function of the intercalated content of water, hexane, and ethanol.

Substance	Cation	interlayer Dist. (Å)		diffusion Coef. ($10^{-5} \text{cm}^2/\text{s}$)
		MD	Exp.	MD
Dry (void)	K^+	10	-	-
	Na^+	9.4	9.6-9.8	-
Hexane (nonpolar)	K^+	10	11.5	-
	Na^+	9.4	-	-
Water (polar)	K^+	12.5 ± 0.5	14.3	0.75
	Na^+	12.8 ± 0.7	12.3-12.6	0.47
Ethanol (polar)	K^+	16 ± 2	18.9	0.068
	Na^+	13.5	-	0.064
Benzene (aromatic)	K^+	15.1 ± 0.3	-	0.067
	Na^+	-	-	-

Table 9.1: Comparison between optimal interlayer distances and diffusion coefficient for the montmorillonite model with K^+ and Na^+ cations separately for dry, water, hexane, ethanol, and benzene obtained from the MD simulations and experiments.

9.3.2 Aromaticity effects

In recent experiments, it is observed that aromatic solvents permeate through clay membranes much faster under humidity in comparison to dry atmosphere. Humidity signifies the cations are hydrated before the introduction of organic molecules. Accordingly, we performed MD simulations to study the impact of adding benzene C_6H_6 , as an example of aromatic molecules, on the

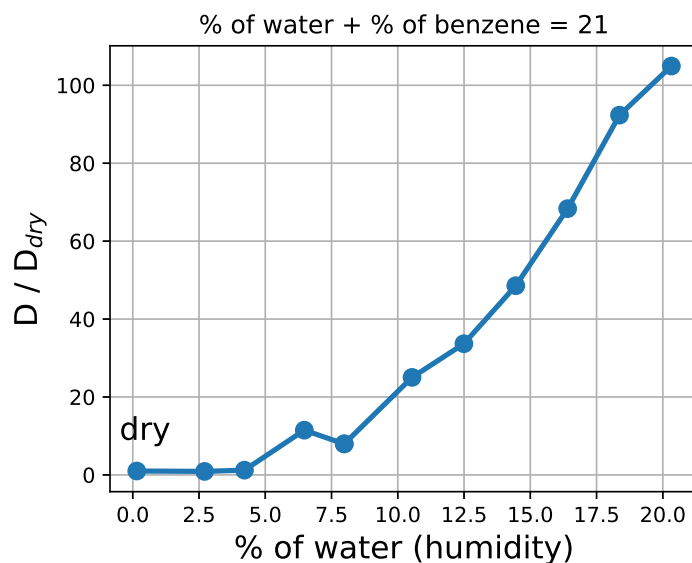


FIGURE 9.5. MD diffusion coefficient ratio for the water-benzene solution as a function of % of water content inside the clay membrane. The term *dry* indicates a clay membrane with no water (pure benzene).

diffusion coefficient and the hydration shells around K^+ cation. For studying the aromaticity effects, we simulated systems consist of benzene and water solution and increased humidity. Benzene molecules is manually replaced by water molecules while having fixed the mass ratio (i.e. 0.21). The mass ration is defined as M_X/M_{clay} , where M_X and M_{clay} refer to the mass of solvent and clay in computational unit cell, respectively.

We believe that strong π -cation interaction underlies the observed anomalous behavior and comparable values of binding energies for benzene- K^+ (19.2 kcal/mol) and water- K^+ (17.9 kcal/mol) support this fact that benzene binds the cation in the same order as water due to the strong π -cation interactions [329, 330]. π -cation interaction is in fact a noncovalent molecular interaction between an electron-rich π system (e.g. benzene, ethylene, acetylene) and an adjacent cation (e.g. K^+ , Na^+). This interaction is an example of noncovalent bonding between a monopole (cation) and a quadrupole (π system) [331].

Figure 9.5 shows the calculated diffusion coefficient ratio for the water-benzene solution as a function of % of water content. It must be noted that

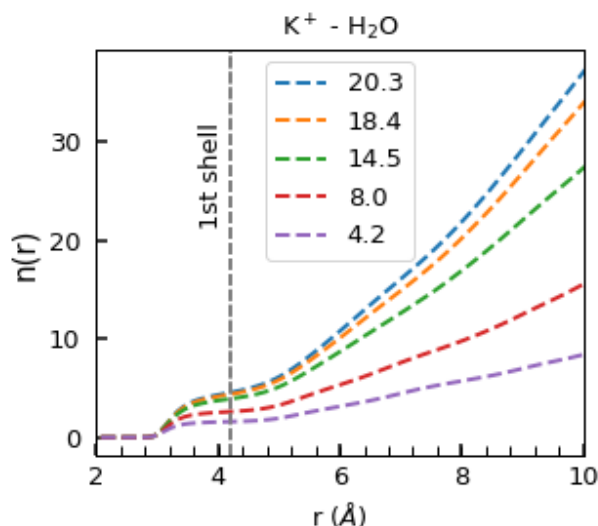


FIGURE 9.6. Coordination number of the K^+ for surrounding water molecules when the humidity (% of water) is varied from 4.2 to 20.3 (see Fig. 9.5). The Dashed-line represent fist hydration shell which is determined the corresponding RDF between cation and water.

the total mass ratio of the solution including water and benzene is fixed at 0.2 while adding the benzene and D_{dry} refers to the clay membrane without water (pure benzene). These results indicate that the diffusion coefficient of the solvent increases when the humidity increases. This gives a hint about how fast it can permeate through the channel and the MD predicts that the humidity (water content) increases the aromatic solvent permeation. Further hydration shells analysis indicates that humidity influences cationic hydration. In fact, there is a competition between the benzene molecules and water molecules through the cation- π and cation-dipole interactions, respectively. Figure 9.6 shows hydration shell of the K^+ cations when % of water molecules (humidity) is varied from 4.2 to 20.3. The number of water $n(r)$ increases even at the first (closest) hydration shell. The density profile shows water stays close to the surface, benzene at the middle, and cations locate between them. As the number of water increases, we have less benzene at the middle and the cations are less situated in the space between benzene and water (see Fig. 9.7). In Table 9.1 it might be noted that the diffusion coefficients for the clay membrane containing only water (no

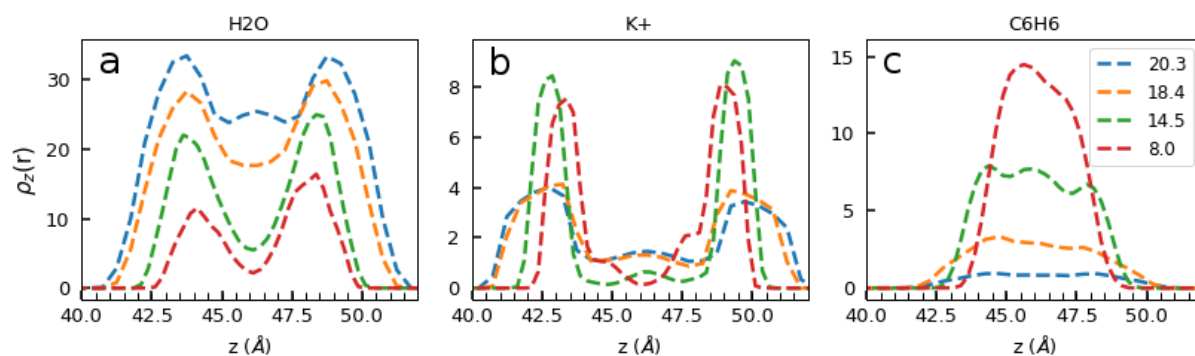


FIGURE 9.7. Density profile of (a) water (b) cation (c) benzene across the simulated clay membrane for several % of water (humidity) 8.0, 14.5, 18.4, and 20.3.

benzene) permeates $11x$ faster than a dry system that contains benzene (no water) at their optimized interlayer spacing.

9.4 Future work

The present MD results confirm the influence of aromaticity which are in good agreement with the experiment and more investigations are required in order to draw a final conclusion. This collaborative research project is in progress. Future work will be devoted to understanding the precise impact of the humidity when only water molecules are present at the first cationic hydration shell, considering solvent flow through the channel (i.e NEMD approach), improving the force field parameters particularly for solvent-cation interactions, and the role of surface interactions (i.e. hydrogen bonds).

10.1 Summary

In this thesis, structural and dynamical properties of graphene-based materials and water confined in nanomembranes were explored using large-scale molecular dynamics simulation aiming to provide theoretical insights into underlying mechanisms at atomic-scale regarding their applications in water purification and ion sieving. LAMMPS software package was extensively used to perform the simulations. In Part 1 (Introduction¹), I gave a brief overview of graphene, graphene-based materials, water, and computer simulations. In Part 2 (Methodology²), theoretical backgrounds and discuss computational approaches were provided that have been used in Part 3 (Results³) as follows:

In Chapter 5, structural and mechanical properties of nitrogen-doped graphene (NG) were investigated using ReaxFF potentials on the basis of molecular dynamics simulations. It was found that ripples, which are induced by the dopants, change the roughness of NG that depend on the number of dopants and their local arrangement. For any doping ratio N/C the NG becomes ferroelectric with a net dipole moment. The formation energy increases non-linearly with N/C ratio, while Young's modulus, tensile strength and

¹Chapter 1

²Chapters 2, 3, and 4

³Chapter 5, 6, 7, 8, and 9

intrinsic strain decreases with the number of dopants.

In Chapter 6, spatial design and control of graphene flake motion was investigated. The force between a sharp scanning probe tip and a surface can drive a graphene flake over crystalline substrates. Design of particular patterns of structural defects on a graphene surface allows proposing an alternative approach for controlling the motion of graphene flake over a graphene substrate. The thermally induced motion of a graphene flake is controlled by engineering topologically defects in the substrate. Such defected regions lead to an inhomogeneous energy landscape and are energetically unfavorable for the motion of the flake, and will scatter graphene flakes when they are moving toward the defected line. Engineering the distribution of these energy barriers results in a controllable trajectory for the thermal motion of the flake without using any external force. We predicted superlubricity of the graphene flake for motion along and between particular defect lines that provided insights into frictional forces of interfaces and opened a novel route to the engineering of the stochastic motion of a graphene flake over any crystalline substrate.

In Chapter 7, we explored the dependence of the shape of graphene nanobubbles on the trapped substance nanobubble. Van der Waals (vdW) interaction between two-dimensional crystals (2D) can trap substances in high pressurized (of order 1 GPa) nanobubbles. Increasing the adhesion between the 2D crystals further enhances the pressure and can lead to a phase transition of the trapped material. We found that the shape of the nanobubble can depend critically on the properties of the trapped substance. In the absence of any residual strain in the top 2D crystal, flat nanobubbles can be formed by trapped long hydrocarbons (*i.e.* hexadecane). For large nanobubbles with radius 130 nm, atomic force microscopy measurements showed nanobubbles filled with hydrocarbons (water) have a cylindrical symmetry (asymmetric) shape which was in good agreement with the molecular dynamics simulations. This work provided insights into the effects of the specific material and the vdW pressure on the microscopic details of graphene bubbles.

In chapter 8, permeation of water between neighboring graphene oxide (GO) flakes, *i.e.* 2D-nanochannels, are investigated using a simple model for

the GO membrane. We simulated the hydrophilic behavior of nanocapillaries and studied the effect of surface charge on the dynamical properties of water flow and the influence of Na^+ and Cl^- ions on water permeation. Our approach was based on extensive equilibrium molecular dynamics simulations to obtain a better understanding of water permeation through charged nanochannels in the presence of ions. We found a significant change in the slippage dynamics of confined water such as a profound increase in viscosity/slip length with increasing charges over the surface. The slip length decreases one order of magnitude (*i.e.* 1/30) with increasing density of surface charge, while it increases by a factor of 2 with ion concentration. We found that commensurability induced by nanoconfinement plays an important role in the intrinsic dynamical properties of water.

Finally, in chapter 9, the swelling properties and the impact of aromaticity on the permeation of montmorillonite clay mineral with K^+ and Na^+ interlayer cations were explored. Polarity effects and how it influences swelling energy and interlayer spacing were discussed. It was found that swelling is energetically favorable for polar (water and ethanol) or aromatic molecules (benzene) due to cationic hydration through dipole-dipole and π -cation interactions, respectively. Therefore, no swelling is predicted for molecules without cationic hydration such as hexane. Furthermore, aromaticity impact on permeation of benzene as typical aromatic hydrocarbon was examined. We showed that benzene, as an aromatic molecule, permeates through the clay membrane much faster when cations are hydrated under humidity. The preliminary results are satisfactory. More studies are still required in order to understand the observed permeation behavior and reach a final conclusion.

10.2 Outlook

Membranes are used for different separation processes, with applications in areas as diverse as water desalination, gas separation, energy technology, microfluidics, and medicine. Despite a large number of experimental attempts that have been devoted to nanomembrane fabrication, with potential applications for water purification, some of them discussed in this thesis, there is a lack of accurate computational models (i.e. force field potentials) that can be applied in a practical sense to large-size systems. For example, the precise molecular mechanism for the observed unimpeded water permeation through stacks of graphene-oxide membranes as well as its ion selectivity, are as yet unidentified. The impact of interactions of the surface functionals on water transport and the impact of nanosize confinement is not known precisely, and it remains an open question. Development of quantum mechanically accurate interatomic potentials within the framework of data-driven approaches would be a key to understand the properties that emerge from the large sample size and the chemistry at the interfacial area.



APPENDIX A

A.1 Different defects in the substrate

In Fig. A.1, we depict four defected graphene substrates that we considered: a) containing two 5-7 defects separated by 1 nm, b) a LAGBI line, c) two Large-Angle Grain Boundary (LAGBI) line separated by 0.3 nm (named 2-LAGBI), and d) a zig-arm GB. The GB line in Figs. A.1(b,d) is located at $x=0$. Notice that at the two sides of the GB lines in Figs. A.1(b,d) the orientation of the sheets are different while in Figs. A.1(a,c) the RHS and LHS of the defects have the same orientation (see shaded hexagons).

A.2 Energy barriers due to LAGBI

We calculated the energy barriers for rotation of a square graphene flake of size 4 nm around the z -axis over pristine graphene. The results are shown in Fig. A.2(a). Depending on the initial stacking, *i.e.* AA- or AB-stacking, the energy profiles are different. For our simulated flake size, the energy barriers for $|\theta| \geq 10^\circ$ are negligible yielding superlubric rotational motion. Below $|\theta| \leq 10^\circ$ the graphene flake locks in a commensurate state [81] with a finite (short) life time when moving. Notice the energy difference between minimum and maximum of the two profiles shown in Fig. A.2(a) which corresponds to Δ_0 .

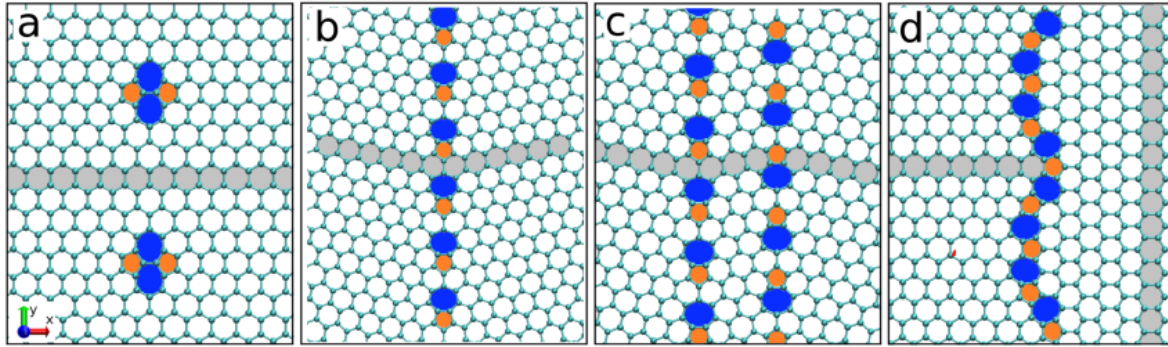


FIGURE A.1. Four types of defected graphene: (a) two 5-7 defects separated by distance 1 nm, (b) a GB having $\theta_L = 21.8^\circ$ with respect to x -axis (LAGBI), (c) two LAGBI separated by 0.3 nm ("2-LAGBI"), and (d) special type of GB which makes the two sides having perpendicular direction with respect to each other (we name it "zig-arm"). The grayed regions are guide to the eyes showing the different crystallographic orientations at both sides of the grain boundary.

Similarly, we rotated the flake \otimes around the z -axis with θ varied in the range $[0^\circ, 60^\circ]$. The obtained energy is shown in Fig. A.2(b). The center of mass of the flake is located at a pentagon or heptagon. We found much smaller energy barriers as a consequence of the rotation on pristine graphene (Fig. A.2(a)). Notice that a partial AA or AB-stacking occurs only on one side of the GB in Fig. A.2(b). These small energy barriers cause backscattering of the moving flake away from the GB line.

A.3 Variation of the force with size of flake

In Fig. A.3, we compare the variation of the x -component of the force for motion along x -direction for three different sizes 3, 4, 5 nm. The curves for 3, 4 nm are shifted by 20 and 10 nN in order to make their variations more clear. It is seen that the smaller flake is affected by the LAGBI line beyond $x_m = -0.5$ nm while the larger one starts to be influenced before -2 nm. This is a consequence of the fact that the edge of the 3(5) nm flake starts to interact with the LAGBI line at that distance of the center of mass of the flake.

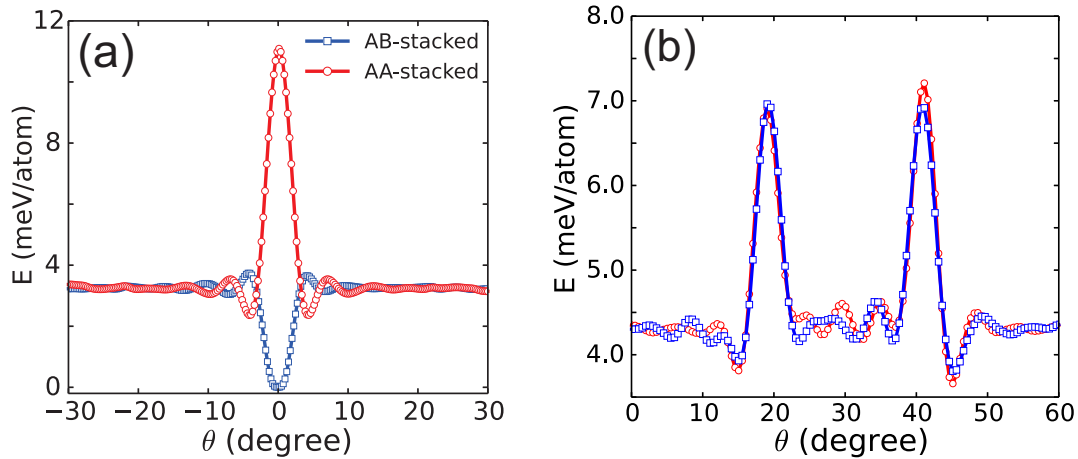


FIGURE A.2. (a) The variation of vdW-energy for rotation of a flake around the z -axis over pristine graphene starting with initial AB-stacking (square blue symbols) and AA-stacking (circle red symbols). The variation of vdW-energy when the flake \otimes shown in Fig. 6.1 is rotated around z -axis where initially the center of mass of the flake is located at the center of a pentagon (blue curve) or heptagon (red curve).

A.4 Trajectory above perfect graphene

In Fig. A.4, we show trajectories for several flakes moving with $v_0 = 100$ m/s over pristine graphene along the x -axis for several different initial θ s (which were set at an incommensurate state). The position (x,y) of the flake refers to the center of mass. Three typical snapshots taken at different times of motion for one flake are shown at the RHS of Figs. A.4(b-d). It is seen that the flake does not change its initial state even after 5 nm displacement.

A.5 Velocity variations

To get more insights, we show in Fig. A.5(a) the variation of the x -component of the velocity (v_x) of one of the flakes moving over pristine graphene with initial $\theta = 30^\circ$ and $v_0 = 100$ m/s. The corresponding variation of θ is shown in Fig. A.5(c). Also shown in Fig. A.5(b) is the variation of v_x of a flake moving with initial $\theta = \theta_L$ and $v_0 = 100$ m/s over graphene containing a LAGBI. The corresponding variation of $\theta + 2\theta_L$ is shown in Fig. A.5(c) (note that final AB

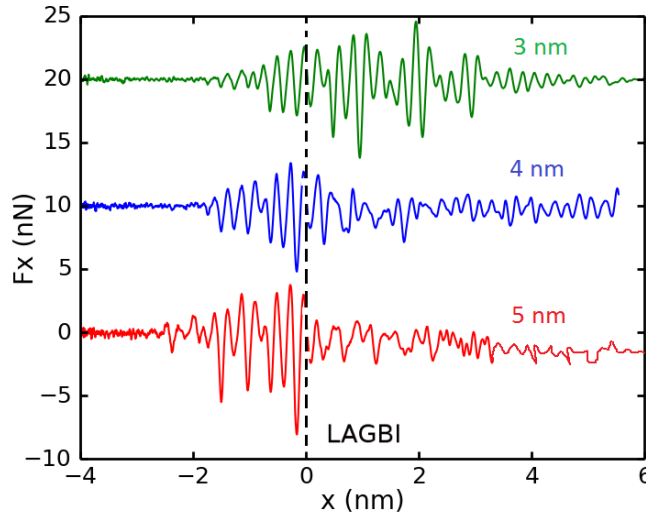


FIGURE A.3. The variations of F_x with x positions of the center of mass for three different flakes with sizes 3, 4, 5 nm, respectively. For 3, 4 nm sizes the curves are shifted by 20, 10 nN, in order to be distinguishable.

state has $\theta + 2\theta_L = 0^\circ$). It is clear that the edge of the flake is repelled by the LAGBI line resulting in backscattering of the flake. Notice that the flake eventually traps into the AB-stacking configuration. The backscattering effect is also found for the other grain boundaries shown in Figs. A.1(c,d). However, we observed that if a substrate contains only a single 5-7 defect, the defect only changes the path of motion of the flake instead of being backscattered.

A.6 Channel design

We designed three particular channels using LAGBI lines and shoot a flake with $v_0 = 100$ m/s over and along the LAGBI lines (see Fig. A.6). In Fig. A.6(a) the flake is moving parallel to the two LAGBI lines which are separated by 3 nm. In Fig. A.6(b) on each side there are two LAGBI lines each are separated by 0.3 nm and the distance between RHS and LHS double lines is ~ 4 nm. In Figs. A.6(c) the flake is moved over two LAGBI lines which are separated by 0.3 nm. We observe superlubricity in the motion of the graphene flakes over and along the double LAGBI line in Fig. A.6(b). In fact, by shooting the flake along the y -axis over the channel (b), it moves continuously inside the

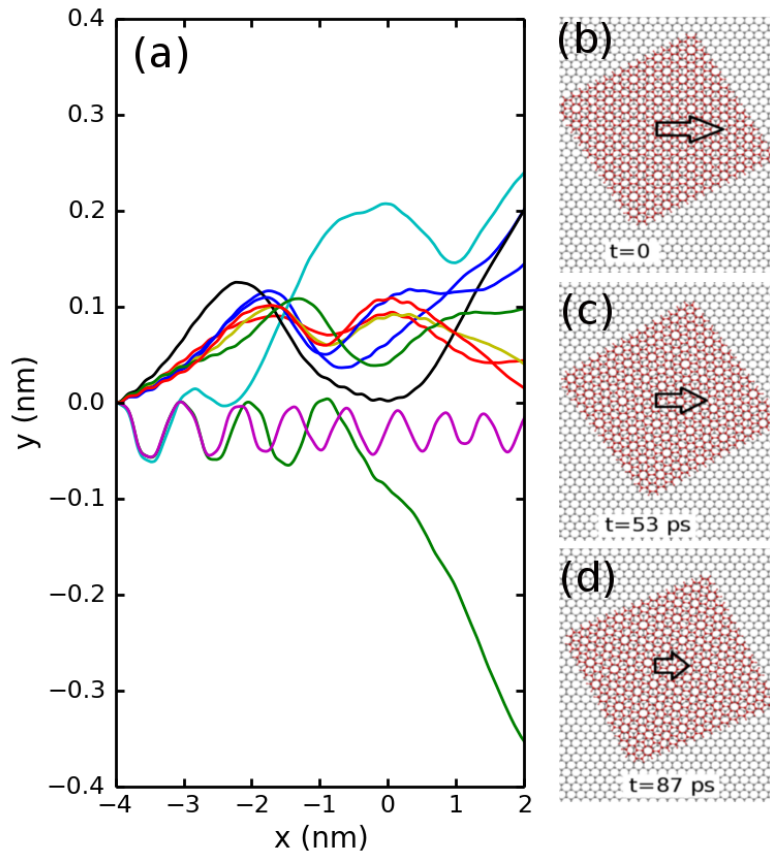


FIGURE A.4. (a) The path of motion of graphene flakes moving over perfect graphene with $v_0 = 100$ m/s for different initial θ which started from incommensurate states (indicated by different colors). In (b,c,d) we show three snapshots taken at three different times for a flake over pristine graphene. The larger the arrows the larger the value of v_x .

channel until it reaches a final commensurate state (the larger the initial velocity v_0 the longer the motion), while it passes the LAGBI lines in (a) and (c). In (d) we show the final state of motion of the flake that started its motion in (c).

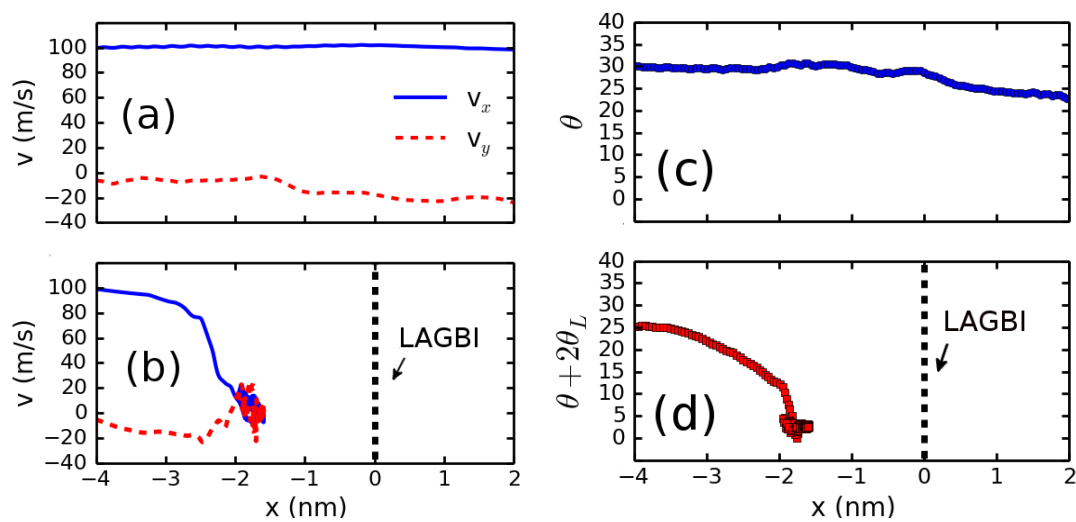


FIGURE A.5. The variation of x-component of the velocity (v_x) of a flake moving on (a) pristine graphene, and (b) a graphene substrate with LAGBI GB. The dotted line in (b) indicates the LAGBI line located at $x=0$. The corresponding variations of θ are shown in (c,d) where in both cases $v_0 = 100$ m/s.

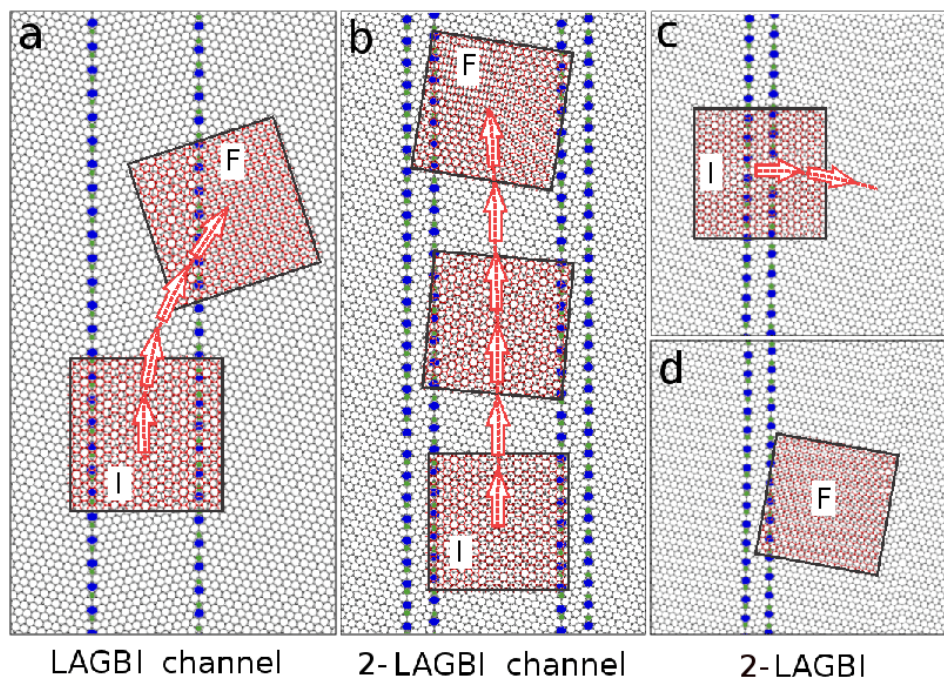


FIGURE A.6. Three different designed channels for controlling the motion of a flake. The initial velocity of the square flake of size $l=4$ nm is $v_0 = 100$ m/s along the LAGBI lines. (a) Two LAGBI separated by 3 nm, (b) two double LAGBI lines which are separated by ~ 4 nm, and (c,d) two LAGBI lines (with opposite directions) separated by 0.3 nm. The arrows indicate the path of motion. The labels “I” and “F” refer to the initial and final (locked) states.

APPENDIX B

B.1 Bubble elasticity

Nonlinear equations for an isotropic elastic thin plate is often used to describe the mechanical behavior of monolayer graphene as given by

$$\kappa \nabla^4 z(r) - N_{ij} \frac{\partial^2 z}{\partial x_i \partial x_j} = q, \quad (\text{B.1})$$

where κ is the bending moduli, $z(r)$ is the deformation, $N_{ij} = \frac{Y}{2(1+\nu)}(\varepsilon_{ij} + \frac{\nu}{1-\nu}\delta_{ij})$ is the in-plane membrane force, and q is the lateral loading intensity (usually external pressure). Note that in N_{ij} definition, Y is linear elastic modulus, ν is Poisson's ratio, and ε_{ij} is the strain tensor. Eq. (B.1) is independent of the trapped material. When the membrane is subjected to a uniform lateral load, neglecting bending stiffness plus applying clamped boundary condition at the edge (i.e. $z = \frac{dz}{dr} = 0$ at $r = R$), this equation can be solved analytically, giving the deflection profile

$$z(r) = h_{\max} \left(1 - \left(\frac{r}{R}\right)^2\right) \quad (\text{B.2})$$

and the radial displacement

$$u(r) = u_0 \frac{r}{R} \left(1 - \frac{r}{R}\right), \quad (\text{B.3})$$

where h_{\max} is the maximum height, and R is radius of the bubble, u_0 is a parameter determined later, and r is the radial distance. In order to estimate

the adhesion energy, we wrote the elastic energy of deformed membrane as a function of the strain tensor components. Using the deformation of graphene described by Eqs. (B.2,B.3), the radial and circumferential strain components are obtained as

$$\begin{aligned}\varepsilon_r &= \frac{\partial u(r)}{\partial r} + \frac{1}{2} \left(\frac{\partial z}{\partial r} \right)^2 = \frac{u_0}{R} \left(1 - \frac{2r}{R} \right) + \frac{2h_{\max}^2 r^2}{R^4}, \\ \varepsilon_\theta &= \frac{u(r)}{r} = \frac{u_0}{R} \left(1 - \frac{r}{R} \right).\end{aligned}\quad (\text{B.4})$$

The corresponding in-plane stretching energy density per unit area is

$$U_s = \frac{Y}{2(1-\nu^2)} [\varepsilon_r^2 + 2\nu\varepsilon_r\varepsilon_\theta + \varepsilon_\theta^2], \quad (\text{B.5})$$

$$= \frac{Y}{2(1-\nu^2)} \left[\frac{4h_{\max}^4 r^4}{R^8} + \left(\frac{u_0}{R} \right)^2 \left(4 - \frac{12r}{R} + \frac{9r^2}{R^2} \right) + \frac{4h_{\max}^2 u_0 r^2}{R^5} \left(1 - \frac{r}{R} \right) \right]. \quad (\text{B.6})$$

The total energy difference per unit area is due to the strain energy of the membrane and the externally induced the deformation energy by the pressure difference between inside and outside of the bubble. It is determined by

$$dF = dU_s - (p - p_0)dV. \quad (\text{B.7})$$

For a bubble in equilibrium with fixed radius (R), we minimize the energy as follows:

$$\frac{\partial F}{\partial u_0} = \frac{\partial F}{\partial h_{\max}} = 0. \quad (\text{B.8})$$

Using $\nu=0.16$, the applied pressure as a function of maximum deflection and bubble radius is given by Eq. (7.1) within the main text. Thus the pressure inside the bubble can be determined from measurement of R and h_{\max} assuming P_0 can be ignored ($P_0 \ll P$). The interface energy ($\pi R^2 \Gamma$) is defined by using adhesion energy between graphene and substrate interface, Γ . The equilibrium bubble radius is obtained by balancing the potential energy of the bubble and the adhesion energy of the graphene-substrate interface,

$$\frac{\partial F}{\partial R} = -2\pi R \Gamma. \quad (\text{B.9})$$

This eventually results in the following equations

$$P_{\text{hyd}} \cong 2.85 \frac{Y h_{\max}^3}{R^4}, \quad \Gamma \cong 1.79 \frac{Y h_{\max}^4}{R^4}. \quad (\text{B.10})$$

Nonlinear plate theory and taking into account the effect of the bending stiffness (κ) that is used in the analysis of graphene bubbles is applied. Using similar approach by treating the graphene monolayer as an elastic plate, the deflection profile and radial displacement can be found to be

$$z(r) = h_{\max} \left(1 - \left(\frac{r}{R}\right)^2\right)^2, \quad (\text{B.11})$$

$$u(r) = r(R - r)(c - dR), \quad (\text{B.12})$$

where c and d are parameters that are determined later. For the radial and circumferential strain components we have

$$\varepsilon_r = -Rc + 2(c + Rd)r - 3dr^2 + \frac{8h_{\max}^2 r^2 (R^2 - r^2)^2}{R^8}, \quad \varepsilon_\theta = (R - r)(c - dr). \quad (\text{B.13})$$

To obtain the strain tensor, we need to consider both in-plane stretching and bending contributions into the energy density, i.e $U = U_s + U_b$ where

$$U_b = \frac{\kappa}{2} \left[\left(\frac{d^2 z}{dr^2}\right)^2 + \frac{1}{r^2} \left(\frac{dz}{dr}\right)^2 + \frac{2\nu}{r} \frac{dz}{dr} \frac{d^2 z}{dr^2} \right] \quad (\text{B.14})$$

$$= \frac{16\kappa h_{\max}^2}{R^8} [R^2(1 + \nu)(R^2 - 4r^2) + (5 + 3\nu)r^4]. \quad (\text{B.15})$$

The introduced parameters (c and d) are obtained by minimizing the total energy $\frac{\partial F}{\partial c} = \frac{\partial F}{\partial d} = 0$. Consequently, $\frac{\partial F}{\partial h_{\max}} = 0$ and assuming $\nu = 0.16$ gives us the pressure as

$$P_{\text{hyd}} \cong 2.56 \frac{Y h_{\max}^3}{R^4} + 64 \frac{\kappa h_{\max}}{R^4}. \quad (\text{B.16})$$

Finally, using Eq. (B.9), we obtained the adhesion energy which is given by

$$\Gamma \cong \frac{Y h_{\max}^4}{R^4} + 32 \frac{\kappa h_{\max}^2}{R^4}. \quad (\text{B.17})$$

Moreover, the stress-strain components σ_r and σ_θ for a 2D plate are given by

$$\sigma_r = \frac{Y}{(\nu + 1)(2\nu - 1)} [(\nu - 1)\varepsilon_r - \nu\varepsilon_\theta], \quad (\text{B.18})$$

$$\sigma_\theta = \frac{Y}{(\nu + 1)(2\nu - 1)} [(\nu - 1)\varepsilon_\theta - \nu\varepsilon_r]. \quad (\text{B.19})$$

Substituting ε_r and ε_θ from Eq. (B.13) into Eqs. (B.18,B.19), each separately results in a polynomial function of $x = r/R$ defined by

$$f_\sigma(x) = 1 + Ax + Bx^2 + Cx^4 \quad (\text{B.20})$$

where A, B, and C are coefficients depending on the elastic constants. Table B.1 shows the corresponding fitting coefficients of the ethanol bubble discussed within main text (Stress Calculations).

TABLE B.1. Fitting parameters of $f_\sigma(x)$ for ethanol bubble ($x < 1$) based on MD data (σ_{rr} and $\sigma_{\theta\theta}$) and quality factor Q.

Fit Coeffs.	$f_{\sigma_{rr}}(x)$	$f_{\sigma_{\theta\theta}}(x)$
A	0.0759	0.265
B	-1.068	-3.098
C	0.396	1.547
Q	0.994	0.987

B.2 Bubble volume and radius calculation

The pressure (P) and density (ρ) of the materials inside the bubble crucially depend on how accurately we determine the bump volume V_b using Eqs. (7.4) and (7.5) within the main text. Furthermore, measuring the height and radius of the bubble is important to obtain the morphology of the bubble. To calculate the volume of the bubble, the top graphene layer is fitted by a function $h(x, y)$ determine the time average xyz coordinate of the carbon atoms. Because not the whole space of the volume is accessible to the trapped atoms -due to repulsive potential between graphene and the atoms- we defined the effective height function $h_{\text{eff}}(x, y)$ which excludes the volume related to the distance between the molecule-graphene ($\sigma_{\text{mol-C}}$):

$$h_{\text{eff}}(x, y) = h(x, y) - \sigma_{\text{mol-C}}, \quad (\text{B.21})$$

where $\sigma_{\text{mol-C}}$ is the average LJ parameter between trapped molecules and C atoms. Then, we estimated the volume and the radius by integrating over the

bump area using the following equations:

$$V = \int_{\text{bump}} h_{\text{eff}}(x, y) dx dy, \quad (\text{B.22})$$

$$A = \int_{\text{bump}} dx dy \Rightarrow r = \sqrt{A/\pi}. \quad (\text{B.23})$$

The bump area is defined by the estimated region where the trapped atoms exist. We admit that without corrections for the effective volume of the bump due to difficulty in estimating the exact accessible volume for the trapped atoms, MD overestimates the measured volume. Consequently, it underestimates the pressure and the density. This effect becomes important for small bubbles when the size of the excluded volume is comparable to the total volume.

B.3 Solvents

We have used water, ethanol and methanol as solvents to fabricate solvent filled graphene nanobubbles. We presented the data and AFM images of water/ethanol filled with graphene nanobubbles in Figs. 4(a,b) and 7(a,b) within the main text. We have also carried out Raman spectroscopy as a characterization technique to probe the presence of trapped substances. As a reference, here we have shown the Raman spectrum of bulk methanol/ethanol and methanol/ethanol filled graphene nanobubbles (see Figs. B.1(a,b)). It is clear that all the Raman bands related to the methanol/ethanol (indicated as red color arrow marks in the inset figures) are present in the corresponding nanobubbles with small shifts in the wavenumbers.

B.4 Atomic force microscopy measurements

We depict the AFM images of two typical water bubbles and four typical hydrocarbon bubbles which the (none-) round-shape hydrocarbon bubbles can be seen from the images shown in Figs. B.2(a-b) and B.3(a-d).

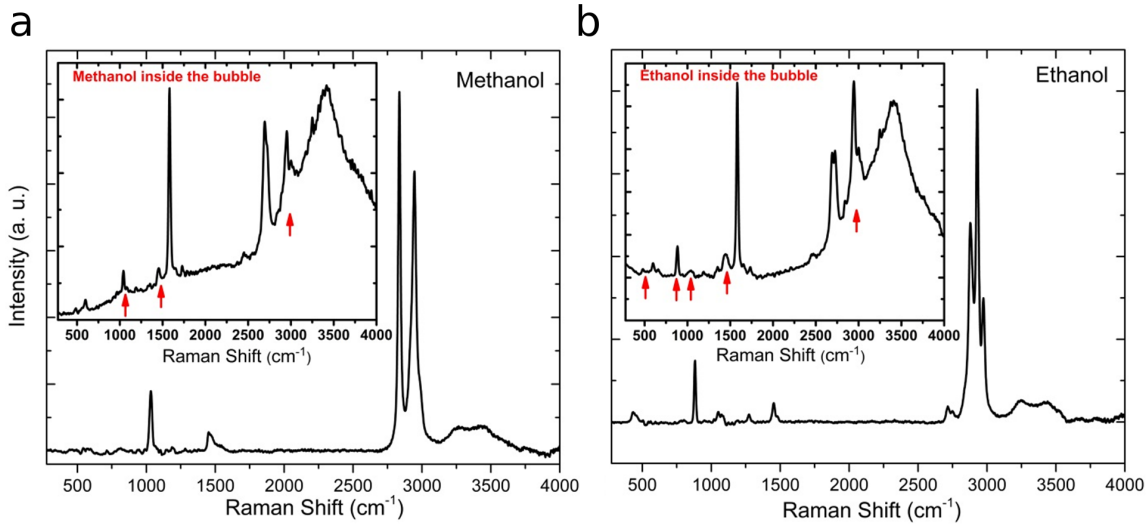


FIGURE B.1. (a) and (b) respectively shows Raman spectrum of bulk methanol/ethanol and methanol/ethanol filled graphene nanobubbles (Inset figures).

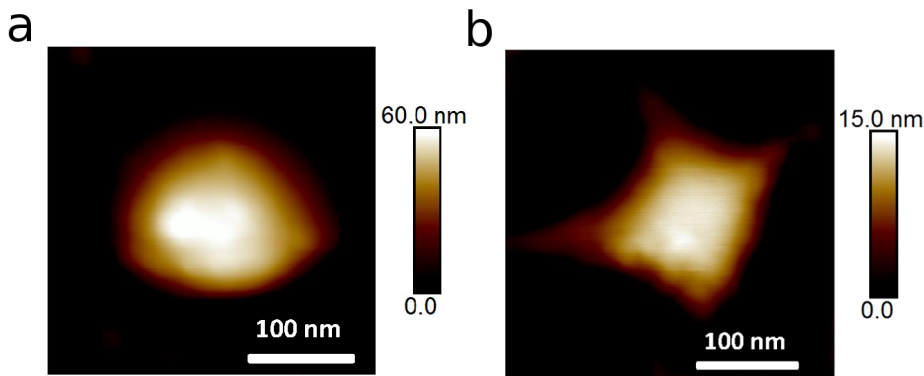


FIGURE B.2. (a-b) two typical AFM images of a water nanobubble.

B.5 Deformation profile

For the deformation profiles of the graphene sheet, based on elastic theory, it is found that it can be fitted by a polynomial function:

$$f(x) = 1 - x^2 + \alpha(x^2 - x^4), \quad x \in [-1, 1], \quad (\text{B.24})$$

where $x = r/R$ and r is the radial distance from the center of the bubble. Notice that $f(\pm 1) = 0$, and the $|\alpha|$ parameter determines the strength of the nonlinear elasticity of the top graphene sheet and it is taken as a fitting parameter (Ref. [85]). In Fig. B.4, we show the height-profile from our MD

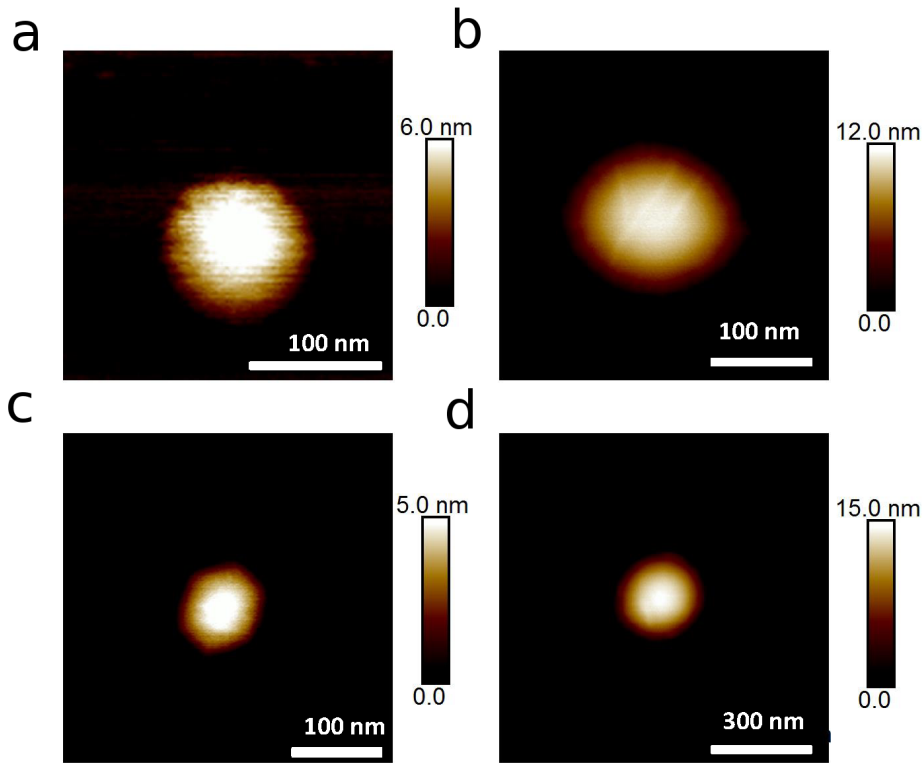


FIGURE B.3. (a-d) four typical AFM images of hydrocarbon nanobubble.

simulations and the fit function $f(x)$ for helium (a), water (b), and ethanol (c) at room temperature. In Table B.2, we provide a list of the corresponding fit parameters for the studied polar liquids and helium at 0 K and 300 K. The sign of α is consistent with the prediction of $\alpha = -1$ (Ref. [85]), however its value is different. The smaller $|\alpha|$ value for ethanol indicates smaller nonlinear effects (and bending stiffness effects). Notice that the deformation profiles for hydrocarbon bubbles have higher quality factor – Q – which is defined by $Q = 1 - \sqrt{\frac{1}{N} \sum_{i=1}^N (h_i/h_{\max} - f(x_i))^2}$ leading us to conclude that the experimental bubbles are filled by hydrocarbons rather than water and helium.

TABLE B.2. Fitting parameter α presented in Eq. (B.24) at zero and room temperature for polar liquids and helium, where Q is the quality factor of the fit and $Q=1$ corresponds to perfect fit.

Trapped substance	0 K		300 K	
	α	Q	α	Q
Helium	-0.56	0.967	-0.21	0.966
Water	-0.37	0.972	-0.54	0.978
Ethanol	-0.13	0.981	-0.39	0.984

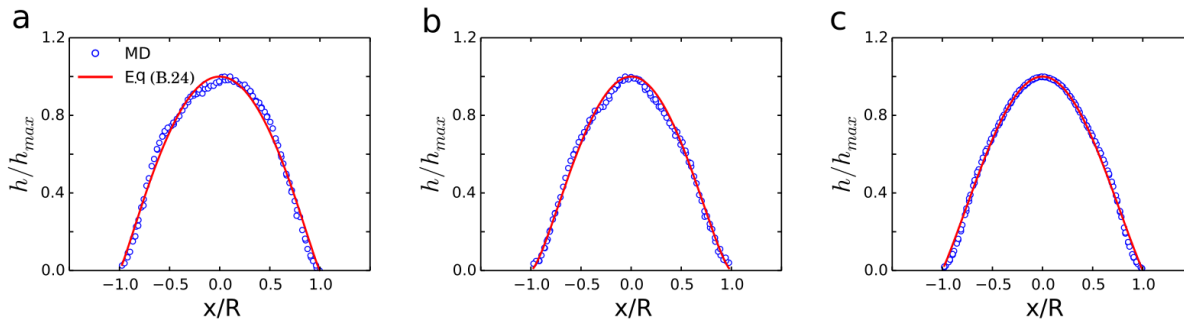


FIGURE B.4. Three horizontal cross sections from graphene bumps containing (a) helium, (b) water and (c) ethanol at 300 K with corresponding fitting function given in Eq. (B.24).

B.6 The effect of bubble size on density profile

Figure B.5(a) shows the average density profile of oxygen atoms along the z -axis for two typical ethanol bubbles with sizes of 150 (blue squares) and 200 (red circles) molecules at 0K. The peak(s) indicate the layered structure of trapped atoms. By increasing the number of atoms more layers are formed. Similarly, density of oxygen atom along z -axis for two typical water bubbles with sizes of 800 (blue squares) and 2300 (red circles) molecules at 0K are shown in Fig. B.5(b).

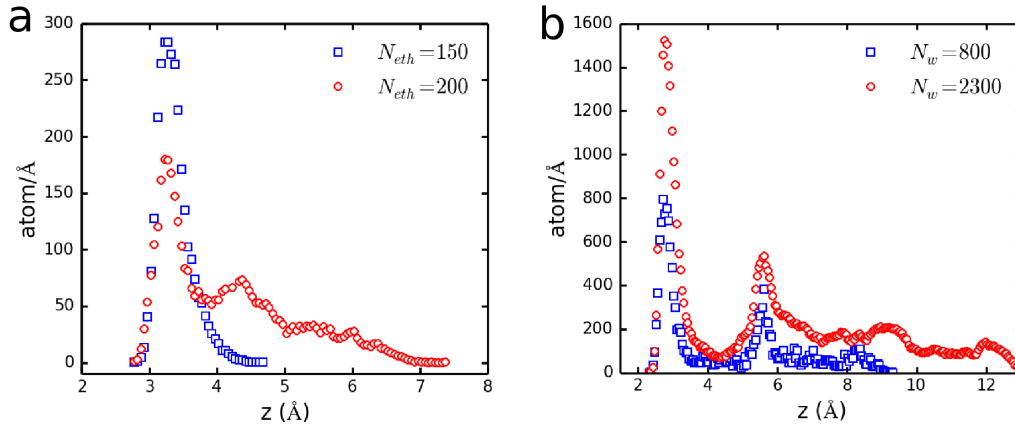


FIGURE B.5. The average density profile of oxygen atoms along z -axis for two different number of trapped molecules for (a) ethanol and (b) water nanobubble.

B.7 The effects of boundary stress

Finally, we studied a strained bubble and its effect on the trapped water structure. In order to induce boundary stress, we carried out two additional simulations: i) fixed the top graphene sheet atoms beyond a circle with radius 15 nm, and ii) we similarly fixed the top graphene sheet atoms beyond a square block of size $15 \times 15 \text{ nm}^2$. The former is equivalent to inducing a triaxial stress Ref. [332] ($\sigma_{xx} = -\sigma_{yy}$, $\sigma_{xy} = \sigma_{yx}$) and the later corresponds to the application of biaxial stress ($\sigma_{xx} = \sigma_{yy}$, $\sigma_{xy} = \sigma_{yx} = 0$). The bubble, subjected to such boundary stress, forms trigon and linear wrinkles and the optimized structure are shown respectively in Figs. B.6(a,b). Wrinkles and ripples are commonly observed in experiment. Such boundary stress fundamentally changes the shape of the bubble (Refs. [333–335]). The circular bubbles filled with water are found to be elongated and flattened due to the applied boundary stress.

B.8 The effect of adhesion energy

To investigate the effect of the van der Waals pressure on the structure of the trapped atoms, we performed several simulations using an extra Lennard-Jones (LJ) interaction between the graphene substrate and the cover layer in case of a water bubble with 792 water molecules at room temperature. In fact

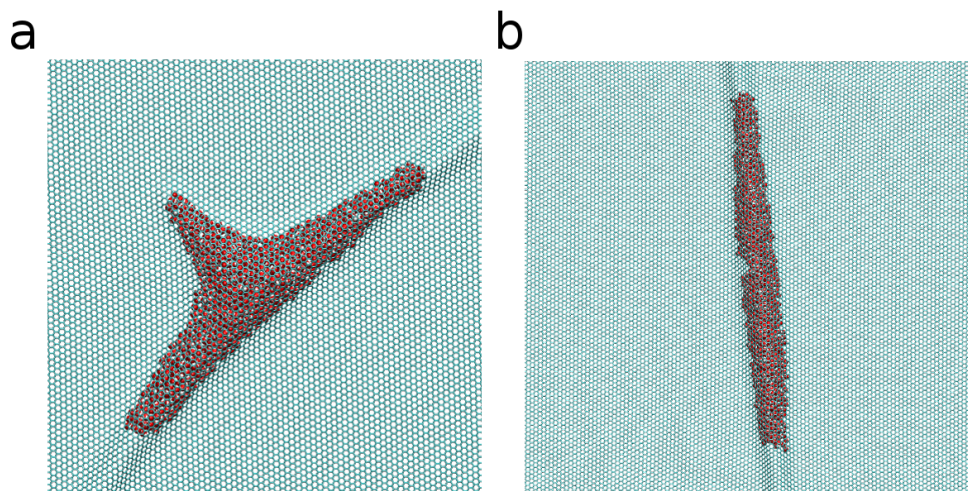


FIGURE B.6. Top view of trigon (a) and linear (b) wrinkle corresponding to triaxial and biaxial stress at $T=0$. The water molecules (dark particles) are partially distributed within the wrinkles. Top graphene sheet is fixed beyond the circular region in (a) and a square region in (b) resulting in different types of wrinkle formation.

by tuning the energy parameter (ϵ) in the LJ potential, we have been able to elucidate the effects of adhesion between the two graphene layers (outside the nanobubble region). Note that increasing the adhesion energy is equivalent to a large vdW pressure.

We calculated the RDF of trapped water for several values of ϵ at room temperature. The second and third peaks become more pronounced when the depth of the potential well in the LJ potential deepens from 0 to 100 meV (see Fig. B.7). This is a signature of increasing long-range ordering due to the crystalline structure of nanoconfined water. Even by increasing the adhesion energy between the two graphene sheets, which is equivalent to increasing the vdW pressure, a more ordered structure for water is obtained, however the square ice structure and its stacking structure are not seen. This casts some doubts on the observation of square ice in Ref. [125]. In contrast, based on our MD data for salt bubble and corresponding RDF with first peak at 2.8 \AA , we argue that the observed square structure belongs to face-centered cubic NaCl lattice.

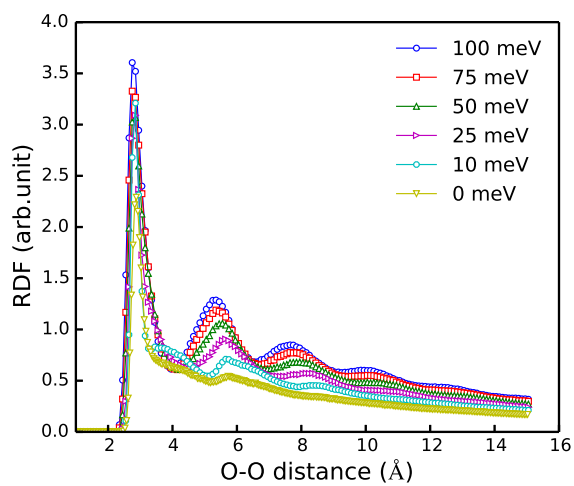


FIGURE B.7. The O-O radial distribution of confined water molecules for different LJ interaction strength (ϵ) between two graphene layers at room temperature.

APPENDIX C

C.1 OPLS model for Graphene Oxide

We performed several extra MD simulations in order to validate how close our simple model, based on surface charges, is to describe more real graphene oxide nanocapillaries. For comparative reason, we simulated two systems, one with excessive surface charges and the other containing functional groups *i.e.* epoxy (-O-) and hydroxyl (-OH) using a similar setup as discussed in the model and method sections of the main text. The -O- and -OH groups are randomly added to both sides of the graphene sheets and they are not allowed to diffuse during simulations. We assumed that the functional groups

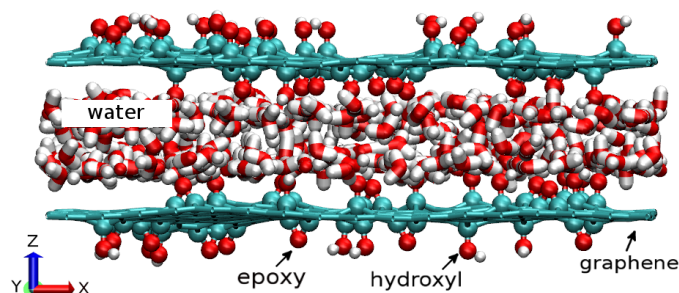


FIGURE C.1. Side view snapshot of water and graphene oxide nanocapillary containing epoxy and hydroxyl functional groups implemented by OPLS potentials.

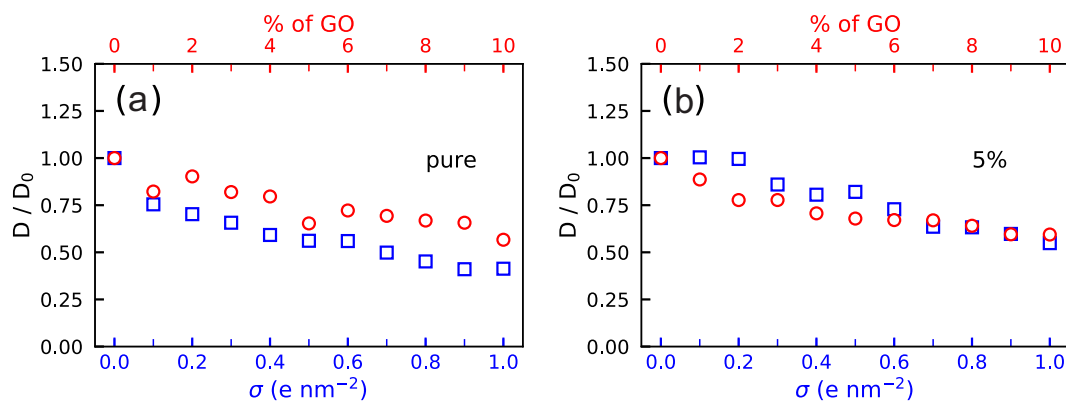


FIGURE C.2. For comparative reason, the diffusion coefficient, as a typical dynamical property, is obtained for pure water (a) and water with 5% ion concentration (b) using our surface charges model and OPLS. Both results are very close supporting the use of our charge surface model (blue bottom scale) to describe the impact of functional groups (red top scale) over GO surface. The scale D_0 refers to the diffusion factor of pristine graphene and the average capillary interlayer distance is 1 nm.

have at least a radial distance of 3\AA . We introduce the ratio n_O/n_C , where n_O and n_C stand for the number of oxide sites and carbon atoms, respectively (see Fig. C.1), in order to make a link with the synthesis of graphene oxide reported in experiments [336]. The same SPC/E model [192] employed for water molecules and optimized potentials for liquid simulations (OPLS) has been used for the functional groups that contains bonds, angles, dihedrals, and non-bonded interactions [192]. The water-GO interaction was described by LJ 6-12 and Coulomb pair potentials [192]. Furthermore, the Adaptive Intermolecular Reactive Empirical Bond Order (AIREBO) potential was used for the graphene layers [196]. The graphene oxide layers are free to move with average separation distance of 1 nm and the total density of 1 g cm^{-3} of water was obtained after relaxing the system.

In Figs. C.2(a,b), we depict the variation of the diffusion coefficient of pure water and 5% concentrations as function of n_O/n_C for graphene oxide (red top scale) and compared it with those obtained from varying surface charge density σ (blue bottom scale). The results are very close which justifies the use of our more simple model in this work. As a result, replacing functional

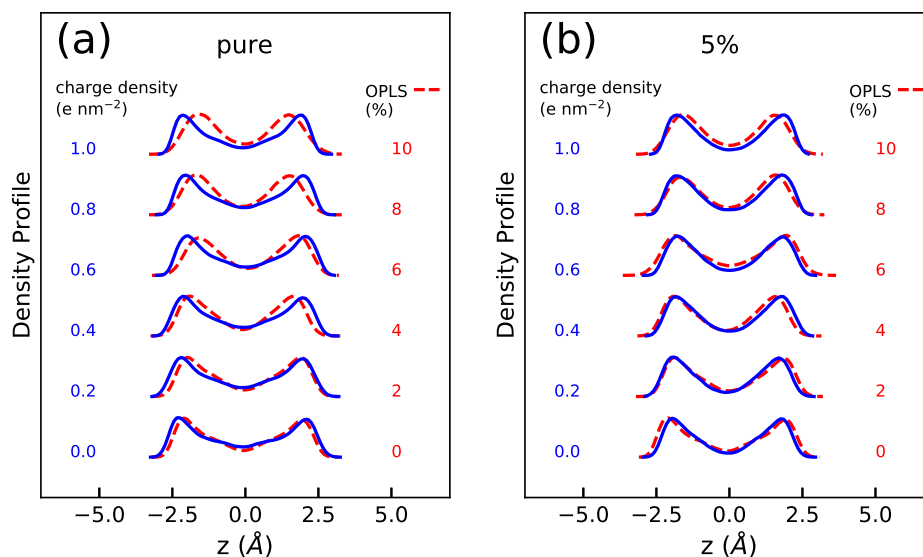


Figure C.3: Corresponding density profiles of oxygen atoms in water along the confinement direction (z -axis) of pure water (a) and 5% ion concentration (b) are evaluated from the surface charge density model (solid blue lines) and the model with functional groups coverage (dashed red lines). The graphs for each surface charge density (functionals) are shifted.

groups with charges over the graphene surface is a physically meaningful simplification in modeling and simulating the dynamical properties of water inside GO membranes.

Figures C.3(a,b) show a comparison of the corresponding density profiles of pure water and water with 5% ion concentration along the confinement direction for the excessive surface charge model (solid blue lines) and the OPLS model (dashed red lines). The results indicate that both are almost the same and commensurability exists in the latter model albeit it is a little suppressed due to the presence of functional groups between the surface and water.

BIBLIOGRAPHY

- [1] V. Singh, D. Joung, L. Zhai, S. Das, S. I. Khondaker, and S. Seal, “Graphene based materials: past, present and future,” *Progress in materials science*, vol. 56, no. 8, pp. 1178–1271, 2011.
- [2] R. R. Nair, H. A. Wu, P. N. Jayaram, I. V. Grigorieva, and A. K. Geim, “Unimpeded permeation of water through helium-leak-tight graphene-based membranes,” *Science*, vol. 335, pp. 442–444, jan 2012.
- [3] K.-G. Zhou, K. Vasu, C. Cherian, M. Neek-Amal, J. C. Zhang, H. Ghorbanfekr-Kalashami, K. Huang, O. Marshall, V. Kravets, J. Abraham, *et al.*, “Electrically controlled water permeation through graphene oxide membranes,” *Nature*, vol. 559, no. 7713, p. 236, 2018.
- [4] A. Esfandiar, B. Radha, F. C. Wang, Q. Yang, S. Hu, S. Garaj, R. R. Nair, A. K. Geim, and K. Gopinadhan, “Size effect in ion transport through ångstrom-scale slits,” *Science*, vol. 358, pp. 511–513, oct 2017.
- [5] L. Chen, G. Shi, J. Shen, B. Peng, B. Zhang, Y. Wang, F. Bian, J. Wang, D. Li, Z. Qian, G. Xu, G. Liu, J. Zeng, L. Zhang, Y. Yang, G. Zhou, M. Wu, W. Jin, J. Li, and H. Fang, “Ion sieving in graphene oxide membranes via cationic control of interlayer spacing,” *Nature*, vol. 550, pp. 380–383, oct 2017.
- [6] J. Abraham, K. S. Vasu, C. D. Williams, K. Gopinadhan, Y. Su, C. T. Cherian, J. Dix, E. Prestat, S. J. Haigh, I. V. Grigorieva, *et al.*, “Tunable sieving of ions using graphene oxide membranes,” *Nature nanotechnology*, vol. 12, no. 6, p. 546, 2017.
- [7] B. Grosjean, M.-L. Bocquet, and R. Vuilleumier, “Versatile electrification of two-dimensional nanomaterials in water,” *Nature Communica-*

- tions, vol. 10, p. 1656, Apr. 2019.
- [8] D. W. Boukhvalov, M. I. Katsnelson, and Y.-W. Son, "Origin of anomalous water permeation through graphene oxide membrane," *Nano letters*, vol. 13, no. 8, pp. 3930–3935, 2013.
- [9] L. Joly, G. Tocci, S. Merabia, and A. Michaelides, "Strong coupling between nanofluidic transport and interfacial chemistry: How defect reactivity controls liquid–solid friction through hydrogen bonding," *The journal of physical chemistry letters*, vol. 7, no. 7, pp. 1381–1386, 2016.
- [10] A. P. Thompson, S. J. Plimpton, and W. Mattson, "General formulation of pressure and stress tensor for arbitrary many-body interaction potentials under periodic boundary conditions," *The Journal of chemical physics*, vol. 131, no. 15, p. 154107, 2009.
- [11] W. A. Harrison, *Electronic structure and the properties of solids: the physics of the chemical bond*. Courier Corporation, 2012.
- [12] K. S. Novoselov, A. K. Geim, S. V. Morozov, D. Jiang, Y. Zhang, S. V. Dubonos, I. V. Grigorieva, and A. A. Firsov, "Electric field effect in atomically thin carbon films," *science*, vol. 306, no. 5696, pp. 666–669, 2004.
- [13] A. K. Geim and K. S. Novoselov, "The rise of graphene," in *Nanoscience and Technology: A Collection of Reviews from Nature Journals*, pp. 11–19, World Scientific, 2010.
- [14] M. Lemme, "Current status of graphene transistors," *Solid State Phenomena*, vol. 156-158, pp. 499–509, oct 2009.
- [15] M. J. Allen, V. C. Tung, and R. B. Kaner, "Honeycomb carbon: a review of graphene," *Chemical reviews*, vol. 110, no. 1, pp. 132–145, 2009.
- [16] P. R. Wallace, "The band theory of graphite," *Physical Review*, vol. 71, pp. 622–634, May 1947.
- [17] N. D. Mermin, "Crystalline order in two dimensions," *Physical Review*, vol. 176, no. 1, p. 250, 1968.
- [18] J. C. Meyer, A. K. Geim, M. I. Katsnelson, K. S. Novoselov, T. J. Booth, and S. Roth, "The structure of suspended graphene sheets," *Nature*,

- vol. 446, no. 7131, p. 60, 2007.
- [19] A. Fasolino, J. Los, and M. I. Katsnelson, “Intrinsic ripples in graphene,” *Nature materials*, vol. 6, no. 11, p. 858, 2007.
- [20] J. Lloyd-Hughes and T.-I. Jeon, “A review of the terahertz conductivity of bulk and nano-materials,” *Journal of Infrared, Millimeter, and Terahertz Waves*, vol. 33, pp. 871–925, may 2012.
- [21] A. Jain and A. J. McGaughey, “Strongly anisotropic in-plane thermal transport in single-layer black phosphorene,” *Scientific reports*, vol. 5, p. 8501, 2015.
- [22] Z. Aslani, E. T. Sisakht, F. Fazileh, H. Ghorbanfekr-Kalashami, and F. Peeters, “Conductance fluctuations of monolayer graphene in the topological phase using a low-energy effective tight-binding hamiltonian,” *Physical Review B*, vol. 99, no. 11, p. 115421, 2019.
- [23] M. Chhowalla, Z. Liu, and H. Zhang, “Two-dimensional transition metal dichalcogenide (tmd) nanosheets,” *Chemical Society Reviews*, vol. 44, no. 9, pp. 2584–2586, 2015.
- [24] A. K. Geim, “Nobel lecture: Random walk to graphene,” *Reviews of Modern Physics*, vol. 83, no. 3, p. 851, 2011.
- [25] M. Yi and Z. Shen, “A review on mechanical exfoliation for the scalable production of graphene,” *Journal of Materials Chemistry A*, vol. 3, no. 22, pp. 11700–11715, 2015.
- [26] Y. Hernandez, V. Nicolosi, M. Lotya, F. M. Blighe, Z. Sun, S. De, I. McGovern, B. Holland, M. Byrne, Y. K. Gun’Ko, *et al.*, “High-yield production of graphene by liquid-phase exfoliation of graphite,” *Nature nanotechnology*, vol. 3, no. 9, p. 563, 2008.
- [27] L. Niu, J. N. Coleman, H. Zhang, H. Shin, M. Chhowalla, and Z. Zheng, “Production of two-dimensional nanomaterials via liquid-based direct exfoliation,” *Small*, vol. 12, no. 3, pp. 272–293, 2016.
- [28] S. Stankovich, D. A. Dikin, R. D. Piner, K. A. Kohlhaas, A. Kleinhammes, Y. Jia, Y. Wu, S. T. Nguyen, and R. S. Ruoff, “Synthesis of graphene-based nanosheets via chemical reduction of exfoliated graphite oxide,” *carbon*, vol. 45, no. 7, pp. 1558–1565, 2007.
- [29] G. Wang, J. Yang, J. Park, X. Gou, B. Wang, H. Liu, and J. Yao, “Facile

- synthesis and characterization of graphene nanosheets,” *The Journal of Physical Chemistry C*, vol. 112, no. 22, pp. 8192–8195, 2008.
- [30] W. Chen, L. Yan, and P. Bangal, “Chemical reduction of graphene oxide to graphene by sulfur-containing compounds,” *The Journal of Physical Chemistry C*, vol. 114, no. 47, pp. 19885–19890, 2010.
- [31] R. Raccichini, A. Varzi, S. Passerini, and B. Scrosati, “The role of graphene for electrochemical energy storage,” *Nature materials*, vol. 14, no. 3, p. 271, 2015.
- [32] T. C. Achee, W. Sun, J. T. Hope, S. G. Quitzau, C. B. Sweeney, S. A. Shah, T. Habib, and M. J. Green, “High-yield scalable graphene nanosheet production from compressed graphite using electrochemical exfoliation,” *Scientific reports*, vol. 8, no. 1, p. 14525, 2018.
- [33] J. M. Tour, “Top-down versus bottom-up fabrication of graphene-based electronics,” *Chemistry of Materials*, vol. 26, no. 1, pp. 163–171, 2013.
- [34] D. G. Papageorgiou, I. A. Kinloch, and R. J. Young, “Mechanical properties of graphene and graphene-based nanocomposites,” *Progress in Materials Science*, vol. 90, pp. 75–127, 2017.
- [35] X. Li, W. Cai, J. An, S. Kim, J. Nah, D. Yang, R. Piner, A. Velamakanni, I. Jung, E. Tutuc, *et al.*, “Large-area synthesis of high-quality and uniform graphene films on copper foils,” *science*, vol. 324, no. 5932, pp. 1312–1314, 2009.
- [36] Z.-J. Wang, G. Weinberg, Q. Zhang, T. Lunkenbein, A. Klein-Hoffmann, M. Kurnatowska, M. Plodinec, Q. Li, L. Chi, R. Schloegl, *et al.*, “Direct observation of graphene growth and associated copper substrate dynamics by in situ scanning electron microscopy,” *ACS nano*, vol. 9, no. 2, pp. 1506–1519, 2015.
- [37] K. Takahashi, K. Yamada, H. Kato, H. Hibino, and Y. Homma, “In situ scanning electron microscopy of graphene growth on polycrystalline ni substrate,” *Surface Science*, vol. 606, no. 7-8, pp. 728–732, 2012.
- [38] A. W. Robertson and J. H. Warner, “Atomic resolution imaging of graphene by transmission electron microscopy,” *Nanoscale*, vol. 5, no. 10, pp. 4079–4093, 2013.

- [39] R. J. Young and I. A. Kinloch, "Graphene and graphene-based nanocomposites," in *Nanoscience*, pp. 145–179, Royal Society of Chemistry.
- [40] A. A. Balandin, S. Ghosh, W. Bao, I. Calizo, D. Teweldebrhan, F. Miao, and C. N. Lau, "Superior thermal conductivity of single-layer graphene," *Nano letters*, vol. 8, no. 3, pp. 902–907, 2008.
- [41] K. S. Novoselov, A. K. Geim, S. Morozov, D. Jiang, M. Katsnelson, I. Grigorieva, S. Dubonos, Firsov, and AA, "Two-dimensional gas of massless dirac fermions in graphene," *nature*, vol. 438, no. 7065, p. 197, 2005.
- [42] C. Lee, X. Wei, J. W. Kysar, and J. Hone, "Measurement of the elastic properties and intrinsic strength of monolayer graphene," *science*, vol. 321, no. 5887, pp. 385–388, 2008.
- [43] Y. Zhu, S. Murali, W. Cai, X. Li, J. W. Suk, J. R. Potts, and R. S. Ruoff, "Graphene and graphene oxide: synthesis, properties, and applications," *Advanced materials*, vol. 22, no. 35, pp. 3906–3924, 2010.
- [44] F. Schwierz, "Graphene transistors," *Nature nanotechnology*, vol. 5, no. 7, p. 487, 2010.
- [45] J. S. Bunch, A. M. Van Der Zande, S. S. Verbridge, I. W. Frank, D. M. Tanenbaum, J. M. Parpia, H. G. Craighead, and P. L. McEuen, "Electromechanical resonators from graphene sheets," *Science*, vol. 315, no. 5811, pp. 490–493, 2007.
- [46] A. P. A. Raju, A. Lewis, B. Derby, R. J. Young, I. A. Kinloch, R. Zan, and K. S. Novoselov, "Wide-area strain sensors based upon graphene-polymer composite coatings probed by raman spectroscopy," *Advanced Functional Materials*, vol. 24, no. 19, pp. 2865–2874, 2014.
- [47] J. J. Yoo, K. Balakrishnan, J. Huang, V. Meunier, B. G. Sumpter, A. Srivastava, M. Conway, A. L. Mohana Reddy, J. Yu, R. Vajtai, *et al.*, "Ultrathin planar graphene supercapacitors," *Nano letters*, vol. 11, no. 4, pp. 1423–1427, 2011.
- [48] D. A. Brownson and C. E. Banks, "Fabricating graphene supercapacitors: highlighting the impact of surfactants and moieties," *Chemical Communications*, vol. 48, no. 10, pp. 1425–1427, 2012.
- [49] S. Patchkovskii, S. T. John, S. N. Yurchenko, L. Zhechkov, T. Heine,

- and G. Seifert, “Graphene nanostructures as tunable storage media for molecular hydrogen,” *Proceedings of the National Academy of Sciences*, vol. 102, no. 30, pp. 10439–10444, 2005.
- [50] X. Wang, L. Zhi, and K. Müllen, “Transparent, conductive graphene electrodes for dye-sensitized solar cells,” *Nano letters*, vol. 8, no. 1, pp. 323–327, 2008.
- [51] X. Miao, S. Tongay, M. K. Petterson, K. Berke, A. G. Rinzler, B. R. Appleton, and A. F. Hebard, “High efficiency graphene solar cells by chemical doping,” *Nano letters*, vol. 12, no. 6, pp. 2745–2750, 2012.
- [52] P. Solís-Fernández, M. Bissett, and H. Ago, “Synthesis, structure and applications of graphene-based 2d heterostructures,” *Chemical Society Reviews*, vol. 46, no. 15, pp. 4572–4613, 2017.
- [53] C. R. Dean, A. F. Young, I. Meric, C. Lee, L. Wang, S. Sorgenfrei, K. Watanabe, T. Taniguchi, P. Kim, K. L. Shepard, *et al.*, “Boron nitride substrates for high-quality graphene electronics,” *Nature nanotechnology*, vol. 5, no. 10, p. 722, 2010.
- [54] B. Radisavljevic, A. Radenovic, J. Brivio, i. V. Giacometti, and A. Kis, “Single-layer mos 2 transistors,” *Nature nanotechnology*, vol. 6, no. 3, p. 147, 2011.
- [55] K. S. Novoselov, A. Mishchenko, A. Carvalho, and A. H. C. Neto, “2d materials and van der waals heterostructures,” *Science*, vol. 353, p. aac9439, jul 2016.
- [56] N. Song, X. Gao, Z. Ma, X. Wang, Y. Wei, and C. Gao, “A review of graphene-based separation membrane: Materials, characteristics, preparation and applications,” *Desalination*, vol. 437, pp. 59–72, jul 2018.
- [57] D. G. Papageorgiou, I. A. Kinloch, and R. J. Young, “Mechanical properties of graphene and graphene-based nanocomposites,” *Progress in Materials Science*, vol. 90, pp. 75–127, oct 2017.
- [58] R. Lv, Q. Li, A. R. Botello-Méndez, T. Hayashi, B. Wang, A. Berkdemir, Q. Hao, A. L. Elías, R. Cruz-Silva, H. R. Gutiérrez, Y. A. Kim, H. Muramatsu, J. Zhu, M. Endo, H. Terrones, J.-C. Charlier, M. Pan, and M. Terrones, “Nitrogen-doped graphene: beyond single substitution

- and enhanced molecular sensing,” *Scientific Reports*, vol. 2, p. 586, aug 2012.
- [59] J.-C. Charlier, M. Terrones, M. Baxendale, V. Meunier, T. Zacharia, N. Rupesinghe, W. Hsu, N. Grobert, H. Terrones, and G. Amaratunga, “Enhanced electron field emission in b-doped carbon nanotubes,” *Nano Letters*, vol. 2, no. 11, pp. 1191–1195, 2002.
- [60] M. Terrones, P. Ajayan, F. Banhart, X. Blase, D. Carroll, J.-C. Charlier, R. Czerw, B. Foley, N. Grobert, R. Kamalakaran, *et al.*, “N-doping and coalescence of carbon nanotubes: synthesis and electronic properties,” *Applied Physics A*, vol. 74, no. 3, pp. 355–361, 2002.
- [61] F. Villalpando-Paez, A. Romero, E. Munoz-Sandoval, L. Martinez, H. Terrones, and M. Terrones, “Fabrication of vapor and gas sensors using films of aligned cnx nanotubes,” *Chemical Physics Letters*, vol. 386, no. 1-3, pp. 137–143, 2004.
- [62] E. Cruz-Silva, Z. Barnett, B. G. Sumpter, and V. Meunier, “Structural, magnetic, and transport properties of substitutionally doped graphene nanoribbons from first principles,” *Physical Review B*, vol. 83, no. 15, p. 155445, 2011.
- [63] L. Zhao, R. He, K. T. Rim, T. Schiros, K. S. Kim, H. Zhou, C. Gutiérrez, S. Chockalingam, C. J. Arguello, L. Pálová, *et al.*, “Visualizing individual nitrogen dopants in monolayer graphene,” *Science*, vol. 333, no. 6045, pp. 999–1003, 2011.
- [64] Y. Fujimoto and S. Saito, “Formation, stabilities, and electronic properties of nitrogen defects in graphene,” *Physical Review B*, vol. 84, no. 24, p. 245446, 2011.
- [65] P. Rani and V. Jindal, “Designing band gap of graphene by b and n dopant atoms,” *Rsc Advances*, vol. 3, no. 3, pp. 802–812, 2013.
- [66] B. Mortazavi, S. Ahzi, V. Toniazzo, and Y. Rémond, “Nitrogen doping and vacancy effects on the mechanical properties of graphene: A molecular dynamics study,” *Physics Letters A*, vol. 376, no. 12-13, pp. 1146–1153, 2012.
- [67] H. Zhao, K. Min, and N. Aluru, “Size and chirality dependent elastic properties of graphene nanoribbons under uniaxial tension,” *Nano*

- letters*, vol. 9, no. 8, pp. 3012–3015, 2009.
- [68] H. Ghorbanfekr-Kalashami, M. Neek-Amal, and F. M. Peeters, “N-doped graphene: Polarization effects and structural properties,” *Phys. Rev. B*, vol. 93, p. 174112, May 2016.
- [69] P. Y. Huang, C. S. Ruiz-Vargas, A. M. van der Zande, W. S. Whitney, M. P. Levendorf, J. W. Kevek, S. Garg, J. S. Alden, C. J. Hustedt, Y. Zhu, J. Park, P. L. McEuen, and D. A. Muller, “Grains and grain boundaries in single-layer graphene atomic patchwork quilts,” *Nature*, vol. 469, pp. 389–392, jan 2011.
- [70] T. Albrecht, H. Mizes, J. Nogami, S.-i. Park, and C. Quate, “Observation of tilt boundaries in graphite by scanning tunneling microscopy and associated multiple tip effects,” *Applied physics letters*, vol. 52, no. 5, pp. 362–364, 1988.
- [71] C. R. Clemmer and T. P. Beebe, “Graphite: a mimic for dna and other biomolecules in scanning tunneling microscope studies,” *Science*, vol. 251, no. 4994, pp. 640–642, 1991.
- [72] O. V. Yazyev and S. G. Louie, “Topological defects in graphene: Dislocations and grain boundaries,” *Physical Review B*, vol. 81, no. 19, p. 195420, 2010.
- [73] O. V. Yazyev and S. G. Louie, “Electronic transport in polycrystalline graphene,” *Nature materials*, vol. 9, no. 10, p. 806, 2010.
- [74] A. W. Robertson, C. S. Allen, Y. A. Wu, K. He, J. Olivier, J. Neethling, A. I. Kirkland, and J. H. Warner, “Spatial control of defect creation in graphene at the nanoscale,” *Nature communications*, vol. 3, p. 1144, 2012.
- [75] D. Boukhvalov, “Dw boukhvalov and mi katsnelson, nano lett. 8, 4373 (2008).,” *Nano Lett.*, vol. 8, p. 4373, 2008.
- [76] M. Dienwiebel, G. S. Verhoeven, N. Pradeep, J. W. Frenken, J. A. Heimberg, and H. W. Zandbergen, “Superlubricity of graphite,” *Physical review letters*, vol. 92, no. 12, p. 126101, 2004.
- [77] M. Reguzzoni, A. Fasolino, E. Molinari, and M. C. Righi, “Potential energy surface for graphene on graphene: Ab initio derivation, analytical description, and microscopic interpretation,” *Physical Review*

- B*, vol. 86, no. 24, p. 245434, 2012.
- [78] I. V. Lebedeva, A. A. Knizhnik, A. M. Popov, O. V. Ershova, Y. E. Lozovik, and B. V. Potapkin, “Fast diffusion of a graphene flake on a graphene layer,” *Physical Review B*, vol. 82, no. 15, p. 155460, 2010.
- [79] H. Ghorbanfekr-Kalashami, F. Peeters, K. Novoselov, and M. Neek-Amal, “Spatial design and control of graphene flake motion,” *Physical Review B*, vol. 96, no. 6, p. 060101, 2017.
- [80] X. Feng, S. Kwon, J. Y. Park, and M. Salmeron, “Superlubric sliding of graphene nanoflakes on graphene,” *ACS nano*, vol. 7, no. 2, pp. 1718–1724, 2013.
- [81] A. E. Filippov, M. Dienwiebel, J. W. Frenken, J. Klafter, and M. Urbakh, “Torque and twist against superlubricity,” *Physical Review Letters*, vol. 100, no. 4, p. 046102, 2008.
- [82] S. Kawai, A. Benassi, E. Gnecco, H. Söde, R. Pawlak, X. Feng, K. Müllen, D. Passerone, C. A. Pignedoli, P. Ruffieux, *et al.*, “Superlubricity of graphene nanoribbons on gold surfaces,” *Science*, vol. 351, no. 6276, pp. 957–961, 2016.
- [83] E. Stolyarova, D. Stolyarov, K. Bolotin, S. Ryu, L. Liu, K. Rim, M. Klima, M. Hybertsen, I. Pogorelsky, I. Pavlishin, *et al.*, “Observation of graphene bubbles and effective mass transport under graphene films,” *Nano letters*, vol. 9, no. 1, pp. 332–337, 2008.
- [84] T. Georgiou, L. Britnell, P. Blake, R. Gorbachev, A. Gholinia, A. Geim, C. Casiraghi, and K. Novoselov, “Graphene bubbles with controllable curvature,” *Applied Physics Letters*, vol. 99, no. 9, p. 093103, 2011.
- [85] K. Yue, W. Gao, R. Huang, and K. M. Liechti, “Analytical methods for the mechanics of graphene bubbles,” *Journal of Applied Physics*, vol. 112, p. 083512, oct 2012.
- [86] J. Lu, A. C. Neto, and K. P. Loh, “Transforming moiré blisters into geometric graphene nano-bubbles,” *Nature communications*, vol. 3, p. 823, 2012.
- [87] N. Levy, S. Burke, K. Meaker, M. Panlasigui, A. Zettl, F. Guinea, A. C. Neto, and M. Crommie, “Strain-induced pseudo-magnetic fields greater than 300 tesla in graphene nanobubbles,” *Science*, vol. 329,

- no. 5991, pp. 544–547, 2010.
- [88] J. Zabel, R. R. Nair, A. Ott, T. Georgiou, A. K. Geim, K. S. Novoselov, and C. Casiraghi, “Raman spectroscopy of graphene and bilayer under biaxial strain: bubbles and balloons,” *Nano letters*, vol. 12, no. 2, pp. 617–621, 2012.
- [89] J. S. Bunch, S. S. Verbridge, J. S. Alden, A. M. Van Der Zande, J. M. Parpia, H. G. Craighead, and P. L. McEuen, “Impermeable atomic membranes from graphene sheets,” *Nano letters*, vol. 8, no. 8, pp. 2458–2462, 2008.
- [90] S. P. Koenig, N. G. Boddeti, M. L. Dunn, and J. S. Bunch, “Ultrastrong adhesion of graphene membranes,” *Nature nanotechnology*, vol. 6, no. 9, p. 543, 2011.
- [91] Z. Zong, C.-L. Chen, M. R. Dokmeci, and K. tak Wan, “Direct measurement of graphene adhesion on silicon surface by intercalation of nanoparticles,” *Journal of Applied Physics*, vol. 107, no. 2, p. 026104, 2010.
- [92] P. Wang, W. Gao, Z. Cao, K. M. Liechti, and R. Huang, “Numerical analysis of circular graphene bubbles,” *Journal of Applied Mechanics*, vol. 80, no. 4, p. 040905, 2013.
- [93] Z. Lu and M. L. Dunn, “van der waals adhesion of graphene membranes,” *Journal of Applied Physics*, vol. 107, no. 4, p. 044301, 2010.
- [94] E. Khestanova, F. Guinea, L. Fumagalli, A. K. Geim, and I. V. Grigorieva, “Universal shape and pressure inside bubbles appearing in van der waals heterostructures,” *Nature Communications*, vol. 7, p. 12587, aug 2016.
- [95] E. Whalley, “Chemical reactions in solution under high pressure,” *Berichte der Bunsengesellschaft für physikalische Chemie*, vol. 70, no. 9-10, pp. 958–968, 1966.
- [96] C. H. Y. X. Lim, M. Nesladek, and K. P. Loh, “Observing high-pressure chemistry in graphene bubbles,” *Angewandte Chemie International Edition*, vol. 53, no. 1, pp. 215–219, 2014.
- [97] K. Vasu, E. Prestat, J. Abraham, J. Dix, R. Kashtiban, J. Beheshtian, J. Sloan, P. Carbone, M. Neek-Amal, S. Haigh, *et al.*, “Van der waals

- pressure and its effect on trapped interlayer molecules,” *Nature communications*, vol. 7, p. 12168, 2016.
- [98] H. Ghorbanfekr-Kalashami, K. Vasu, R. Nair, F. M. Peeters, and M. Neek-Amal, “Dependence of the shape of graphene nanobubbles on trapped substance,” *Nature communications*, vol. 8, p. 15844, 2017.
- [99] N. Alberto, C. Vigário, D. Duarte, N. A. Almeida, G. Gonçalves, J. L. Pinto, P. A. Marques, R. Nogueira, and V. Neto, “Characterization of graphene oxide coatings onto optical fibers for sensing applications,” *Materials Today: Proceedings*, vol. 2, no. 1, pp. 171–177, 2015.
- [100] Q. Zheng, Z. Li, J. Yang, and J.-K. Kim, “Graphene oxide-based transparent conductive films,” *Progress in Materials Science*, vol. 64, pp. 200–247, jul 2014.
- [101] M. Kammoun, S. Berg, and H. Ardebili, “Flexible thin-film battery based on graphene-oxide embedded in solid polymer electrolyte,” *Nanoscale*, vol. 7, no. 41, pp. 17516–17522, 2015.
- [102] Y. Su, V. G. Kravets, S. L. Wong, J. Waters, A. K. Geim, and R. R. Nair, “Impermeable barrier films and protective coatings based on reduced graphene oxide,” *Nature Communications*, vol. 5, p. 4843, sep 2014.
- [103] A. C. Grimsdale and K. Müllen, “The chemistry of organic nanomaterials,” *Angewandte Chemie International Edition*, vol. 44, no. 35, pp. 5592–5629, 2005.
- [104] A. Lerf, H. He, M. Forster, and J. Klinowski, “Structure of graphite oxide revisited,” *The Journal of Physical Chemistry B*, vol. 102, no. 23, pp. 4477–4482, 1998.
- [105] Y. Han, Z. Xu, and C. Gao, “Ultrathin graphene nanofiltration membrane for water purification,” *Advanced Functional Materials*, vol. 23, no. 29, pp. 3693–3700, 2013.
- [106] R. Joshi, P. Carbone, F. C. Wang, V. G. Kravets, Y. Su, I. V. Grigorieva, H. Wu, A. K. Geim, and R. R. Nair, “Precise and ultrafast molecular sieving through graphene oxide membranes,” *science*, vol. 343, no. 6172, pp. 752–754, 2014.
- [107] S. Han, D. Wu, S. Li, F. Zhang, and X. Feng, “Porous graphene materials

- for advanced electrochemical energy storage and conversion devices,” *Advanced materials*, vol. 26, no. 6, pp. 849–864, 2014.
- [108] G. Liu, W. Jin, and N. Xu, “Graphene-based membranes,” *Chemical Society Reviews*, vol. 44, no. 15, pp. 5016–5030, 2015.
- [109] K. Huang, G. Liu, J. Shen, Z. Chu, H. Zhou, X. Gu, W. Jin, and N. Xu, “High-efficiency water-transport channels using the synergistic effect of a hydrophilic polymer and graphene oxide laminates,” *Advanced Functional Materials*, vol. 25, no. 36, pp. 5809–5815, 2015.
- [110] G. Hummer, J. C. Rasaiah, and J. P. Noworyta, “Water conduction through the hydrophobic channel of a carbon nanotube,” *Nature*, vol. 414, pp. 188–190, nov 2001.
- [111] M. Majumder, A. Siria, and L. Bocquet, “Flows in one-dimensional and two-dimensional carbon nanochannels: Fast and curious,” *MRS Bulletin*, vol. 42, pp. 278–282, apr 2017.
- [112] M. Neek-Amal, F. M. Peeters, I. V. Grigorieva, and A. K. Geim, “Commensurability effects in viscosity of nanoconfined water,” *ACS Nano*, vol. 10, pp. 3685–3692, feb 2016.
- [113] Y. Liu and Q. Wang, “Transport behavior of water confined in carbon nanotubes,” *Physical Review B*, vol. 72, p. 085420, aug 2005.
- [114] H. Kalashami, M. Neek-Amal, and F. Peeters, “Slippage dynamics of confined water in graphene oxide capillaries,” *Physical Review Materials*, vol. 2, no. 7, p. 074004, 2018.
- [115] J. Carrasco, A. Hodgson, and A. Michaelides, “A molecular perspective of water at metal interfaces,” *Nature Materials*, vol. 11, pp. 667–674, aug 2012.
- [116] J. Hasted, “Liquid water: Dielectric properties,” in *The Physics and Physical Chemistry of Water*, pp. 255–309, Springer, 1972.
- [117] D. R. Lide, *CRC handbook of chemistry and physics: a ready-reference book of chemical and physical data*.
CRC press, 1995.
- [118] X.-Z. Li, B. Walker, and A. Michaelides, “Quantum nature of the hydrogen bond,” *Proceedings of the National Academy of Sciences*, vol. 108, no. 16, pp. 6369–6373, 2011.

- [119] J. V. Barth, G. Costantini, and K. Kern, "Engineering atomic and molecular nanostructures at surfaces," in *Nanoscience And Technology: A Collection of Reviews from Nature Journals*, pp. 67–75, World Scientific, 2010.
- [120] V. Voloshin and Y. I. Naberukhin, "Proper and improper hydrogen bonds in liquid water," *Journal of Structural Chemistry*, vol. 57, no. 3, pp. 497–506, 2016.
- [121] M. Gordillo and J. Martí, "Hydrogen bond structure of liquid water confined in nanotubes," *Chemical Physics Letters*, vol. 329, no. 5-6, pp. 341–345, 2000.
- [122] H. Qiu, X. C. Zeng, and W. Guo, "Water in inhomogeneous nanoconfinement: Coexistence of multilayered liquid and transition to ice nanoribbons," *ACS nano*, vol. 9, no. 10, pp. 9877–9884, 2015.
- [123] J. Chen, A. Zen, J. G. Brandenburg, D. Alfè, and A. Michaelides, "Evidence for stable square ice from quantum monte carlo," *Physical Review B*, vol. 94, no. 22, p. 220102, 2016.
- [124] J. Chen, G. Schusteritsch, C. J. Pickard, C. G. Salzmann, and A. Michaelides, "Two dimensional ice from first principles: Structures and phase transitions," *Physical Review Letters*, vol. 116, p. 025501, jan 2016.
- [125] G. Algara-Siller, O. Lehtinen, F. Wang, R. Nair, U. Kaiser, H. Wu, A. Geim, and I. Grigorieva, "Square ice in graphene nanocapillaries," *Nature*, vol. 519, no. 7544, p. 443, 2015.
- [126] W. Zhou, K. Yin, C. Wang, Y. Zhang, T. Xu, A. Borisevich, L. Sun, J. C. Idrobo, M. F. Chisholm, S. T. Pantelides, *et al.*, "The observation of square ice in graphene questioned," *Nature*, vol. 528, no. 7583, p. E1, 2015.
- [127] M. P. Allen and D. J. Tildesley, *Computer simulation of liquids*. Oxford university press, 2017.
- [128] T. Gates and J. Hinkley, "Computational materials: modeling and simulation of nanostructured materials and systems," in *44th AIAA/ASME/ASCE/AHS/ASC Structures, Structural Dynamics, and Materials Conference*, p. 1534, 2003.

- [129] V. R. Subramanian and R. D. Braatz, "Current needs in electrochemical engineering education," *The Electrochemical Society Interface*, vol. 19, no. 2, pp. 37–38, 2010.
- [130] E. Schrödinger, "An undulatory theory of the mechanics of atoms and molecules," *Physical review*, vol. 28, no. 6, p. 1049, 1926.
- [131] D. J. Griffiths and D. F. Schroeter, *Introduction to quantum mechanics*. Cambridge University Press, 2018.
- [132] G. Grosso, *Solid state physics*. Waltham, Massachusetts: Elsevier, 2014.
- [133] P. Giannozzi, F. Ercolessi, and S. de Gironcoli, *Numerical methods in quantum mechanics*. University of Udine, 2013.
- [134] M. Born and R. Oppenheimer, "Zur quantentheorie der molekeln," *Annalen der Physik*, vol. 389, no. 20, pp. 457–484, 1927.
- [135] D. Sholl and J. A. Steckel, *Density functional theory: a practical introduction*. John Wiley & Sons, 2011.
- [136] W. Kohn, A. D. Becke, and R. G. Parr, "Density functional theory of electronic structure," *The Journal of Physical Chemistry*, vol. 100, no. 31, pp. 12974–12980, 1996.
- [137] P. Güttinger, "Das verhalten von atomen im magnetischen drehfeld," *Zeitschrift für Physik*, vol. 73, no. 3-4, pp. 169–184, 1932.
- [138] H. Hellmann, "Zur rolle der kinetischen elektronenenergie für die zwischenatomaren kräfte," *Zeitschrift für Physik*, vol. 85, no. 3-4, pp. 180–190, 1933.
- [139] R. P. Feynman, "Forces in molecules," *Physical Review*, vol. 56, no. 4, p. 340, 1939.
- [140] A. D. McNaught and A. D. McNaught, *Compendium of chemical terminology*, vol. 1669. Blackwell Science Oxford, 1997.
- [141] A. Hinchliffe, *Molecular modelling for beginners*. John Wiley & Sons, 2005.
- [142] D. Marx and J. Hutter, "Ab initio molecular dynamics," *Parallel com-*

- puting*, vol. 309, no. 309, p. 327, 2009.
- [143] W. Kohn and L. J. Sham, “Self-consistent equations including exchange and correlation effects,” *Physical review*, vol. 140, no. 4A, p. A1133, 1965.
- [144] G. Pastore, E. Smargiassi, and F. Buda, “Theory of ab initio molecular-dynamics calculations,” *Physical Review A*, vol. 44, no. 10, p. 6334, 1991.
- [145] R. Z. Khaliullin and T. D. Kühne, “Microscopic properties of liquid water from combined ab initio molecular dynamics and energy decomposition studies,” *Physical Chemistry Chemical Physics*, vol. 15, no. 38, p. 15746, 2013.
- [146] J. M. Sorenson, G. Hura, R. M. Glaeser, and T. Head-Gordon, “What can x-ray scattering tell us about the radial distribution functions of water?,” *The Journal of Chemical Physics*, vol. 113, pp. 9149–9161, Nov. 2000.
- [147] A. K. Soper, “The radial distribution functions of water as derived from radiation total scattering experiments: Is there anything we can say for sure?,” *ISRN Physical Chemistry*, vol. 2013, pp. 1–67, 2013.
- [148] D. Frenkel and B. Smit, *Understanding molecular simulation: from algorithms to applications*, vol. 1. Elsevier, 2001.
- [149] W. Cai, J. Li, and S. Yip, “1.09 molecular dynamics,” *Compr. Nucl. Mater.*, edited by JMK Rudy (Elsevier, Oxford, 2012), pp. 249–265, 2012.
- [150] R. K. Pathria, *Statistical Mechanics*. Butterworth Heinemann, 1996.
- [151] W. Greiner, L. Neise, and H. Stöcker, *Thermodynamics and statistical mechanics*. Springer Science & Business Media, 2012.
- [152] K. Huang, *Statistical mechanics*. New York: Wiley, 1987.
- [153] P. Walters, *An introduction to ergodic theory*, vol. 79. Springer Science & Business Media, 2000.

- [154] H. Touchette, "Ensemble equivalence for general many-body systems," *EPL (Europhysics Letters)*, vol. 96, p. 50010, nov 2011.
- [155] E. Cancès, F. Legoll, and G. Stoltz, "Theoretical and numerical comparison of some sampling methods for molecular dynamics," *ESAIM: Mathematical Modelling and Numerical Analysis*, vol. 41, no. 2, p. 351–389, 2007.
- [156] G. Torrie and J. Valleau, "Nonphysical sampling distributions in monte carlo free-energy estimation: Umbrella sampling," *Journal of Computational Physics*, vol. 23, no. 2, pp. 187–199, 1977.
- [157] P. Bash, U. Singh, R. Langridge, and P. Kollman, "Free energy calculations by computer simulation," *Science*, vol. 236, pp. 564–568, may 1987.
- [158] Y. Poggi, J. Filippini, and R. Aleonard, "The free energy as a function of the order parameter in nematic liquid crystals," *Physics Letters A*, vol. 57, pp. 53–56, may 1976.
- [159] N. Metropolis, A. W. Rosenbluth, M. N. Rosenbluth, A. H. Teller, and E. Teller, "Equation of state calculations by fast computing machines," *The journal of chemical physics*, vol. 21, no. 6, pp. 1087–1092, 1953.
- [160] N. Cooper, *From cardinals to chaos : reflections on the life and legacy of Stanislaw Ulam*.
Cambridge New York: Cambridge University Press, 1989.
- [161] L. Verlet, "Computer" experiments" on classical fluids. i. thermodynamical properties of lennard-jones molecules," *Physical review*, vol. 159, no. 1, p. 98, 1967.
- [162] W. C. Swope, H. C. Andersen, P. H. Berens, and K. R. Wilson, "A computer simulation method for the calculation of equilibrium constants for the formation of physical clusters of molecules: Application to small water clusters," *The Journal of Chemical Physics*, vol. 76, no. 1, pp. 637–649, 1982.
- [163] F. Hedman, *Algorithms for Molecular Dynamics Simulations*.
PhD thesis, Institutionen för fysikalisk kemi, oorganisk kemi och strukturkemi, 2006.

- [164] M. Steinhauser and S. Hiermaier, “A review of computational methods in materials science: examples from shock-wave and polymer physics,” *International journal of molecular sciences*, vol. 10, no. 12, pp. 5135–5216, 2009.
- [165] J. J. Erpenbeck and W. W. Wood, “Molecular dynamics calculations of the hard-sphere equation of state,” *Journal of Statistical Physics*, vol. 35, pp. 321–340, may 1984.
- [166] H. C. Andersen, “Molecular dynamics simulations at constant pressure and/or temperature,” *The Journal of chemical physics*, vol. 72, no. 4, pp. 2384–2393, 1980.
- [167] H. J. Berendsen, J. v. Postma, W. F. van Gunsteren, A. DiNola, and J. Haak, “Molecular dynamics with coupling to an external bath,” *The Journal of chemical physics*, vol. 81, no. 8, pp. 3684–3690, 1984.
- [168] W. G. Hoover, “Canonical dynamics: equilibrium phase-space distributions,” *Physical review A*, vol. 31, no. 3, p. 1695, 1985.
- [169] S. Nosé, “A unified formulation of the constant temperature molecular dynamics methods,” *The Journal of chemical physics*, vol. 81, no. 1, pp. 511–519, 1984.
- [170] R. Clausius, “Xvi. on a mechanical theorem applicable to heat,” *The London, Edinburgh, and Dublin Philosophical Magazine and Journal of Science*, vol. 40, no. 265, pp. 122–127, 1870.
- [171] E. N. Parker, “Tensor virial equations,” *Physical review*, vol. 96, no. 6, p. 1686, 1954.
- [172] M. E. Tuckerman, J. Alejandre, R. López-Rendón, A. L. Jochim, and G. J. Martyna, “A liouville-operator derived measure-preserving integrator for molecular dynamics simulations in the isothermal–isobaric ensemble,” *Journal of Physics A: Mathematical and General*, vol. 39, no. 19, p. 5629, 2006.
- [173] P. M. Morse, “Diatomic molecules according to the wave mechanics. ii. vibrational levels,” *Physical Review*, vol. 34, no. 1, p. 57, 1929.
- [174] C. S. Ewig, R. Berry, U. Dinur, J.-R. Hill, M.-J. Hwang, H. Li, C. Liang, J. Maple, Z. Peng, T. P. Stockfish, *et al.*, “Derivation of class ii force fields. viii. derivation of a general quantum mechanical force field

- for organic compounds,” *Journal of computational chemistry*, vol. 22, no. 15, pp. 1782–1800, 2001.
- [175] J. E. Jones, “On the determination of molecular fields.—ii. from the equation of state of a gas,” *Proc. R. Soc. Lond. A*, vol. 106, no. 738, pp. 463–477, 1924.
- [176] J. E. Mayer, “Dispersion and polarizability and the van der waals potential in the alkali halides,” *The Journal of Chemical Physics*, vol. 1, no. 4, pp. 270–279, 1933.
- [177] H. Lorentz, “Ueber die anwendung des satzes vom virial in der kinetischen theorie der gase,” *Annalen der physik*, vol. 248, no. 1, pp. 127–136, 1881.
- [178] P. P. Ewald, “Die berechnung optischer und elektrostatischer gitterpotentiale,” *Annalen der physik*, vol. 369, no. 3, pp. 253–287, 1921.
- [179] R. Hockney, *Computer Simulation Using Particles*.
Routledge, jan 1989.
- [180] E. Pollock and J. Glosli, “Comments on p3m, fmm, and the ewald method for large periodic coulombic systems,” *Computer Physics Communications*, vol. 95, no. 2-3, pp. 93–110, 1996.
- [181] M. González, “Force fields and molecular dynamics simulations,” *École thématique de la Société Française de la Neutronique*, vol. 12, pp. 169–200, 2011.
- [182] S. L. Mayo, B. D. Olafson, and W. A. Goddard, “Dreiding: a generic force field for molecular simulations,” *Journal of Physical chemistry*, vol. 94, no. 26, pp. 8897–8909, 1990.
- [183] A. K. Rappé, C. J. Casewit, K. Colwell, W. A. Goddard III, and W. Skiff, “Uff, a full periodic table force field for molecular mechanics and molecular dynamics simulations,” *Journal of the American chemical society*, vol. 114, no. 25, pp. 10024–10035, 1992.
- [184] B. R. Brooks, R. E. Bruccoleri, B. D. Olafson, D. J. States, S. a. Swaminathan, and M. Karplus, “Charmm: a program for macromolecular energy, minimization, and dynamics calculations,” *Journal of computational chemistry*, vol. 4, no. 2, pp. 187–217, 1983.
- [185] W. D. Cornell, P. Cieplak, C. I. Bayly, I. R. Gould, K. M. Merz, D. M.

- Ferguson, D. C. Spellmeyer, T. Fox, J. W. Caldwell, and P. A. Kollman, "A second generation force field for the simulation of proteins, nucleic acids, and organic molecules," *Journal of the American Chemical Society*, vol. 117, no. 19, pp. 5179–5197, 1995.
- [186] C. Oostenbrink, A. Villa, A. E. Mark, and W. F. Van Gunsteren, "A biomolecular force field based on the free enthalpy of hydration and solvation: the gromos force-field parameter sets 53a5 and 53a6," *Journal of computational chemistry*, vol. 25, no. 13, pp. 1656–1676, 2004.
- [187] W. L. Jorgensen and J. Tirado-Rives, "The opls [optimized potentials for liquid simulations] potential functions for proteins, energy minimizations for crystals of cyclic peptides and crambin," *Journal of the American Chemical Society*, vol. 110, no. 6, pp. 1657–1666, 1988.
- [188] H. Sun, "Compass: an ab initio force-field optimized for condensed-phase applications overview with details on alkane and benzene compounds," *The Journal of Physical Chemistry B*, vol. 102, no. 38, pp. 7338–7364, 1998.
- [189] W. L. Jorgensen, J. Chandrasekhar, J. D. Madura, R. W. Impey, and M. L. Klein, "Comparison of simple potential functions for simulating liquid water," *The Journal of chemical physics*, vol. 79, no. 2, pp. 926–935, 1983.
- [190] M. W. Mahoney and W. L. Jorgensen, "A five-site model for liquid water and the reproduction of the density anomaly by rigid, nonpolarizable potential functions," *The Journal of Chemical Physics*, vol. 112, no. 20, pp. 8910–8922, 2000.
- [191] H. J. Berendsen, J. P. Postma, W. F. van Gunsteren, and J. Hermans, *Interaction models for water in relation to protein hydration*. Springer, 1981.
- [192] H. Berendsen, J. Grigera, and T. Straatsma, "The missing term in effective pair potentials," *Journal of Physical Chemistry*, vol. 91, no. 24, pp. 6269–6271, 1987.
- [193] J. Barker, R. Fisher, and R. Watts, "Liquid argon: Monte carlo and molecular dynamics calculations," *Molecular Physics*, vol. 21, no. 4,

pp. 657–673, 1971.

- [194] M. S. Daw and M. I. Baskes, “Embedded-atom method: Derivation and application to impurities, surfaces, and other defects in metals,” *Physical Review B*, vol. 29, no. 12, p. 6443, 1984.
- [195] M. S. Daw and M. I. Baskes, “Semiempirical, quantum mechanical calculation of hydrogen embrittlement in metals,” *Physical review letters*, vol. 50, no. 17, p. 1285, 1983.
- [196] S. J. Stuart, A. B. Tutein, and J. A. Harrison, “A reactive potential for hydrocarbons with intermolecular interactions,” *The Journal of chemical physics*, vol. 112, no. 14, pp. 6472–6486, 2000.
- [197] J. Tersoff, “New empirical approach for the structure and energy of covalent systems,” *Physical Review B*, vol. 37, no. 12, p. 6991, 1988.
- [198] D. W. Brenner, O. A. Shenderova, J. A. Harrison, S. J. Stuart, B. Ni, and S. B. Sinnott, “A second-generation reactive empirical bond order (rebo) potential energy expression for hydrocarbons,” *Journal of Physics: Condensed Matter*, vol. 14, no. 4, p. 783, 2002.
- [199] A. C. Van Duin, S. Dasgupta, F. Lorant, and W. A. Goddard, “Reaxff: a reactive force field for hydrocarbons,” *The Journal of Physical Chemistry A*, vol. 105, no. 41, pp. 9396–9409, 2001.
- [200] V. Vinš, D. Celný, B. Planková, T. Němec, M. Duška, and J. Hrubý, “Molecular simulations of the vapor–liquid phase interfaces of pure water modeled with the SPC/e and the TIP4p/2005 molecular models,” *EPJ Web of Conferences*, vol. 114, p. 02136, 2016.
- [201] Y. Wu, H. L. Tepper, and G. A. Voth, “Flexible simple point-charge water model with improved liquid-state properties,” *The Journal of chemical physics*, vol. 124, no. 2, p. 024503, 2006.
- [202] B. R. H. de Aquino, H. Ghorbanfekr-Kalashami, M. Neek-Amal, and F. M. Peeters, “Ionized water confined in graphene nanochannels,” *Physical Chemistry Chemical Physics*, vol. -, no. -, pp. –, 2019.
- [203] W. Zhang and A. C. Van Duin, “Second-generation reaxff water force field: Improvements in the description of water density and oh-anion diffusion,” *The Journal of Physical Chemistry B*, vol. 121, no. 24, pp. 6021–6032, 2017.

- [204] W. L. Jorgensen, D. S. Maxwell, and J. Tirado-Rives, "Development and testing of the opls all-atom force field on conformational energetics and properties of organic liquids," *Journal of the American Chemical Society*, vol. 118, no. 45, pp. 11225–11236, 1996.
- [205] W. J. Mortier, S. K. Ghosh, and S. Shankar, "Electronegativity-equalization method for the calculation of atomic charges in molecules," *Journal of the American Chemical Society*, vol. 108, no. 15, pp. 4315–4320, 1986.
- [206] S. Chmiela, H. E. Sauceda, K.-R. Müller, and A. Tkatchenko, "Towards exact molecular dynamics simulations with machine-learned force fields," *Nature communications*, vol. 9, no. 1, p. 3887, 2018.
- [207] B. Cheng, E. A. Engel, J. Behler, C. Dellago, and M. Ceriotti, "Ab initio thermodynamics of liquid and solid water," *Proceedings of the National Academy of Sciences*, vol. 116, no. 4, pp. 1110–1115, 2019.
- [208] A. P. Bartók and G. Csányi, "Gaussian approximation potentials: A brief tutorial introduction," *International Journal of Quantum Chemistry*, vol. 115, no. 16, pp. 1051–1057, 2015.
- [209] V. L. Deringer and G. Csányi, "Machine learning based interatomic potential for amorphous carbon," *Physical Review B*, vol. 95, no. 9, p. 094203, 2017.
- [210] J. Behler, "Perspective: Machine learning potentials for atomistic simulations," *The Journal of chemical physics*, vol. 145, no. 17, p. 170901, 2016.
- [211] L. T. Kong, "Phonon dispersion measured directly from molecular dynamics simulations," *Computer Physics Communications*, vol. 182, no. 10, pp. 2201–2207, 2011.
- [212] C. Campaná and M. H. Müser, "Practical green's function approach to the simulation of elastic semi-infinite solids," *Physical Review B*, vol. 74, no. 7, p. 075420, 2006.
- [213] P. Rowe, G. Csányi, D. Alfè, and A. Michaelides, "Development of a machine learning potential for graphene," *Physical Review B*, vol. 97, no. 5, p. 054303, 2018.
- [214] A. Singraber, J. Behler, and C. Dellago, "Library-based LAMMPS imple-

- mentation of high-dimensional neural network potentials,” *Journal of Chemical Theory and Computation*, vol. 15, pp. 1827–1840, jan 2019.
- [215] V. Quaranta, J. Behler, and M. Hellström, “Structure and dynamics of the liquid–water/zinc-oxide interface from machine learning potential simulations,” *The Journal of Physical Chemistry C*, vol. 123, pp. 1293–1304, dec 2018.
- [216] J. Behler, “First principles neural network potentials for reactive simulations of large molecular and condensed systems,” *Angewandte Chemie International Edition*, vol. 56, pp. 12828–12840, aug 2017.
- [217] D. Chandler, *Introduction to Modern Statistical Mechanics*. Oxford University Press, sep 1987.
- [218] P. Kumar, S. V. Buldyrev, F. W. Starr, N. Giovambattista, and H. E. Stanley, “Thermodynamics, structure, and dynamics of water confined between hydrophobic plates,” *Physical Review E*, vol. 72, no. 5, p. 051503, 2005.
- [219] R. Zangi, “Water confined to a slab geometry: a review of recent computer simulation studies,” *Journal of Physics: Condensed Matter*, vol. 16, no. 45, p. S5371, 2004.
- [220] I. Svishchev and P. Kusalik, “Structure in liquid water: A study of spatial distribution functions,” *The Journal of chemical physics*, vol. 99, no. 4, pp. 3049–3058, 1993.
- [221] J. Martı, “Analysis of the hydrogen bonding and vibrational spectra of supercritical model water by molecular dynamics simulations,” *The Journal of chemical physics*, vol. 110, no. 14, pp. 6876–6886, 1999.
- [222] J. Dannenberg, L. Haskamp, and A. Masunov, “Are hydrogen bonds covalent or electrostatic? a molecular orbital comparison of molecules in electric fields and h-bonding environments,” *The Journal of Physical Chemistry A*, vol. 103, no. 35, pp. 7083–7086, 1999.
- [223] D. Bertolini, M. Cassetari, M. Ferrario, P. Grigolini, and G. Salvetti, *Dynamical Properties of Hydrogen-Bonded Liquids*. John Wiley & Sons, Inc., mar 2007.
- [224] J. C. Dore and J. Teixeira, *Hydrogen-bonded liquids*.

- Springer Science & Business Media, 2012.
- [225] B. R. de Aquino, H. Ghorbanfekr-Kalashami, M. Neek-Amal, and F. Peeters, “Electrostrictive behavior of confined water subjected to gpa pressure,” *Physical Review B*, vol. 97, no. 14, p. 144111, 2018.
- [226] O. Nwobi, L. Long, M. Micci, O. Nwobi, L. Long, and M. Micci, *Molecular dynamics studies of transport properties of supercritical fluids*. American Institute of Aeronautics and Astronautics, jan 1997.
- [227] R. E. Jones and K. K. Mandadapu, “Adaptive green-kubo estimates of transport coefficients from molecular dynamics based on robust error analysis,” *The Journal of chemical physics*, vol. 136, no. 15, p. 154102, 2012.
- [228] B. Alder, D. Gass, and T. Wainwright, “Studies in molecular dynamics. viii. the transport coefficients for a hard-sphere fluid,” *The Journal of Chemical Physics*, vol. 53, no. 10, pp. 3813–3826, 1970.
- [229] G. S. Fanourgakis, J. Medina, and R. Prosimiti, “Determining the bulk viscosity of rigid water models,” *The Journal of Physical Chemistry A*, vol. 116, no. 10, pp. 2564–2570, 2012.
- [230] M. A. González and J. L. Abascal, “The shear viscosity of rigid water models,” *The Journal of Chemical Physics*, vol. 132, no. 9, p. 096101, 2010.
- [231] V. Levashov, “Contribution to viscosity from the structural relaxation via the atomic scale green-kubo stress correlation function,” *The Journal of chemical physics*, vol. 147, no. 18, p. 184502, 2017.
- [232] X. Chen, G. Cao, A. Han, V. K. Punyamurtula, L. Liu, P. J. Culligan, T. Kim, and Y. Qiao, “Nanoscale fluid transport: size and rate effects,” *Nano letters*, vol. 8, no. 9, pp. 2988–2992, 2008.
- [233] S. Viscardy and P. Gaspard, “Viscosity in molecular dynamics with periodic boundary conditions,” *Physical Review E*, vol. 68, no. 4, p. 041204, 2003.
- [234] B. Ramos-Alvarado, S. Kumar, and G. Peterson, “Hydrodynamic slip length as a surface property,” *Physical Review E*, vol. 93, no. 2, p. 023101, 2016.
- [235] L. Bocquet and J.-L. Barrat, “Hydrodynamic boundary conditions, cor-

- relation functions, and kubo relations for confined fluids,” *Physical review E*, vol. 49, no. 4, p. 3079, 1994.
- [236] G. Tocci, L. Joly, and A. Michaelides, “Friction of water on graphene and hexagonal boron nitride from ab initio methods: very different slippage despite very similar interface structures,” *Nano letters*, vol. 14, no. 12, pp. 6872–6877, 2014.
- [237] L. Li, J. Mo, and Z. Li, “Flow and slip transition in nanochannels,” *Physical Review E*, vol. 90, no. 3, p. 033003, 2014.
- [238] H. Zhang, Z. Zhang, and H. Ye, “Molecular dynamics-based prediction of boundary slip of fluids in nanochannels,” *Microfluidics and Nanofluidics*, vol. 12, no. 1-4, pp. 107–115, 2012.
- [239] K. Huang and I. Szlufarska, “Green-kubo relation for friction at liquid-solid interfaces,” *Physical Review E*, vol. 89, no. 3, p. 032119, 2014.
- [240] E. Cadelano, P. L. Palla, S. Giordano, and L. Colombo, “Nonlinear elasticity of monolayer graphene,” *Physical review letters*, vol. 102, no. 23, p. 235502, 2009.
- [241] C. Metzger, S. Reñi, M. Liu, S. V. Kusminskiy, A. H. C. Neto, A. K. Swan, and B. B. Goldberg, “Biaxial strain in graphene adhered to shallow depressions,” *Nano Letters*, vol. 10, pp. 6–10, jan 2010.
- [242] B. D. Jensen, K. E. Wise, and G. M. Odegard, “Simulation of the elastic and ultimate tensile properties of diamond, graphene, carbon nanotubes, and amorphous carbon using a revised reaxff parametrization,” *The Journal of Physical Chemistry A*, vol. 119, no. 37, pp. 9710–9721, 2015.
- [243] A. K. Geim, “Graphene: status and prospects,” *science*, vol. 324, no. 5934, pp. 1530–1534, 2009.
- [244] C. Xu and H. Li, “C. xu, h. li, and k. banerjee, iee trans. electron devices 55, 3264 (2008).,” *IEEE Trans. Electron Devices*, vol. 55, p. 3264, 2008.
- [245] S. Mahnia and A. Phirouznia, “The influence of the zigzag and armchair leads on quantum transport through the graphene based quantum rings,” *Journal of Computational Electronics*, vol. 13, no. 1, pp. 224–229, 2014.

- [246] F. Wang, Y. Zhang, C. Tian, C. Girit, A. Zettl, M. Crommie, and Y. R. Shen, "Gate-variable optical transitions in graphene," *science*, vol. 320, no. 5873, pp. 206–209, 2008.
- [247] D. Geng, S. Yang, Y. Zhang, J. Yang, J. Liu, R. Li, T.-K. Sham, X. Sun, S. Ye, and S. Knights, "Nitrogen doping effects on the structure of graphene," *Applied Surface Science*, vol. 257, no. 21, pp. 9193–9198, 2011.
- [248] Y.-F. Lu, S.-T. Lo, J.-C. Lin, W. Zhang, J.-Y. Lu, F.-H. Liu, C.-M. Tseng, Y.-H. Lee, C.-T. Liang, and L.-J. Li, "Nitrogen-doped graphene sheets grown by chemical vapor deposition: synthesis and influence of nitrogen impurities on carrier transport," *ACS nano*, vol. 7, no. 8, pp. 6522–6532, 2013.
- [249] H. Wang, T. Maiyalagan, and X. Wang, "Review on recent progress in nitrogen-doped graphene: synthesis, characterization, and its potential applications," *Acs Catalysis*, vol. 2, no. 5, pp. 781–794, 2012.
- [250] T. Cui, R. Lv, Z.-H. Huang, H. Zhu, J. Zhang, Z. Li, Y. Jia, F. Kang, K. Wang, and D. Wu, "Synthesis of nitrogen-doped carbon thin films and their applications in solar cells," *Carbon*, vol. 49, no. 15, pp. 5022–5028, 2011.
- [251] R. Lv, T. Cui, M.-S. Jun, Q. Zhang, A. Cao, D. S. Su, Z. Zhang, S.-H. Yoon, J. Miyawaki, I. Mochida, *et al.*, "Open-ended, n-doped carbon nanotube–graphene hybrid nanostructures as high-performance catalyst support," *Advanced Functional Materials*, vol. 21, no. 5, pp. 999–1006, 2011.
- [252] J. Budzien, A. P. Thompson, and S. V. Zybin, "Reactive molecular dynamics simulations of shock through a single crystal of pentaerythritol tetranitrate," *The Journal of Physical Chemistry B*, vol. 113, no. 40, pp. 13142–13151, 2009.
- [253] S. Plimpton, "Fast parallel algorithms for short-range molecular dynamics," *Journal of computational physics*, vol. 117, no. 1, pp. 1–19, 1995.
- [254] H. M. Aktulga, J. C. Fogarty, S. A. Pandit, and A. Y. Grama, "Parallel

- reactive molecular dynamics: Numerical methods and algorithmic techniques,” *Parallel Computing*, vol. 38, no. 4-5, pp. 245–259, 2012.
- [255] A. Zandiatashbar, G. Lee, S. J. An, and S. Lee, “A. zandiatashbar, gh lee, sj an, s. lee, n. mathew, m. terrones, t. hayashi, cr picu, j. hone, and n. koratkar, nat. commun. 5, 3186 (2014).,” *Nat. Commun.*, vol. 5, p. 3186, 2014.
- [256] H. Liu, Y. Liu, and D. Zhu, “Chemical doping of graphene,” *Journal of materials chemistry*, vol. 21, no. 10, pp. 3335–3345, 2011.
- [257] M. Zelisko, Y. Hanlumyuang, S. Yang, Y. Liu, C. Lei, J. Li, P. M. Ajayan, and P. Sharma, “Anomalous piezoelectricity in two-dimensional graphene nitride nanosheets,” *Nature communications*, vol. 5, p. 4284, 2014.
- [258] K. N. Kudin, G. E. Scuseria, and B. I. Yakobson, “C 2 f, bn, and c nanoshell elasticity from ab initio computations,” *Physical Review B*, vol. 64, no. 23, p. 235406, 2001.
- [259] M. Sammalkorpi, A. Krashennnikov, A. Kuronen, K. Nordlund, and K. Kaski, “Mechanical properties of carbon nanotubes with vacancies and related defects,” *Physical Review B*, vol. 70, no. 24, p. 245416, 2004.
- [260] G. Cao, “Atomistic studies of mechanical properties of graphene,” *Polymers*, vol. 6, no. 9, pp. 2404–2432, 2014.
- [261] T. Fang, W. Chang, and J. Yang, “Molecular dynamics study on mechanical properties of graphene sheets with a hole,” *Dig. J. Nanomater. Biostruct*, vol. 9, pp. 1207–1214, 2014.
- [262] L. Colombo and S. Giordano, “Nonlinear elasticity in nanostructured materials,” *Reports on Progress in Physics*, vol. 74, no. 11, p. 116501, 2011.
- [263] C. Woods, F. Withers, M. Zhu, Y. Cao, G. Yu, A. Kozikov, M. B. Shalom, S. Morozov, M. Van Wijk, A. Fasolino, *et al.*, “Macroscopic self-reorientation of interacting two-dimensional crystals,” *Nature communications*, vol. 7, p. 10800, 2016.
- [264] D. Wang, G. Chen, C. Li, M. Cheng, W. Yang, S. Wu, G. Xie, J. Zhang, J. Zhao, X. Lu, *et al.*, “Thermally induced graphene rotation on

- hexagonal boron nitride,” *Physical review letters*, vol. 116, no. 12, p. 126101, 2016.
- [265] J. Cai, P. Ruffieux, R. Jaafar, M. Bieri, T. Braun, S. Blankenburg, M. Muoth, A. P. Seitsonen, M. Saleh, X. Feng, *et al.*, “Atomically precise bottom-up fabrication of graphene nanoribbons,” *Nature*, vol. 466, no. 7305, p. 470, 2010.
- [266] A. N. Kolmogorov and V. H. Crespi, “Registry-dependent interlayer potential for graphitic systems,” *Physical Review B*, vol. 71, no. 23, p. 235415, 2005.
- [267] F. Peymanirad, “F. peymanirad, s. singh kumar, h. ghorbanfekr-kalashami, ks novoselov, fm peeters, and m. neek-amal, 2d mater. 4, 025015 (2017).,” *2D Mater.*, vol. 4, p. 025015, 2017.
- [268] D. Dietzel, M. Feldmann, U. D. Schwarz, H. Fuchs, and A. Schirmeisen, “Scaling laws of structural lubricity,” *Physical review letters*, vol. 111, no. 23, p. 235502, 2013.
- [269] E. Koren and U. Duerig, “Moiré scaling of the sliding force in twisted bilayer graphene,” *Physical Review B*, vol. 94, no. 4, p. 045401, 2016.
- [270] M. Ma, A. Benassi, A. Vanossi, and M. Urbakh, “Critical length limiting superlow friction,” *Physical review letters*, vol. 114, no. 5, p. 055501, 2015.
- [271] J. Lahiri, Y. Lin, P. Bozkurt, I. I. Oleynik, and M. Batzill, “An extended defect in graphene as a metallic wire,” *Nature nanotechnology*, vol. 5, no. 5, p. 326, 2010.
- [272] N. Tambe, “Ns tambe and b. bhushan, nanotechnology 16, 2309 (2005).,” *Nanotechnology*, vol. 16, p. 2309, 2005.
- [273] J. Yang, Z. Liu, F. Grey, Z. Xu, X. Li, Y. Liu, M. Urbakh, Y. Cheng, and Q. Zheng, “Observation of high-speed microscale superlubricity in graphite,” *Physical review letters*, vol. 110, no. 25, p. 255504, 2013.
- [274] G. Zamborlini, M. Imam, L. L. Patera, T. O. Menteş, N. Stojić, C. Africh, A. Sala, N. Binggeli, G. Comelli, and A. Locatelli, “Nanobubbles at GPa pressure under graphene,” *Nano Letters*, vol. 15, pp. 6162–6169, aug 2015.
- [275] K. Xu, P. Cao, and J. R. Heath, “Graphene visualizes the first water

- adlayers on mica at ambient conditions,” *Science*, vol. 329, no. 5996, pp. 1188–1191, 2010.
- [276] C. H. Y. X. Lim, A. Sorkin, Q. Bao, A. Li, K. Zhang, M. Nesladek, and K. P. Loh, “A hydrothermal anvil made of graphene nanobubbles on diamond,” *Nature communications*, vol. 4, p. 1556, 2013.
- [277] R. Mu, Q. Fu, L. Jin, L. Yu, G. Fang, D. Tan, and X. Bao, “Visualizing chemical reactions confined under graphene,” *Angewandte Chemie International Edition*, vol. 51, no. 20, pp. 4856–4859, 2012.
- [278] M. S. F. Mario, M. Neek-Amal, and F. Peeters, “Aa-stacked bilayer square ice between graphene layers,” *Physical Review B*, vol. 92, no. 24, p. 245428, 2015.
- [279] A. K. Soper and M. A. Ricci, “Structures of high-density and low-density water,” *Physical review letters*, vol. 84, no. 13, p. 2881, 2000.
- [280] A. Polian and M. Grimsditch, “Elastic properties and density of helium up to 20 gpa,” *EPL (Europhysics Letters)*, vol. 2, no. 11, p. 849, 1986.
- [281] W. L. Jorgensen, J. D. Madura, and C. J. Swenson, “Optimized intermolecular potential functions for liquid hydrocarbons,” *Journal of the American Chemical Society*, vol. 106, pp. 6638–6646, oct 1984.
- [282] G. Sesé and R. Palomar, “Molecular dynamics studies of supercooled ethanol,” *The Journal of Chemical Physics*, vol. 114, no. 22, pp. 9975–9981, 2001.
- [283] K. Kholmurodov, E. Dushanov, K. Yasuoka, H. Khalil, A. Galal, S. Ahmed, N. Sweilam, and H. Moharram, “Molecular dynamics simulation of the interaction of ethanol-water mixture with a pt surface,” *Natural Science*, vol. 3, no. 12, p. 1011, 2011.
- [284] X. Zhou and F. P. Doty, “Embedded-ion method: An analytical energy-conserving charge-transfer interatomic potential and its application to the la-br system,” *Physical Review B*, vol. 78, no. 22, p. 224307, 2008.
- [285] J. P. Brodholt, “Molecular dynamics simulations of aqueous nacl solutions at high pressures and temperatures,” *Chemical Geology*, vol. 151, no. 1-4, pp. 11–19, 1998.
- [286] W. Humphrey, A. Dalke, and K. Schulten, “VMD – Visual Molecular

- Dynamics,” *Journal of Molecular Graphics*, vol. 14, pp. 33–38, 1996.
- [287] A. Kohlmeyer and J. Vermaas, “Akohlmey/topotools: Release 1.7,” 2017.
- [288] T. Björkman, A. Gulans, A. V. Krashennnikov, and R. M. Nieminen, “van der waals bonding in layered compounds from advanced density-functional first-principles calculations,” *Physical review letters*, vol. 108, no. 23, p. 235502, 2012.
- [289] M. Neek-Amal and F. Peeters, “Strain-engineered graphene through a nanostructured substrate. i. deformations,” *Physical Review B*, vol. 85, no. 19, p. 195445, 2012.
- [290] I. E. Berinskii, A. M. Krivtsov, and A. M. Kudarova, “Bending stiffness of a graphene sheet,” *Physical Mesomechanics*, vol. 17, pp. 356–364, oct 2014.
- [291] K. Zakharchenko, J. Los, M. I. Katsnelson, and A. Fasolino, “Atomistic simulations of structural and thermodynamic properties of bilayer graphene,” *Physical Review B*, vol. 81, no. 23, p. 235439, 2010.
- [292] D. Tsai, “The virial theorem and stress calculation in molecular dynamics,” *The Journal of Chemical Physics*, vol. 70, no. 3, pp. 1375–1382, 1979.
- [293] J. A. Hodgdon and F. H. Stillinger, “Inherent structures in the potential energy landscape of solid 4he,” *The Journal of chemical physics*, vol. 102, no. 1, pp. 457–464, 1995.
- [294] H. Mao, R. Hemley, Y. Wu, A. Jephcoat, L. Finger, C. Zha, and W. Bassett, “High-pressure phase diagram and equation of state of solid helium from single-crystal x-ray diffraction to 23.3 gpa,” *Physical review letters*, vol. 60, no. 25, p. 2649, 1988.
- [295] M. Kondrin, A. Pronin, and V. Brazhkin, “Crystallization and vitrification of ethanol at high pressures,” *The Journal of chemical physics*, vol. 141, no. 19, p. 194504, 2014.
- [296] H. Rafii-Tabar, “Computational modelling of thermo-mechanical and transport properties of carbon nanotubes,” *Physics Reports*, vol. 390, no. 4-5, pp. 235–452, 2004.
- [297] Z. Mi, *Strength, Elasticity and Phase Transition Study on NaCl and MgO-NaCl Mixture to Mantle Pressures*.

- PhD thesis, The University of Western Ontario London, 2013.
- [298] S. J. Haigh, A. Gholinia, R. Jalil, S. Romani, L. Britnell, D. C. Elias, K. S. Novoselov, L. A. Ponomarenko, A. K. Geim, and R. Gorbachev, “Cross-sectional imaging of individual layers and buried interfaces of graphene-based heterostructures and superlattices,” *Nature Materials*, vol. 11, pp. 764–767, jul 2012.
- [299] A. V. Kretinin, Y. Cao, J. S. Tu, G. L. Yu, R. Jalil, K. S. Novoselov, S. J. Haigh, A. Gholinia, A. Mishchenko, M. Lozada, T. Georgiou, C. R. Woods, F. Withers, P. Blake, G. Eda, A. Wirsig, C. Hucho, K. Watanabe, T. Taniguchi, A. K. Geim, and R. V. Gorbachev, “Electronic properties of graphene encapsulated with different two-dimensional atomic crystals,” *Nano Letters*, vol. 14, pp. 3270–3276, may 2014.
- [300] H. W. Kim, H. W. Yoon, S.-M. Yoon, B. M. Yoo, B. K. Ahn, Y. H. Cho, H. J. Shin, H. Yang, U. Paik, S. Kwon, J.-Y. Choi, and H. B. Park, “Selective gas transport through few-layered graphene and graphene oxide membranes,” *Science*, vol. 342, pp. 91–95, oct 2013.
- [301] B. Radha, A. Esfandiar, F. C. Wang, A. P. Rooney, K. Gopinadhan, A. Keerthi, A. Mishchenko, A. Janardanan, P. Blake, L. Fumagalli, M. Lozada-Hidalgo, S. Garaj, S. J. Haigh, I. V. Grigorieva, H. A. Wu, and A. K. Geim, “Molecular transport through capillaries made with atomic-scale precision,” *Nature*, vol. 538, pp. 222–225, sep 2016.
- [302] H. Li, Z. Song, X. Zhang, Y. Huang, S. Li, Y. Mao, H. J. Ploehn, Y. Bao, and M. Yu, “Ultrathin, molecular-sieving graphene oxide membranes for selective hydrogen separation,” *Science*, vol. 342, pp. 95–98, oct 2013.
- [303] S. Sahu and M. Zwolak, “Golden aspect ratio for ion transport simulation in nanopores,” *Physical Review E*, vol. 98, p. 012404, jul 2018.
- [304] S. K. Kannam, B. D. Todd, J. S. Hansen, and P. J. Daivis, “How fast does water flow in carbon nanotubes?,” *The Journal of Chemical Physics*, vol. 138, p. 094701, mar 2013.
- [305] N. Wei, X. Peng, and Z. Xu, “Breakdown of fast water transport in graphene oxides,” *Physical Review E*, vol. 89, p. 012113, jan 2014.

- [306] S. Chowdhuri and A. Chandra, "Molecular dynamics simulations of aqueous nacl and kcl solutions: Effects of ion concentration on the single-particle, pair, and collective dynamical properties of ions and water molecules," *The Journal of Chemical Physics*, vol. 115, no. 8, pp. 3732–3741, 2001.
- [307] J.-P. Ryckaert, G. Ciccotti, and H. J. Berendsen, "Numerical integration of the cartesian equations of motion of a system with constraints: molecular dynamics of n-alkanes," *Journal of computational physics*, vol. 23, no. 3, pp. 327–341, 1977.
- [308] A. P. Lyubartsev and A. Laaksonen, "Concentration effects in aqueous nacl solutions. a molecular dynamics simulation," *The Journal of Physical Chemistry*, vol. 100, no. 40, pp. 16410–16418, 1996.
- [309] B. Hess, "Determining the shear viscosity of model liquids from molecular dynamics simulations," *The Journal of chemical physics*, vol. 116, no. 1, pp. 209–217, 2002.
- [310] M. H. Köhler and L. B. da Silva, "Size effects and the role of density on the viscosity of water confined in carbon nanotubes," *Chemical Physics Letters*, vol. 645, pp. 38–41, 2016.
- [311] H. Qiu and W. Guo, "Electromelting of confined monolayer ice," *Physical Review Letters*, vol. 110, p. 195701, may 2013.
- [312] H. Qiu and W. Guo, "Electromelting of confined monolayer ice," *Phys. Rev. Lett.*, vol. 110, p. 195701, May 2013.
- [313] A. Siria, P. Poncharal, A.-L. Biance, R. Fulcrand, X. Blase, S. T. Purcell, and L. Bocquet, "Giant osmotic energy conversion measured in a single transmembrane boron nitride nanotube," *Nature*, vol. 494, pp. 455–458, feb 2013.
- [314] P. Mark and L. Nilsson, "Structure and dynamics of the TIP3p, SPC, and SPC/e water models at 298 k," *The Journal of Physical Chemistry A*, vol. 105, pp. 9954–9960, nov 2001.
- [315] D. W. McCall and D. C. Douglass, "The effect of ions on the self-diffusion of water. i. concentration dependence," *The Journal of Physical Chemistry*, vol. 69, pp. 2001–2011, jun 1965.
- [316] H. Huang, Z. Song, N. Wei, L. Shi, Y. Mao, Y. Ying, L. Sun, Z. Xu,

- and X. Peng, “Ultrafast viscous water flow through nanostrand-channelled graphene oxide membranes,” *Nature Communications*, vol. 4, p. 2979, dec 2013.
- [317] B. Rotenberg, “Water in clay nanopores,” *MRS Bulletin*, vol. 39, no. 12, pp. 1074–1081, 2014.
- [318] M. Suzuki, N. Wada, D. R. Hines, and M. Whittingham, “Hydration states and phase transitions in vermiculite intercalation compounds,” *Physical Review B*, vol. 36, no. 5, p. 2844, 1987.
- [319] D. A. Young and D. E. Smith, “Simulations of clay mineral swelling and hydration: dependence upon interlayer ion size and charge,” *The Journal of Physical Chemistry B*, vol. 104, no. 39, pp. 9163–9170, 2000.
- [320] E. Boek, P. Coveney, and N. Skipper, “Monte carlo molecular modeling studies of hydrated li-, na-, and k-smectites: Understanding the role of potassium as a clay swelling inhibitor,” *Journal of the American Chemical Society*, vol. 117, no. 50, pp. 12608–12617, 1995.
- [321] S. L. Teich-McGoldrick, J. A. Greathouse, C. F. Jové-Colón, and R. T. Cygan, “Swelling properties of montmorillonite and beidellite clay minerals from molecular simulation: Comparison of temperature, interlayer cation, and charge location effects,” *The Journal of Physical Chemistry C*, vol. 119, pp. 20880–20891, aug 2015.
- [322] N. Skipper, K. Refson, and J. McConnell, “Computer simulation of interlayer water in 2: 1 clays,” *The Journal of Chemical Physics*, vol. 94, no. 11, pp. 7434–7445, 1991.
- [323] L. Jin, A. Jamili, L. Huang, and F. Perez, “Modeling the mechanisms of clay damage by molecular dynamic simulation,” *Geofluids*, vol. 2017, pp. 1–8, 2017.
- [324] P. Demontis, M. Masia, and G. B. Suffritti, “Water nanoconfined in clays: the structure of na vermiculite revisited by ab initio simulations,” *The Journal of Physical Chemistry C*, vol. 117, no. 30, pp. 15583–15592, 2013.
- [325] P. Demontis, M. Masia, and G. B. Suffritti, “Peculiar structure of water in slightly superhydrated vermiculite clay studied by car-parrinello

- molecular dynamics simulations,” *The Journal of Physical Chemistry C*, vol. 118, no. 15, pp. 7923–7931, 2014.
- [326] A. Delville, “Structure and properties of confined liquids: a molecular model of the clay-water interface,” *The Journal of Physical Chemistry*, vol. 97, no. 38, pp. 9703–9712, 1993.
- [327] J. A. Greathouse, R. T. Cygan, J. T. Fredrich, and G. R. Jerauld, “Adsorption of aqueous crude oil components on the basal surfaces of clay minerals: Molecular simulations including salinity and temperature effects,” *The Journal of Physical Chemistry C*, vol. 121, pp. 22773–22786, sep 2017.
- [328] A. Kadoura, A. K. Narayanan Nair, and S. Sun, “Molecular dynamics simulations of carbon dioxide, methane, and their mixture in montmorillonite clay hydrates,” *The Journal of Physical Chemistry C*, vol. 120, no. 23, pp. 12517–12529, 2016.
- [329] J. Sunner, K. Nishizawa, and P. Kebarle, “Ion-solvent molecule interactions in the gas phase. the potassium ion and benzene,” *The Journal of Physical Chemistry*, vol. 85, no. 13, pp. 1814–1820, 1981.
- [330] M. Meot-Ner and C. A. Deakyne, “Unconventional ionic hydrogen bonds. 1. CH_{δ+}...O...X complexes of quaternary ions with n- and π-donors,” *Journal of the American Chemical Society*, vol. 107, pp. 469–474, jan 1985.
- [331] J. C. Ma and D. A. Dougherty, “The cation-π interaction,” *Chemical Reviews*, vol. 97, pp. 1303–1324, aug 1997.
- [332] M. Neek-Amal, L. Covaci, K. Shakouri, and F. Peeters, “Electronic structure of a hexagonal graphene flake subjected to triaxial stress,” *Physical Review B*, vol. 88, no. 11, p. 115428, 2013.
- [333] V. Calado, G. Schneider, A. Theulings, C. Dekker, and L. Vandersypen, “Formation and control of wrinkles in graphene by the wedging transfer method,” *Applied Physics Letters*, vol. 101, no. 10, p. 103116, 2012.
- [334] C. Wang, Y. Liu, L. Lan, and H. Tan, “Graphene wrinkling: formation, evolution and collapse,” *Nanoscale*, vol. 5, no. 10, pp. 4454–4461, 2013.

- [335] S. Deng and V. Berry, “Wrinkled, rippled and crumpled graphene: an overview of formation mechanism, electronic properties, and applications,” *Materials Today*, vol. 19, no. 4, pp. 197–212, 2015.
- [336] D. R. Dreyer, S. Park, C. W. Bielawski, and R. S. Ruoff, “The chemistry of graphene oxide,” *Chem. Soc. Rev.*, vol. 39, no. 1, pp. 228–240, 2010.

LIST OF PUBLICATIONS

- [1] H. Ghorbanfekr-Kalashami, M. Neek-Amal, and F. M. Peeters, “Slip-page dynamics of confined water in graphene oxide capillaries”, *Physical Review Materials* **2**, 074004 (2018).
- [2] H. Ghorbanfekr-Kalashami, K. S. Vasu, R. R. Nair, F. M. Peeters & M. Neek-Amal, “Dependence of the shape of graphene nanobubbles on trapped substance”, *Nature Communications* **8**, 15844 (2017).
- [3] H. Ghorbanfekr-Kalashami, F. M. Peeters, K. S. Novoselov, and M. Neek-Amal, “Spatial design and control of graphene flake motion”, *Physical Review B(R)* **96**, 060101 (2017).
- [4] H. Ghorbanfekr-Kalashami, M. Neek-Amal, and F. M. Peeters, “N-doped graphene: Polarization effects and structural properties”, *Physical Review B* **93**, 174112 (2016).
- [5] K.-G. Zhou, K. S. Vasu, C. T. Cherian, M. Neek-Amal, J. C. Zhang, H. Ghorbanfekr-Kalashami, K. Huang, O. P. Marshall, V. G. Kravets, J. Abraham, Y. Su, A. N. Grigorenko, A. Pratt, A. K. Geim, F. M. Peeters, K. S. Novoselov & R. R. Nair, “Electrically controlled water permeation through graphene oxide membranes”, *Nature* **559**, 236 (2018).
My contribution was the computational modeling of the ionized water permeation through the graphene-oxide membrane using classical MD simulations.
- [6] R. Deaquino, H. Ghorbanfekr-Kalashami, Mehdi Neek-Amal, François M Peeters, “Ionized water confined in graphene nanochannels”, *Physical Chemistry Chemical Physics* (2019).
I performed a series of ab initio MD simulations in order to calculate the recombination time of ionized water confined between graphene layers.

- [7] Belisa R. H. de Aquino, H. Ghorbanfekr-Kalashami, M. Neek-Amal, and F. M. Peeters, “Electrostrictive behavior of confined water subjected to GPa pressure”, *Physical Review B* **97**, 144111 (2018).

I was involved in performing MD simulations of the confined water under an out-of-plane external electric field in μVT ensemble (model B).

- [8] F. Peymanirad, S. K. Singh, H. Ghorbanfekr-Kalashami, K. S. Novoselov, F. M. Peeters, and M. Neek-Amal, “Thermal activated rotation of graphene flake on graphene”, *2D Materials* **4**, 025015 (2017).

I performed classical MD simulations concerning the binding energy of a graphene flake to the graphene at different alignments and interlayer distances.

CIRRUCULUM VITAE

Hossein Ghorbanfekr

CONTACT

Campus Groenenborger (G.U.210)
 Groenenborgerlaan 171, 2020 Antwerp, Belgium
 Mobile: +32 483 647 388
 Email: hgh.comphys@gmail.com
 Skype: [hgh.comphys](https://www.skype.com/people/hgh.comphys)



PORTFOLIO (hyperlinks)

ResearchGate GitHub LinkedIn

EDUCATION

Ph.D. in Physics, University of Antwerp, Belgium *Jul 2015 - present*

Thesis: “*Graphene-based Membranes and Nano-confined Water: Molecular Dynamics Simulation Study*“ under the supervision of Profs. François Peeters and Mehdi Neek-Amal.

M.Sc. in Physics, Sharif University of Technology, Iran *Sep 2008 - Jan 2011*

Thesis: “*Quantum Walk Applications in Search Algorithms*” under the supervision of Prof. Vahid Karimipour.

B.Sc. in Physics, University of Guilan, Iran *Sep 2004 - Sep 2008*

Thesis: “*Binding Energy and Excitonic States in Double Quantum Wells GaAs-AlGaAs in Homogeneous Magnetic Field*” under the supervision of Prof. Hossein Panahi.

Diploma in Physics and Mathematics.

PROFESSIONAL SKILLS

Nanophysics:

2D Materials, Graphene, Nanoconfined Water, Nanomembranes

Programming:

Python, C/C++, Fortran, Git, OOP, HPC, OSSD

Molecular Simulations:

LAMMPS, CPMD, QE, VASP, VMD

Machine Learning:

Scikit-learn, Tensorflow (Keras, C API), NNP

COLLABORATIVE EXPERIENCES

National Graphene Institute and School of Chemical Engineering and Analytical Science, University of Manchester *Jun 2016 - present*

Successfully collaborated with the experimental team led by Prof. R. R. Nair, performing fundamental research on graphene nanobubbles that involved in carrying out molecular dynamics simulations and interpreting physical aspects. This project was published in Nature Communications (2017), collaborated with the same group

for another research project on smart graphene-oxide membrane development that involved modeling and simulations. This project was published in Nature (2018).

School of Physics and Astronomy, University of Manchester *Aug 2016 - 2017*

This research project in collaboration with Prof. K. S. Novoselov, the Nobel prize winner in physics 2010, has been published in Physical Review B (2017).

VISITS

Helmholtz-Zentrum Dresden-Rossendorf, Dresden, Germany *Aug 2018*

Atomistic simulations of irradiation-induced phenomena group lead by Prof. Arkady Krashennnikov was a great opportunity to present him and his group members my research works and had a chance to have in-depth discussions on relevant computational tools in particular density functional theory and molecular simulations.

SCHOOLS AND WORKSHOPS

Schools: 2D Materials for Environment and Energy Applications, Graphene Study Summer School, Gothenburg, Sweden (*Jul 2018*) • Simulation Techniques for the Study of Many Particles Systems, MolSim2016, University of Amsterdam (*Jan 2016*) • Computer Simulations of Biological Systems, IPM, Iran (*Apr 2014*)

Workshops: Machine-Learning for Material Science, ML4MS 2019, Aalto University, Helsinki, Finland (*May 2019*) • Advanced techniques for scientific programming and management of open source software packages, SAIFR, Brazil (*Apr 2015*) • Parallel programming and parallel architecture for HPC and developer school for HPC applications in earth sciences, ICTP, Italy (*Oct 2014*)

PRESENTATIONS

Posters: Slippage dynamics of confined water in graphene oxide capillaries, Graphene study summer school, Gothenburg, Sweden (*Jul 2018*) • Spatial design and control of graphene flake motion, From Physics of Graphene to Graphene for Physics, Solvay conference, Belgium (*Sep 2017*)

TALKS

Talks: LAMMPS and GROMACS molecular dynamics packages on GPU, 4th workshop on high performance and grid computing (HPC4), institute for research in fundamental sciences, Iran (*Dec 2011*)

OTHER RELEVANT INFORMATION

Languages: Persian (native), English (fluent), Dutch (basic)

Awards: Doctoral fellowship from Antwerp University, Belgium (*Jul 2015*) • Gold medal at regional physics olympiad of undergraduate students at Mazandaran University, Iran (*Jan 2008*) • Ranked 14th among ~15,000 participants in Iran's physics graduate studies entrance Exam (*Mar 2008*) • Ranked 3rd among physics undergraduate students at University of Guilan, Iran (*Sep 2008*)

Hobbies: Active member of Ichi Dai kyokushin karate, Antwerp, Belgium